Master's thesis

NTNU
Norwegian University of Science and Technology
Faculty of Information Technology and Electrical Engineering
Department of Engineering Cybernetics

Jenny Bogen Griffiths

Multivariable Super-Twisting Control of Fixed-Wing UAVs

Master's thesis in Cybernetics and Robotics
Supervisor: Tor Arne Johansen, Erlend Magnus Lervik Coates
January 2021

NTNU
Kunnskap for en bedre verden

Jenny Bogen Griffiths

Multivariable Super-Twisting Control of Fixed-Wing UAVs

Master's thesis in Cybernetics and Robotics
Supervisor: Tor Arne Johansen, Erlend Magnus Lervik Coates
January 2021

Norwegian University of Science and Technology
Faculty of Information Technology and Electrical Engineering
Department of Engineering Cybernetics

NTNU
Norwegian University of
Science and Technology

Abstract

This thesis investigates the performance of several sliding mode control (SMC) algorithms and evaluates their robustness to disturbances, parametric uncertainties and modeling discrepancies. This is done by applying them to a simulation model of a fixed-wing unmanned aerial vehicle (UAV) operating in an uncertain environment where external disturbances are present. Both a decoupled model of the longitudinal dynamics of the unmanned aerial vehicle and a full six-degrees-of-freedom (6DOF) model is implemented in MATLAB/Simulink. For the 6DOF model of the UAV, the performance of a decoupled control design is compared to that of a multivariable control design.

The SMC algorithms that are considered in this report include the first-order saturation controller and several versions of the super-twisting algorithm (STA), which is known as an especially robust second-order sliding mode (SOSM) algorithm. The single-input-single-output (SISO) versions of these control algorithms are implemented for the model of the decoupled longitudinal UAV-dynamics, while multivariable versions are implemented for the 6DOF UAV-model.

The control algorithms are implemented in MATLAB/Simulink, and the assumptions that guarantee the stability of each algorithm are discussed. Additionally, a stability analysis of the internal dynamics of the decoupled longitudinal model is performed.

The simulation results show that all the SMC designs considered in this report are capable of following a set of waypoints by tracking a roll and pitch reference. Even when external disturbances, unmodeled dynamics, process noise and modeling uncertainties are present in the system, most of the control designs show promising results. Based on the results, the most promising SMC algorithms in terms of tracking performance, robustness, and smoothness of the control input are the saturation controller, the generalized STA (GSTA), and the generalized multivariable STA (GMSTA).

Sammendrag

I denne oppgaven blir robustheten til flere sliding mode kontroll (SMC)-algoritmer undersøkt ved å implementere dem for en usikker simuleringsmodell av et lite ubemannet fly som opererer i et miljø hvor den er påvirket av eksterne forstyrrelser. Både en forenklet modell av dronens langsgående dynamikk og en komplett dronemodell med seks frihetsgrader er implementert i MATLAB/Simulink for å teste både endimensjonale og multivariable kontrollalgoritmer. For den komplette dronemodellen blir også ytelsen til et multivariabelt kontrolldesign sammenlignet med et design basert på flere parallelle endimensjonale regulatorer.

Algoritmene som blir undersøkt i denne rapporten er en førsteordens konvensjonell SMC-algoritme, og tre versjoner av super-twisting-algoritmen (STA), som er kjent som en spesielt robust SMC-algoritme. Endimensjonale implementasjoner av SMC-algoritmene blir brukt på modellen av fixed-wing dronens langsgående dynamikk, mens multivariable implementasjoner av de samme algoritmene blir brukt på den komplette dronemodellen.

Alle algoritmene blir implementert i MATLAB/Simulink, og forutsetningene som garanterer stabiliteten til hver algoritme blir diskutert. I tillegg utføres en stabilitetsanalyse av den interne dynamikken til modellen av den langsgående dynamikken til dronen.

Simuleringsresultatene viser at alle SMC-designene er i stand til å følge et sett med veipunkter ved å følge en rull- og pitchreferanse. Selv når eksterne forstyrrelser, umodellert dynamikk, prosesstøy og modelleringsusikkerhet er tilstede i systemet, viser de fleste av kontrolldesignene lovende resultater. Basert på resultatene er metningsregulatoren, generalisert STA og generalisert multivariabel STA de mest lovende SMC-algoritmene når det gjelder følging av referansen, robusthet og hvor implementerbart kontrollsignalet er.

Preface

This thesis marks the end of my time at the Department of Engineering Cybernetics at the Norwegian University of Science and Technology (NTNU) and is the final step towards an M.Sc. in cybernetics and robotics. This report documents the work done during the fall of 2020 and is a continuation of my project thesis from the spring of 2020.

The MATLAB-model of the 6DOF fixed-wing UAV that is used in this report was provided by my co-supervisor Erlend Magnus Lervik Coates, in addition to a MATLAB-script that calculates the trim conditions for the UAV-model.

I would like to thank my main supervisor Tor Arne Johansen for allowing me to work on this project. Furthermore, I would like to thank my co-supervisor Erlend for extremely valuable guidance and feedback, both for this thesis and for my project thesis.

Table of Contents

List of Tables

List of Figures

List of Symbols

The list of symbol is in alphabetical order. The symbol $*$ is used to denote symbols that are used for multiple quantities with different subscripts, i.e. a_{*_1} is both a_{ϕ_1} and a_{θ_1}. Additionally, an arbitrary number is denoted by i so that k_{*_i} can mean both k_{a_1} and k_{e_2}.

a_{*_1}	Sliding variable gain
$a(\cdot)$	Multivariable sliding dynamics function
$a_*(\cdot)$	SISO sliding dynamics function
A	Bound on $\left\|a(\cdot)\right\|$
$\bar{A}$	Bound on $\left\|\dot{a}(\cdot)\right\|$
A_*	Bound on $\left\|a_*(\cdot)\right\|$
A_{ij}	Matrix in the regular form decomposition of a system
α	Angle of attack
α_g	Parameter in the GMSTA design
$\alpha_u(\cdot)$	Unit vector control function
$\alpha_i(\cdot)$	Adaptive control gains
α_{*_m}	Threshold value in adaptive gain update rules
b	Wing span
$b(\cdot)$	Multivariable sliding dynamics function
$b_*(\cdot)$	SISO sliding dynamics function
$b_0(\cdot)$	Lower bound on $b_*(\cdot)$
B	Bound on $\left\|b(\cdot)\right\|$
$\bar{B}$	Bound on $\left\|\dot{b}(\cdot)\right\|$
B_*	Bound on $\left\|b_*(\cdot)\right\|$
B_2	Matrix in the UVC design

β	Sideslip angle
β_g	Parameter in the GMSTA design
$\beta_*(\cdot)$	Adaptive control gain
β_{*_g}	Control gain
c	Mean aerodynamic chord of the UAV wing
C_D	Aerodynamic drag coefficient
χ	Course angle
C_l	Aerodynamic moment coefficient along the body frame x-axis
C_L	Aerodynamic lift coefficient
C_m	Aerodynamic pitching moment coefficient
C_n	Aerodynamic moment coefficient along body frame x-axis
C_{prop}	Aerodynamic coefficient for the propeller
C_Y	Aerodynamic force coefficient along the body frame y-axis
C_i	Bound on $\left\|\varphi_i(\cdot)\right\|$
$d_g(\cdot)$	Disturbance signal due to wind gusts in the decoupled longitudinal model
$d_*(\cdot)$	Disturbance signal due to modeling errors and uncertainties
$d(\cdot)$	Disturbance signal in the aerodynamic forces and moments in the 6DOF model with components denoted as d_f and d_m
D	Force due to drag
δ	Bound on disturbances and perturbations
δ_i	Bound on disturbances and perturbations
δ_a	Control signal denoting the aileron deflection
δ_e	Control signal denoting the elevator deflection
$\delta_{e_{eq}}$	Longitudinal equivalent control
δ_r	Control signal denoting the rudder deflection
δ_t	Control signal denoting the throttle deflection
δ_{*_0}	Control signal at trim conditions
$\bar{\delta}_*$	Control signal that is transformed by a control coefficient transformation
$\mathcal{D}$	Set in which the 6DOF system dynamics are bounded
$\mathcal{D}_*$	Set in which the decoupled system dynamics are bounded
e_*	Tracking error
ϵ_i	Positive constant in adaptive gain update rules
η	Reaching condition constant
f	External force applied to the UAV expressed in the inertial frame

f_a	Vector of aerodynamic forces with components D, L, and f_y
f_b	Sum of external forces acting on the UAV expressed in the body frame with components denoted as f_x, f_y, and f_z
f_{b_u}	The control-dependent part of f_b
f_{b_x}	The state-dependent part of f_b
f_g	Force due to gravity
f_m	Matched disturbances in the UVC design
f_s	Sampling frequency
f_σ	Function in the multivariable sliding dynamics
f_t	Force due to thrust
f_u	Unmatched disturbances in the UVC design
f_y	Forces acting on the UAV in the body frame y-axis
$f_{*_i}(\cdot)$	State-space functions
$\mathcal{F}^b$	Body coordinate frame
$\mathcal{F}^i$	Inertial coordinate frame
$\mathcal{F}^s$	Stability coordinate frame
$\mathcal{F}^v$	Vehicle coordinate frame
$\mathcal{F}^w$	Wind coordinate frame
g	Gravitational acceleration
$g_{*_i}(\cdot)$	State-space functions
G	Bound on $\left\|\gamma(\cdot)\right\|$
G_*	Bound on $\left\|\gamma_*(\cdot)\right\|$
G_i	Bound on the perturbations in the GMSTA design
$\gamma(\cdot)$	Perturbation in the multivariable sliding dynamics
γ_1	Positive constant in the multivariable gain update rules
γ_f	Flight-path angle
γ_g	Parameter in the GMSTA design
$\gamma_i, i = 2, 3$	Unit vector control gains
$\gamma_*(\cdot)$	Perturbation in the SISO sliding dynamics
γ_{*_i}	Positive constant in adaptive gain update rules
Γ	The reduced-attitude of the UAV
Γ_b	Products of inertia
Γ_d	Desired reduced-attitude vector
h	Altitude
h_d	Desired altitude

$h_{*_i}(\cdot)$	State-space functions
$(\mathbf{i}^b, \mathbf{j}^b, \mathbf{k}^b)$	Unit vectors defining the body frame
$(\mathbf{i}^i, \mathbf{j}^i, \mathbf{k}^i)$	Unit vectors defining the inertial frame
$(\mathbf{i}^s, \mathbf{j}^s, \mathbf{k}^s)$	Unit vectors defining the stability frame
$(\mathbf{i}^v, \mathbf{j}^v, \mathbf{k}^v)$	Unit vectors defining the vehicle frame
$(\mathbf{i}^w, \mathbf{j}^w, \mathbf{k}^w)$	Unit vectors defining the wind frame
I_b	The inertia matrix with elements denoted as I_x, I_y, I_z, and I_{xz}
K	Control gain
k_Γ	Multivariable sliding variable gain
k_*	Control gain
k_{*_i}	Control gain
k_{i_*}	PI integral gain
k_{p_*}	PI proportional gain
k_{motor}	Constant that specifies the efficiency of the motor
l	External moment applied to the UAV about the body frame x-axis
L	Force due to lift
λ_{*_i}	Positive constant in the adaptive gain update rules
λ_1	Positive constant in the multivariable adaptive gain update rules
λ_i	Eigenvalues
Λ	Matrix in the UVC design
m	Mass of the UAV
m	External moment applied to the UAV about the body frame y-axis
M	Matrix in the UVC design
m_a	Vector of aerodynamic moments with components denoted as l, m, and n
m_b	External moments applied to the UAV expressed in the body frame
m_{b_u}	The control-dependent part of m_b
m_{b_x}	The state-dependent part of m_b
m_i	External moments applied to the UAV expressed in the inertial frame
m_t	Moment due to thrust
μ_i	Parameters in the GSTA design

n	External moment applied to the UAV about the body frame z-axis
ω	Angular rate of the body frame w.r.t. the inertial frame
Ω	Propeller speed
ω_0	Natural frequency of the second-order actuator dynamics
ω_i	Parameters in the AMSTA design
ω_b	Angular rate of the body frame w.r.t. to the inertial frame projected onto the body frame axes with components denoted as p, q, and r
$\omega_b^{\perp}$	The component of ω_b orthogonal to Γ
$\omega_b^{\parallel}$	The component of ω_b parallel to Γ
ω_d	Vector of the desired angular rates with components denoted as p_d, q_d, and r_d
ω_w	The effect of the wind on the angular velocity of the UAV
ω_1	Positive constant in the multivariable adaptive gain update rules
ω_{*_i}	Positive constant in the adaptive gain update rules
p	Roll rate of the UAV along the body frame x-axis
p_d	Inertial down position of the UAV
p_e	Inertial east position of the UAV
p_g	Parameter in the GMSTA design
p_n	Inertial north position of the UAV
p_r	Relative roll rate of the UAV along the body frame x-axis
ϕ	Roll angle
$\phi_{*_i}(\cdot)$	Generalized super-twisting algorithm control design functions
P_2	Matrix in the UVC design
Φ	Matrix in the UVC design
ψ	Yaw angle
q	Pitch rate along the body frame y-axis
$\mathbf{q}$	A quaternion
q_g	Parameter in the GMSTA design
q_r	Relative pitch rate along the body frame y-axis
q_i	The elements of a quaternion $\mathbf{q}$
$\mathbf{r}$	Position vector containing the inertial position states (p_n, p_e, p_d)
r	Yaw rate along the body frame z-axis
ρ	Density of air
$\rho_u(\cdot)$	Unit vector control function

r_r	Relative yaw rate along the body frame z-axis
$\mathcal{R}_a^b$	Rotation matrix from frame a to frame b
S	Surface area of the wing
S_i	Matrix in the UVC design
$\mathbb{S}^2$	The two-sphere
$\mathbb{S}^3$	The three-sphere
S_{prop}	Area of the propeller
σ	Multivariable sliding variable
σ_*	Sliding variable
σ_T	Threshold value in multivariable adaptive gain update rules
$\underline{\sigma}(\cdot)$	Spectral decomposition
$\mathcal{S}$	The zero-measure set
T	Thrust along body frame x-axis
T_p	Torque applied to the motor
$T_\Gamma\mathbb{S}^2$	The tangent space at Γ
T_Θ	High-pass filter time constant
T_*	Low-pass filter time constant
Θ	Angular position vector that contains the Euler angles (ϕ, θ, ψ)
θ	Pitch angle
Θ_d	Euler angle reference vector with components denoted ϕ_d, θ_d and ψ_d
$\mathbb{T}^3$	The three-torus
u	Inertial velocity of the UAV projected onto the body frame x-axis
$u(\cdot)$	Control input
$u_{eq}(\cdot)$	Equivalent control
$\bar{u}(\cdot)$	Manipulated control input by a control coefficient transformation
$u_*(\cdot)$	The parts of UVC law
u_r	Relative velocity projected onto the body frame x-axis
u_{smc}	Control generated by the SMC algoritms with components denoted δ_a, δ_e and δ_r
u_w	Inertial wind velocity projected onto the body frame x-axis
v	Inertial velocity of the UAV projected onto the body frame y-axis
V	Lyapunov function candidate
V_a	Airspeed of the UAV

V_{a_0}	Airspeed at trim conditions
$\mathbf{v}_b$	Ground velocity expressed as the velocity of the UAV w.r.t. the body frame
$\mathbf{v}_g$	Ground velocity defined as the velocity of the UAV w.r.t. the inertial frame
V_g	Ground speed
$\mathbf{v}_r$	Velocity vector defined as the airspeed of the UAV w.r.t. the air mass
v_r	Relative velocity projected onto the body frame y-axis
$\mathbf{v}_w$	Wind velocity defined as the velocity of the wind w.r.t. the inertial frame
V_w	Wind speed
v_w	Inertial wind velocity projected onto the body frame y-axis
$\mathbf{v}_{w_g}$	Stochastic process that represents wind gusts
$\mathbf{v}_{w_s}$	Constant vector that represents steady ambient wind
$\varphi_i(\cdot)$	Sliding dynamics perturbation
ε	Size of boundary layer in the sat-function and the update laws for the adaptive control algorithms
$\vartheta(\cdot)$	Perturbation in the multivariable sliding dynamics
w	Inertial velocity of the UAV projected onto the body frame z-axis
w_*	Band-limited white noise
$\mathbf{w}_i$	Waypoint in $\mathbb{R}^3$
w_d	Component of $\mathbf{v}_w$ in the down direction
w_e	Component of $\mathbf{v}_w$ in the east direction
w_n	Component of $\mathbf{v}_w$ in the north direction
w_r	Relative velocity projected onto the body frame z-axis
w_w	Inertial wind velocity projected onto the body frame z-axis
$\mathcal{W}$	Set of waypoints
x	State of the 6DOF model
x_*	State variable
x_*^*	Equilibrium state
z	Function in control designs for the multivariable super-twisting algorithm and its extensions
z_*	Function in control designs for the super-twisting algorithm and its extensions
ζ	Damping factor in the second-order actuator dynamics

List of Abbreviations

AMGSTA	Adaptive Multivariable Generalized Super-Twisting Algorithm
AMSTA	Adaptive Multivariable Super-Twisting Algorithm
AoA	Angle of Attack
ASTA	Adaptive Super-Twisting Algorithm
DOF	Degrees Of Freedom
GMSTA	Generalized Multivariable Super-Twisting Algorithm
GSTA	Generalized Super-Twisting Algorithm
IAE	Integral Absolute Error
IAI	Integral Absolute Input
ISE	Integral Square Error
ISI	Integral Square Input
MIMO	Multiple-Input Multiple-Output
MSTA	Multivariable Super-Twisting Algorithm
PI	Proportional-Integral
PID	Proportional–Integral–Derivative
RLV	Reusable Launch Vehicle
SISO	Single-Input Single-Output
SMC	Sliding Mode Control
SOSM	Second Order Sliding Mode
STA	Super-Twisting Algorithm
TF	Transfer Function
UAV	Unmanned Aerial Vehicle
UVC	Unit Vector Control
VGMSTA	Variable Gain Multivariable Super-Twisting Algorithm

Chapter 1

Introduction

1.1 Motivation

Designing an attitude control system for an unmanned aerial vehicle (UAV) is a challenging task as it is typically required to maintain stability and robustness while operating in uncertain environments. There are two main types of UAVs; multirotor UAVs, which generate lift using rotors, and fixed-wing UAVs, which use their forward speed to generate lift. Figure 1.1 shows an example of a fixed-wing UAV.

Figure 1.1: The Skywalker X8 Fixed-Wing UAV (picture from Bøhn et al. (2019)).

Exact modeling of both the multirotor and fixed-wing UAV is difficult due to uncertainties in the aerodynamic coefficients and other system parameters and the fact that they are highly coupled and nonlinear systems. The aerodynamic coefficients are both difficult and expensive to estimate, and it is, therefore, necessary to develop an autopilot that is robust and effective even though there are uncertainties in the system parameters.

An example of a robust control method is the sliding mode control (SMC), which is known for its insensitivity to parametric uncertainties and matched disturbances. It is also known for eliminating the need for exact modeling of the system, so it can be used in control designs for uncertain systems, such as a UAV. This comes at a cost, however, as SMC is based on high-frequency switching of the control action, which may cause

unwanted chattering in the control signal. The chattering phenomenon is typically caused by characteristics in the system that are unaccounted for in the control design, such as delays or unmodeled fast dynamics.

Several chattering-reducing techniques exist. These include both conventional first-order algorithms and second-order algorithms such as the super-twisting algorithm (STA). The latter is known as an especially powerful and robust control algorithm. Several extensions, both single-input and multivariable, of the basic STA exist. By applying the STA and its extensions to the model of a UAV in flight, when it is subject to disturbances due to wind gusts and parametric uncertainties, it is possible to investigate and compare the robustness of the different control algorithms.

The work in this report is a continuation of Griffiths (2020), where the saturation controller, the STA, and an adaptive and a generalized version of the STA were implemented for an uncertain decoupled model of the lateral dynamics of a fixed-wing UAV. All the controllers performed satisfactory tracking of a roll angle reference even in the presence of external disturbances and unmodeled dynamics. Applying the same controllers to a decoupled model of the longitudinal dynamics of a UAV in this report is the first step to verifying if it is possible to use controllers based on simplified UAV-models on a full six-degrees-of-freedom (6DOF) UAV-model.

Additionally, it is interesting to investigate the performance of a single-input single-output (SISO), and a multiple-input multiple-output (MIMO) control design using the same type of control algorithm applied to the same model. The difference between the two control designs is that the coupling between the subsystems is viewed as an additional disturbance in the system in the modeling of the SISO control design, whereas the coupling is accounted for in the MIMO control design.

1.2 Scope of the Project

There are two main objectives of this report. The first one is to compare the tracking performance of several single-input SMC algorithms applied to a decoupled model of the longitudinal dynamics of a fixed-wing UAV. The second objective is to compare the performance of two different control designs, one based on single-input controllers, and one on multivariable controllers, applied to the same UAV model. The control objective is to perform tracking of one or more reference signals, depending on the UAV-model and the control design.

Figure 1.2 shows the typical software architecture for autonomous or semi-autonomous navigation, guidance, and control of a UAV model. Since the objective in this report is to assess the performance of different control designs applied to a UAV, the main focus is on the contents of the Autopilot- and UAV-blocks in Figure 1.2. Additionally, a brief presentation of the contents of the Path planning-, Path manager-, and Path following-blocks is included in the explanation of the reference trajectory for the 6DOF UAV model.

The SMC algorithms that are presented and implemented in this report are the saturation controller, the super-twisting algorithm, the adaptive STA (ASTA), the generalized STA (GSTA), the multivariable saturation controller (MSAT), the multivariable STA (MSTA), the adaptive MSTA (AMSTA), and the generalized MSTA (GMSTA). For each

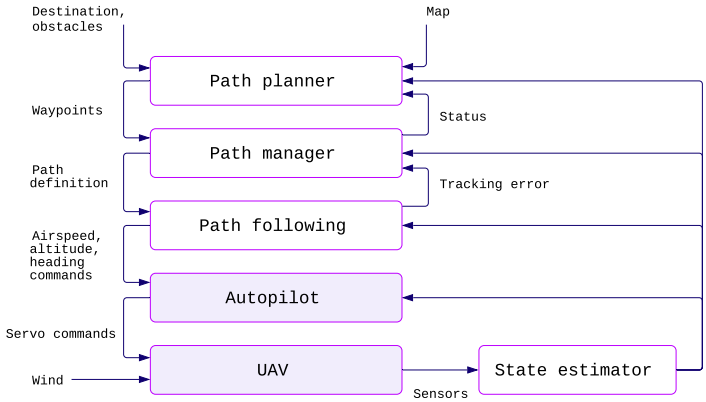

Figure 1.2: A typical system architecture for control of unmanned aircrafts.

of these algorithms, the theory is presented, and the necessary model assumptions guaranteeing the stability of the system are discussed.

1.3 Contributions

The main contributions of this thesis are

- A simulation model of the longitudinal dynamics of a fixed-wing UAV is implemented. For this model, four SISO SMC algorithms are designed and implemented. All four algorithms are able to follow a reference signal consisting of both step-inputs and a sine wave in the presence of process noise and external disturbances.
- The internal stability of the longitudinal dynamics of a fixed-wing UAV is investigated.
- Four multivariable SMC algorithms are designed and implemented for a 6DOF model of a fixed-wing UAV, and their applicability to the 6DOF model is discussed and verified.
- An existing implementation of a 6DOF simulation model for the Aerosonde UAV was provided to me, based on Beard and McLain (2012). This has been extended to include process noise, modeling discrepancies and external disturbances in the form of wind gusts and constant wind. Two different control designs, a decoupled design and a multivariable one, are developed and implemented for this model. The properties and performance of each control design are investigated and compared by performing simulations with an increasing amount of disturbances present in the system, to determine which control approach is the most promising.

1.4 Report Outline

This report is divided into nine chapters. Chapter 2 presents the theory behind the model of the fixed-wing UAV, while chapter 3 presents the theory of SMC and of the STA its extensions. A literature review on the application of the MSTA and extensions of it to attitude control problems is presented in chapter 4. Chapter 5 presents the design of the controllers implemented in this report, in addition to a stability analysis of the longitudinal decoupled model presented in chapter 2, and a discussion of the stability of the proposed control designs. The UAV simulation model that is implemented to test the control algorithms designed in chapter 5 is presented in chapter 6. Chapter 7 presents the results of applying the different controllers to the decoupled longitudinal UAV model, as well as a discussion of these results. The results of applying two different control designs to the 6DOF model are presented and discussed in chapter 8. Finally, chapter 9 presents a conclusion, in addition to suggestions for future work.

1.5 Reuse of Material

The material in this report that concerns the design of single-input control algorithms applied a decoupled longitudinal model of a fixed-wing UAV mirrors the work that was done in Griffiths (2020) for a decoupled lateral UAV model. Thus, much of the work in this report is based on the same theory and methodology as Griffiths (2020). The relevant material from Griffiths (2020) is therefore also included in this report.

The parts of chapter 2 that are taken from Griffiths (2020) are the introduction to section 2.1, subsections 2.1.2, 2.1.6, 2.1.7, and 2.1.8, the paragraphs *Control Surfaces* and *Lateral Forces and Moments* in subsection 2.4.2, and subsection 2.6.1. Some of chapter 3 is also from Griffiths (2020), namely section 3.1, section 3.2, section 3.7, and section 3.5. The final parts that are taken directly from Griffiths (2020) are section 5.2 and subsection 5.7.1.

Some material is also taken from Griffiths (2020) with a few changes. This material is parts of section 1.1, the introduction to chapter 2, the introduction to subsection 2.4.2, the introduction to chapter 3, and section 3.4. Additionally, the simulation model presented in section 6.1 has the same layout as the lateral simulation model presented in Griffiths (2020), with some changes in notation.

Chapter 2

UAV Dynamics

This chapter describes the theoretical background needed to understand the UAV simulation models that are implemented in chapter 6. All the material in this chapter is based on chapter 1-4 and appendix B in Beard and McLain (2012), and follows the structure of Beard and McLain (2012) closely.

Section 2.1 contains a description of the relevant coordinate frames. Section 2.2 explains how the velocity of the UAV is modeled. The kinematics and dynamics of a UAV in motion is presented in section 2.3, and the forces and moments acting on the UAV are presented in section 2.4. A summary of the full 6DOF model of the UAV developed in this chapter is given in section 2.5. Section 2.6 contains simplified decoupled models for the lateral and longitudinal dynamics, which are used in the control designs in chapter 5. Finally, sections 2.7 and 2.8 present alternative ways of representing the attitude of a UAV, which can be useful in simulations or control design.

2.1 Coordinate Frames

To describe the orientation and position of a UAV, several coordinate frames are needed. The transformation of coordinates from one frame of reference to another is done through rotation and translation. The coordinate systems of interest are the inertial frame, the vehicle frames, the body frame, the stability frame, and the wind frame. The relative orientation of the body frame can be parameterized by the Euler angles roll ϕ, pitch θ, and yaw ψ, while the orientations of the stability and wind frames relative to the body frame are described by the angle of attack (AoA) α and sideslip angle β respectively. The Euler angles, the AoA, and the sideslip angle are defined in the following subsections.

This section gives a brief description of the relevant coordinate frames and the transformations from one reference frame to another. A short explanation of rotation matrices, which are used in the transformations in the following subsections, is presented in the next subsection.

2.1.1 Rotation Matrices

A vector $\mathbf{p} = [p_x, p_y, p_z]^\top$ expressed in the coordinate frame $\mathcal{F}^a$ specified by the unit vectors $(\mathbf{i}^a, \mathbf{j}^a, \mathbf{k}^a)$ can also be expressed in any arbitrary coordinate frame $\mathcal{F}^b$ specified by $(\mathbf{i}^b, \mathbf{j}^b, \mathbf{k}^b)$. To rotate a vector from one frame $\mathcal{F}^a$ to another frame $\mathcal{F}^b$, we use rotation matrices. A rotation about the z-axis by an angle θ is given by the rotation matrix

$$\mathcal{R}_a^b = \begin{bmatrix} \cos\theta & \sin\theta & 0 \\ -\sin\theta & \cos\theta & 0 \\ 0 & 0 & 1 \end{bmatrix}, \tag{2.1}$$

while a rotation about the y-axis is given by

$$\mathcal{R}_a^b = \begin{bmatrix} \cos\theta & 0 & -\sin\theta \\ 0 & 1 & 0 \\ \sin\theta & 0 & \cos\theta \end{bmatrix}, \tag{2.2}$$

and a rotation about the x-axis is given by

$$\mathcal{R}_a^b = \begin{bmatrix} 1 & 0 & 0 \\ 0 & \cos\theta & \sin\theta \\ 0 & -\sin\theta & \cos\theta \end{bmatrix}. \tag{2.3}$$

These rotation matrices have the following properties

(P1) $(\mathcal{R}_a^b)^{-1} = (\mathcal{R}_a^b)^\top = \mathcal{R}_b^a$

(P2) $\mathcal{R}_b^c \mathcal{R}_a^b = \mathcal{R}_a^c$

(P3) $\det(\mathcal{R}_a^b) = 1$.

2.1.2 The Inertial Frame $\mathcal{F}^i$

The inertial coordinate system is earth-fixed, with the unit vector $\mathbf{i}^i$ directed north, $\mathbf{j}^i$ directed east and $\mathbf{k}^i$ directed toward the center of the earth. These unit vectors are denoted as the inertial x, y, and z directions respectively. The origin of the system is at the defined home location. The inertial frame is sometimes also known as a north-east-down (NED) reference frame since the NED frame can be assumed to be inertial when using local navigation instead of global. The necessary assumptions for when it is possible to use local navigation is discussed further in subsection 2.3.3.

2.1.3 The Vehicle Frame $\mathcal{F}^v$

The vehicle frame is obtained by a translation of the inertial frame so that the origin is at the center of mass of the UAV. The axes of the frame are still aligned with the axes of the inertial frame so that $\mathbf{i}^v$ points north, $\mathbf{j}^v$ points east, and $\mathbf{k}^v$ points towards the center of the earth.

2.1.4 The Vehicle-1 Frame $\mathcal{F}^{v1}$

The vehicle-1 frame is defined by a rotation in the positive right-handed direction about $\mathbf{k}^v$ by the yaw angle ψ. The origin of the vehicle-1 frame is, therefore, the same as the origin of the vehicle frame, but $\mathbf{i}^{v1}$ points out the nose of the airframe and $\mathbf{j}^{v1}$ points out the right wing when the roll angle ϕ and pitch angle θ are zero. $\mathbf{k}^{v1}$ is aligned with $\mathbf{k}^v$ so that it points towards the center of the earth. The transformation from $\mathcal{F}^v$ to $\mathcal{F}^{v1}$ is given by

$$\mathbf{p}^{v1} = \mathcal{R}_v^{v1}(\psi)\mathbf{p}^v = \begin{bmatrix} \cos\psi & \sin\psi & 0 \\ -\sin\psi & \cos\psi & 0 \\ 0 & 0 & 1 \end{bmatrix} \mathbf{p}^v. \tag{2.4}$$

2.1.5 The Vehicle-2 Frame $\mathcal{F}^{v2}$

The vehicle-2 frame is defined by a rotation in the positive right-handed direction about $\mathbf{j}^{v1}$ by the pitch angle θ. The origin of the vehicle-2 frame is, therefore, the same as the origin of the vehicle and vehicle-1 frames. The unit vector $\mathbf{i}^{v2}$ always points out the nose of the airframe, while $\mathbf{j}^{v2}$ points out the right wing and $\mathbf{k}^{v2}$ points out the belly of the UAV when the roll angle ϕ is zero. The transformation from $\mathcal{F}^{v1}$ to $\mathcal{F}^{v2}$ is given by

$$\mathbf{p}^{v2} = \mathcal{R}_{v1}^{v2}(\theta)\mathbf{p}^{v1} = \begin{bmatrix} \cos\theta & 0 & -\sin\theta \\ 0 & 1 & 0 \\ \sin\theta & 0 & \cos\theta \end{bmatrix} \mathbf{p}^{v1}. \tag{2.5}$$

2.1.6 The Body Frame $\mathcal{F}^b$

The body frame is defined with the origin at the center of mass of the UAV. $\mathbf{i}^b$ points out of the nose of the airframe, $\mathbf{j}^b$ points out the right wing, and $\mathbf{k}^b$ points out of the belly of the UAV. The body frame is thus defined by a positive right-handed rotation about $\mathbf{i}^{v2}$ by the roll angle ϕ so that the transformation from $\mathcal{F}^{v2}$ to $\mathcal{F}^b$ is given by

$$\mathbf{p}^b = \mathcal{R}_{v2}^b(\phi)\mathbf{p}^{v2} = \begin{bmatrix} 1 & 0 & 0 \\ 0 & \cos\phi & \sin\phi \\ 0 & -\sin\phi & \cos\phi \end{bmatrix} \mathbf{p}^{v2}. \tag{2.6}$$

The transformation from the vehicle frame to the body frame is given by

$$\mathbf{p}^b = \mathcal{R}_v^b(\theta)\mathbf{p}^v, \quad \mathcal{R}_v^b(\phi,\theta,\psi) = \mathcal{R}_{v2}^b(\phi)\mathcal{R}_{v1}^{v2}(\theta)\mathcal{R}_v^{v1}(\psi). \tag{2.7}$$

2.1.7 The Stability Frame $\mathcal{F}^s$

The stability frame is defined by a left-handed rotation about $\mathbf{j}^b$ by the angle of attack α, which is the angle between the body frame x-axis and the relative velocity vector, $\mathbf{v}_r$, which is the velocity of the UAV relative to the surrounding air. By doing this left-handed rotation, $\mathbf{i}^s$ is aligned with the projection of $\mathbf{v}_r$ onto the $\mathbf{i}^b$- $\mathbf{k}^b$ plane. The transformation

from $\mathcal{F}^b$ to $\mathcal{F}^s$ is given by

$$\mathbf{p}^s = \mathcal{R}_b^s(\alpha)\mathbf{p}^b = \begin{bmatrix} \cos\alpha & 0 & -\sin\alpha \\ 0 & 1 & 0 \\ \sin\alpha & 0 & \cos\alpha \end{bmatrix} \mathbf{p}^b. \tag{2.8}$$

2.1.8 The Wind Frame $\mathcal{F}^w$

The wind frame is obtained through rotating the stability frame by a right-handed rotation about $\mathbf{k}^s$ by the sideslip angle β, which is the angle between the airspeed vector and the $\mathbf{i}^b$-$\mathbf{k}^b$ plane. Thus, the airspeed vector is aligned with the unit vector $\mathbf{i}^w$. The transformation from $\mathcal{F}^s$ to $\mathcal{F}^v$ is given by

$$\mathbf{p}^w = \mathcal{R}_s^w(\beta)\mathbf{p}^s = \begin{bmatrix} \cos\beta & \sin\beta & 0 \\ -\sin\beta & \cos\beta & 0 \\ 0 & 0 & 1 \end{bmatrix} \mathbf{p}^s. \tag{2.9}$$

2.2 The Wind Triangle

When modeling the dynamics of a UAV, it is important to distinguish between the inertial forces, which are dependent on velocities and accelerations relative to a fixed frame, and aerodynamic forces, which are dependent on velocities relative to the surrounding air. Since UAVs operate in environments where wind is almost always present, the velocity of the UAV relative to the fixed frame, $\mathbf{v}_g$, and relative to the surrounding air, $\mathbf{v}_r$, are not the same. This is especially important when modeling UAVs as the wind velocity can sometimes be almost as great as the velocity of the UAV. The relation between $\mathbf{v}_g$ and $\mathbf{v}_r$ in the inertial frame is given by

$$\mathbf{v}_r = \mathbf{v}_g - \mathbf{v}_w, \tag{2.10}$$

where $\mathbf{v}_w$ is the wind velocity vector relative to the fixed frame.

The ground velocity of the UAV with respect to the inertial frame expressed in the body frame is given by

$$\mathbf{v}_b \triangleq \mathbf{v}_g^b = \begin{bmatrix} u \\ v \\ w \end{bmatrix} = \mathcal{R}_v^b \mathbf{v}_g, \tag{2.11}$$

where the components of $\mathbf{v}_b$ are given along the $\mathbf{i}^b, \mathbf{j}^b$, and $\mathbf{k}^b$ axes. The components of the wind velocity vector can also be expressed in the body frame in a similar way so that the wind velocity in the inertial frame expressed in the body frame is

$$\mathbf{v}_w^b = \begin{bmatrix} u_w \\ v_w \\ w_w \end{bmatrix} = \mathcal{R}_v^b(\phi, \theta, \psi) \begin{bmatrix} w_n \\ w_e \\ w_d \end{bmatrix}, \tag{2.12}$$

where w_n, w_e, and w_d are the components of the wind in the NED-frame. Finally, the relative airspeed in the body frame is given by

$$\mathbf{v}_r^b = \begin{bmatrix} u_r \\ v_r \\ w_r \end{bmatrix} = \begin{bmatrix} u - u_w \\ v - v_w \\ w - w_w \end{bmatrix}. \tag{2.13}$$

From the information above about the wind velocity, relative air velocity, and ground velocity, it is possible to formulate expressions for the airspeed V_a, the AoA α, and the sideslip angle β as

$$V_a = \|\mathbf{v}_r\| \tag{2.14}$$

$$\alpha = \tan^{-1}\left(\frac{w_r}{u_r}\right) \tag{2.15}$$

$$\beta = \sin^{-1}\left(\frac{v_r}{V_a}\right), \tag{2.16}$$

where the four-quadrant inverse tangent $\texttt{atan2}(y, x)$ (MathWorks, 2020c), which maps the resulting angle to the interval $[-\pi, \pi]$ for any x and y, is typically used to calculate the AoA above. The equations in (2.14)-(2.16) are convenient given that aerodynamic forces and moments are usually formulated using V_a, α, and β.

The presence of wind in the system does not only affect the velocity of the UAV, but also the angular velocity ω_i, where ω_i is the angular velocity of the UAV relative to the inertial frame. The angular velocity in the body frame is denoted as ω_b and is given in terms of the components u, v and w so that

$$\omega_b = \begin{bmatrix} p \\ q \\ r \end{bmatrix}. \tag{2.17}$$

The relative angular velocity of the UAV in the body frame is then given by

$$\omega_r^b = \begin{bmatrix} p_r \\ q_r \\ r_r \end{bmatrix} = \omega_b - \omega_w^b, \tag{2.18}$$

where ω_w^b is the effect of the wind on the angular velocity of the UAV in the body frame, which is described in more detail in subsection 2.4.4.

2.2.1 Course Angle and Flight-Path Angle

Two additional angles are introduced relating to the navigation of the UAV, namely the course angle χ and flight-path angle γ_f, which are used to describe the direction of the ground velocity $\mathbf{v}_g$ relative to an inertial frame. These angles are used in chapter 6 to calculate the desired trajectory for the UAV during simulation.

The flight-path angle γ_f is the angle between the $\mathbf{i}^i$-$\mathbf{j}^i$ plane and the ground velocity $\mathbf{v}_g$, so that it is given by the relation

$$\dot{h} = V_g \sin\gamma_f, \tag{2.19}$$

where h is the altitude of the UAV and V_g is the ground speed of the UAV.

The course angle χ is the angle between the inertial north $\mathbf{i}^i$ and the projection of $\mathbf{v}_g$ onto the $\mathbf{i}^i$-$\mathbf{j}^i$ plane so that

$$\chi = \tan^{-1}(\frac{v_y}{v_x}), \tag{2.20}$$

where v_y is the component of $\mathbf{v}_g$ along $\mathbf{j}^i$, and v_x is the component of $\mathbf{v}_g$ along $\mathbf{i}^i$.

2.3 Kinematics and Dynamics

To derive the equations of motion for a UAV, the expressions for the kinematics and the dynamics of the UAV have to be defined. In this section, Newton's laws are applied to the translational and rotational motion of the UAV to express the relations between positions and velocities, and between forces and moments.

2.3.1 State Variables

The equations of motion for a UAV can be defined by introducing twelve state variables. There are three position states and three velocity states associated with both the translational and the rotational motion of the UAV. The state variables can be found in Table 2.1.

Name	Description
p_n	Inertial north position of the UAV along $\mathbf{i}^i$ in $\mathcal{F}^i$
p_e	Inertial east position of the UAV along $\mathbf{j}^i$ in $\mathcal{F}^i$
p_d	Inertial down position (negative of altitude) of the UAV along $\mathbf{k}^i$ in $\mathcal{F}^i$
u	Body frame velocity measured along $\mathbf{i}^b$ in $\mathcal{F}^b$
v	Body frame velocity measured along $\mathbf{j}^b$ in $\mathcal{F}^b$
w	Body frame velocity measured along $\mathbf{k}^b$ in $\mathcal{F}^b$
ϕ	Roll angle defined with respect to $\mathcal{F}^{v2}$
θ	Pitch angle defined with respect to $\mathcal{F}^{v1}$
ψ	Heading (yaw) angle defined with respect to $\mathcal{F}^v$
p	Roll rate measured along $\mathbf{i}^b$ in $\mathcal{F}^b$
q	Pitch rate measured along $\mathbf{j}^b$ in $\mathcal{F}^b$
r	Yaw rate measured along $\mathbf{k}^b$ in $\mathcal{F}^b$

Table 2.1: UAV state variables (from Beard and McLain (2012)).

The translational position states (p_n, p_e, p_d) are defined relative to the inertial frame, while the rotational position states, i.e. the Euler angles ϕ, θ, ψ, are defined with respect to the vehicle-2, the vehicle-1, and the vehicle frame, respectively. The velocity states (u, v, w) and (p, q, r) are defined with respect to the body frame.

2.3.2 Kinematics

The components of the velocity of the UAV in the body frame are denoted u, v and w, and correspond to the inertial velocity of the UAV projected onto the body frame axes. However, the position of the UAV is usually expressed in an inertial reference frame. It is therefore necessary to perform a differentiation and a rotational transformation to relate the position and velocity:

$$\dot{\mathbf{r}} = \begin{bmatrix} \dot{p}_n \\ \dot{p}_e \\ \dot{p}_d \end{bmatrix} = \mathcal{R}_b^v \begin{bmatrix} u \\ v \\ w \end{bmatrix}, \tag{2.21}$$

where $\mathbf{r}$ is the position vector.

The problem of relating quantities that are defined in different coordinate frames also arises in the relationship between the angular positions ϕ, θ, and ψ and the angular rates p, q, and r. As previously described, the angular positions are defined in three different coordinate frames, and the angular rates are defined in the body frame. The transformations that expresses the body frame angular rates in terms of the derivatives of the angular positions are

$$\begin{bmatrix} p \\ q \\ r \end{bmatrix} = \begin{bmatrix} \dot{\phi} \\ 0 \\ 0 \end{bmatrix} + \mathcal{R}_{v2}^b(\phi) \begin{bmatrix} 0 \\ \dot{\theta} \\ 0 \end{bmatrix} + \mathcal{R}_{v2}^b(\phi)\mathcal{R}_{v1}^{v2}(\theta) \begin{bmatrix} 0 \\ 0 \\ \dot{\psi}, \end{bmatrix} \tag{2.22}$$

which means that the differential equations for the angular positions are obtained as

$$\dot{\Theta} = \begin{bmatrix} \dot{\phi} \\ \dot{\theta} \\ \dot{\psi} \end{bmatrix} = \begin{bmatrix} 1 & \sin\phi\cos\theta & \cos\phi\tan\theta \\ 0 & \cos\phi & -\sin\phi \\ 0 & \sin\phi\sec\theta & \cos\phi\sec\theta \end{bmatrix} \begin{bmatrix} p \\ q \\ r \end{bmatrix}, \tag{2.23}$$

where $\sec(\cdot) = \frac{1}{\cos(\cdot)}$ and $\Theta = [\phi,\ \theta,\ \psi]^\top \in \mathbb{T}^3$ is the vector of Euler angles. The three-torus $\mathbb{T}^3$ is defined as the Cartesian product of three circles, i.e. $\mathbb{T}^3 = \mathbb{S}^1 \times \mathbb{S}^1 \times \mathbb{S}^1$.

2.3.3 Rigid-Body Dynamics

To derive the rest of the equations of motions for a UAV, Newton's second law is applied to the translational and rotational degrees of freedom. The motion of the UAV needs to be described relative to a fixed reference, as Newton's laws only hold in inertial frames. For small air vehicles, it is reasonable to assume a flat earth model, which means that it is possible to use the ground as a fixed frame of reference for the motion of the UAV. The fact that it is possible to assume a flat earth model is because the maneuvering of a UAV only require local navigation instead of global since the flight range is small compared to the Earth's surface (Lovren and Pieper, 1997). This means that the effects of the accelerations associated with Earth's rotation can be ignored as they are negligible in size compared to the accelerations produced by the UAV. This is what allows us to view the NED frame as inertial when using local navigation, even though it is actually both accelerating and rotating (Lovren and Pieper, 1997).

Translational Motion

For a UAV that is undergoing translational motion, Newton's second law can be formulated in the inertial frame as

$$\mathrm{m}\frac{d\mathbf{v}_g}{dt_i} = f, \tag{2.24}$$

where m is the mass of the UAV, $\frac{d}{dt_i}$ is the time derivative in the inertial frame, and f is the external forces acting on the UAV, which are described later in this chapter.

It is desirable to express (2.24) in the body frame to describe the motion of the UAV since we wish to develop the equation for the rate of change in the velocity of the UAV, which is dependent on the angular velocity of the UAV and on the forces acting on the UAV. The aerodynamic and thrust forces, which are described later in this chapter, are commonly expressed in the body frame, and the angular rates are measured in the body frame. Therefore, it is convenient to express the equation for $\mathbf{v}_b$ in the body frame. This requires the time derivative of the UAV velocity vector, $\mathbf{v}_g$, to be reformulated as

$$\frac{d\mathbf{v}_g}{dt_i} = \frac{d\mathbf{v}_g}{dt_b} + \omega_i \times \mathbf{v}_g, \tag{2.25}$$

where ω_i is the angular velocity of the UAV with respect to the inertial frame. Newton's second law in the body frame can then be found by combining (2.24) and (2.25) as

$$\mathrm{m}\left(\frac{d\mathbf{v}_b}{dt_b} + \omega_b \times \mathbf{v}_b\right) = f_b, \tag{2.26}$$

where $\mathbf{v}_b = [u, v, w]^\top$ is the ground velocity expressed in the body frame, $\omega_b = [p, q, r]^\top$ is the angular velocity in the body frame, and $f_b = [f_x, f_y, f_z]^\top$ is the sum of external forces acting on the UAV in the body frame.

Furthermore, since

$$\dot{\mathbf{v}}_b = \frac{d\mathbf{v}_b}{dt_b} = \begin{bmatrix} \dot{u} \\ \dot{v} \\ \dot{w} \end{bmatrix}, \tag{2.27}$$

it follows that the dynamic equation for the rate of change in velocity expressed in the body frame is given by

$$\dot{\mathbf{v}}_b = -\omega_b \times \mathbf{v}_b + \frac{1}{\mathrm{m}} f_b. \tag{2.28}$$

Rotational Motion

For a UAV that is undergoing rotational motion, Newton's second law can be formulated in the inertial frame as

$$\frac{dh}{dt_i} = m_i, \tag{2.29}$$

where h is the angular momentum in vector form, and m_i is the sum of all external moments applied to the UAV with respect to the inertial frame.

Since the rate of change in angular velocity depends on the aerodynamic and thrust moments, which are both given in the body frame, it is desirable to express (2.29) in the

body frame as well. Additionally, the angular velocity of the UAV is commonly measured as body frame angular velocities, which also makes it convenient to express (2.29) in the body frame. To express the rate of change in angular velocity in the body frame, the derivative of the angular momentum in the inertial frame has to be rewritten as

$$\frac{dh}{dt_i} = \frac{dh}{dt_b} + \omega_{b/i} \times h = m_i. \tag{2.30}$$

Thus, Newton's second law in the body frame becomes

$$\frac{dh_b}{dt_b} + \omega_b \times h_b = m_b, \tag{2.31}$$

where h_b is the angular momentum, and m_b the externally applied moments, both expressed in the body frame.

To formulate the expression for $\dot{\omega}_b$, it is necessary to rewrite the angular velocity vector as

$$h_b = I_b \omega_b,$$

where $I_b = I_b^\top > 0$ is the symmetric and positive definite inertia matrix which is given by

$$I_b = \begin{bmatrix} I_x & 0 & -I_{xz} \\ 0 & I_y & 0 \\ -I_{xz} & 0 & I_z \end{bmatrix}, \tag{2.32}$$

where it is assumed that the UAV is symmetric about the plane spanned by $\mathbf{i}^b$ and $\mathbf{k}^b$, which means that $I_{xy} = I_{yz} = 0$. The inverse of I_b is then given by

$$I_b^{-1} = \begin{bmatrix} \frac{I_z}{\Gamma_b} & 0 & \frac{I_{xz}}{\Gamma_b} \\ 0 & \frac{1}{I_y} & 0 \\ \frac{I_{xz}}{\Gamma_b} & 0 & \frac{I_x}{\Gamma_b} \end{bmatrix}, \quad \Gamma_b \triangleq I_x I_z - I_{xz}^2. \tag{2.33}$$

Thus, (2.31) can be reformulated as

$$I_b \frac{d\omega_b}{dt_b} + \omega_b \times (I_b \omega_b) = m_b, \tag{2.34}$$

which means that the dynamic equation for the rate of change of the angular velocity in the body frame is

$$\dot{\omega}_b = I_b^{-1}(-\omega_b \times (I_b \omega_b) + m_b), \tag{2.35}$$

where $\dot{\omega}_b = [\dot{p}, \dot{q}, \dot{r}]^\top$.

2.4 Forces and Moments

The common approach to modeling the effect of the pressure distribution around the body of a UAV as it passes through the air is to describe it using a combination of forces and moments. The distribution of the pressure acting on the UAV is modeled as a function of

the airspeed, the air density, and the shape and attitude of the UAV (Beard and McLain, 2012). The total forces f_b and moments m_b acting on the UAV in the body frame are typically modeled using a combination of the effects of gravitation, aerodynamics, and propulsion on the UAV, so that

$$\begin{aligned} f_b &= f_g + f_a + f_t \\ m_b &= m_a + m_t, \end{aligned}$$

where f_g is the gravitational force, f_a and m_a are the aerodynamic forces and moments, and f_t and m_t are the propulsion force and moment in vector form.

2.4.1 Gravitational Forces

The gravitational force acting on the UAV is modeled as a force acting along $\mathbf{k}^i$ that is proportional to the mass of the UAV by the gravitational constant g. To express this force in the body frame, it is necessary to rotate it from the vehicle frame to the body frame. The gravitational force in the body frame is therefore formulated as

$$f_g^b = \mathcal{R}_v^b(\phi, \theta, \psi) \begin{bmatrix} 0 \\ 0 \\ \mathrm{m}g \end{bmatrix}. \tag{2.36}$$

2.4.2 Aerodynamic Forces and Moments

The effect of the pressure distribution around the UAV as it passes through the air is modeled using both forces and moments. The aerodynamic forces and moments are usually decomposed into two groups: longitudinal and lateral, both of which are described in the following paragraphs. This decoupling simplifies modeling and analysis, which is useful in for example control design. When modeling the system as decoupled, the coupling between the lateral and longitudinal subsystems is viewed as a disturbance in the model. This kind of decoupling is only possible when assuming typical low-angle-of-attack flight conditions and small deviations from the equilibrium when both the roll and pitch angles are small, or when performing decoupled maneuvers. Decoupled maneuvers are when there is only motion in either the pitching plane (longitudinal motion) or in the $\mathbf{i}^b$- $\mathbf{j}^b$ plane (lateral motion). Examples of longitudinal motion are changes in altitude and airspeed, while an example of lateral motion is banked turns.

Note that the expressions for both the longitudinal and the lateral forces and moments presented here are based on linearized coefficients. This means that they are only valid for small deviations from the equilibrium. Therefore, the model presented in this report cannot be used to model systems that are required to perform more advanced aerobatic maneuvers. The reason for using these linearized coefficients that limit the application of the model is that it is both expensive and difficult to obtain accurate models of the nonlinear aerodynamic coefficients, which is either done through wind tunnel testing, computational fluid dynamics simulations, or by system identification based on flight experiments. It is easier to limit the behavior of the system to typical flight conditions and view the linearized coefficients and large deviations from the typical flight conditions as sources of uncertainty in the model instead.

Control Surfaces

Three primary control surfaces can be used to maneuver a UAV by modifying the aerodynamic forces and moments: the elevator, ailerons, and rudder. These can be seen in Figure 2.1. The ailerons are used to generate roll moment, the elevators generate pitch moment,

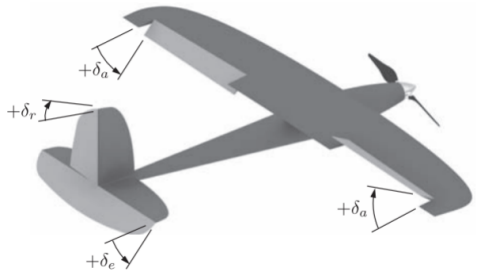

Figure 2.1: The primary control surfaces of a UAV (figure from Beard and McLain (2012))

and the rudder generates yaw moment. The aileron, elevator and rudder deflections are denoted δ_a, δ_e, and δ_r respectively.

In Figure 2.1 the positive directions of the control surface deflections are determined, which is done by applying the right-hand rule to the hinge axis of each control surface. Therefore, the positive direction of the elevator deflection is trailing edge down. For the rudder, the positive direction is the trailing edge left. The positive direction for the aileron is when the left aileron is trailing edge down and the right aileron is trailing edge up since the aileron deflection is given by

$$\delta_a = \frac{1}{2}(\delta_{a-left} - \delta_{a-right}).$$

The configuration of control surfaces shown in Figure 2.1 is not the only standard configuration for fixed-wing UAVs. Two examples of common configurations are shown in Figure 2.2, where ruddervators are used instead of both an elevator and a rudder. The

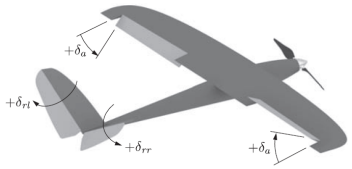

(a) An example of a fixed-wing UAV with ruddervators (figure from Beard and McLain (2012)).

(b) The Aerosonde model (figure from Beard and McLain (2012)).

Figure 2.2: Two examples of a control surface configuration of a UAV with ruddervators.

relationship between the deflections of the ruddervators, and the elevator and rudder deflections is given by

$$\begin{bmatrix} \delta_e \\ \delta_a \end{bmatrix} = \begin{bmatrix} 1 & 1 \\ -1 & 1 \end{bmatrix} \begin{bmatrix} \delta_{rr} \\ \delta_{rl} \end{bmatrix},$$

where δ_{rr} is the right ruddervator and δ_{rl} is the left ruddervator. Thus, driving the ruddervators together will have the same effect as an elevator, while driving the ruddervators differentially will have the same effect as a rudder.

Lateral Forces and Moments

The lateral aerodynamic force and moments are

$$f_y = \frac{1}{2}\rho V_a^2 S C_Y(\beta, p_r, r_r, \delta_a, \delta_r) \tag{2.37}$$

$$l = \frac{1}{2}\rho V_a^2 S b C_l(\beta, p_r, r_r, \delta_a, \delta_r) \tag{2.38}$$

$$n = \frac{1}{2}\rho V_a^2 S b C_n(\beta, p_r, r_r, \delta_a, \delta_r), \tag{2.39}$$

where f_y is the force acting on the UAV in the lateral direction along $\mathbf{j}^b$, and l and n are the roll and yaw moments respectively. The constant ρ is the air density, S is the wing area, and b is the wing span.

The equations for the aerodynamic coefficients are nonlinear and difficult to characterize. Therefore, it is common to use linear approximations which are found through first-order Taylor series approximation as

$$C_Y = C_{Y_0} + C_{Y_\beta}\beta + C_{Y_p}\frac{b}{2V_a}p_r + C_{Y_r}\frac{b}{2V_a}r_r + C_{Y_{\delta_a}}\delta_a + C_{Y_{\delta_r}}\delta_r \tag{2.40}$$

$$C_l = C_{l_0} + C_{l_\beta}\beta + C_{l_p}\frac{b}{2V_a}p_r + C_{l_r}\frac{b}{2V_a}r_r + C_{l_{\delta_a}}\delta_a + C_{l_{\delta_r}}\delta_r \tag{2.41}$$

$$C_n = C_{n_0} + C_{n_\beta}\beta + C_{n_p}\frac{b}{2V_a}p_r + C_{n_r}\frac{b}{2V_a}r_r + C_{n_{\delta_a}}\delta_a + C_{n_{\delta_r}}\delta_r, \tag{2.42}$$

where $C_{Y_0} = C_{l_0} = C_{n_0} = 0$ if the UAV is symmetric about the plane spanned by $\mathbf{i}^b$ and $\mathbf{k}^b$. These linearized coefficients are only valid under typical, low-angle-of-attack flight conditions where the flow over the UAV body is laminar so that the UAV is quasi-steady. This quasi-steady behaviour, which is fairly predictable, allows us to use these simplified expressions which are proven to yield acceptable accuracy.

Longitudinal Forces and Moments

The longitudinal aerodynamic forces and moment are denoted L, D and m, where L is the lift force, D is the drag force and m is the pitching moment. These are the forces and moments that cause motion in the body $\mathbf{i}^b$- $\mathbf{k}^b$ plane, known as the pitch plane. The lift and drag forces are aligned with the axes of the stability frame $\mathcal{F}^s$, and the pitching moment defined as the moment about the $\mathbf{j}^s$ axis. The longitudinal aerodynamic forces and

moments are heavily influenced by the angle of attack, and are therefore often expressed as

$$L = \frac{1}{2}\rho V_a^2 S C_L(\alpha, q_r, \delta_e) \tag{2.43}$$

$$D = \frac{1}{2}\rho V_a^2 S C_D(\alpha, q_r, \delta_e) \tag{2.44}$$

$$m = \frac{1}{2}\rho V_a^2 S c C_m(\alpha, q_r, \delta_e), \tag{2.45}$$

where C_L, C_D, and C_m are nondimensional aerodynamic coefficients, and c is the mean chord of the wing.

The longitudinal linearized aerodynamic coefficients are

$$C_L = C_{L_0} + C_{L_\alpha}\alpha + C_{L_q}\frac{c}{2V_a}q_r + C_{L_{\delta_e}}\delta_e \tag{2.46}$$

$$C_D = C_{D_0} + C_{D_\alpha}\alpha + C_{D_q}\frac{c}{2V_a}q_r + C_{D_{\delta_e}}\delta_e \tag{2.47}$$

$$C_m = C_{m_0} + C_{m_\alpha}\alpha + C_{m_q}\frac{c}{2V_a}q_r + C_{m_{\delta_e}}\delta_e, \tag{2.48}$$

Similarly to the lateral linearized coefficients, (2.46)-(2.48) are only valid for small values of the AoA when the flow over the UAV wing can be characterized as laminar. When the AoA grows too large, stall may occur when the airflow separates from the wing resulting in a loss in lift. Under these conditions, the linearized coefficients in (2.46)-(2.48) produce too optimistic estimates of the forces, and can no longer be used to provide an accurate model of the UAV.

Aerodynamic Force Vector and Moment Vector

The aerodynamic forces f_a and moments m_a mentioned in the introduction to this section are expressed by combining the lateral and longitudinal aerodynamic forces and moments in the paragraphs above. The aerodynamic forces are the forces acting in the lateral direction f_y (2.37), the lift force L (2.43), and the drag force D (2.43). By combining these we find the aerodynamic force vector in the body frame as

$$f_a = \frac{1}{2}\rho V_a^2 S \mathcal{R}_s^b(\alpha) \begin{bmatrix} -C_D \\ C_Y \\ -C_L \end{bmatrix}, \tag{2.49}$$

where $\mathcal{R}_s^b(\alpha)$ is the rotation matrix from the stability frame to the body frame.

The aerodynamic moment vector in the body frame is found by combining the roll, pitch, and yaw moments in (2.38), (2.45), and (2.39) respectively. The vector m_a is thus given by

$$m_a = \frac{1}{2}\rho V_a^2 S \begin{bmatrix} bC_l \\ cC_m \\ bC_n \end{bmatrix}. \tag{2.50}$$

Uncertainty in the Aerodynamic Forces and Moments

The presence of wind in the system has already been discussed in section 2.2. However, this is not the only disturbance that affects the UAV. As previously mentioned, the aerodynamic forces f_a and moments m_a are based on linearized coefficients that describe the aerodynamic properties of the UAV. Because of the linearization, the fact that the coefficients are difficult to determine, and additional model parametric errors, there is an uncertainty in the system that has not yet been modeled.

In this report, a time varying signal $d(t)$ that represents the modeling uncertainties in the system parameters is added to the aerodynamic forces and moments. The vectors f_a and m_a with this disturbance accounted for is given by

$$f_a = \frac{1}{2}\rho V_a^2 S \mathcal{R}_s^b(\alpha) \begin{bmatrix} -C_D \\ C_Y \\ -C_L \end{bmatrix} + d_f(t) \tag{2.51}$$

$$m_a = \frac{1}{2}\rho V_a^2 S \begin{bmatrix} bC_l \\ cC_m \\ bC_n \end{bmatrix} + d_m(t), \tag{2.52}$$

where d_f is given in [N] and d_m is given in [N m]. Both d_f and d_m are components of the disturbance signal d, i.e.

$$d = \begin{bmatrix} d_f \\ d_m \end{bmatrix}. \tag{2.53}$$

The signal d is in this report modeled as low-pass filtered white noise, and is given by

$$\dot{d} = -\frac{1}{T_d} d + \frac{1}{T_d} \mathrm{w}_d, \tag{2.54}$$

where T_d is the time constant of the filter and w_d is band-limited white noise. The values of these parameters are given in chapter 6.

2.4.3 Propulsion Forces and Moments

Propeller Thrust

To develop a model of the thrust generated by a propeller, Bernoulli's principle can be applied to calculate the pressure ahead and behind the propeller so that the pressure difference can be applied to the propeller area. The thrust is then given by

$$T = \frac{1}{2}\rho S_{prop} C_{prop}((k_{motor}\delta_t)^2 - V_a^2), \tag{2.55}$$

where S_{prop} is the area swept out by the propeller, C_{prop} is an aerodynamic coefficient for the propeller, k_{motor} is a constant that specifies the efficiency of the motor, and $\delta_t \in [0, 1]$ is the throttle. The trust T is non-negative, so the function in (2.55) is limited to $T = \max(0, T)$. The propeller force is given by

$$f_t = \begin{bmatrix} T \\ 0 \\ 0 \end{bmatrix}, \tag{2.56}$$

where it is assumed that the thrust acts along the $\mathbf{i}^b$ axis.

Propeller Torque

When the propeller on the UAV spins, a torque applied by the propeller to the motor fixed on the UAV body is created. This effect is due to the increased momentum of the air that passes through the propeller. The torque applied to the motor, and thus the UAV body is opposite to the direction of the propeller rotation and is given by

$$T_p = -k_{T_p}(k_\Omega \delta_t)^2 \tag{2.57}$$

where $\Omega = k_\Omega \delta_t$ is the propeller speed and k_{T_p} is a constant that can be determined through experiments. The propulsion moment is thus given by

$$m_t = \begin{bmatrix} T_p \\ 0 \\ 0 \end{bmatrix}. \tag{2.58}$$

2.4.4 Atmospheric Disturbances

Usually, the wind vector $\mathbf{v}_w$ is modeled as the sum of two vectors:

$$\mathbf{v}_w = \mathbf{v}_{w_s} + \mathbf{v}_{w_g} \tag{2.59}$$

where $\mathbf{v}_{w_s}$ is constant and $\mathbf{v}_{w_g}$ is the output of a stochastic process. The vector $\mathbf{v}_{w_s}$ represents steady ambient wind and is usually expressed in the inertial frame as

$$\mathbf{v}_{w_s} = \begin{bmatrix} w_{n_s} \\ w_{e_s} \\ w_{d_s} \end{bmatrix}, \tag{2.60}$$

while the vector $\mathbf{v}_{w_g}$ represents wind gusts and other atmospheric disturbances, and is typically expressed in the body frame as

$$\mathbf{v}^b_{w_g} = \begin{bmatrix} u_{w_g} \\ v_{w_g} \\ w_{w_g} \end{bmatrix}. \tag{2.61}$$

The wind vector $\mathbf{v}^b_w$ in the body frame is therefore

$$\mathbf{v}^b_w = \begin{bmatrix} u_w \\ v_w \\ w_w \end{bmatrix} = \mathcal{R}^b_v(\phi, \theta, \psi) \begin{bmatrix} w_{n_s} \\ w_{e_s} \\ w_{d_s} \end{bmatrix} + \begin{bmatrix} u_{w_g} \\ v_{w_g} \\ w_{w_g} \end{bmatrix}. \tag{2.62}$$

An approximate model of the gust portion of the wind model, $\mathbf{v}^b_{w_g}$, is the Dryden model (MathWorks, 2020b; Chalk et al., 1969), which approximates $\mathbf{v}^b_{w_g}$ by passing white noise through shaping filters.

Atmospheric disturbances also affect the rotational motion of the UAV. The Dryden model also creates a stochastic vector $\omega^b_w = [p_w, q_w, r_w]^\top$ that represents the effect of gusts on the rotational motion of the UAV. The vector ω^b_w is used in (2.18) to calculate the relative angular velocity ω^b_r in the body frame.

2.5 Summary of the Nonlinear Equations of Motions

The equations of motion that defines the full 12-state 6DOF model developed in the previous sections are summarized below:

$$\dot{\mathbf{r}} = \mathcal{R}_b^v \mathbf{v}_b \tag{2.63}$$

$$\dot{\mathbf{v}}_b = \mathbf{v}_b \times \omega_b + \frac{1}{\mathrm{m}} f_b \tag{2.64}$$

$$\dot{\Theta} = \begin{bmatrix} 1 & \sin\phi\cos\theta & \cos\phi\tan\theta \\ 0 & \cos\phi & -\sin\phi \\ 0 & \sin\phi\sec\theta & \cos\phi\sec\theta \end{bmatrix} \omega_b \tag{2.65}$$

$$\dot{\omega}_b = I_b^{-1}(-\omega_b \times (I_b\omega_b) + m_b), \tag{2.66}$$

where $\mathbf{r}$ is the position vector in the NED-frame, $\mathbf{v}_b$ is the velocity vector in the body frame, Θ is the vector containing the Euler angles, and ω_b is the body angular rate vector. The state vector of the system is thus

$$x = \begin{bmatrix} \mathbf{r} \\ \mathbf{v}_b \\ \Theta \\ \omega_b \end{bmatrix}, \tag{2.67}$$

where $x \in \mathbb{R}^3 \times \mathbb{R}^3 \times \mathbb{T}^3 \times \mathbb{R}^3$.

The forces and moments acting on the UAV in the body frame, denoted f_b and m_b respectively, are given by

$$f_b = f_a + f_t + f_g \tag{2.68}$$

$$m_b = m_a + m_t, \tag{2.69}$$

where the aerodynamic forces, the thrust and the gravitational force acting on the UAV are

$$f_a = \frac{1}{2}\rho V_a^2 S \mathcal{R}_s^b(\alpha) \begin{bmatrix} -C_D \\ C_Y \\ -C_L \end{bmatrix}, \quad f_t = \begin{bmatrix} T \\ 0 \\ 0 \end{bmatrix}, \quad f_g = \mathcal{R}_v^b \begin{bmatrix} 0 \\ 0 \\ \mathrm{m}g \end{bmatrix}, \tag{2.70}$$

and the aerodynamic and thrust moments are

$$m_a = \frac{1}{2}\rho V_a^2 S \begin{bmatrix} bC_l \\ cC_m \\ bC_n \end{bmatrix}, \quad m_t = \begin{bmatrix} T_p \\ 0 \\ 0 \end{bmatrix}. \tag{2.71}$$

The thrust T is calculated as in (2.55), and the thrust moment T_p as in (2.57). The force coefficients are

$$C_D = C_{D_0} + C_{D_\alpha}\alpha + C_{D_q}\frac{c}{2V_a}q + C_{D_{\delta_e}}\delta_e \tag{2.72}$$

$$C_Y = C_{Y_\beta}\beta + C_{Y_p}\frac{b}{2V_a}p + C_{Y_r}\frac{b}{2V_a}r + C_{Y_{\delta_a}}\delta_a + C_{Y_{\delta_r}}\delta_r \tag{2.73}$$

$$C_L = C_{L_0} + C_{L_\alpha}\alpha + C_{L_q}\frac{c}{2V_a}q + C_{L_{\delta_e}}\delta_e \tag{2.74}$$

and the moment coefficients are

$$C_l = C_{l_\beta}\beta + C_{l_p}\frac{b}{2V_a}p + C_{l_r}\frac{b}{2V_a}r + C_{l_{\delta_a}}\delta_a + C_{l_{\delta_r}}\delta_r \tag{2.75}$$

$$C_m = C_{m_0} + C_{m_\alpha}\alpha + C_{m_q}\frac{c}{2V_a}q + C_{m_{\delta_e}}\delta_e \tag{2.76}$$

$$C_n = C_{n_\beta}\beta + C_{n_p}\frac{b}{2V_a}p + C_{n_r}\frac{b}{2V_a}r + C_{n_{\delta_a}}\delta_a + C_{n_{\delta_r}}\delta_r. \tag{2.77}$$

2.6 Simplified Decoupled Dynamics

The dynamic equations for the full 6DOF model presented in the previous section are complicated and nonlinear, and can in many cases be simplified for the design and analysis of UAV control algorithms. The aerodynamic coefficients used to formulate the forces and moments acting on the UAV are already linearized, but further simplifying assumptions about the system can be made. A common approach is to model the system as decoupled in the longitudinal and lateral directions. This means that when assuming certain flight conditions, which are specified in the following subsections, it is possible to view the effect of the longitudinal dynamics in the lateral system as an unknown disturbance and vice versa.

2.6.1 Lateral Dynamics

The simplifying assumption for the lateral decoupled model is that we only have horizontal, fixed altitude flight. This means that the pitch rate q can be set to zero and that the pitch angle θ is small. When the pitch angle is small, we have that $\tan\theta \approx \sin\theta \approx 0$ and $\cos\theta \approx 1$. Furthermore, it is assumed that the AoA is also small, which means that $\tan\alpha \approx \sin\alpha \approx 0$ and $\cos\alpha \approx 1$. Additionally, the airspeed V_a and thrust T are assumed to be constant. Then, the 6DOF equations in (2.63)-(2.66) can be simplified to

$$\mathrm{m}V_a\dot{\beta} = \mathrm{m}g\cos\beta\sin\phi + f_y - T\sin\beta - \mathrm{m}V_a r \tag{2.78}$$

$$\dot{\phi} = p \tag{2.79}$$

$$\dot{p} = \frac{I_z}{\Gamma_b}l + \frac{I_{xz}}{\Gamma_b}n \tag{2.80}$$

$$\dot{r} = \frac{I_{xz}}{\Gamma_b}l + \frac{I_x}{\Gamma_b}n \tag{2.81}$$

defined in terms of the sideslip angle β based on Stevens et al. (2015). The inertia matrix I_b is defined in (2.32), and the force f_y and moments l and m are defined in (2.37)-(2.39). The model in (2.78)-(2.81) is the basis for the SISO lateral control algorithms developed in chapter 5.

2.6.2 Longitudinal Dynamics

When assuming wings-levels flight with zero sideslip we have that $\cos\phi \approx 1$ and $\sin\phi \approx 0$ since $\phi \approx 0$. Furthermore, it is assumed that $p = r = 0$, and that $\beta \approx 0$ so that $\cos\beta \approx 1$. The decoupled longitudinal dynamics based on the 6DOF model in (2.63)-(2.66) are then given by

$$\dot{\theta} = q \tag{2.82}$$

$$\dot{q} = \frac{1}{I_y} m \tag{2.83}$$

$$\mathrm{m}\dot{V}_a = T\cos\alpha - D - \mathrm{m}g\sin(\theta - \alpha) \tag{2.84}$$

$$\mathrm{m}V_a\dot{\alpha} = \mathrm{m}V_a q + \mathrm{m}g\cos(\theta - \alpha) - L - T\sin\alpha \tag{2.85}$$

defined in terms of the airspeed V_a and angle of attack α, following the modeling method in Stevens et al. (2015). I_y is a moment of inertia given in (2.32), and the forces and moment L, D and m are given in (2.43)-(2.45). The model in (2.82)-(2.85) is the basis for the SISO longitudinal control algorithms developed in chapter 5.

2.7 Attitude Representation Using Quaternions

A drawback to using the Euler angle representation in (2.63)-(2.66) is that it has a singularity when the pitch angle is at ± 90 degrees which can be seen from (2.23), in which several elements of the matrix will grow unbounded since $\sec\theta, \tan\theta \to \infty$ when $\theta = \pm 90$. This means that it is impossible to distinguish the roll and yaw angles when $\theta = \pm 90$ degrees. An alternative singularity-free way of representing the attitude of a UAV is to use quaternions.

A quaternion, $\mathbf{q}$, is an ordered list of four real numbers, which is required to be a unit quaternion, i.e. $\|\mathbf{q}\| = 1$, when representing a rotation. A quaternion $\mathbf{q}$ is commonly represented as a vector:

$$\mathbf{q} = \begin{bmatrix} q_0 \\ q_1 \\ q_2 \\ q_3 \end{bmatrix} \in \mathbb{S}^3, \tag{2.86}$$

where $\mathbb{S}^3$ is the space of unit quaternions called the three-sphere, which is defined as

$$\mathbb{S}^3 = \{x \in \mathbb{R}^4 \, : \|x\|^2 = 1\}.$$

The first part, q_0, of the quaternion is called the scalar part of the quaternion, and the vector part of the quaternion is

$$\mathbf{e} = q_1\mathbf{i}^i + q_2\mathbf{j}^i + q_3\mathbf{k}^i. \tag{2.87}$$

The difference between the Euler angle representation and the quaternion representation is the way a rotation from one frame to another is defined. When using Euler angles, the rotation is defined by a sequence of rotations around different axes by different angles. When using quaternions, the rotation from one frame to another is defined by a single rotation about an axis in three-dimensional space.

In addition to the fact that using quaternions provides a singularity-free attitude representation, it is also computationally efficient to use quaternions, since it is a representation that does not rely on trigonometric functions when computing the derivative, unlike the Euler angle representation. However, there are also some drawbacks to using quaternions including the fact that the quaternion has to be normalized during simulation so that $\|\mathbf{q}\| = 1$, and that $\pm\mathbf{q}$ is achieved by the same rotation.

The equations of motions for the 6DOF model when using quaternions to represent the attitude of the UAV is given by

$$\dot{\mathbf{r}} = \mathcal{R}_b^v \mathbf{v}_b \tag{2.88}$$

$$\dot{\mathbf{v}}_b = \mathbf{v}_b \times \omega_b + \frac{1}{\mathrm{m}} f_b \tag{2.89}$$

$$\dot{\mathbf{q}} = T_q \omega_b + k_q (1 - \|\mathbf{q}\|)\mathbf{q} \tag{2.90}$$

$$\dot{\omega}_b = I_b^{-1}(-\omega_b \times (I_b \omega_b) + m_b) \tag{2.91}$$

so that the state vector is

$$x = \begin{bmatrix} \mathbf{r} \\ \mathbf{v}_b \\ \mathbf{q} \\ \omega_b \end{bmatrix}, \tag{2.92}$$

where $x \in \mathbb{R}^3 \times \mathbb{R}^3 \times \mathbb{S}^3 \times \mathbb{R}^3$. The model equations in (2.88)-(2.91) are used in the simulation model described in chapter 6, while the model using Euler angles to represent the attitude of the UAV (2.63)-(2.66) is used as the basis for the single-input control algorithm designs.

2.8 Reduced-Attitude Representation

Another way of representing the roll and pitch angle kinematics of a UAV is to use a reduced-attitude representation (Coates et al., 2020; Reinhardt et al., 2020). This method does not suffer from the same problem with singularity as the Euler representation and is more intuitive than the quaternion representation, but it only models roll and pitch, rather than a full rotation that also includes yaw. However, the reduced-attitude representation presented in this section can still be used in control design and is used in chapter 5 to design multivariable control algorithms.

When using the reduced-attitude representation, the attitude of the UAV is given by the reduced-attitude vector

$$\Gamma = \begin{bmatrix} -\sin\theta \\ \cos\theta \sin\phi \\ \cos\theta \cos\phi \end{bmatrix}, \tag{2.93}$$

which corresponds to the third row of the rotation matrix $\mathcal{R}_b^v$. This means that Γ represents the direction of gravity expressed in the body frame, i.e.

$$\Gamma = \mathcal{R}_b^{v\top} \mathbf{e}_3, \tag{2.94}$$

where $\mathbf{e}_3 = [0\ 0\ 1]^\top$. From the equation above, it can be concluded that $\|\Gamma\| = 1$, as the rotation of a unit vector results in a new unit vector. The sphere that makes up all possible directions Γ is called the two-sphere and is defined as

$$\mathbb{S}^2 = \{x \in \mathbb{R}^3 : \|x\| = 1\}, \quad \Gamma \in \mathbb{S}^2. \tag{2.95}$$

The reduced-attitude vector can then be seen as a point on the two-sphere.

The set of all possible vectors orthogonal to Γ span an infinite plane tangent to the sphere, which is called the tangent space at Γ. This space is denoted by

$$\mathrm{T}_\Gamma\mathbb{S}^2 = \{v \in \mathbb{R}^3 : x^\top v = 0\}. \tag{2.96}$$

2.8.1 Reduced-Attitude Kinematics

The kinematic differential equation for Γ is given by

$$\dot{\Gamma} = \Gamma \times \omega_b, \tag{2.97}$$

where ω_b is the angular velocity in the body frame. This equation can further be simplified by decomposing the angular velocity as

$$\omega_b = \omega_b^\perp + \omega_b^\parallel, \tag{2.98}$$

where $\omega_b^\parallel$ is the component of ω_b parallel to Γ, and $\omega_b^\perp$ is the component of ω_b perpendicular to Γ. According to Coates et al. (2020), the parallel and orthogonal components of ω_b are given by

$$\omega_b^\parallel = \mathrm{proj}_\Gamma(\omega_b) = (\omega_b^\top \Gamma)\Gamma \tag{2.99}$$

and

$$\omega_b^\perp = \mathrm{proj}_{\mathrm{T}_\Gamma\mathbb{S}^2}(\omega_b) = \Pi_\Gamma^\perp \omega_b \in \mathrm{T}_\Gamma\mathbb{S}^2, \quad \Pi_\Gamma^\perp \triangleq \mathbb{I}_3 - \Gamma\Gamma^\top, \tag{2.100}$$

where $\mathbb{I}_3 \in \mathbb{R}^{3\times 3}$ is the identity matrix.

Since the cross product of two parallel vectors is zero, we have that $\Gamma \times \omega_b^\parallel = 0$, and it is therefore possible to simplify the reduced-attitude kinematics (2.97) to

$$\dot{\Gamma} = \Gamma \times \omega_b^\perp. \tag{2.101}$$

This means that only the perpendicular component of the angular velocity changes Γ, and thus changes the roll and pitch angles, ϕ and θ.

Chapter 3

Sliding Mode Control

The SMC technique is an approach to robust controller design. The control objective is to provide the desired performance of the closed-loop system when there are discrepancies between the mathematical model and the plant it describes. These discrepancies can arise from external disturbances, errors in plant parameters, and parasitic/unmodeled dynamics (Shtessel et al., 2014). This chapter explains the sliding mode and several conventional SMC techniques, as well as the use of both the single-input and the multivariable super-twisting algorithm in SMC-design.

Section 3.1 contains an explanation of the sliding mode. Section 3.2 presents the theory behind conventional SMC, while section 3.3 explains a conventional multivariable SMC method. Section 3.4 gives a brief description of second-order SMC. Section 3.5 presents the original single-input STA and several extensions of the basic algorithm. Finally, section 3.6 presents the multivariable STA and its extensions.

Note that the notation in this chapter is independent of the notation used in the rest of the report, so some symbols have different meanings in this chapter and the other chapters in this report. This is done to follow as much of the notation used in the literature referenced in this chapter as possible.

3.1 The Sliding Mode

The sliding mode is a mode that may as a phenomenon appear in dynamic systems governed by ordinary differential equations with discontinuous right-hand sides (Utkin et al., 2009). The main features of the sliding mode are its insensitivity to disturbances, both internal and external, its ultimate accuracy, and its finite-time transient. Exploiting the sliding mode in the control design means that these features will also be present in the closed-loop system, even in the presence of parametric uncertainties, unmodeled dynamics, and external disturbances.

The objective of SMC is to keep exactly a chosen constraint by employing a high-frequency switching control. This constraint is given in terms of a new variable introduced

in the system state-space:

$$\sigma \equiv 0, \ \forall t. \tag{3.1}$$

The new variable, σ, is called the sliding variable. The control design objective is then to find a control, u, so that (3.1) is satisfied for a smooth dynamic system described by nonlinear differential equations in

$$\dot{x} = f(t, x, u), \tag{3.2}$$

where $x \in \mathbb{R}^n$, $u \in \mathbb{R}^m, t \in \mathbb{R}$, and u is selected as a discontinuous function of the state.

An example of a discontinuous control can be

$$u_i = \begin{cases} u_i^+(t,x), & \text{if } \sigma_i(x) > 0, \\ u_i^-(t,x), & \text{if } \sigma_i(x) < 0 \end{cases} \quad i = 1, \ldots, m, \tag{3.3}$$

where $u_i^+(t,x)$ and $u_i^-(t,x)$ are continuous state functions, and $u_i^+(t,x) \neq u_i^-(t,x)$. The sliding mode will then occur in the intersection of the m smooth sliding surfaces $\sigma_i = 0$, and the motion of the system in these intersections will be of order $n - m$. This order reduction property that results from enforcing sliding modes in systems with discontinuous control is one of the many interesting features of sliding mode control as it enables decoupling and simplification of the design procedure.

3.1.1 Ideal and Real Sliding

As described in Levant (1993), every motion that takes place strictly on the constraint manifold $\sigma = 0$ is called an ideal sliding. Motion in a small neighborhood of the manifold is called real sliding. The notion of infinite-frequency switching of the control is only theoretical and cannot exist in physical systems due to switching imperfections. Thus, ideal sliding cannot be attained (Levant, 2003).

The fact that ideal sliding is unattainable is due to the presence of parasitic dynamics in the system, and to switching nonidealities such as delays (Young et al., 1999). Both result in high-frequency oscillations in the neighborhood of the sliding manifold. The parasitic dynamics are excited by the high-frequency switching of the switching device and represent the fast actuator and sensor dynamics. The high-frequency oscillations caused by these factors are called chattering and are a significant problem in SMC design which is investigated further in the next section.

3.2 First-Order Sliding Mode Control

In conventional SMC the idea is to first design a sliding surface from a combination of the system states that gives appropriate closed-loop dynamics when a sliding motion is induced, and then to develop a control law that guarantees the existence of a sliding motion in finite-time (Shtessel et al., 2014). The systems that are considered in first-order SMC are systems that are of relative degree 1, i.e. the control input appears in the first-derivative of the sliding variable, and also, the control that appears in the first-order derivative is discontinuous.

In this section a simple second-order system is used as a motivating example to explain the main concepts of SMC:

$$\begin{cases} \dot{x}_1 = x_2, & x_1(0) = x_{1_0} \\ \dot{x}_2 = h(t,x) + u + d(t), & x_2(0) = x_{2_0}, \end{cases} \tag{3.4}$$

where h is an uncertain nonlinear function, and d is a Lipschitz continuous external disturbance with $|d(t)| \leq D$. This system is based on an example given in Shtessel et al. (2014), but a few modifications have been made to follow the notation that is introduced in chapter 5 and chapter 6. Note that the system is affine in the control input and that the disturbance is matched by the control. If the disturbances in a system is matched by the control, it means that the control appears in every equation in which the disturbance also appears. For example, if both $\dot{x}_1$ and $\dot{x}_2$ in (3.4) contained a disturbance term, then the disturbance in $\dot{x}_2$ would be matched, while the disturbance in $\dot{x}_1$ would be unmatched. The fact that there are no unmatched disturbances present in the system is one of the main assumptions in SMC-design.

3.2.1 Methodology

The design methodology in first-order SMC consists of two stages: design of the sliding surface such that the system's motion on the surface will exhibit the desired properties, and design of a discontinuous controller to enforce sliding mode on the surface.

Design of Sliding Surface

The sliding surface is designed such that the system's motion on it is governed by the desired compensated dynamics. The compensated dynamics are chosen to achieve some control objective. Say the goal is to design a control law to stabilize the origin of the system (3.4). Choosing the sliding surface as

$$\sigma = a_1 x_1 + x_2 = 0, \quad a_1 > 0 \tag{3.5}$$

ensures exponential convergence of the state $x = (x_1, x_2)$ to the origin as the compensated dynamics on the surface are

$$\begin{cases} \dot{x}_1 = -a_1 x_1 \\ \dot{x}_2 = -a_1 x_2. \end{cases} \tag{3.6}$$

These compensated dynamics can be found by combining the equation for $\dot{x}_1$ in (3.4) and (3.5). From (3.4) and (3.5) we know that

$$x_2 = -a_1 x_1 \implies \dot{x}_1 = x_2 = -a_1 x_1,$$

and that

$$\dot{x}_2 = -a_1 \dot{x}_1 \implies \dot{x}_2 = -a_1 x_2.$$

Here it can be noted that the compensated dynamics (3.6) are independent of h and d. This means that if it is possible to find a control law that achieves these compensated

dynamics, convergence to the origin can be guaranteed even in the presence of parametric uncertainties and external disturbances. The fact that the compensated dynamics do not depend on either the plant parameters or the external disturbance is called the invariance property.

Design of a Sliding Mode Control Law

After the sliding surface has been defined, the problem of designing a control law u that drives the state to the origin or desired reference remains. A simple feedback control law that provides asymptotic stability is

$$u = -k_1 x_1 - k_2 x_2 - h(t,x) - d(t), \quad k_1 > 0, k_2 > 0. \tag{3.7}$$

However, convergence is guaranteed only if both h and d are known, or if h is known and $d(t) \equiv 0$, which is typically not the case. In SMC the design of the control law is based on the sliding-dynamics:

$$\dot{\sigma} = a_1 x_2 + h(t,x) + u + d(t), \quad \sigma(0) = \sigma_0. \tag{3.8}$$

In Khalil (2002) the Lyapunov-function candidate

$$V = \frac{1}{2}\sigma^2 \tag{3.9}$$

is used to find a control law u that asymptotically stabilizes the origin of (3.8). This control law is given as

$$u = -K\text{sign}(\sigma) = \begin{cases} -K, & \sigma > 0 \\ 0, & \sigma = 0 \\ K, & \sigma < 0, \end{cases} \tag{3.10}$$

which is the simplest type of SMC, called an ideal relay controller. This kind of controller can be seen in Figure 3.1.

In the analysis of the Lyapunov-function candidate in (3.9) several assumptions about the system are made in order to prove asymptotic convergence. It is already assumed that d is bounded. From Shtessel et al. (2014), the condition on $\dot{V}$ for finite-time convergence is given as

$$\dot{V} \leq -\eta V^{\frac{1}{2}} = -\frac{\eta}{\sqrt{2}}|\sigma|, \quad \eta > 0, \tag{3.11}$$

which is called the reaching or existence condition. If this condition is met, then the trajectory of (3.4) will approach the sliding surface in finite-time and remain on it thereafter.

From differentiation of (3.9) we have

$$\begin{aligned} \dot{V} &= \sigma\dot{\sigma} = \sigma(a_1 x_2 + h(t,x) + u + d(t)) \\ &\leq |\sigma|(C_1 + D) + \sigma u \end{aligned}$$

where the perturbation term $\varphi_1(t,x) = a_1 x_2 + h(t,x)$ has been defined, which is assumed to be uniformly bounded by $|\varphi_1(t,x)| \leq C_1 \ \forall t$. Insert the ideal relay controller (3.10) to obtain

$$\dot{V} \leq |\sigma|(C_1 + D) - \sigma K\text{sign}(\sigma)$$

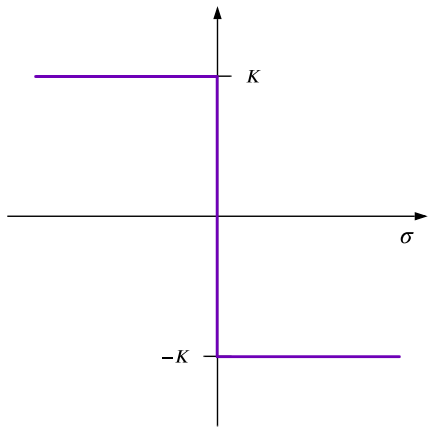

Figure 3.1: The ideal relay controller.

$$\begin{aligned} &\leq -|\sigma|(K - C_1 - D) \\ &= -\frac{\eta}{\sqrt{2}}|\sigma| < 0, \ \forall \sigma \neq 0. \end{aligned}$$

The last inequality holds if the control gain is chosen to satisfy

$$K = \frac{\eta}{\sqrt{2}} + C_1 + D. \tag{3.12}$$

The fact that the Lyapunov-function candidate V (3.9) satisfies the following conditions

$$V > 0, \quad \forall \sigma \neq 0 \tag{3.13}$$

$$\sigma = 0 \implies V(\sigma) = 0 \tag{3.14}$$

$$\|\sigma\| \to \infty \implies V \to \infty \tag{3.15}$$

means that $\dot{V} \leq -\eta V^{\frac{1}{2}}$, $\forall \sigma \neq 0$ implies that σ is driven to zero in finite-time, i.e. the sliding dynamics are finite-time stable, after which the motion is confined to the surface $\sigma = 0$. The motion of the system can thus be split into two phases; a reaching phase and a sliding phase. During the reaching phase, the trajectory starts to move towards the surface $\sigma = 0$. After it has reached the surface the sliding phase begins, in which the system is represented by the desired compensated dynamics (3.6) and moves towards the desired reference. This behavior for the system (3.4) is illustrated in Figure 3.2.

The Lyapunov-analysis above is based on the assumption that $|\varphi_1(t, x)| \leq C_1$. Say there exists a domain $\mathcal{D} \subset \mathbb{R}^n$ which contains an equilibrium, and let it be defined by

$$\mathcal{D} = \{x \in \mathbb{R}^2 : \ |x| < r\},$$

where r is chosen so that $|\varphi_1(t, x)| \leq C_1, \ \forall t$. Then we have that $\dot{V} < 0 \, \forall x \in \mathcal{D}, \ \sigma \neq 0$. Therefore it can be concluded that all trajectories with initial values $x(0) = x_0 \in \mathcal{D}$ will

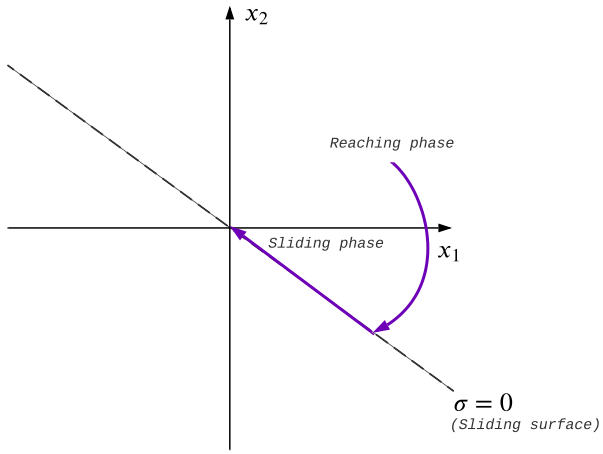

Figure 3.2: The reaching phase and the sliding phase for the system (3.4) with the sliding variable given in (3.5).

be contained in $\mathcal{D}$ $\forall t \geq 0$, and will also approach the equilibrium in $\mathcal{D}$. This means that the Lyapunov-analysis that is performed in this report can only guarantee convergence for values of x contained in a subset of the set $\mathbb{R}^n$, in which the state is assumed to be bounded. The Lyapunov-analysis of the saturation controller above is therefore only able to guarantee a local result instead of a global one.

3.2.2 Chattering

In the ideal relay controller, the switching frequency is supposed to be infinitely high, which means that ideal sliding happens on the surface $\sigma = 0$. However, due to imperfections in the switching devices, such as delays, dead zones, or hysteresis, SMC suffers from chattering. This means that in reality, the trajectory of the system is affected by these high-frequency small-amplitude oscillations, and is therefore confined to some vicinity of the switching surface, as seen in Figure 3.3.

Several design techniques can be applied to the control design to prevent chattering. Fortunately, these techniques do not rely upon a more detailed model of the system. The controller may still be designed under idealized conditions and then modified to be more robust to chattering and provide continuous control (Utkin et al., 2009). These chattering avoidance techniques can either be used to attenuate or eliminate the chattering effect (Shtessel et al., 2014).

3.2.3 Saturation Controller

One approach to chattering attenuation is to replace the relay control (3.10) with some continuous or smooth approximation. One such approximation is presented in the boundary layer solution in Utkin et al. (2009), in which the $sign$-function in (3.10) is replaced

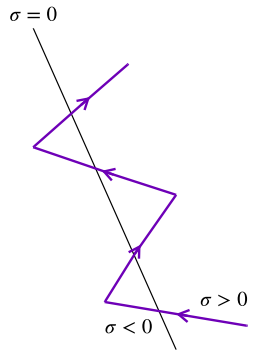

Figure 3.3: Chattering due to switching delay.

with a saturation-function, $sat(\sigma)$. The controller is then given by

$$u = -K\text{sat}(\sigma) = \begin{cases} -K\text{sign}(\sigma), & |\sigma| > \varepsilon \\ -\frac{K}{\varepsilon}\sigma, & |\sigma| \leq \varepsilon \end{cases} \tag{3.16}$$

and can be seen in Figure 3.4.

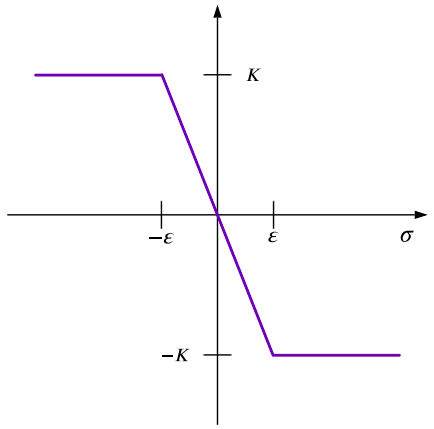

Figure 3.4: The ideal saturation controller.

The sat-function takes the form of the $sign$-function except for in a boundary layer around the sliding surface. In this layer, it is a linear function of the sliding variable σ, and the control law is thus continuous in this layer. This kind of control retains several of the properties of the ideal relay controller (3.10), such as finite-time convergence, and partly also the invariance property. However, convergence can only be guaranteed to the boundary layer and not to the desired reference, as the system behavior inside the boundary

layer is not determined. This means that there is no ideal sliding mode in the system (3.4), so the cost of providing a smooth control signal is the loss of robustness and accuracy, which is a trade-off in this kind of SMC design.

3.3 Multivariable Conventional Sliding Mode Control

Suppose that for a general n-dimensional system

$$\dot{x} = f(t,x) + g(t,x)\bar{u} + h(t,x), \tag{3.17}$$

where $f, h \in \mathbb{R}^n, g \in \mathbb{R}^{n\times m}$ and $\bar{u} \in \mathbb{R}^m$, it is possible to define an m-dimensional sliding variable with sliding dynamics on the form

$$\dot{\sigma} = a(t,x) + b(t,x)u + \gamma(t,x), \tag{3.18}$$

where $a, \gamma \in \mathbb{R}^m$, and $b \in \mathbb{R}^{m\times m}$. Here, a is an uncertain system function, b is the uncertain control coefficient, and γ is an unknown disturbance in the system.

If the sliding dynamics (3.18) can be decoupled into m independent subsystems, then it is possible to design a single-input sliding mode control law $\bar{u}_i, i = 1, ..., m$ to drive the corresponding sliding variable σ_i to zero. Should it not be possible to decouple the sliding dynamics due to nonlinearities in the system, it may be possible to simplify the system into subsystems and then view the coupling between the subsystems as disturbances in the system. However, if the coupling between the plant variables is too strong, the strategy of applying SISO control loops in a multivariable system may fail (Dong et al., 2016). In this case, a multivariable control scheme needs to be designed.

3.3.1 Unit Vector Control

An example of first-order multivariable SMC is the unit vector control (UVC), which is an extended multivariable version of the relay controller (3.10). In Edwards and Spurgeon (1998) the uncertain system

$$\dot{x} = Ax(t) + Bu(t) + f_u(t,x) + f_m(t,x,u) \tag{3.19}$$

is considered in the design of the UVC law. In the system (3.19) above, the functions $f_u : \mathbb{R} \times \mathbb{R}^n$ and $f_m : \mathbb{R} \times \mathbb{R}^n \times \mathbb{R}^m$ are unknown unmatched and matched uncertainties, which are assumed to be bounded by

$$\|f_u\| \leq k_1\|x\| + k_2 \tag{3.20}$$

$$\|f_m\| \leq k_3\|u\| + \alpha_u(t,x), \tag{3.21}$$

where $\alpha_u(t,x)$ is a known function, and $k_1, k_2, k_3 \geq 0$ are known constants. The constant k_3 is bounded by

$$k_3 < \sqrt{\lambda_{min}(B^\top B)}. \tag{3.22}$$

It is assumed that (3.19) is in regular form which means that the system can be written on the form

$$\dot{x}_1 = A_{11}x_1(t) + A_{12}x_2(t) + f_u \tag{3.23}$$

$$\dot{x}_2 = A_{21}x_1(t) + A_{22}x_2(t) + B_2u(t) + f_m. \tag{3.24}$$

From the uncertain system (3.19) and the regular form decomposition (3.23)-(3.24), it can be seen that $B^\top B = B_2^\top B_2$. This allows us to define

$$\sqrt{\lambda_{min}(B^\top B)} = \underline{\sigma}(B_2) = (\underline{\sigma}(B_2))^{-1} = \left\| B_2^{-1} \right\|^{-1}. \tag{3.25}$$

The bound on k_3 can then be rewritten as

$$k_3 \left\| B_2^{-1} \right\| < 1. \tag{3.26}$$

In Edwards and Spurgeon (1998) the sliding surface is expressed as

$$\sigma = S_2 M x_1(t) + S_2 x_2(t), \tag{3.27}$$

where σ is assumed to be continuous and differentiable everywhere. The choice of $S_2 \in \mathbb{R}^{m\times m}$ is arbitrary, but is often chosen so that

$$S_2 B_2 = \Lambda, \tag{3.28}$$

where Λ is a nonsingular diagonal matrix which can be determined from

$$k_3 \kappa(\Lambda) \left\| B_2^{-1} \right\| < 1. \tag{3.29}$$

In the expression above, $\kappa(\Lambda)$ is the condition number of Λ. It is convenient to choose Λ to be a scaled identity matrix, which means that $\kappa(\Lambda) = 1$ and (3.29) becomes (3.26).

The control law u is given as the sum of a linear and a discontinuous component:

$$u(t) = u_l(t) + u_n(t), \tag{3.30}$$

where the linear component is designed as an equivalent control term which stabilizes the ideal nominal system without uncertainties or disturbances. The linear term u_l is given by

$$\begin{aligned} u_l(t) &= \Lambda^{-1}(-S_2\bar{A}_{21}x_1(t) - (S_2\bar{A}_{22}S_2^{-1} - \Phi)\sigma) \\ \bar{A}_{11} &= A_{11} - A_{12}M \\ \bar{A}_{21} &= M\bar{A}_{11} + A_{21} - A_{22}M \\ \bar{A}_{22} &= A_{22} + A_{12}M, \end{aligned} \tag{3.31}$$

where $\Phi \in \mathbb{R}^{m\times m}$ is an arbitrary stable design matrix. The choice of M is described later in this subsection.

The nonlinear component u_n of the control law is

$$u_n(t) = -\rho_u(t,x)\Lambda^{-1}\frac{P_2\sigma}{\|P_2\sigma\|}, \quad \text{for } \sigma \neq 0, \tag{3.32}$$

where $P_2 \in \mathbb{R}^{m\times m}$ is a symmetric positive definite matrix determined from

$$P_2\Phi + \Phi^\top P_2 = \mathbb{I}. \tag{3.33}$$

The function $\rho_u(t,x)$ is designed to satisfy

$$\rho_u(t,x) \geq \frac{\|S_2\| \left(\|M\| \left(k_1 \left\|x(t)\right\| + k_2\right) + k_3 \left\|u_l(t)\right\| + \alpha_u(t,x)\right) + \gamma_2}{\left(1 - k_3\kappa(\Lambda)\left\|B_2^{-1}\right\|\right)}, \tag{3.34}$$

where γ_2 is the tuning variable. Note that in the scalar case with a one-dimensional sliding variable σ, the UVC law reduces to the ideal relay controller (3.10) with a variable gain $\rho_u(t,x)$. By comparing the function ρ_u with (3.20)-(3.21), it is easy to see that ρ_u depends only on the magnitude of the matched and unmatched uncertainties f_m and f_u.

Choice of Stabilizing Matrix M

In Edwards and Spurgeon (1998), the matrix M is chosen to stabilize the pair (A_{11}, A_{12}). Say the sliding function can be partitioned into

$$S = \begin{bmatrix} S_1 & S_2 \end{bmatrix} \implies \sigma = S_1 x_1 + S_2 x_2, \tag{3.35}$$

which is compatible with the regular form representation of the system given in (3.23)-(3.24), where $S_1 \in \mathbb{R}^{m\times(n-m)}$ and $S_2 \in \mathbb{R}^{m\times m}$. The motion of the system on the sliding surface is then given by

$$S_1 x_1(t) + S_2 x_2(t) = 0 \tag{3.36}$$

$$\implies x_2(t) = -M x_1(t), \quad M \triangleq S_2^{-1} S_1 \tag{3.37}$$

$$\implies \dot{x}_1(t) = (A_{11} - A_{12}M) x_1(t) \tag{3.38}$$

so that the system is stable if the matrix $(A_{11} - A_{12}M)$ has stable eigenvalues.

3.3.2 Boundary Layer Solution

A modified continuous version of the unit vector control presented in Edwards and Spurgeon (1998) is given by

$$u_n^{\varepsilon}(t) = \begin{cases} -\rho_u(t,x)\Lambda^{-1}\frac{P_2\sigma}{\|P_2\sigma\|}, & \text{if } \|P_2\sigma\| \geq \varepsilon \\ -\varepsilon^{-1}\rho_u(t,x)\Lambda^{-1}P_2\sigma, & \text{otherwise,} \end{cases} \tag{3.39}$$

where a boundary layer approach is utilised in the control design. The control law u is now composed of a linear term u_l and a continuous nonlinear approximation u_n^{ε}. In the single-input case, the control law (3.39) reduces to the boundary solution (3.16) with a variable gain ρ_u instead of a constant gain K.

Since the nonlinear control law (3.39) is an approximation, there exists no ideal sliding in the system as the state x is no longer confined to the sliding surface $\sigma = 0$ once it has been reached. As a consequence, the system is no longer totally invariant to matched uncertainties (Edwards and Spurgeon, 1998).

3.3.3 Multivariable Boundary Solution

The UVC design presented in the previous subsection is a substantially more complicated design than the SISO boundary layer solution in (3.10). If it is assumed that there are no unmatched disturbances present in the system, which is an important assumption in SMC-design, the UVC method from Edwards and Spurgeon (1998) can be simplified to a control algorithm that is a more direct extension of the saturation controller (3.16) to a multivariable framework.

The multivariable extension of the SISO saturation controller is given by

$$u = -K\text{sat}(\sigma) = \begin{cases} -K\frac{\sigma}{\|\sigma\|}, & \text{if } \|\sigma\| > \varepsilon \\ -\frac{K}{\varepsilon}\sigma, & \text{if } \|\sigma\| \leq \varepsilon, \end{cases} \quad \text{sat}(0) = 0, \tag{3.40}$$

where ε is the size of the boundary layer in which the control is a linear function of σ, and K is a scalar control gain. The MSAT (3.40) can be viewed as a simplification of the UVC boundary solution, where a constant control gain K is used instead of the time- and state-varying function $\rho_u(t,x)$. In chapter 5, the MSAT (3.40) is designed for the UAV-model as the multivariable version of the boundary solution. This is because the MSAT is more compatible than the UVC with the multivariable super-twisting algorithms that are presented in section 3.6.

If assuming that the sliding variable σ for the system (3.18) is both bounded and differentiable, it is possible to define the Lyapunov candidate

$$V = \frac{1}{2}\sigma^\top\sigma \tag{3.41}$$

to prove the stability of the multivariable saturation controller (3.40). Furthermore, if the function b is assumed to be known, we can use a manipulated control $\bar{u}$ as the input to the sliding dynamics, where the control $\bar{u}$ is given by

$$\bar{u} = b^{-1}(t,x)u \tag{3.42}$$

if we also assume that $\det(b) \neq 0, \forall t, x$. The derivative of the Lyapunov function is then given as

$$\begin{aligned} \dot{V} &= \sigma^\top\dot{\sigma} \\ &= \sigma^\top(a(t,x) + b(t,x)\bar{u} + \gamma(t,x)) \\ &\leq (A+G)\|\sigma\| - \sigma^\top(K\text{sat}(\sigma)) \end{aligned} \tag{3.43}$$

where it is assumed that the function a and the disturbance γ are uniformly bounded by $\|a(t,x)\| \leq A$ and $\|\gamma(t,x)\| \leq G$, where the bounds are given by positive constants A and G.

The derivative of the Lyapunov function for the case when $\|\sigma\| > \varepsilon$ can be written as

$$\begin{aligned} \dot{V} &\leq (A+G)\|\sigma\| - K\frac{\sigma^\top\sigma}{\|\sigma\|} \\ &\leq -(K-A-G)\|\sigma\| \\ &= -\frac{\eta}{\sqrt{2}}\|\sigma\| < 0, \ \forall\sigma \neq 0 \end{aligned}$$

where we have used that $\sigma^\top \sigma = \|\sigma\|^2$. The last inequality above holds if the control gain is chosen as

$$K = \frac{\eta}{\sqrt{2}} + A + G, \tag{3.44}$$

where η is a positive constant from the reaching condition (3.11).

For the case when $\|\sigma\| \leq \varepsilon$, the Lyapunov function candidate becomes

$$\begin{aligned}
\dot{V} &\leq (A+G)\|\sigma\| - k\frac{\sigma^\top \sigma}{\varepsilon} \\
&\leq (A+G)\|\sigma\| - K\frac{\|\sigma\|^2}{\varepsilon} \\
&\leq -(K-A-G)\|\sigma\| \\
&= -\frac{\eta}{\sqrt{2}}\|\sigma\| < 0, \; \forall \sigma \neq 0
\end{aligned}$$

since $\|\sigma\| \leq \varepsilon \implies \frac{\|\sigma\|}{\varepsilon} \leq 1$. We have that $\dot{V} \leq \frac{\eta}{\sqrt{2}}$, $\forall \sigma \neq 0$ if the control gain K is chosen as in (3.44). Thus, the MSAT controller in (3.40) is stable if the control gain K is chosen to fulfil (3.44).

3.4 Second-Order Sliding Mode Control

Even though conventional SMC methods achieve exact compensation of bounded matched uncertainties, reduced-order sliding equations, and finite-time convergence to the sliding surface, there are still several challenges that remain to be solved. Among the disadvantages of the conventional methods are chattering, asymptotic convergence of the state variables, and insensitivity only to matched disturbances (Fridman et al., 2011). Furthermore, the constraint, σ, has to be of relative degree 1 which means that the control needs to appear in the first time derivative of the constraint, $\dot{\sigma}$.

Second-order sliding mode (SOSM) control algorithms is an attempt at solving some of the issues that remain for conventional SMC methods. In SOSM algorithms, a continuous control signal is produced by considering the control derivative as a new virtual control to drive both σ and $\dot{\sigma}$ to zero so that a 2-sliding mode ($\sigma = \dot{\sigma} = 0$) is enforced in the system. This means that the discontinuous term of the control appears only in $\ddot{\sigma}$, not in $\dot{\sigma}$, so that the chattering effect is significantly attenuated (Shtessel et al., 2014). However, this requires the derivative $\dot{\sigma}$ to be available, which may not always be the case unless, for example, observers are added to the control design in addition to controllers.

3.5 The SISO Super-Twisting Algorithm and Extensions

A well-known second-order approach that seeks to attenuate chattering while still guaranteeing robustness to disturbances and uncertainties is the super-twisting algorithm (Levant, 1993), which is applicable to systems of relative degree 1. This means that it can be used instead of the conventional first-order SMC algorithms, which separates it from other second or higher-order sliding algorithms that require the system to be of relative degree $r > 1$.

3.5.1 Super-Twisting Algorithm Control Law

Suppose that a sliding variable σ is designed for a system such that the sliding dynamics can be written on the form

$$\dot{\sigma} = a(t,x) + b(t,x)u, \tag{3.45}$$

so that the system is of relative degree 1. The function a is considered an unknown, but bounded, function satisfying $|a(t,x)| \leq A$ with a bounded first derivative $|\dot{a}(t,x)| \leq \bar{A}$. Furthermore it is assumed that

$$0 < b_0 \leq b(t,x) \leq B \tag{3.46}$$

and that $\dot{b}$ is bounded by $|\dot{b}(t,x)| \leq \bar{B}$.

As before, the design objective is to design a discontinuous control law that ensures $\sigma \equiv 0$ in finite-time. The super-twisting controller that is presented in Levant (1993) achieves this design objective, and is given by

$$\begin{aligned} u &= -k_1 |\sigma|^{\frac{1}{2}} \text{sign}(\sigma) + z \\ \dot{z} &= -k_2 \text{sign}(\sigma). \end{aligned} \tag{3.47}$$

Note that even though this controller guarantees the appearance of a 2-sliding mode $\sigma = \dot{\sigma} = 0$, no measurement of $\dot{\sigma}$ is needed, which is an advantage that separates the STA from other second-order SMC techniques.

For the STA, the problem of choosing the control gains k_1 and k_2 remains. A number of sufficient conditions for finite-time stability have been proposed. The sufficient condition for convergence given in Levant (1998) is

$$k_2 > \bar{A}, \quad k_1^2 \geq 4\bar{A}\frac{k_2 + \bar{A}}{k_2 - \bar{A}}. \tag{3.48}$$

This condition arises from a very crude estimation, so another modified condition is given in Moreno and Osorio (2012):

$$k_2 > \bar{A}, \quad k_1 > 2\sqrt{k_2 - \sqrt{k_2^2 - \bar{A}^2}}. \tag{3.49}$$

Another popular parameter configuration is

$$k_1 = 1.5\sqrt{\bar{A}}, \quad k_2 = 1.1\bar{A}. \tag{3.50}$$

Note that this configuration does not satisfy (3.49), but they do satisfy a more recent sufficient condition for stability given in Seeber and Horn (2017):

$$k_2 > \bar{A}, \quad k_1 > \sqrt{k_2 + \bar{A}}. \tag{3.51}$$

These conditions are discussed further in chapter 7.

3.5.2 Adaptive Gains Super-Twisting Algorithm

The STA only provides chattering attenuation and not elimination, as the control law contains a discontinuous function under the integral. A disadvantage of the method is that the choice of control gains is made based on the estimated boundary of the perturbation gradient, which is easily overestimated. This yields larger control gains than what is necessary, which in the worst-case scenario can amplify chattering in the system.

A solution to this problem is the adaptive STA presented in Shtessel et al. (2010). Similarly to the STA, the adaptive version of the control law continuously drives the sliding variable and its derivative to zero in the presence of the bounded disturbance. The advantage of this method is that the boundary of the disturbance is not required in the control design, and can thus be unknown.

Problem Formulation

The problem formulation given in Shtessel et al. (2010) is as follows: Consider a single-input uncertain nonlinear system

$$\dot{x} = f(t,x) + g(t,x)u, \tag{3.52}$$

where $x \in \mathbb{R}^n$ is a state vector, $u \in \mathbb{R}$ is a control function, $f(t,x) \in \mathbb{R}^n$ is a differentiable, partially known vector field. Assume that

(A1) A sliding variable $\sigma = \sigma(t,x) \in \mathbb{R}$ is designed so that the system's (3.52) desirable compensated dynamics are achieved in the sliding mode $\sigma = 0$.

(A2) The system's (3.52) input-output ($u \to \sigma$) dynamics are of a relative degree 1, and the internal dynamics are stable.

(A3) The function $b(t,x) \in \mathbb{R}$ is known and not equal to zero $\forall x$ and $t \in [0,\infty)$.

(A4) The function $\varphi(t,x) \in \mathbb{R}$ is bounded

$$|\varphi(t,x)| \leq \delta |\sigma|^{\frac{1}{2}}, \tag{3.53}$$

where the finite boundary $\delta > 0$ exists, but is unknown.

The control objective is then to find a control law that drives the sliding variable σ and its derivative $\dot{\sigma}$ to zero in finite-time in the presence of its bounded perturbation with the unknown boundary through continuous control.

Control Structure

The following super-twisting control is proposed in Shtessel et al. (2010):

$$\begin{cases} \omega = -\alpha |\sigma|^{\frac{1}{2}} \text{sign}(\sigma) + z \\ \dot{z} = -\beta \text{sign}(\sigma), \end{cases} \tag{3.54}$$

where α, β are adaptive gains

$$\begin{aligned} \alpha &= \alpha(\sigma, \dot{\sigma}, t) \\ \beta &= \beta(\sigma, \dot{\sigma}, t) \end{aligned} \tag{3.55}$$

to be defined. Note that α, β in relation to the ASTA are control gains, and are thus not the same as the angle of attack and the sideslip angle defined in chapter 2. The reason for this is to follow the notation in Shtessel et al. (2010).

The control system given by (3.54) can be written in a closed-loop system as

$$\begin{cases} \dot{\sigma} = -\alpha|\sigma|^{\frac{1}{2}}\text{sign}(\sigma) + z + \varphi(t, x) \\ \dot{z} = -\beta\text{sign}(\sigma). \end{cases} \tag{3.56}$$

The control design problem is then reduced to designing an ASTA control (3.54), (3.55) that drives $\sigma, \dot{\sigma} \to 0$ in finite-time in the presence of the bounded perturbation with the unknown boundary.

The main result of Shtessel et al. (2010) is formulated as follows: Consider system (3.56). Suppose that the perturbation $\varphi(t, x)$ satisfies Assumption (A4) for some unknown constant $\delta > 0$. Then for any initial conditions $x(0), \sigma(0)$ the sliding surface $\sigma = 0$ will be reached in finite-time via the ASTA control (3.54) with the adaptive gains

$$\begin{aligned} \dot{\alpha} &= \begin{cases} \omega_1\sqrt{\frac{\gamma_1}{2}}, & \text{if } \sigma \neq 0 \\ 0, & \text{if } \sigma = 0 \end{cases} \\ \beta &= 2\epsilon\alpha + \lambda + 4\epsilon^2, \end{aligned} \tag{3.57}$$

where $\epsilon, \lambda, \gamma_1, \omega_1$ are arbitrary positive constants. It is also proposed in Shtessel et al. (2010) that the adaptive gains α, β are bounded.

However, since σ is rarely exactly equal to 0, a modification of the update laws in which a small threshold value for σ is used instead is given by

$$\begin{aligned} \dot{\alpha} &= \begin{cases} \omega_1\sqrt{\frac{\gamma_1}{2}}, & \text{if } |\sigma| > \alpha_m \\ 0, & \text{if } |\sigma| \leq \alpha_m \end{cases} \\ \beta &= 2\epsilon\alpha + \lambda + 4\epsilon^2. \end{aligned} \tag{3.58}$$

3.5.3 Generalized Super-Twisting Algorithm

A modified version of the STA is the generalized STA, which includes added linear correction terms to the purely nonlinear terms of the STA, and a generalization of the nonlinear terms in the original STA. The added linear terms give the control design extra degrees of freedom, which will provide a stronger attraction force to the algorithm when the trajectories are far away from the origin (Moreno, 2009). Thus, we obtain faster convergence and enhanced stability robustness through the GSTA.

In Moreno (2009) the GSTA, for the case when there are no perturbations present in the system, is presented as

$$\begin{aligned} u &= -k_1\phi_1(\sigma) + z \\ \dot{z} &= -k_2\phi_2(\sigma), \end{aligned} \tag{3.59}$$

where k_1, k_2 are positive control gains, and

$$\begin{aligned}\phi_1(\sigma) &= \mu_1|\sigma|^{\frac{1}{2}}\text{sign}(\sigma) + \mu_2\sigma \\ \phi_2(\sigma) &= \frac{\mu_1^2}{2}\text{sign}(\sigma) + \frac{3}{2}\mu_1\mu_2|\sigma|^{\frac{1}{2}}\text{sign}(\sigma) + \mu_2^2\sigma\end{aligned} \tag{3.60}$$

are the nonlinear stabilizing terms. The only values for μ_1 that are considered are $\mu_1 = 0$ and $\mu_1 = 1$ without loss of generality. Furthermore, note that when $\mu_1 = 1$ and $\mu_2 = 0$, the unmodified STA is recovered. The GSTA, however, is obtained from (3.59) and (3.60) when $\mu_1 = 1$ and $\mu_2 > 0$. This means that we can rewrite the nonlinear stabilizing terms (3.60) as

$$\begin{aligned}\phi_1(\sigma) &= |\sigma|^{\frac{1}{2}}\text{sign}(\sigma) + \beta\sigma \\ \phi_2(\sigma) &= \frac{1}{2}\text{sign}(\sigma) + \frac{3}{2}\beta|\sigma|^{\frac{1}{2}}\text{sign}(\sigma) + \beta^2\sigma,\end{aligned} \tag{3.61}$$

where μ_2 has been redefined as $\beta = \mu_2$. As for the ASTA, note that β is a control gain in relation to the GSTA, and different from the sideslip angle in this chapter.

What remains of the control design problem is choosing the control gains β, k_1, k_2. In Castillo et al. (2018) the conditions for the control gains are presented for the application of GSTA to a nonlinear system with state- and time-dependent uncertain control coefficient and perturbations. The following problem definition and control design are based on Castillo et al. (2018).

Problem Formulation

We still consider the system (3.52) with sliding dynamics given by

$$\dot{\sigma} = a(t, x) + b(t, x)u, \tag{3.62}$$

where $\sigma \in \mathbb{R}$ and the functions $a(t, x)$ and $b(t, x)$ are uncertain functions dependent on the time and state. The uncertain function a and control coefficient b should be continuous in order to produce a continuous control signal. Assume that

(A1) The functions a and b are Lipschitz continuous functions with respect to t.

(A2) $a, b \in \mathcal{C}^1$ with respect to x.

(A3) The uncertain control coefficient is bounded by

$$0 < b_0 \leq b(t, x) \leq B. \tag{3.63}$$

(A4) The uncertain function can be split into two parts

$$a(t, x) = a_1(t, x) + a_2(t, x) \tag{3.64}$$

such that the first term is vanishing at the origin, i.e. $a_1(0, t) = 0$, $\forall t \geq 0$, and bounded by

$$|a_1(t, x)| \leq \alpha|\phi_1(\sigma)|, \quad \alpha > 0. \tag{3.65}$$

(A5) The total time-derivative of the second term of the perturbation function (divided by the control coefficient $b(t,x)$) can be written as

$$\begin{aligned}\frac{d}{dt}\left(\frac{a_2(t,x)}{b(t,x)}\right) &= \frac{1}{b}\frac{\partial a_2}{\partial t} - \frac{a_2}{b^2}\frac{\partial b}{\partial t} + \left(\frac{1}{b}\frac{\partial a_2}{\partial x} - \frac{a_2}{b^2}\frac{\partial b}{\partial x}\right)\dot{x} \\ &= \delta_1(t,x) + \delta_2(t,x)\dot{x},\end{aligned} \tag{3.66}$$

and the terms δ_1, δ_2 are bounded by positive constants

$$|\delta_1(t,x)| \leq \bar{\delta}_1, \quad |\delta_2(t,x)| \leq \bar{\delta}_2. \tag{3.67}$$

Control Structure

The main result of Castillo et al. (2018) is as follows: Suppose that $a(t,x)$ and $b(t,x)$ of (3.62) satisfy assumption (A3) and (A5). Then σ will converge to zero globally and in finite-time, if GSTA gains $k_1, k_2, \beta > 0$ are designed to satisfy the conditions given in Castillo et al. (2018). As the conditions are quite substantial and elaborate, they are not included here.

3.6 Multivariable Second-Order Sliding Mode Control

Suppose that the sliding dynamics for a nonlinear system can be written on the form

$$\dot{\sigma} = a(t,x) + b(t,x)\bar{u} + \gamma(t,\sigma), \tag{3.68}$$

where $a \in \mathbb{R}^m$ is the system functions, $b \in \mathbb{R}^{m\times m}$ is the control coefficient, and $\gamma \in \mathbb{R}^m$ is an unknown disturbance. Furthermore, the control variable $\bar{u}$ is given by

$$\bar{u} = b^{-1}(t,x)(u - a(t,x)) \tag{3.69}$$

if $\det(b(t,x)) \neq 0$, where $u \in \mathbb{R}^m$ is the control signal generated by one of the MSTA versions presented in this section. This means that the closed-loop sliding dynamics have the form

$$\dot{\sigma} = u + \gamma(t,\sigma) \tag{3.70}$$

To perform the transformation in (3.69) so that the sliding dynamics can be written on the form above, the functions a and b need to be known, and b has to be nonsingular.

The fact that a and b have to be known to complete the control coefficient transformation in (3.69) makes it difficult to use the multivariable controllers presented in this section since most systems contain disturbances due to modeling uncertainties. Therefore it may be possible to modify the transformation in (3.69). This can be done either by regarding the function a as a part of the perturbation in the sliding dynamics so that the transformation is given by

$$\bar{u} = b^{-1}(t,x)u, \tag{3.71}$$

if b is known, or by implementing the original transformation in (3.69) with nominal functions a_{nom} and b_{nom} and assume that the transformation contribute to the perturbation in the sliding dynamics with an uncertain term so that the total perturbation is given by

$$\vartheta = \Delta b^{-1}(t,x)(u - \Delta a(t,x)) + \gamma(t,\sigma).$$

A final alternative is a combination of both alternatives above. This means that the function a is disregarded in the transformation which is implemented with a nominal control coefficient b_{nom}. The total perturbation in the sliding dynamics in this case becomes

$$\vartheta = \Delta b^{-1}(t,x)u + a(t,x) + \gamma(t,\sigma).$$

This last alternative is easier to implement since the transformation only relies on b_{nom}, but the total perturbation ϑ will also be greater.

Note that the notation used in this report varies slightly from the notations used in the original publications of the different algorithms. The reason for this is to make all three following subsections cohesive in notation.

Subsection 3.6.1 presents the multivariable STA, while an adaptive extension and a generalized version of the MSTA are presented in subsections 3.6.2 and 3.6.3, respectively.

3.6.1 Multivariable Super-Twisting Algorithm

Consider the sliding dynamics (3.68), the transformation (3.69), and the single-input STA (3.47). Suppose that for a $\dot{\sigma} \in \mathbb{R}^m$, we can formulate a control law $u \in \mathbb{R}^m$ in terms of m decoupled injection terms given by

$$u_i = -k_1|\sigma_i|^{\frac{1}{2}}\text{sign}(\sigma_i) - k_2\sigma_i + z_i \tag{3.72}$$

$$\dot{z}_i = -k_3\text{sign}(\sigma_i) - k_4\sigma_i \tag{3.73}$$

for $i = 1 \dots m$, where k_2 and k_4 are usually chosen as $k_2 = k_4 = 0$ in the scalar case (Nagesh and Edwards, 2014) so that the original STA in (3.47) is recovered. Using these decoupled injection terms, the sliding dynamics become

$$\dot{\sigma}_i = -k_1|\sigma_i|^{\frac{1}{2}}\text{sign}(\sigma_i) - k_2\sigma_i + z_i + \gamma_i(t,\sigma) \tag{3.74}$$

for $i = 1 \dots m$. It can be proven that $\sigma_i = \dot{\sigma}_i = 0$ in finite-time for the case when $|\gamma_i| \leq d_i|\sigma_i|$ for some finite scalars d_i and properly chosen gains $k_1 \dots k_4$ (Moreno and Osorio, 2012), and the case when $|\dot{\gamma}_i| \leq \bar{d}_i$ for some finite scalars $\bar{d}_i$ and appropriate gains $k_1 \dots k_4$ (Levant, 1993; Moreno and Osorio, 2012).

However, suppose that a non-decoupled injection term is used instead of the decoupled structure in (3.72)-(3.73). Such a non-decoupled control is formulated as

$$u(\sigma) = -k_1\frac{\sigma}{\|\sigma\|^{1/2}} + z - k_2\sigma, \quad u(0) \coloneqq 0 \tag{3.75}$$

$$\dot{z}(\sigma) = -k_3\frac{\sigma}{\|\sigma\|} - k_4\sigma + \varphi(t), \quad \dot{z}(0) \coloneqq 0, \tag{3.76}$$

which is the MSTA presented in Nagesh and Edwards (2014). Note that for $m = 1$, the original STA is recovered given that $k_2 = k_4 = 0$ and that $\varphi \equiv 0$. The finite-time stability of the MSTA (3.75)-(3.76) is proven in Nagesh and Edwards (2014) through Lyapunov-methods for an appropriate configuration of control gains $k_1 \dots k_4$, given that the inequalities

$$\left\|\gamma(t,\sigma)\right\| \leq \delta_1\|\sigma\| \tag{3.77}$$

$$\left\|\varphi(t)\right\| \leq \delta_2 \tag{3.78}$$

hold for scalars $\delta_1, \delta_2 > 0$. Additionally, it is assumed in the Lyapunov-analysis presented in Nagesh and Edwards (2014) that both σ and z in (3.75)-(3.76) are continuous and differentiable everywhere except on the subspace

$$\mathcal{S} = \{(\sigma, z) \in \mathbb{R}^{2m} \ : \ \sigma = 0\}, \tag{3.79}$$

which is called the zero-measure set (López-Caamal and Moreno, 2019).

3.6.2 Adaptive Multivariable Super-Twisting Algorithm

Several examples of implementations of an adaptive MSTA can be found in the literature (Dong et al., 2016; Hu et al., 2019; Fan and Tian, 2016; Tian et al., 2019). The focus in this report is on the version found in Hu et al. (2019) and Dong et al. (2016).

Consider still the sliding dynamics (3.68) and the transformation (3.69). The AMSTA presented in Hu et al. (2019) and Dong et al. (2016) is given by

$$u(\sigma) = \alpha_1 \frac{\sigma}{\|\sigma\|^{1/2}} + z, \quad u(0) \coloneqq 0 \tag{3.80}$$

$$\dot{z}(\sigma) = -\frac{\alpha_2}{2}\frac{\sigma}{\|\sigma\|} + \varphi(t), \quad \dot{z}(0) \coloneqq 0, \tag{3.81}$$

with adaptive gain update laws given by

$$\dot{\alpha}_1 = \begin{cases} \omega_1 \sqrt{\frac{\gamma_1}{2}}, & \text{if } \|\sigma\| > \sigma_T \\ 0, & \text{if } \|\sigma\| \leq \sigma_T \end{cases} \tag{3.82}$$

$$\alpha_2 = 2\epsilon_1 \alpha_1, \tag{3.83}$$

where $\sigma_T > 0$ is some small threshold value, and ω_1, γ_1, and ϵ_1 are positive constants. Furthermore, according to Hu et al. (2019) and Dong et al. (2016), the constant ϵ_1 should be chosen as

$$\epsilon_1 = \frac{\omega_3}{2\omega_1}\sqrt{\frac{\gamma_3}{\gamma_1}} \tag{3.84}$$

for positive constants ω_3 and γ_3.

In Hu et al. (2019) and Dong et al. (2016) Lyapunov-methods are employed to prove that $\sigma = \dot{\sigma} = 0$ in finite-time for the AMSTA in (3.80)-(3.81) with the gain adaption laws given in (3.82)-(3.83). As in the Lyapunov-analysis of the MSTA, the functions σ and z are assumed to be continuous and differentiable everywhere except on the zero-measure set $\mathcal{S}$ given in (3.79).

Furthermore, the perturbations $\gamma(t, \sigma)$ and $\varphi(t)$ are assumed to be bounded by

$$\|\gamma\| \leq \delta_1 \|\sigma\|^{\frac{1}{2}} \tag{3.85}$$

$$\|\varphi\| \leq \delta_2, \tag{3.86}$$

and γ is also assumed to be differentiable so that

$$\|\dot{\gamma}\| \leq \delta_3, \tag{3.87}$$

where the bounds $\delta_1, \delta_2, \delta_3 > 0$ exist, but are unknown.

3.6.3 Generalized Multivariable Super-Twisting Algorithm

A generalized version of the MSTA is presented in López-Caamal and Moreno (2019). The sliding dynamics that are considered are still (3.68) with the transformation (3.69), with the additional assumption that the control coefficient b in (3.68) is a regular matrix.

The GMSTA presented in López-Caamal and Moreno (2019) is

$$u = -k_1\phi_1(\sigma) + k_3 z \tag{3.88}$$
$$\dot{z} = -k_2\phi_2(\sigma) + \varphi(t,\sigma), \tag{3.89}$$

where

$$\phi_1(\sigma) = (\alpha_g\|\sigma\|^{-p_g} + \beta_g + \gamma_g\|\sigma\|^{q_g})\sigma, \quad \phi_1(0) \coloneqq 0 \tag{3.90}$$
$$\phi_2(\sigma) = (\alpha_g(1-p_g)\|\sigma\|^{-p_g} + \beta_g + \gamma_g(1+q_g)\|\sigma\|^{q_g})\phi_1(\sigma), \quad \phi_2(0) \coloneqq 0 \tag{3.91}$$

with

$$0 < p_g \leq \frac{1}{2}, \quad q_g > 0, \quad \alpha_g > 0, \quad \beta_g, \gamma_g \geq 0$$

and $k_i \in \mathbb{R}^{m\times m}$, $\forall j \in [1,3]$ are diagonal matrices with positive entries. Furthermore, we have that $\phi_j : \mathbb{R}^m \to \mathbb{R}^m$ and $\varphi : \mathbb{R}_{\geq 0} \times \mathbb{R}^m \to \mathbb{R}^m$. If the control is designed following (3.88)-(3.91), then the origin of the sliding dynamics (3.68) is finite-time stable (López-Caamal and Moreno, 2019). Furthermore, according to López-Caamal and Moreno (2019), choosing $p_g = 1/2$ in (3.90)-(3.91) gives the algorithm robustness against nonvanishing perturbations φ. Additionally, it can be noted that all coordinates in σ converge to $\sigma = 0$ at the same time.

In López-Caamal and Moreno (2019) a vector $\zeta \in \mathbb{R}^{2m}$ is defined as

$$\zeta(\sigma, z) = [\phi_1(\sigma)^\top \; z^\top]^\top, \tag{3.92}$$

which is assumed to be continuous and differentiable everywhere, except on the zero-measure set $\mathcal{S}$ defined in (3.79). This implies that the function ϕ_2 is also continuous everywhere except, possibly, in $\mathcal{S}$. Furthermore, the function $\phi_1 = 0$ if and only if $\sigma = 0$, and we have that $\left\|\phi_1(\sigma)\right\| \to \infty$ as $\|\sigma\| \to \infty$. Additionally, the function ϕ_2 can be expressed by the function ϕ_1 and its gradient $\nabla_\sigma\phi_1(\sigma)$, which is denoted $J(\sigma)$, so that

$$\phi_2(\sigma) = J(\sigma)\phi_1(\sigma), \; J(\sigma) > 0, \forall\sigma \in \mathbb{R}^m \setminus \mathcal{S}, \tag{3.93}$$

where $\mathcal{S}$ is the zero-measure set.

Furthermore, according to López-Caamal and Moreno (2019), the perturbations γ and φ can be written in terms of the vector ζ via the matrices $G_j(t)$:

$$\gamma(t,\sigma,z) = G_1(t)\phi_1(\sigma) + G_3(t)z \tag{3.94}$$
$$\varphi(t,\sigma) = G_2(t)\phi_2(\sigma), \tag{3.95}$$

where the matrices $G_j(t)$ are possibly unknown and possibly time-varying, yet element-wise bounded. The equations above state that the perturbation terms γ and φ may grow proportional to the functions ϕ_1, z, and ϕ_2 (López-Caamal and Moreno, 2019).

The reason the algorithm in (3.88)-(3.91) is called a generalized version of the MSTA is that from the framework in (3.88)-(3.91) several versions of the original MSTA can be recovered. As previously mentioned, the control gains k_2, k_4 in (3.75)-(3.76) are usually chosen as $k_2, k_4 = 0$ (Nagesh and Edwards, 2014). This version of the MSTA can be recovered from (3.88)-(3.91) if $l = \frac{1}{2}, \alpha_g, k_3 = 1$, $\beta_g = 0$ and $\gamma_g = 0$. The original MSTA with $k_1, k_2 > 0$ is recovered if $\alpha_g, k_3 = 1$ and $\gamma_g = 0$. Finally, a multivariable version of the single-input GSTA given in (3.59)-(3.60) can be recovered from (3.88)-(3.91) if $\gamma_g = 0$ and $k_3 = 1$, with $\alpha_g = \mu_1$ and $\beta_g = \mu_2$.

3.7 Analysis of Internal Dynamics

3.7.1 Concept of Equivalent Control

Until now, the control laws that have been formulated have been based solely on SMC. However, it is possible to formulate the control law, u, with both a discontinuous SMC term and an equivalent control term. The equivalent control is defined as the control input that is needed to maintain the sliding mode once it has been reached. The idea is that when a sliding mode is obtained in the system, then we also have that $\dot{\sigma} = 0$. From this constraint, it is possible to find the equivalent control, u_{eq}.

Consider again the system (3.4). The equivalent control for (3.4) is found by solving for u in $\dot{\sigma} = 0$ with $\dot{\sigma}$ as in (3.8). But as mentioned earlier, it is not possible to implement this control law since it requires exact knowledge about the system parameters and the disturbance. Therefore, formulating the equivalent control can have two purposes in the control design. Firstly, it can be seen as a tool to facilitate analysis of the system behavior in the sliding mode, which is discussed further in the following subsections. Secondly, it can be used in the design of a control law to relax the conditions on the control gain K of the discontinuous control term. The latter is the topic of this subsection.

The system (3.4) can be rewritten as

$$\begin{cases} \dot{x}_1 = x_2, & x_1(0) = x_{1_0} \\ \dot{x}_2 = h_0(t,x) + \Delta h(t,x) + u + d(t), & x_2(0) = x_{2_0}, \end{cases} \tag{3.96}$$

where we have defined $h(t,x) = h_0(t,x) + \Delta h(t,x)$, with h_0 being an estimate of the uncertain function h, and Δh representing the error in our estimate. It is assumed that the uncertainties are bounded by $|\Delta h(t,x)| \leq H$. It is then possible to formulate the equivalent control assuming ideal conditions, which in this case means that $d(t) = \Delta h(t,x) = 0$ in the system (3.96) above. The sliding dynamics given in (3.8) then simplifies to

$$\dot{\sigma} = a_1 x_2 + h_0(t,x) + u. \tag{3.97}$$

Solving this expression for the control u yields the equivalent control u_{eq}:

$$u_{eq} = -a_1 x_2 - h_0(t,x). \tag{3.98}$$

Now that the equivalent control has been found, it is possible to formulate the control law as a combination of the equivalent control, u_{eq}, and the discontinuous SMC, u_s:

$$u = u_{eq} + u_s = -a_1 x_2 - h_0(t,x) - K\text{sign}(\sigma), \tag{3.99}$$

with σ as in (3.5). Using this control law will soften the condition for the control gain K given in (3.12), as the dynamics of the Lyapunov-function (3.9) with the control law (3.99) are given by

$$\begin{aligned}\dot{V} &= \sigma\dot{\sigma} \\ &= \sigma(a_1 x_2 + h(t,x) + u + d(t)) \\ &= \sigma(\Delta h(t,x) + d(t) - K\text{sign}(\sigma)) \\ &\leq -|\sigma|(K - D - H) \\ &= -\frac{\eta}{\sqrt{2}}|\sigma| < 0,\ \forall \sigma \neq 0\end{aligned} \tag{3.100}$$

as long as the control gain is chosen to satisfy

$$K = \frac{\eta}{\sqrt{2}} + D + H. \tag{3.101}$$

This condition will give a less conservative estimate of K than the one given in (3.12), as we no longer view the entire system dynamics as a perturbation in the control design as in subsection 3.2. Combining feedback control based on equivalent control with SMC can thus reduce chattering, as it allows for smaller control gains.

3.7.2 Internal Dynamics

As previously mentioned, the equivalent control can be a tool for analysis of the system dynamics in the sliding mode. This becomes relevant when there exist some nontrivial internal dynamics in the system which are not directly stabilized by the control law.

In the sliding mode enforced by the equivalent control (3.98), the states x_1 and x_2 in the example system given in (3.4) are governed by the compensated dynamics

$$\begin{cases}\dot{x}_1 = -a_1 x_1 \\ \dot{x}_2 = -a_1 x_2,\end{cases} \tag{3.102}$$

which are exponentially stable. The fact that the compensated dynamics are stable in the sliding mode is trivial, as the control law is designed to achieve just this.

Now, say there exist two additional internal states of the system (3.4), so that it expands to

$$\begin{cases}\dot{x}_1 = x_2, & x_1(0) = x_{10} \\ \dot{x}_2 = h(t,x) + u, & x_2(0) = x_{20} \\ \dot{x}_3 = h_1(x,u,t), & x_3(0) = x_{30} \\ \dot{x}_4 = h_2(x,u,t), & x_4(0) = x_{40},\end{cases} \tag{3.103}$$

where h_1 and h_2 are estimates of uncertain functions, which are assumed to be bounded. Note that the function h is a function of the full state x so the equivalent control (3.98) is also a function of the internal states x_3 and x_4. This is an important detail, as the equivalent control may grow unbounded if the states x_3, x_4 are unstable in the sliding mode.

Now that the equivalent control u_{eq} has been determined, it is possible to find the system's (3.103) compensated dynamics in the sliding mode by inserting u_{eq} given in

(3.98) for the control u. The resulting compensated dynamics in the sliding mode are given by

$$\begin{cases} \dot{x}_1 = -a_1 x_1 \\ \dot{x}_2 = -a_1 x_2 \\ \dot{x}_3 = h_1(x, u_{eq}, t) \\ \dot{x}_4 = h_2(x, u_{eq}, t), \end{cases} \tag{3.104}$$

where the unknown internal dynamics in the sliding mode are given by $\dot{x}_3$ and $\dot{x}_4$. For the internal dynamics to be stable in the sliding mode, the dynamics described by $\dot{x}_3$ and $\dot{x}_4$ should guarantee that x_3 and x_4 are bounded, so that $h(t, x)$ and u_{eq} are also bounded. This is investigated in the next subsection.

3.7.3 Zero Dynamics

According to Khalil (2002), the zero dynamics of a system are found by setting the output of the system, which is in this case taken to be σ, equal to zero. The fact that $\sigma = 0$ implies that $\dot{\sigma} = 0$ as long as a sliding mode is enforced in the system, which means the stability of the zero dynamics of the system (3.103) can be determined by looking at the stability of the dynamics of the equivalent system given in (3.104), keeping in mind that $\sigma = \dot{\sigma} = 0$.

In the case that the functions h, h_1, h_2 are nonlinear, one possible approach is to linearize the system around an equilibrium x^* to analyze the local stability of the internal dynamics in the sliding mode. Once the system has been linearized, the compensated dynamics can be written in a state-space form as

$$\dot{x} = Ax \tag{3.105}$$

which means that the local asymptotic stability of the zero dynamics can simply be determined from the eigenvalues of the linearized system matrix A if A is constant. The eigenvalues are denoted $\lambda_i, i = 1, ..., 4$, and it can easily be determined from (3.104) that $\lambda_1 = \lambda_2 = -a_1$. The remaining eigenvalues can then be determined from (3.105).

If we have that the eigenvalues $\lambda_{3,4} < 0$ then the system (3.103) is stable, which means that the internal dynamics are locally asymptotically stable in the sliding mode. However, if either $\lambda_3 \geq 0$ or $\lambda_4 \geq 0$, then the internal dynamics of the system (3.103) in the sliding mode are unstable. In this case, the equivalent control grows unbounded. Another result of this kind of analysis can be that either $\lambda_3 = 0$ or $\lambda_4 = 0$ while the other eigenvalue is negative. Then it is not possible to make any conclusions about the stability of the internal dynamics from the analysis in this section.

Another disadvantage of this kind of stability analysis is that it only guarantees the stability of the system in the sliding mode. If $\sigma \neq 0$ at the beginning of a simulation, it is not possible to say whether x_3 or x_4 can grow unbounded before the sliding surface is reached should it not be possible to guarantee that the functions h_3 and h_4 are bounded. However, the stability of the internal dynamics, which is analyzed above, is still a necessary condition for the SMC algorithms presented earlier in this chapter to be stable.

Chapter 4

Literature Review

This literature review aims to give an insight into the use of the MSTA, and extensions to the basic algorithm, in applications for aerospace and attitude control designs.

Aerospace systems are often highly uncertain, nonlinear, and coupled systems that need a robust control strategy to operate safely and accurately. They often operate in unpredictable and uncertain environments, where there are external disturbances present. It is sometimes possible to decouple a multi-input system into several SISO control loops so that single-input control strategies can be applied. However, this approach may fail if the interaction between the plant variables is too strong (Dong et al., 2016). Therefore, it may be advantageous to design a multi-input control system that enables more accurate modeling of nonlinear and coupled systems.

Even though the super twisting approach (Levant, 1993) has existed for quite some time, a multivariable version of the original STA was only recently presented in Nagesh and Edwards (2014), and extensions of it is still an area of research with a great deal of activity. Several extensions exist, for example, the variable-gain, the adaptive-gain, and the generalized MSTA (Vidal et al., 2017; Dong et al., 2016; López-Caamal and Moreno, 2019).

Section 4.1 of this chapter contains a brief discussion of the original MSTA and its extensions. Section 4.2 presents research on the use of the MSTA in aerospace and attitude control design. Finally, section 4.3 presents several papers in which extensions of the MSTA are employed in aerospace and attitude control design.

4.1 Extensions of the Multivariable STA

The multivariable STA for MIMO systems is presented in Nagesh and Edwards (2014) as an extension to the original super-twisting approach presented in Levant (1993) that includes linear terms in the sliding surface σ. The stability and robustness properties and convergence rates of the original STA in Levant (1993) have been analyzed in several papers (Moreno and Osorio, 2008, 2012) by employing Lyapunov methods. However, these papers consider only single-input structures. In Nagesh and Edwards (2014) the

proposed multivariable super-twisting structure is analyzed using Lyapunov ideas from Moreno and Osorio (2012). The finite-time stability of the sliding dynamics is proven given that the system is only affected by unknown perturbations and uncertainties that are bounded by sliding variable-dependent linear growth constraints.

A drawback of the algorithm presented in Nagesh and Edwards (2014) is the need for a complete knowledge of the input matrix $b(t, x)$ to generate the control signal u. Another version of the approach in Nagesh and Edwards (2014) that removes the requirement of an exactly known input matrix by extending the stability analysis is presented in Vidal et al. (2016). However, it is necessary to know the upper and lower bounds for the largest and smallest eigenvalues of the input matrix $b(t, x)$ to prove finite-time stability.

An approach to variable gain MSTA (VGMSTA) is presented in Gonzalez et al. (2012) for a linear time-invariant (LTI) MIMO system subjected to an absolutely continuous uncertainty/disturbance. In this case, the variable gains are dependent on both time and state. The approach in Gonzalez et al. (2012) is further extended in Vidal et al. (2017) where a global output-feedback VGMSTA design is presented. In this paper, a controller based on a VGMSTA approach for an uncertain nonlinear system is described. The paper by Vidal et al. (2017) proves through Lyapunov-analysis that the control strategy achieves global finite-time convergence to the equilibrium point in the presence of parametric uncertainties and absolutely continuous matched nonlinear disturbances. The advantage of variable gains is that it is possible to compensate for a bounded (matched) perturbation if the perturbation bound is not known a priori, or if the bound is time- or state-varying (Gonzalez et al., 2012).

The MSTA with variable gains is a robust control strategy that can be applied to a broader class of uncertain systems (Vidal et al., 2017). However, some knowledge about the disturbances is still required, and the disadvantage of overestimating control gains that both the MSTA and the VGMSTA suffer from remains. An alternative approach that does not suffer from these disadvantages is the adaptive MSTA (AMSTA). Several versions of the MSTA with adaptive gains have been used in attitude-control applications, for example Tian et al. (2019), Fan and Tian (2016), Dong et al. (2016), and Hu et al. (2019). The control objective in these papers is to perform trajectory tracking by generating a continuous control signal in the presence of matched disturbances with unknown bounds. The finite-time convergence of the AMSTA is proven by Lyapunov methods in both Dong et al. (2016) and Hu et al. (2019).

Another version of the MSTA is the generalized MSTA (GMSTA), which is presented in López-Caamal and Moreno (2019). The GMSTA is an extension of the GSTA for the single-input case presented in Moreno (2009), to a multivariable framework. Several versions of the GMSTA are introduced in López-Caamal and Moreno (2019). One of them is a direct generalization of the MSTA (Nagesh and Edwards, 2014), which is proven to be globally finite-time stable through Lyapunov-analysis, which even accounts for the case in which the gains are time-varying.

The adaptive and generalized versions of the MSTA can be combined in an adaptive multivariable generalized STA (AMGSTA) presented in Borlaug et al. (2020). The AMGSTA in this paper is proposed for systems whose perturbations and uncertain control coefficients are time- and state-dependent. The global finite-time convergence of these systems is guaranteed due to the dynamically adapted control gains and proven through

Lyapunov-analysis. The proof in Borlaug et al. (2020) is performed for a single-input system, but it also holds for n-dimensional systems that can be separated into n one-dimensional cases.

4.2 Multivariable STA Applied to Attitude Control Design

An example of the use of the MSTA in attitude control problems in aerospace applications is given in Xuehui et al. (2015). In this paper, the control objective is to achieve continuous finite-time tracking of a trajectory for a spacecraft in the presence of external disturbances. Lyapunov methods are employed to prove the finite-time convergence of the closed-loop system to the equilibrium. Numerical simulations are performed to show the performance characteristics of the proposed controller. The simulations show the robustness of the controller in the presence of cyclic disturbance torques. Additionally, the resulting control signal is shown to be continuous and the error trajectories reach the equilibrium point in finite-time.

Another example of the application of the MSTA in attitude control design is presented in Fang et al. (2015). In this paper, a robust trajectory tracking controller for a small unmanned helicopter with model uncertainties and external disturbances is designed. The controller is paired with a disturbance observer which is designed based on both backstepping and the MSTA. The system with the controller and disturbance observer is proven to be globally asymptotically stable through Lyapunov-analysis. Lastly, the proposed control design is compared through simulations with another control system design based only on backstepping. The tracking performance of the method proposed in Fang et al. (2015) is shown to be more effective than the backstepping method, with smaller overshoot, faster tracking, and less chattering in the system.

The MSTA has also been applied in control design for attitude control of quadrotor UAVs, such as in Tian et al. (2018). Here, the control objective is to achieve continuous finite-time trajectory tracking. The finite-time stability of the closed-loop system is determined using the Lyapunov method and the homogeneous technique (Tian et al., 2018). The performance of the control strategy is confirmed first through numerical simulations, then through experimental tests on a quadrotor UAV indoors. During the performance testing, the proposed method is compared with a PID controller. The controller based on the MSTA demonstrates better robustness and higher tracking accuracy than the PID controller due to the ability of the MSTA of rejecting disturbances.

4.3 Extensions of the Multivariable STA Applied to Attitude Control Design

An example of the application of the AMSTA in attitude control design is presented in Dong et al. (2016) where an autopilot based on the AMSTA for a reusable launch vehicle (RLV) is presented. The control objective is to design the control torque so that the RLV can track the guidance commands in finite-time in the presence of model uncertainties

and external disturbances with unknown boundaries (Dong et al., 2016). The paper states that the AMSTA based controller can adapt to additive and multiplicative perturbations with unknown boundaries while avoiding gain overestimation. It is confirmed through simulations that the proposed controller is effective and robust, and can provide fast and accurate tracking, and chattering suppression.

The control strategy presented in Fan and Tian (2016) is another approach to AMSTA. In this paper, an AMSTA is implemented for a hypersonic vehicle with the control objective of tracking a velocity and altitude reference in the presence of bounded but unknown perturbations. While the control objective in this article may not be to perform attitude control, the problem of following a velocity and altitude reference is in many ways similar to attitude control. Designing control systems for hypersonic vehicles is a challenging task due to the high-speed flight conditions and severe aerodynamic uncertainties (Fan and Tian, 2016). It is, therefore, necessary to design a robust and effective controller to guarantee adequate tracking of the references. In Fan and Tian (2016) the controller is combined with a disturbance observer to further improve the tracking results.

In Tian et al. (2019) an attitude control design for a quadrotor UAV using an AMSTA is presented. The UAV is assumed to be affected by unknown external disturbances with unknown bounds so that gain adaptation is necessary to avoid overestimation of the control gains. The proof of finite-time stability of the closed-loop dynamics is derived using the Lyapunov technique (Tian et al., 2019). A comparison between using the AMSTA and single-input ASTA controllers is investigated, where the single-input design exhibits better accuracy in theory, while in practice the multivariable design proved to be easier to tune and gave the best results.

The AMSTA has also been employed in the control design for other autonomous vehicles, for example in Hu et al. (2019). In this paper, an AMSTA control strategy is applied to the problem of designing a lane-keeping control for four-wheel independently actuated autonomous vehicles. Since it is difficult to measure the lateral velocity (Hu et al., 2019) a high-order sliding mode observer is included in the system. Lyapunov methods are employed to prove the finite-time convergence of the closed-loop system. To verify the effectiveness of the proposed control strategy, simulations were performed in which the proposed controller was compared to a more traditional SMC approach. The simulations show the robustness of the adaptive controller in yielding a high-performance, fast and accurate lane keeping control in a faulty steering situation Hu et al. (2019).

An example of the application of the GMSTA to a problem that is similar to the problem of attitude control is presented in Singh et al. (2020). In this paper, an event-based GMSTA is used to perform path tracking to achieve safe navigation of a nonholonomic mobile-robot in an unknown indoor environment. The event-triggered condition is obtained using Lyapunov theory to minimize the utilization of the resources. In addition to the Lyapunov-analysis, a sensitivity analysis of the proposed controller is performed to ensure that the GMSTA is more robust than the MSTA from Nagesh and Edwards (2014). The performance of the proposed control strategy is compared to several other controllers through experiments for obstacle avoidance applications. The effectiveness of the proposed controller is shown in terms of error convergence rate and disturbance rejection capability with minimum control effort compared to the other controllers.

Another extension of the MSTA is the previously discussed AMGSTA. A version of

this algorithm is implemented in Wei et al. (2019) in the control scheme for a space robot with coupled uncertainties and external disturbances. The space robot is a system with strongly coupled characteristics between the robot platform and the manipulators due to the absence of a fixed base. The advantages of the proposed controller over the original MSTA presented in Nagesh and Edwards (2014) are that there are fewer conditions and parameters to design, and the ability to compensate for both Lipschitz continuous disturbances and state-dependent uncertainties in finite-time (Wei et al., 2019). In addition to the AMGSTA, a sliding mode disturbance observer is introduced in the system to alleviate the system conservatism and improve convergence rate and accuracy (Wei et al., 2019). Numerical simulations show the efficiency of the proposed control design in achieving tracking of the reference trajectory while compensating for external disturbances and coupled uncertainties. The simulations also show that improved convergence accuracy and rate is achieved when the disturbance observer is added to the control design.

Chapter 5

Control Design

In this chapter, the control designs for the decoupled lateral and longitudinal models, and the multivariable 6DOF system are presented. Furthermore, the necessary assumptions for the SISO control algorithms to be applicable to the longitudinal model, and for the MIMO algorithms to be applicable to the 6DOF model, are verified.

Section 5.1 gives a brief description of the PI-controllers that are paired with the sliding mode controllers in some of the control designs in this chapter. Section 5.2 presents the single-input control design for the lateral model, and section 5.3 presents the single-input control design for the longitudinal model. Section 5.4 presents the control design for the 6DOF model using decoupled sliding surfaces, while section 5.5 contains the multivariable control design for the 6DOF model. In section 5.6 an analysis of the internal longitudinal dynamics is performed. Finally, section 5.7 presents the methods that are used to evaluate the performance of the control algorithms.

5.1 PI-controllers

There are four possible control commands that are generated by the control designs in this chapter; $u = [\delta_t, \delta_a, \delta_e, \delta_r]^\top$. The throttle command δ_t is always generated by a PI-controller, while δ_a and δ_e are always generated by sliding mode controllers. The rudder deflection δ_r however, is generated by either a sliding mode controller or a PI-controller depending on the control design.

5.1.1 Airspeed Hold Using Throttle

The design of the PI-controller that generates δ_t is based on the airspeed hold using throttle design in Beard and McLain (2012). The throttle command is given by

$$\delta_t = \delta_{t_0} + k_{p_{V_a}} \tilde{V}_a + k_{i_{V_a}} \int_0^t \tilde{V}_a \, d\tau, \tag{5.1}$$

with

$$\tilde{V}_a = V_{a_0} - V_a, \tag{5.2}$$

where δ_{t_0} is the throttle command at trim conditions and $k_{p_{V_a}}, k_{i_{V_a}} > 0$ are control gains. The PI-controller (5.1) is used in the control designs in section 5.2-5.5 to keep the UAV at a constant airspeed $V_a = V_{a_0}$. An example of the performance of the controller (5.1) can be found in Figure 5.1.

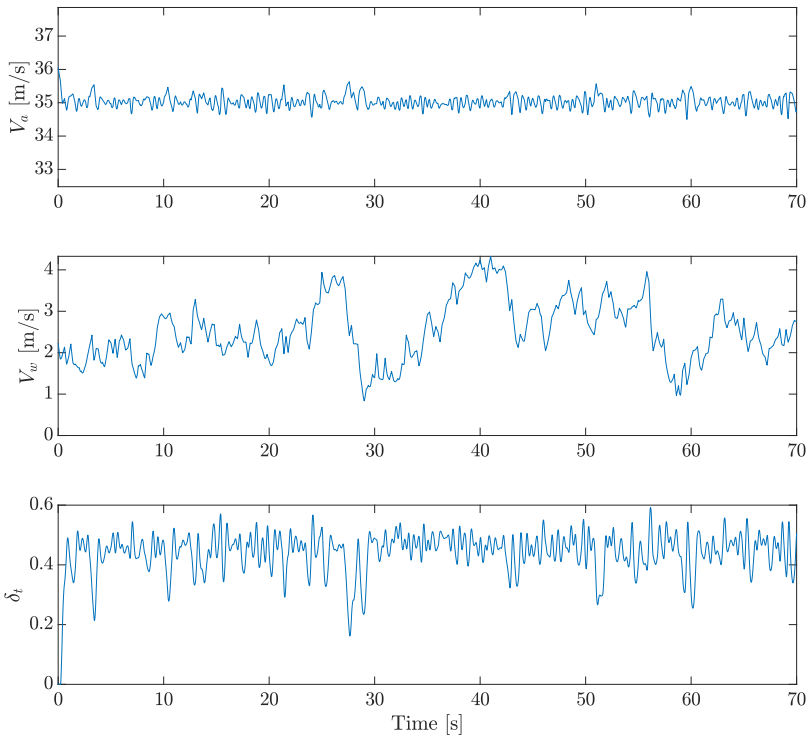

Figure 5.1: An example of the performance of the airspeed hold controller (5.1) applied to the 6DOF model when wind and external disturbances are present in the system for a constant reference $V_{a_0} = 35$ m/s. The control gains are chosen by trial and error as $k_{p_{V_a}} = 0.6$ and $k_{i_{V_a}} = 0.0009$.

5.1.2 Sideslip Hold

In the decoupled control design for the 6DOF model presented in section 5.4, the SMC design only generates the aileron and elevator deflections. Based on the design of the sideslip hold loop in Beard and McLain (2012), the PI-controller that generates δ_r is given by

$$\delta_r = -k_{p_\beta}\beta - k_{i_\beta}\int_0^t \beta \, d\tau, \tag{5.3}$$

where $k_{p_\beta}, k_{i_\beta} > 0$ are control gains. Thus, the PI-controller (5.3) is used to maintain zero sideslip angle, i.e. $\beta(t) = 0$ (Beard and McLain, 2012). An example of the performance of the controller (5.3) can be found in Figure 5.2.

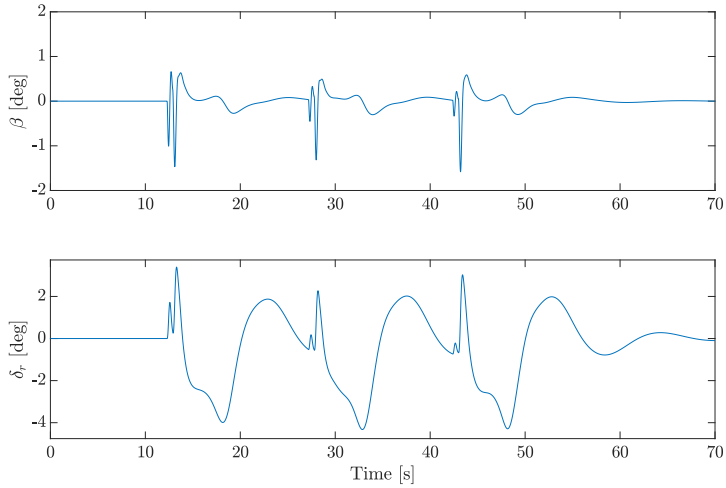

(a) An example of the response of the sideslip hold controller (5.3) to a step input reference in ideal conditions without disturbances in the system.

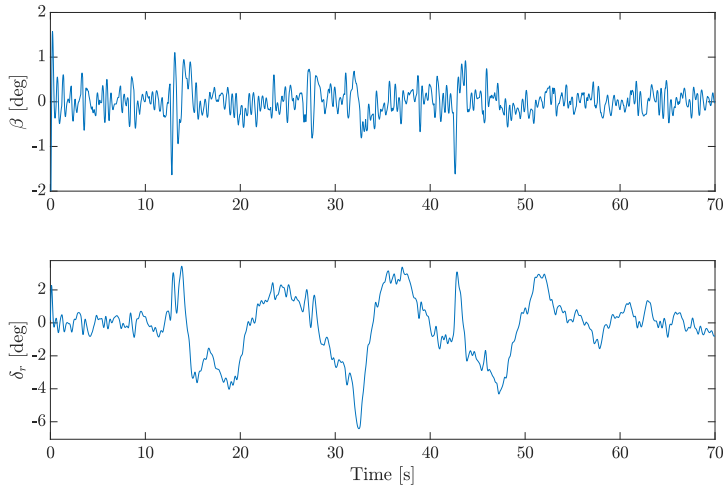

(b) An example of the performance of the sideslip hold controller (5.3) when wind and external disturbances are present in the system.

Figure 5.2: Two examples of the performance of the sideslip hold controller (5.3) when applied to the 6DOF model with control gains chosen by trial and error as $k_{p_\beta} = 10$ and $k_{i_\beta} = 0.05$.

5.2 Control Design for the Decoupled Lateral Model

This section presents the control design for the decoupled lateral model (2.78)-(2.81). First, the system is written in state-space form, then the sliding variable is determined, and finally, the sliding mode controllers are presented.

5.2.1 State-Space Representation

It is useful to write the dynamics of a system on state-space form since the compactness of this standard form facilitates the verification of the assumptions made about the system for the control algorithms presented in chapter 3. It is also helpful in determining the sliding variable and sliding dynamics, which is necessary to design the SMC algorithms presented in chapter 3.

The decoupled lateral dynamics (2.78)-(2.81) can be written in state-space form as

$$\dot{x}_\phi = f_\phi(t,x) + g_\phi(t)\delta_a + h_\phi(t)d_\phi(t), \tag{5.4}$$

where $x_\phi \in \mathbb{S}^1 \times \mathbb{S}^1 \times \mathbb{R} \times \mathbb{R}$ and $d_\phi \in \mathbb{R}^3$ are given by

$$x_\phi = \begin{bmatrix} \beta \\ \phi \\ p \\ r \end{bmatrix}, \quad d_\phi = \begin{bmatrix} d_{\phi_1} \\ d_{\phi_2} \\ d_{\phi_3} \end{bmatrix}.$$

The function $f_\phi : \mathbb{R}^4 \to \mathbb{R}^4$ accounts for the uncertain system functions, the function $g_\phi : \mathbb{R}^4 \to \mathbb{R}^4$ is the uncertain control coefficient, and the matrix $h_\phi \in \mathbb{R}^{4\times 3}$ accounts for the contribution of the disturbances d_{ϕ_i} to each state variable.

The elements of f_ϕ, denoted $f_{\phi_i}, i = 1, ..., 4$, are

$$\begin{aligned} f_{\phi_1} &= \frac{g}{V_a}\cos\beta\sin\phi - \frac{T}{\mathrm{m}V_a}\sin\beta - r \\ &\quad + \frac{\rho V_a S}{2\mathrm{m}}(C_{Y_\beta}\beta + (C_{Y_p}p + C_{Y_r}r)) \end{aligned} \tag{5.5}$$

$$f_{\phi_2} = p \tag{5.6}$$

$$\begin{aligned} f_{\phi_3} &= \frac{1}{2}\rho V_a^2 S b\left(\frac{I_z}{\Gamma_b}(C_{l_\beta}\beta + C_{l_p}\frac{b}{2V_a}p + C_{l_r}\frac{b}{2V_a}r)\right. \\ &\quad \left. + \frac{I_{xz}}{\Gamma_b}(C_{n_\beta}\beta + C_{n_p}\frac{b}{2V_a}p + C_{n_r}\frac{b}{2V_a}r)\right) \end{aligned} \tag{5.7}$$

$$\begin{aligned} f_{\phi_4} &= \frac{1}{2}\rho V_a^2 S b\left(\frac{I_{xz}}{\Gamma_b}(C_{l_\beta}\beta + C_{l_p}\frac{b}{2V_a}p + C_{l_r}\frac{b}{2V_a}r)\right. \\ &\quad \left. + \frac{I_x}{\Gamma_b}(C_{n_\beta}\beta + C_{n_p}\frac{b}{2V_a}p + C_{n_r}\frac{b}{2V_a}r)\right) \end{aligned}, \tag{5.8}$$

while the elements of g_ϕ are

$$g_{\phi_1} = \frac{\rho V_a S}{2\mathrm{m}}C_{Y_{\delta_a}} \tag{5.9}$$

$$g_{\phi_2} = 0 \tag{5.10}$$

$$g_{\phi_3} = \frac{1}{2}\rho V_a^2 Sb \left(\frac{I_z}{\Gamma_b} C_{l_{\delta_a}} + \frac{I_{xz}}{\Gamma_b} C_{n_{\delta_a}} \right) \tag{5.11}$$

$$g_{\phi_4} = \frac{1}{2}\rho V_a^2 Sb \left(\frac{I_{xz}}{\Gamma_b} C_{l_{\delta_a}} + \frac{I_x}{\Gamma_b} C_{n_{\delta_a}} \right). \tag{5.12}$$

Lastly, the rows of the matrix h_ϕ are given by

$$h_{\phi_1} = \begin{bmatrix} \frac{1}{\mathrm{m} V_a} & 0 & 0 \end{bmatrix} \tag{5.13}$$

$$h_{\phi_2} = \begin{bmatrix} 0 & 0 & 0 \end{bmatrix} \tag{5.14}$$

$$h_{\phi_3} = \begin{bmatrix} 0 & \frac{I_z}{\Gamma_b} & \frac{I_{xz}}{\Gamma_b} \end{bmatrix} \tag{5.15}$$

$$h_{\phi_4} = \begin{bmatrix} 0 & \frac{I_z}{\Gamma_b} & \frac{I_{xz}}{\Gamma_b} \end{bmatrix}. \tag{5.16}$$

A discussion of the boundedness of the decoupled lateral dynamics is presented in Griffiths (2020). It was concluded that the system functions f_ϕ, g_ϕ, and h_ϕ, as well as the disturbance d_ϕ are all bounded if the state x_ϕ is restricted to a domain

$$\mathcal{D}_\phi = \{x_\phi \in \mathbb{R}^4 : |x_\phi| \leq r_\phi\} \subset \mathbb{R}^4, \tag{5.17}$$

where r_ϕ is a vector of the bounds on each element of x_ϕ. The bounds were chosen as

$$|\beta| \leq 0.1 \text{ rad} \tag{5.18}$$

$$|\phi| \leq \frac{\pi}{2} \text{ rad} \tag{5.19}$$

$$|p| \leq 1.2 \text{ rad/s} \tag{5.20}$$

$$|r| \leq 0.5 \text{ rad/s} \tag{5.21}$$

for the lateral state variables. Additionally, the airspeed and the disturbance were restricted to

$$|d_i| \leq 4 \tag{5.22}$$

$$V_a \in [25, 40] \text{ m/s} \tag{5.23}$$

where the bound on the disturbance d_i is given in [N] for $i = 1$ and [Nm] for $i = 2, 3$. Under the conditions defined in (5.18)-(5.23), the state dynamics, in addition to the derivatives of the system functions $\dot{f}_\phi, \dot{g}_\phi$, and $\dot{h}_\phi$, were concluded to be bounded. This fact was used to determine the stability of the control algorithms designed in Griffiths (2020) when applied to the decoupled lateral dynamics.

5.2.2 Sliding Surface Design

The control objective for the lateral control system is to perform output tracking of the roll angle reference ϕ_r, so that $\phi \to \phi_r$ asymptotically. Following the methodology in 3.2.1, the sliding surface for the lateral system is defined as

$$\sigma_\phi = a_{\phi_1} e_\phi + \dot{e}_\phi, \tag{5.24}$$

where the error and error dynamics are

$$e_\phi = \phi - \phi_d \tag{5.25}$$
$$\dot{e}_\phi = p - p_d \tag{5.26}$$
$$\ddot{e}_\phi = \dot{p} - \dot{p}_d, \tag{5.27}$$

where it is assumed that $\dot{p}_d$ is bounded.

The sliding dynamics are then

$$\dot{\sigma}_\phi = a_{\phi_1}\dot{e}_\phi + \ddot{e}_\phi \tag{5.28}$$
$$= a_{\phi_1}\dot{e}_\phi + f_{\phi_3}(t,x) + g_{\phi_3}(t,x)\delta_a + h_{\phi_3}d_\phi(t) - \dot{p}_d, \tag{5.29}$$

which can be written on the more general form

$$\dot{\sigma}_\phi = a_\phi(t,x) + b_\phi(t,x)\delta_a + \gamma_\phi(t,x), \tag{5.30}$$

where

$$a_\phi(t,x) = a_{\phi_1}\dot{e}_\phi + f_{\phi_3}(t,x) - \dot{p}_d \tag{5.31}$$
$$b_\phi(t,x) = g_{\phi_3}(t,x) \tag{5.32}$$
$$\gamma_\phi(t) = h_{\phi_3}d(t). \tag{5.33}$$

The function $\dot{e}_\phi$ is defined in (5.26), f_{ϕ_3} is defined in (5.7), g_{ϕ_3} in (5.11), and h_{ϕ_3} in (5.15). Note that even though the new notation in (5.32)-(5.32) is not necessary, it is still introduced to follow the notation in chapter 3.

A discussion of the boundedness of the decoupled lateral sliding dynamics is presented in Griffiths (2020). In Griffiths (2020) it was concluded that when the state x_ϕ, the disturbance d_ϕ, and the airspeed V_a are all bounded by (5.18)-(5.23), the functions in the lateral sliding dynamics are all uniformly bounded by uniformly bounded by

$$|a_\phi| \leq A_\phi \tag{5.34}$$
$$|b_\phi| \leq B_\phi \tag{5.35}$$
$$|\gamma_\phi| \leq G_\phi. \tag{5.36}$$

This was used in Griffiths (2020) to verify the stability of the lateral control algorithms presented in the next subsection.

5.2.3 Sliding Mode Control Design

The four lateral control algorithms that are implemented are the saturation controller, the STA, the ASTA, and the GSTA, the equations for which are presented below. The saturation controller is given by

$$\delta_a = -k_a \text{sat}(\sigma_\phi), \tag{5.37}$$

the STA by

$$\begin{aligned} \delta_a &= -k_{a_1}|\sigma_\phi|^{\frac{1}{2}}\text{sign}(\sigma_\phi) + z_a \\ \dot{z}_a &= -k_{a_2}\text{sign}(\sigma_\phi), \end{aligned} \tag{5.38}$$

the ASTA by

$$\begin{aligned} \delta_a &= -\alpha_a |\sigma_\phi|^{\frac{1}{2}} \text{sign}(\sigma_\phi) + z_a \\ \dot{z}_a &= -\beta_a \text{sign}(\sigma_\phi), \end{aligned} \tag{5.39}$$

with update rules for the adaptive gains α_a and β_a given as

$$\begin{aligned} \dot{\alpha}_a &= \begin{cases} \omega_{a_1} \sqrt{\frac{\gamma_{a_1}}{2}}, & \text{if } |\sigma_\phi| > \alpha_{a_m} \\ 0, & \text{if } |\sigma_\phi| \leq \alpha_{a_m} \end{cases} \\ \beta_a &= 2\epsilon_a \alpha_a + \lambda_a + 4\epsilon_a^2, \end{aligned} \tag{5.40}$$

and finally, the GSTA is given by

$$\begin{aligned} \delta_a &= -k_{a_1} \phi_{a_1}(\sigma_\phi) + z_a, \dot{z}_a = -k_{a_2} \phi_{a_2}(\sigma_\phi) \\ \phi_{a_1}(\sigma_\phi) &= |\sigma_\phi|^{\frac{1}{2}} \text{sign}(\sigma_\phi) + \beta_{a_g} \sigma_\phi \\ \phi_{a_2}(\sigma_\phi) &= \frac{1}{2} \text{sign}(\sigma_\phi) + \frac{3}{2} \beta_{a_g} |\sigma_\phi|^{\frac{1}{2}} \text{sign}(\sigma_\phi) + \beta_{a_g}^2 \sigma_\phi \end{aligned} \tag{5.41}$$

A discussion of the system assumptions that guarantee the stability of the controllers above when applied to the decoupled lateral dynamics is presented in Griffiths (2020). The discussion was based on the boundedness of the system and sliding dynamics, which has been briefly summarized in the previous subsections in this report. All of the assumptions about the saturation controller, the STA, and the GSTA were found to be valid, while the requirement that the function b_ϕ in (5.30) is known is the only assumption that is not valid for the ASTA. Thus, the stability of the saturation controller, the STA and the GSTA presented above was verified, while the stability of the ASTA was not completely verified.

5.3 Control Design for the Decoupled Longitudinal Model

Now that the lateral control algorithms have been designed, the design process is repeated for the decoupled longitudinal dynamics in (2.82)-(2.85). First, the system is written in state-space form, then the sliding variable σ_e is designed. Then the sliding mode controllers are determined, and their applicability to the decoupled longitudinal model is discussed.

5.3.1 State-Space Representation

In the subsequent section an analysis of the applicability of the SISO algorithms presented in chapter 3 to the longitudinal model is performed. It is therefore convenient to write the system dynamics in state-space form as this form is the basis for the stability assumptions presented in chapter 3. The longitudinal dynamics (2.82)-(2.85) can be written in state-space form as

$$\dot{x}_\theta = f_\theta(t, x) + g_\theta(t, x)\delta_e + h(t)_\theta d_\theta(t), \tag{5.42}$$

where $x_\theta \in \mathbb{S}^1 \times \mathbb{R} \times \mathbb{R} \times \mathbb{S}^1$ and $d_\theta \in \mathbb{R}^3$ are given by

$$x_\theta = \begin{bmatrix} \theta \\ q \\ V_a \\ \alpha \end{bmatrix}, \quad d_\theta = \begin{bmatrix} d_{\theta_1} \\ d_{\theta_2} \\ d_{\theta_3} \end{bmatrix}.$$

The elements of the vector f_θ, denoted $f_{\theta_i}, i = 1, ..., 4$, are

$$f_{\theta_1} = q \tag{5.43}$$

$$f_{\theta_2} = \frac{\rho V_a^2 Sc}{2I_y}(C_{m_0} + C_{m_\alpha}\alpha + C_{m_q}\frac{c}{2V_a}q) \tag{5.44}$$

$$\begin{aligned} f_{\theta_3} = {} & \frac{T}{\mathrm{m}}\cos\alpha - \frac{\rho V_a^2 S}{2\mathrm{m}}(C_{D_0} \\ & + C_{D_\alpha}\alpha + C_{D_q}\frac{c}{2V_a}q) - g\sin(\theta - \alpha) \end{aligned} \tag{5.45}$$

$$\begin{aligned} f_{\theta_4} = {} & q + \frac{g}{V_a}\cos(\theta - \alpha) - \frac{T}{\mathrm{m}V_a}\sin\alpha \\ & - \frac{\rho V_a^2 S}{2\mathrm{m}}(C_{L_0} + C_{L_\alpha}\alpha + C_{L_q}\frac{c}{2V_a}q) \end{aligned} \tag{5.46}$$

while the elements of the vector g_θ, denoted as denoted $g_{\theta_i}, i = 1, ..., 4$, are

$$g_{\theta_1} = 0 \tag{5.47}$$

$$g_{\theta_2} = \frac{\rho V_a^2 Sc}{2I_y}C_{m_{\delta_e}} \tag{5.48}$$

$$g_{\theta_3} = -\frac{\rho V_a^2 S}{2\mathrm{m}}C_{D_{\delta_e}} \tag{5.49}$$

$$g_{\theta_4} = -\frac{\rho V_a^2 S}{2\mathrm{m}}C_{L_{\delta_e}} \tag{5.50}$$

Lastly, the rows of the matrix $h_\theta \in \mathbb{R}^{4\times 3}$ are given by

$$h_{\theta_1} = \begin{bmatrix} 0 & 0 & 0 \end{bmatrix} \tag{5.51}$$

$$h_{\theta_2} = \begin{bmatrix} 0 & 0 & \frac{1}{I_y} \end{bmatrix} \tag{5.52}$$

$$h_{\theta_3} = \begin{bmatrix} 0 & -1 & 0 \end{bmatrix} \tag{5.53}$$

$$h_{\theta_4} = \begin{bmatrix} -1 & 0 & 0 \end{bmatrix}, \tag{5.54}$$

so that $f_\theta : \mathbb{R}^4 \to \mathbb{R}^4$ are the uncertain system functions, $g_\theta : \mathbb{R}^4 \to \mathbb{R}^4$ are the uncertain control coefficients, and $h_\theta \in \mathbb{R}^{3\times 4}$ is the contribution of the disturbances $d_{\theta_i}, i = 1...3$ to the state variables. The elements of f_θ and g_θ are denoted $f_{\theta_i}, i = 1 \dots 4$ and $g_{\theta_i}, i = 1...4$ respectively, while the elements of h_θ are denoted $h_{\theta_{ij}}, i = 1, ..., 4, j = 1 \dots 3$.

Boundedness of the Longitudinal State-Space

To verify the stability assumptions for the control algorithms presented in chapter 3, it is helpful to determine the boundedness of the system dynamics. It is reasonable to restrict

the analysis to a compact set in which the state variables are bounded by some maximal values due to both physical limitations and the fact that the scope of this report limits the analysis to typical flight conditions. In typical flight conditions, the pitch angle and AoA are small, and the airflow is laminar so that it can be characterized by the linearized coefficients in (2.46)-(2.48).

The bounds on the state variables are

$$|\theta| < \theta_{max} = \frac{\pi}{6} \text{ rad} \tag{5.55}$$

$$|q| \leq q_{max} = 90 \text{ rad/s} \tag{5.56}$$

$$0 < V_a \in [V_{a_{min}}, V_{a_{max}}] = [25, 45] \text{ m/s} \tag{5.57}$$

$$|\alpha| \leq \alpha_{max} = \frac{\pi}{12} \text{ rad.} \tag{5.58}$$

Furthermore, the disturbances d_i are assumed to be bounded by

$$|d_{\theta_i}| \leq d_{\theta_{i,max}} = 4, \tag{5.59}$$

where $d_{\theta_{i,max}}$ is given in [N] for $i = 1, 2$ and in [Nm] for $i = 3$.

The fact that the state variables are restricted to a compact set means that the stability analysis in section 5.3.3 is only valid on a domain $\mathcal{D}_\theta$ in $\mathbb{R}^4$ given by

$$\mathcal{D}_\theta = \{x_\theta \in \mathbb{R}^4 : |x_\theta| \leq r_\theta\} \subset \mathbb{R}^4, \tag{5.60}$$

where $r_\theta \in \mathbb{R}^4$ is a vector of the bounds given in (5.55)-(5.58). However, since the UAV is assumed to be operating under the typical flight conditions described above, it will not operate outside these bounds, and the analysis will therefore be valid for the scope of this report.

Whether f_θ, g_θ, and h_θ are bounded remains to be determined. Both f_θ and g_θ are continuous functions of the state x_θ since the state is restricted to a compact set. They contain divisions by V_a, but since V_a is always greater than zero, these divisions cannot make the system grow unbounded. Finally, the matrix h_θ is constant, and is therefore bounded. The bounds on the elements of f_θ, g_θ, and h_θ are denoted $F_{\theta_i}, G_{\theta_i}$ and $H_{\theta_{ij}}$ respectively for $i = 1, ...4, j = 1, ...3$.

Furthermore, since it is ascertained that f_θ, g_θ, and h_θ are bounded, so are the system dynamics $\dot{x}_\theta$. This follows from the fact that the system functions and the disturbance d_θ are bounded, and that the control δ_e is bounded by

$$|\delta_e| \leq \delta_{e_{max}} = \frac{\pi}{6} \text{ rad.} \tag{5.61}$$

From this it is possible to conclude that $\dot{f}_\theta, \dot{g}_\theta$, and $\dot{h}_\theta$ are bounded as well, since they are function of x_θ and $\dot{x}_\theta$, which are bounded.

5.3.2 Sliding Surface Design

The control objective is to perform output tracking, i.e. design a sliding surface and a control law such that $\theta \to \theta_r$ asymptotically. First, define the tracking error e_θ and error dynamics $\dot{e}_\theta$ and $\ddot{e}_\theta$ as

$$e_\theta = \theta - \theta_d \tag{5.62}$$

$$\dot{e}_\theta = q - q_d \tag{5.63}$$
$$\ddot{e}_\theta = \dot{q} - \dot{q}_d, \tag{5.64}$$

where it is assumed that $\dot{q}_d$ is bounded.

An appropriate sliding surface is now chosen as

$$\sigma_\theta = a_{\theta_1} e_\theta + \dot{e}_\theta \tag{5.65}$$

following the methodology described in 3.2.1. The sliding dynamics are then given by

$$\begin{aligned} \dot{\sigma}_\theta &= a_{\theta_1}\dot{e}_\theta + \ddot{e}_\theta \\ &= a_{\theta_1}\dot{e}_\theta + f_{\theta_2}(t,x) + g_{\theta_2}(t,x)\delta_e + h_{\theta_2} d_\theta(t) - \dot{q}_d, \end{aligned} \tag{5.66}$$

which can be written on a more general form as

$$\dot{\sigma}_\theta = a_\theta(t,x) + b_\theta(t,x)\delta_e + \gamma_\theta(t,x), \tag{5.67}$$

where

$$a_\theta(t,x) = a_{\theta_1}\dot{e}_\theta + f_{\theta_2}(t,x) - \dot{q}_d \tag{5.68}$$
$$b_\theta(t,x) = g_{\theta_2}(t,x) \tag{5.69}$$
$$\gamma_\theta(t) = h_{\theta_2} d(t), \tag{5.70}$$

with $\dot{e}_\theta$ defined in (5.63), f_{θ_2} in (5.44), g_{θ_2} in (5.48), and h_{θ_2} in (5.52).

Boundedness of the Longitudinal Sliding Dynamics

Determining if the sliding dynamics are bounded or not is necessary to verify the stability of the SMC algorithms presented in chapter 3. Unbounded system dynamics may mean that the system is not stable in the sliding mode, and the SMC algorithms are in that case not applicable to the system.

The sliding dynamics in (5.67) are bounded if a_θ, b_θ, and γ_θ are bounded. Firstly, a_θ is bounded if $\dot{e}_\theta$, f_{θ_2}, and $\dot{q}_d$ are bounded. The function f_{θ_2} is bounded following the argumentation in subsection 5.3.1, and $\dot{e}_\theta$ is bounded since both q and q_d are bounded. The fact that q_d is bounded can be seen from (6.11) since both θ_r and θ_d are bounded, as can be seen from (6.6). Finally, $\dot{q}_d$ is assumed to be bounded by design.

Furthermore, b_θ is bounded since g_{θ_2} is bounded. Finally, γ_θ is bounded since h_{θ_2} is a constant and d_θ is bounded due to the assumption in (5.59). Therefore, it is possible to conclude that the sliding dynamics (5.67) are bounded in the domain $\mathcal{D}_\theta$ defined in (5.60).

The functions a_θ, b_θ, and γ_θ is bounded by maximal values A_θ, B_θ, and G_θ respectively, given by

$$|a_\theta| \leq A_\theta = a_1 \dot{e}_{\theta_{max}} + F_2 + \dot{q}_{d_{max}} \tag{5.71}$$
$$|b_\theta| \leq B_\theta = G_{\theta_2} \tag{5.72}$$
$$|\gamma_\theta| \leq G_\theta = H_{\theta_{23}} d_{\theta_{3,max}}. \tag{5.73}$$

Furthermore, the function b_θ is bounded from below by

$$0 < b_{\theta_0} \leq b_\theta \leq B_\theta, \tag{5.74}$$

where b_{θ_0} is the lower bound of b_θ that can be found by inserting $V_{a_{min}}$ in (5.52), while the upper bound B_θ can be found by inserting $V_{a_{max}}$ in (5.52). Note that the coefficient $C_{m_{\delta_e}}$ in (5.52) is negative so that b_θ in itself is negative. However, to better follow the notation in which the assumptions about the control algorithms are presented, b_θ is regarded as positive, while the control δ_e is modeled as having a negative sign.

5.3.3 Sliding Mode Control Design

Now that the design of the sliding surface is complete, the design of the control algorithms that drives the system to the sliding surface remains to be determined. All the single-input SMC algorithms presented in chapter 3 are designed for the longitudinal system, except for the relay controller in (3.10). Furthermore, an analysis of the assumptions that are made about the system to guarantee convergence to the sliding surface is performed for each algorithm.

Saturation Control

The saturation controller is given by

$$\delta_e = -k_e \text{sat}(\sigma_\theta), \tag{5.75}$$

and is implemented as shown in Figure B.5.

The stability of the saturation controller is proven through Lyapunov analysis in subsection 3.2.1, where it is determined that the saturation controller is stable for a control gain k_e chosen as

$$k_e = \frac{1}{b_{\theta_0}} \left(\frac{\eta}{\sqrt{2}} + A_\theta + G_\theta \right), \tag{5.76}$$

where b_{θ_0} is the lower bound of $b_\theta(t)$ and the constant η is chosen so that the reaching condition defined in (3.11) is satisfied. For any choice of control gain k_e that satisfies (5.76), the convergence of the system to the sliding surface can be guaranteed if the following assumptions are also satisfied.

Firstly, from chapter 3 it is known that the disturbance d_θ needs to be matched by the control δ_e. The only system equation the control does not appear in is the equation for $\dot{\theta}$, which is also the only equation where the disturbance does not appear. This means that the assumption that the disturbance is matched by the control is valid. Secondly, the functions a_θ, b_θ, and γ_θ have to be bounded. In this case the bounds are assumed to be given by $|a_\theta(t,x)| \leq A_\theta, 0 < b_{\theta_0} \leq b_\theta(t,x) \leq B_\theta$ and $|\gamma_\theta| \leq G_\theta$. The assumption that these uncertain functions are bounded is valid following the discussion in subsection 5.3.2.

Furthermore, the sliding variable σ_θ has to be differentiable. We know that σ_θ is differentiable since $\dot{\sigma}_\theta$ is bounded from the discussion in the previous paragraph where it is determined that a_θ, b_θ, and γ_θ are all bounded.

A summary of the stability assumptions that have been discussed for the saturation controller (5.75), and whether they are valid or not can be found in Table 5.1.

Assumption	**Saturation controller**
The sliding variable σ_θ is differentiable	
The disturbance d is matched by the control	Yes
The disturbance γ_θ is bounded	Yes
The perturbation a_θ is bounded	Yes
The uncertain control function b_θ is bounded	Yes
The uncertain control function b_θ is bounded from below by $0 < b_{\theta_0} \leq b_\theta \leq B_\theta$	Yes

Table 5.1: A summary of the assumptions made about the saturation controller. "Yes" implies that the assumption is valid, while "No" implies the opposite.

Super-Twisting Algorithm

The STA is given by

$$\begin{aligned} \delta_e &= -k_{e_1}|\sigma_\theta|^{\frac{1}{2}}\text{sign}(\sigma_\theta) + z \\ \dot{z} &= -k_{e_2}\text{sign}(\sigma_\theta), \end{aligned} \tag{5.77}$$

and is implemented as shown in Figure B.6.

As mentioned in chapter 3, the STA is only applicable to systems of relative degree 1. From (5.66) it is clear that the control δ_e appears in the first derivative of the sliding surface, which means the system is of relative degree 1.

To guarantee convergence to the reference signal, several additional assumptions about the system have to be made. Firstly, the sliding surface has to be differentiable. This means that $\dot{\sigma}_\theta$ has to be bounded, i.e. that the uncertain functions a_θ, b_θ, and γ_θ in (5.67) are bounded, and also that b_θ is bounded from below. From the previous discussion about the saturation controller, it is known that these assumptions are valid for the longitudinal system.

Additionally, the first derivatives of a_θ, b_θ, and γ_θ are required to be bounded by $|\dot{a}_\theta| \leq \bar{A}_\theta, |\dot{b}_\theta| \leq \bar{B}_\theta$, and $|\dot{\gamma}_\theta| \leq \bar{G}_\theta$. In the discussion in 5.3.1, it is determined that $\dot{f}_\theta, \dot{g}_\theta$, and $\dot{h}_\theta$ are bounded. From (5.69) it can be concluded that $\dot{b}_\theta$ is therefore also bounded, and from (5.70) it can be seen that $\dot{\gamma}_\theta$ is bounded if $\dot{d}_\theta$ is bounded. The disturbance d_θ has a bounded first derivative, which can be seen in (6.2) since d_θ and $\text{w}_{d_{\theta_i}}$ are bounded. For $\dot{a}_\theta$ to be bounded, it is necessary for $\ddot{e}_\theta$ to be bounded, in addition to the function $\dot{f}_{\theta_2}$, which is already known to be bounded. From (5.64) it can be seen that $\ddot{e}_\theta$ is bounded if $\dot{q}$ and $\dot{q}_d$ are bounded. It is determined in subsection 5.3.1 that the system dynamics $\dot{x}_\theta$ are bounded, and in subsection 5.3.2 that $\dot{q}_d$ is bounded, which means that $\ddot{e}_\theta$ is also bounded.

A summary of the previously discussed assumptions can be found in Table 5.2.

Adaptive-Gains Super-Twisting Algorithm

The adaptive STA is given by

$$\begin{aligned} \delta_e &= -\alpha_e |\sigma_\theta|^{\frac{1}{2}} \text{sign}(\sigma_\theta) + z_e \\ \dot{z}_e &= -\beta_e \text{sign}(\sigma_\theta), \end{aligned} \tag{5.78}$$

where the update rules for the adaptive control gains α_e and β_e are defined as

$$\begin{aligned} \dot{\alpha}_e &= \begin{cases} \omega_{e_1} \sqrt{\frac{\gamma_{e_1}}{2}}, & \text{if } \sigma_\theta \neq 0 \\ 0, & \text{if } \sigma_\theta = 0 \end{cases} \\ \beta_e &= 2\epsilon_e \alpha_e + \lambda_e + 4\epsilon_e^2, \end{aligned} \tag{5.79}$$

with $\gamma_{e_1}, \lambda_e, \omega_{e_1}, \epsilon_e$ being arbitrary positive constants. However, since σ_θ is rarely exactly equal to zero, a modification of the update laws is implemented instead:

$$\begin{aligned} \dot{\alpha}_e &= \begin{cases} \omega_{e_1} \sqrt{\frac{\gamma_{e_1}}{2}}, & \text{if } |\sigma_\theta| > \alpha_{e_m} \\ 0, & \text{if } |\sigma_\theta| \leq \alpha_{e_m} \end{cases} \\ \beta_e &= 2\epsilon_e \alpha_e + \lambda_e + 4\epsilon_e^2, \end{aligned} \tag{5.80}$$

where α_{e_m} is an arbitrarily small constant. The Simulink-implementation of the ASTA is shown in Figure B.7.

Assumption	**STA**	**ASTA**
System is of relative degree 1	Yes	Yes
The vector field $f_\theta(t, x)$ is differentiable	-	Yes
The functions a_θ and γ_θ are bounded by (5.81)	-	No
The derivative of the disturbance γ_θ is bounded	Yes	Yes
The sliding dynamics $\dot{\sigma}_\theta$ is bounded	Yes	Yes
The derivative of the function a_θ is bounded	Yes	Yes
The function b_θ is bounded from below by $0 < b_{\theta_0} \leq b_\theta$	Yes	-
The function b_θ is not equal to zero $\forall x_\theta$ and $\forall t > 0$	-	Yes
The function b_θ is known	-	No
The derivative of the function b_θ is bounded	Yes	-

Table 5.2: A summary of the assumptions made about the STA and ASTA controllers. "Yes" implies that the assumption is valid, while "No" implies the opposite. "-" implies that the controller does not rely upon the assumption.

For the ASTA to guarantee convergence to the reference trajectory, the system needs to fulfill several requirements. Firstly, as for the STA, the input-output dynamics need

to be of relative degree 1. This is true following the previous discussion about the STA. Next, the function f_θ has to be differentiable. It is already established that $\dot{f}_\theta$ is bounded, which means that f_θ is differentiable as the derivative exists at all points in the domain $\mathcal{D}_\theta$ defined in (5.60).

Another assumption about the system is that the function b_θ is known and not equal to zero $\forall x_\theta$ and $\forall t > 0$. Since b_θ depends on the airspeed which is affected by unknown disturbances due to wind, the airspeed is not exactly known at all times. Additionally, b_θ depends on several system parameters that are difficult to determine exactly, so the assumption that b_θ is known is not valid. However, since $V_a > 0 \, \forall t > 0$ the second part of the assumption about b_θ is valid.

Furthermore, the functions a_θ and γ_θ are assumed to be bounded by

$$|a_\theta + \gamma_\theta| \leq \delta |\sigma_\theta|^{\frac{1}{2}}, \; \delta > 0, \tag{5.81}$$

where the constant δ is assumed to exist, but is unknown. From the discussion in subsection 5.3.2 and the discussion about the STA, it is determined that both a_θ and γ_θ are bounded. Therefore it is reasonable to assume that there exists some constant δ that is large enough for (5.81) to be true except for when σ_θ is very small or zero. Since it is not possible to guarantee that both $a_\theta, \gamma_\theta = 0$ when $\sigma_\theta = 0$, the bound in (5.81) is not true for all σ, and is therefore not valid.

A summary of the previously discussed assumptions for the ASTA, and the assumptions that the ASTA share with the STA, can be found in Table 5.2.

Generalized Super-Twisting Algorithm

The GSTA is given by

$$\begin{aligned} \delta_e &= -k_{e_1} \phi_{e_1}(\sigma_\theta) + z_e, \dot{z}_e = -k_{e_2} \phi_{e_2}(\sigma_\theta) \\ \phi_{e_1}(\sigma_\theta) &= |\sigma_\theta|^{\frac{1}{2}} \text{sign}(\sigma_\theta) + \beta_{e_g} \sigma_\theta \\ \phi_{e_2}(\sigma_\theta) &= \frac{1}{2} \text{sign}(\sigma_\theta) + \frac{3}{2} \beta_{e_g} |\sigma_\theta|^{\frac{1}{2}} \text{sign}(\sigma_\theta) + \beta_{e_g}^2 \sigma_\theta, \end{aligned} \tag{5.82}$$

and is implemented as shown in Figure B.8.

As for the STA and the ASTA, the first requirement for the GSTA to be applicable is that the input-output dynamics are of relative degree 1, which they are. Other assumptions about the system include that the function b_θ is bounded from below by $0 < b_{\theta_0} \leq b_\theta \leq B_\theta$, which is true from the discussion about the previous control algorithms.

Furthermore, the functions a_θ, b_θ, and γ_θ have to be Lipschitz-continuous with respect to t. Since any function with a bounded first derivative is Lipschitz-continuous, this assumption is valid, as it has already been determined that $\dot{a}_\theta, \dot{b}_\theta$, and $\dot{\gamma}_\theta$ are bounded.

Additionally, a_θ, b_θ, and γ_θ need to be continuously differentiable, i.e. $a_\theta, b_\theta, \gamma_\theta \in \mathcal{C}^1$ with respect to x_θ. For these functions to be continuously differentiable, they need to have bounded second derivatives with respect to x_θ. It is easy to see that γ_θ is in in $\mathcal{C}^1$ as it does not depend on x_θ so that $\frac{\partial \gamma_\theta}{\partial x_\theta} = 0$. For a_θ and b_θ it is necessary to determine whether the expressions below are bounded:

$$\frac{\partial^2 a_\theta}{\partial x_\theta^2} = \frac{\partial^2}{\partial x^2} (a_{\theta_1} \dot{e}_\theta + f_{\theta_2}) \tag{5.83}$$

$$\frac{\partial^2 b_\theta}{\partial x_\theta^2} = \frac{\partial^2 g_{\theta_2}}{\partial x_\theta^2}. \tag{5.84}$$

Since $\dot{x}_\theta$ is bounded following the discussion in subsection 5.3.1, it follows that $\ddot{x}_\theta$ is bounded since it is a function of the state vector x_θ and its first derivative $\dot{x}_\theta$ which are known to be bounded. Because of this it can be concluded that both expressions (5.83)-(5.84) above are bounded, so that $a_\theta, b_\theta \in \mathcal{C}^1$.

To check the validity of the other assumptions presented in chapter 3, the sliding dynamics (5.67) need to be rewritten slightly:

$$\sigma_e = \varphi_e + b_\theta \delta_e \tag{5.85}$$
$$\varphi_e = a_\theta + \gamma_\theta \tag{5.86}$$
$$= \varphi_1 + \varphi_2, \tag{5.87}$$

where the total perturbation φ_e is split into two parts where the first term φ_1 is vanishing at the origin of the sliding dynamics, i.e.

$$\varphi_1(t, x_\theta^*) = 0, \ \forall t > 0, \tag{5.88}$$

where x_θ^* is the state vector in the sliding mode. The other part of the perturbation φ_2 contains the remaining terms of φ_e. This means that φ_1 and φ_2 are given by

$$\varphi_1 = a_{e_1} \dot{e}_\theta \tag{5.89}$$
$$\varphi_2 = f_{\theta_2} + \gamma_\theta. \tag{5.90}$$

since the error dynamics $\dot{e}_\theta = 0$ in the sliding mode, while the function $f_{\theta_2}(t, x_\theta^*) \neq 0$ due to its dependence on V_a, which is always greater than zero. The disturbance d_θ is assumed to be only time-dependent, and there is, therefore, no guarantee that it is equal to zero in the sliding mode.

The first part of the perturbation is assumed to be bounded by

$$|\varphi_1(t, x_\theta)| \leq \mu |\phi_{\theta_1}(\sigma_\theta)| \tag{5.91}$$

for some constant $\mu > 0$. This is a reasonable assumption as we know that $\dot{e}_\theta$ is bounded, so there will exist some μ for which condition (5.91) is true.

Furthermore, it is necessary that the total time derivative of φ_2 divided by b_θ is bounded. The derivative of φ_2 divided by b_θ is

$$\frac{d}{dt}\left(\frac{\varphi_2}{b_\theta}\right) = \frac{1}{b_\theta}\frac{\partial \varphi_2}{\partial t} - \frac{\varphi_2}{b_\theta^2}\frac{\partial b_\theta}{\partial t} + \left(\frac{1}{b_\theta}\frac{\partial \varphi_2}{\partial x_\theta} - \frac{\varphi_2}{b_\theta^2}\frac{\partial b_\theta}{\partial x_\theta}\right)\dot{x}_\theta \tag{5.92}$$
$$= \frac{1}{b_\theta}(\dot{f}_{\theta_2} + \dot{\gamma}_\theta) - \frac{\varphi_2}{b_\theta^2}\dot{b}_\theta + \left(\frac{1}{b_\theta}\frac{\partial f_{\theta_2}}{\partial x_\theta} - \frac{\varphi_2}{b_\theta^2}\frac{\partial b_\theta}{\partial V_a}\right)\dot{x}_\theta \tag{5.93}$$
$$= \delta_1 + \delta_2 \dot{x}_\theta, \tag{5.94}$$

where it is assumed that δ_1, δ_2 are bounded by

$$|\delta_1| \leq \bar{\delta}_1, \quad |\delta_2| \leq \bar{\delta}_2. \tag{5.95}$$

Firstly, since $\dot{f}_\theta$ and $\dot{\gamma}_\theta$ are known to be bounded, the constant $\bar{\delta}_1$ does exist. Secondly, from looking at the system matrix with elements defined in (5.43)-(5.46) it is evident that the derivative of f_{θ_2} with respect to x_θ is bounded since it is a polynomial, and $\dot{x}_\theta$ is known to be bounded. The derivative of γ_θ with respect to x_θ on the other hand, will always be zero as γ_θ is not a state-dependent function. Finally, since b_θ is only dependent on V_a and no other states, the derivative of b_θ with respect to x_θ has to be bounded as both V_a and $\dot{V}_a$ are bounded. Therefore, it can be concluded that the constant δ_2 also exists.

The assumptions for the GSTA and whether they are valid or not is summarized in Table 5.3.

Assumption	**GSTA**
The system is of relative degree 1	Yes
The functions a_θ and b_θ are Lipschitz-continuous w.r.t. t	Yes
The functions a_θ and b_θ satisfy $a_\theta, b_\theta \in \mathcal{C}^1$ w.r.t. x_θ	Yes
The function b_θ is bounded by $0 < b_{\theta_0} \leq b_\theta \leq B_\theta$	Yes
The function φ_1 is bounded by $\varphi_1(t,x) \leq \eta\lvert\phi_{\theta_1}(\sigma_\theta)\rvert$	Yes
The function δ_1 is bounded	Yes
The function δ_2 is bounded	Yes

Table 5.3: A summary of the assumptions made about the GSTA controller. "Yes" implies that the assumption is valid, while "No" implies the opposite.

Control Coefficient Transformation

In subsection 3.5.2 the control input is transformed by a control coefficient transformation:

$$\bar{\delta}_e = b_\theta(t,x)^{-1}\delta_e, \tag{5.96}$$

where b_θ is the control coefficient and $\bar{\delta}_e$ is the input to the UAV model. As discussed in the previous paragraphs, the control coefficient b_θ is uncertain due to uncertainties in the model so the transformation (5.96) cannot be implemented perfectly. However, it is possible to split the function b_θ into a nominal part and an uncertain part:

$$b_\theta(t,x) = b_{\theta_{nom}}(t,x) + \Delta b_\theta(t,x) \tag{5.97}$$

and then implement a control coefficient transformation based on the nominal part. This means that the control input to the UAV model is

$$\bar{\delta}_e = b_{\theta_{nom}}^{-1}(t,x)\delta_e. \tag{5.98}$$

Even though only the ASTA requires this kind of input transformation, it may be beneficial to apply the same transformation to the control law generated by the saturation controller, the STA, and the GSTA as well, as this may make it easier to dominate the

perturbation term in the sliding dynamics so that the control system is more robust. These properties are investigated in subsection 7.7, which contains the simulation results for the longitudinal model without using the transformation (5.96), i.e. $\bar{\delta}_e = \delta_e$, with the transformation using a nominal b_θ (5.98), and with the transformation using an exactly known b_θ (5.96).

5.4 Single-Input Control Design for the 6DOF Model

In the single-input control design for the 6DOF model, the lateral controllers presented in subsection 5.2.3 are paired with the longitudinal controllers presented in subsection 5.3.3 based on a decoupled sliding variable.

5.4.1 Sliding surface design

Since the lateral and longitudinal controllers designs are still based on the decoupled models, it is possible to formulate a two-dimensional decoupled sliding variable, σ_s, from σ_ϕ and σ_θ:

$$\sigma_s = \begin{bmatrix} \sigma_\phi \\ \sigma_\theta \end{bmatrix}, \tag{5.99}$$

with σ_ϕ from (5.24) and σ_θ from (5.65). Note that a slight modification is made in the design of the sliding surfaces. Instead of using the body angular rates and angle rate references p_d and q_d, the angle rates $\dot{\phi}$ and $\dot{\theta}$, and references $\dot{\phi}_d$ and $\dot{\theta}_d$ are used instead. This means that the error dynamics for the lateral and longitudinal dynamics in (5.26) and (5.63), respectively, are now given by

$$\dot{e}_\phi = \dot{\phi} - \dot{\phi}_d \tag{5.100}$$

$$\dot{e}_\theta = \dot{\theta} - \dot{\theta}_d. \tag{5.101}$$

This is because of the difference between the decoupled lateral and longitudinal models, and the 6DOF model in the modeling of the dynamics of the Euler angles. For the decoupled lateral and longitudinal dynamics, the roll and pitch dynamics are simply given by

$$\dot{\phi} = p$$
$$\dot{\theta} = q.$$

However, for the 6DOF model, $\dot{\phi}$ and $\dot{\theta}$ are given by the expression

$$\dot{\Theta} = \begin{bmatrix} 1 & \sin\phi\cos\theta & \cos\phi\tan\theta \\ 0 & \cos\phi & -\sin\phi \\ 0 & \sin\phi\sec\theta & \cos\phi\sec\theta \end{bmatrix} \omega_b$$

so the relation between the $\dot{\phi}$ and $\dot{\theta}$ and p and q is not that simple anymore. Therefore, the error terms in (5.100) and (5.101) are used instead of the error terms in (5.26) and (5.63).

The sliding dynamics of σ_s are simply given by $\dot{\sigma}_\phi$ in (5.30) and $\dot{\sigma}_\theta$ in (5.67) so that

$$\dot{\sigma}_s = \begin{bmatrix} a_\phi(t,x) + b_\phi(t,x)\delta_a + \gamma_\phi(t,x) \\ a_\theta(t,x) + b_\theta(t,x)\delta_e + \gamma_\theta(t,x) \end{bmatrix}. \tag{5.102}$$

Even though the model is viewed as decoupled when designing the controllers, the actual model the control laws are applied to is the full 6DOF one given in (2.88)-(2.91) instead of the simplified lateral dynamics given by (2.78)-(2.81) and the simplified longitudinal dynamics given by (2.82)-(2.85). The unmodeled dynamics in the control design due to coupling are assumed to be included in the perturbations γ_ϕ and γ_θ.

5.4.2 Control Design

The lateral and longitudinal sliding mode controllers output the control commands δ_a and δ_e respectively. These two control signals are then transformed following the methodology in section 3.6, so that the control inputs to the 6DOF model are given by

$$\bar{\delta}_a = b_\phi(t,x)^{-1}\delta_a \tag{5.103}$$

$$\bar{\delta}_e = b_\theta(t,x)^{-1}\delta_e, \tag{5.104}$$

with b_ϕ as in (5.32) and b_θ in (5.69).

The full control vector $\bar{u}$ is given by

$$\bar{u} = \begin{bmatrix} \delta_t \\ \bar{\delta}_a \\ \bar{\delta}_e \\ \delta_r \end{bmatrix}, \tag{5.105}$$

where the two PI-controllers that generate the throttle δ_t and rudder δ_r commands are given in (5.1) and (5.3) respectively.

5.5 Multivariable Control Design for the 6DOF Model

In this section, the design of the multivariable sliding variable is presented, as well as the design of the MSAT, the MSTA, the AMSTA, and the GMSTA for the 6DOF model.

5.5.1 State-Space Representation

As for the lateral and longitudinal models in 5.2.1 and 5.3.1, the 6DOF model in (2.88)-(2.91) has to be written on a state-space form to analyze the applicability of the multivariable control algorithms to the UAV model.

We wish to write the 6DOF model equations on the form

$$\dot{x} = f(t,x,\delta_t) + g(t,x)\bar{u}_{smc} + h(t), \tag{5.106}$$

where f are the uncertain system functions, g is the control coefficient, and $h(t)$ is a disturbance in the system. Note that δ_t is included in the system functions f since it is generated by the airspeed hold controller described in subsection 5.1.1 and is therefore not dependent on the sliding mode control design, which is the subject of this section. The control vector in (5.106) contains the control commands generated by the SMC algorithms, i.e. $\bar{u}_{smc} = [\bar{\delta}_a, \bar{\delta}_e, \bar{\delta}_r]^\top$.

Based on (2.88)-(2.91), the functions f, g, and h are

$$f(t,x,\delta_t) = \begin{bmatrix} \mathcal{R}_b^v \mathbf{v}_b \\ \mathbf{v}_b \times \omega_b + \frac{1}{\mathrm{m}} f_{b_x}(t,x) \\ T_q \omega_b \\ I_b^{-1}(-\omega_b \times (I_b \omega_b) + m_{b_x}(t,x)) \end{bmatrix} \tag{5.107}$$

$$g(t,x) = \begin{bmatrix} \mathbf{0}_{3\times 4} \\ \frac{1}{\mathrm{m}} f_{b_u}(t,x) \\ \mathbf{0}_{4\times 4} \\ I_b^{-1} m_{b_u}(t,x) \end{bmatrix} \tag{5.108}$$

$$h(t,x) = \begin{bmatrix} \mathbf{0}_{3\times 4} \\ \frac{1}{\mathrm{m}} d_f(t) \\ \mathbf{0}_{4\times 4} \\ I_b^{-1} d_m(t) \end{bmatrix}, \tag{5.109}$$

where the functions f_{b_x} and m_{b_x} are the parts of the body forces and moments that depend solely on the state x, and are given by

$$f_{b_x} = \frac{1}{2}\rho V_a^2 S \mathcal{R}_s^b(\alpha) \begin{bmatrix} -(C_{D_0} + C_{D_\alpha}\alpha + C_{D_q}\frac{c}{2V_a}q) \\ (C_{Y_\beta}\beta + C_{Y_p}\frac{b}{2V_a}p + C_{Y_r}\frac{b}{2V_a}r) \\ -(C_{L_0} + C_{L_\alpha}\alpha + C_{L_q}\frac{c}{2V_a}q) \end{bmatrix} + f_t + f_g \tag{5.110}$$

$$m_{b_x} = \frac{1}{2}\rho V_a^2 S I_b^{-1} \begin{bmatrix} b(C_{l_\beta}\beta + C_{l_p}\frac{b}{2V_a}p + C_{l_r}\frac{b}{2V_a}r) \\ c(C_{m_0} + C_{m_\alpha}\alpha + C_{m_q}\frac{c}{2V_a}q) \\ b(C_{n_\beta}\beta + C_{n_p}\frac{b}{2V_a}p + C_{n_r}\frac{b}{2V_a}r) \end{bmatrix} + m_t, \tag{5.111}$$

and the functions f_{b_u} and m_{b_u} are the parts of the body forces and moments that are dependent on u_{smc}, which are given by

$$f_{b_u} = \frac{1}{2}\rho V_a^2 S \mathcal{R}_s^b(\alpha) \begin{bmatrix} 0 & -C_{D_{\delta_e}} & 0 \\ C_{Y_{\delta_a}} & 0 & C_{Y_{\delta_r}} \\ 0 & -C_{L_{\delta_e}} & 0 \end{bmatrix} \tag{5.112}$$

$$m_{b_u} = \frac{1}{2}\rho V_a^2 S I_b^{-1} \begin{bmatrix} bC_{l_{\delta_a}} & 0 & bC_{l_{\delta_r}} \\ 0 & cC_{m_{\delta_e}} & 0 \\ bC_{n_{\delta_a}} & 0 & bC_{n_{\delta_r}} \end{bmatrix}. \tag{5.113}$$

Boundedness of the State-Space Representation

Let us assume that the functions f, g and h in (5.106) are elementwise bounded so that $|f_i| \leq F_i$, $|g_i| \leq G_i$, and $|h_i| \leq H_i$ for some finite bounds F_i, G_i, and H_i. For this assumption to be valid, it is necessary to constrain the values of the state variables to a subset $\mathcal{D}$ of the space spanned by the unconstrained state x. The space $\mathcal{D}$ is given by

$$\mathcal{D} = \{x \in \mathbb{R}^3 \times \mathbb{R}^3 \times \mathbb{S}^3 \times \mathbb{R}^3 \ : \|x\| \leq r_x\} \subset \mathbb{R}^3 \times \mathbb{R}^3 \times \mathbb{S}^3 \times \mathbb{R}^3, \tag{5.114}$$

where r_x is a vector of the bounds on the state variables. Since the scope of this report limits the behaviour of the UAV to typical low-angle-of-attack flight conditions, it is reasonable to assume that the state is bounded so that

$$\|\mathbf{r}\| \leq r_{max}, \quad \|\mathbf{v}_b\| \leq v_{b_{max}}, \quad \|\mathbf{q}\| \leq q_{max}, \quad \text{and } \|\omega_b\| \leq \omega_{b_{max}}. \tag{5.115}$$

Firstly, the fact that the position vector $\mathbf{r}$ is bounded follows from the typical operations of the UAV, in which it will never happen that $\mathbf{r} \to \infty$. Secondly, the velocity $\mathbf{v}_b$ of the UAV is always bounded due to the physical limitations of the UAV and the external wind $\mathbf{v}_w$ affecting it. Since the velocity of the UAV is bounded, it is possible to conclude that the airspeed V_a, the sideslip angle β, and the AoA α are all bounded, since they are calculated from the relative velocity $\mathbf{v}_r^b$, which is bounded since $\mathbf{v}_b$ and $\mathbf{v}_w^b$ are bounded. Additionally, it is possible to assume that there is a lower bound on the airspeed V_a since the fixed-wing UAV is always moving when in the air. Furthermore, the quaternion $\mathbf{q}$ in the state x is always bounded since it is a unit quaternion, i.e. $\|\mathbf{q}\| \leq 1$. Finally, the assumption that ω_b is bounded is reasonable due to the physical limitations of the UAV and since the state is bounded as in (5.115).

Furthermore, the force f_t and moment m_t generated by the throttle δ_t are bounded since it is limited to $\delta_t \in [0, 1]$ and the thrust T is limited so that it is always non-negative. This means that the equations in (2.55) and (2.57) for the thrust and thrust moment can never grow unbounded since the airspeed is also bounded. The remaining force in the system that has not yet been discussed is the gravitational force f_g, which is constant in magnitude and therefore also bounded. It can therefore be concluded that both functions f and g are bounded. Additionally, the function h is bounded since the disturbances in the forces d_f and moments d_m are bounded, which is can be seen from (2.54). Since the functions f, g, and h are bounded and we have that $\|\delta_a\|, \|\delta_e\|, \|\delta_r\| \leq \frac{\pi}{6}$, the system dynamics $\dot{x}$ are also bounded in the subspace $\mathcal{D}$.

5.5.2 Sliding Surface Design

Following the methodology in Coates et al. (2020); Reinhardt et al. (2020), the control objective when using the reduced-attitude representation is to follow a desired reference Γ_d that satisfies

$$\dot{\Gamma}_d = \Gamma_d \times \omega_d, \tag{5.116}$$

where ω_d satisfies $\omega_d^\top \Gamma_d = 0$, i.e. $\omega_d \in \mathrm{T}_{\Gamma_d}\mathbb{S}^2$. The error states can then be defined as

$$e_\Gamma = \Gamma \times \Gamma_d \in \mathrm{T}_{\Gamma_d}\mathbb{S}^2 \tag{5.117}$$

$$e_\omega = \omega_b^\perp - \mathrm{proj}_{\mathrm{T}_\Gamma \mathbb{S}^2}(\omega_d) \in \mathrm{T}_\Gamma \mathbb{S}^2. \tag{5.118}$$

Now let the sliding variable be given by

$$\sigma = e_\omega + k_\Gamma e_\Gamma + \omega_b^\parallel - \frac{g\tan\phi}{V_a}\Gamma. \tag{5.119}$$

If σ is driven to zero in finite time, then $e_\omega = -k_\Gamma e_\Gamma$ and $\omega_b^\parallel = \frac{g\tan\phi}{V_a}\Gamma$. This is due to the fact that the perpendicular and parallel components are decoupled. Note that it is necessary to constrict the airspeed V_a and the roll angle ϕ to $V_a > 0$ and $|\phi| < \pi/2$ to avoid singularity in the last term of (5.119).

Sliding Dynamics

It is possible to rewrite the sliding variable as

$$\sigma = \omega_b - \Pi_\Gamma^\perp \omega_d + k_\Gamma e_\Gamma - \frac{g\tan\phi}{V_a}\Gamma, \tag{5.120}$$

which is helpful in writing the sliding dynamics on the desired form as

$$\dot{\sigma} = a(t,x) + b(t,x)\bar{u} + \gamma(t,x). \tag{5.121}$$

The sliding dynamics based on (5.120) can be defined as

$$\begin{aligned}\dot{\sigma} &= \dot{\omega}_b + \frac{d}{dt}(-\Pi_\Gamma^\perp \omega_d + k_\Gamma e_\Gamma - \frac{g\tan\phi}{V_a}\Gamma) \\ &= \dot{\omega}_b + f_\sigma(t, \Gamma, \omega_b, \Gamma_d, \omega_d, \dot{\omega}_d, V_a, \dot{V}_a).\end{aligned} \tag{5.122}$$

If making the simplifying assumption that $\dot{V}_a$ is simply a time-varying state-independent signal, $\dot{V}_a = \dot{V}_a(t)$, then the only place the body moments, m_b, appear in (5.122) is in $\dot{\omega}_b$. The functions b and γ in (5.121) can therefore be found by expanding $\dot{\omega}_b$ in (2.91) with the disturbance $d_m(t)$ described in chapter 2 added to the body moment m_b. The functions a, b and γ in (5.121) are then given by

$$a(t,x) = f_\sigma - I_b^{-1}(\omega_b \times (I_b \omega_b)) + m_{b_x} \tag{5.123}$$

$$b(t,x) = m_{b_u} \tag{5.124}$$

$$\gamma(t,x) = I_b^{-1} d_m(t), \tag{5.125}$$

where m_{b_x} and m_{b_u} are given in (5.111) and (5.113) respectively.

Boundedness of the Sliding Dynamics

As previously discussed, both the function m_{b_u} and the disturbance d_m are bounded signals, so the functions b and γ in the sliding dynamics (5.121) are therefore also bounded

when restricting the state to the subspace $\mathcal{D}$ defined in (5.114) as previously discussed. The function m_{b_x} and the body angle rates ω_b are also bounded, which means that the function a in (5.121) is bounded if f_σ is bounded within the subspace $\mathcal{D}$.

From the discussion about the boundedness of the state-space representation in subsection 5.5.1, it is already known that ω_b and V_a are bounded and that V_a is bounded from below. Furthermore, we know that Γ is bounded by design, since $\|\Gamma\| = 1$. Since both Γ and ω_b are bounded, $\dot{\Gamma}$ in (2.97) is also bounded in $\mathcal{D}$.

The reference reduced-attitude signal Γ_d is bounded for the same reason that Γ is bounded. It is also reasonable to assume that the reference angle rates ω_d are bounded, since it is part of the control design, and can thus be designed as a bounded signal. Since both Γ_d and ω_d are bounded, it follows from (5.116) that Γ_d is also bounded.

Let us make the additional assumption about the wind velocity $\mathbf{v}_w^b$ that the wind acceleration $\dot{\mathbf{v}}_w^b$ is bounded. Then we can conclude that $\dot{V}_a$ is bounded, since it depends only on $\dot{\mathbf{v}}_r^b$, which is bounded if both $\dot{\mathbf{v}}_b$ and $\dot{\mathbf{v}}_w^b$ are bounded. The UAV acceleration $\dot{\mathbf{v}}_b$ is bounded following the discussion in subsection 5.5.1 where it is concluded that the $\dot{x}$ is bounded.

Since all the signals the function f_σ in (5.122) depends on are bounded, it is reasonable to assume that the function f_σ is also bounded. This means that we can conclude that $\dot{\sigma}$ in (5.122) is bounded. Additionally, this implies that the sliding variable σ in (5.119) is continuous, and differentiable in $\mathcal{D}$ since it has a bounded first derivative in $\mathcal{D}$.

5.5.3 Multivariable SMC Algorithms

This subsection presents the multivariable control algorithms that are applied to the 6DOF model. Following the methodology in section 3.6, the control law u generated by the MSAT and the multivariable super-twisting controllers is transformed by

$$\bar{u} = b^{-1}(t, x)u, \tag{5.126}$$

where $b(t, x)$ is defined in (5.124). The control law $\bar{u}$ is the control input to the 6DOF model. Note that the transformation above differs from the one in section 3.6, which also includes the function $a(t, x)$. The reason for this is that the function a is regarded as uncertain, and is therefore a disturbance in the control design instead of a known function. This means that the sliding dynamics in (5.121) can be written on the form

$$\dot{\sigma} = b(t, x)\bar{u} + \vartheta(t, x), \quad \vartheta(t, x) \triangleq a(t, x) + \gamma(t, x), \tag{5.127}$$

where ϑ is the total perturbation term in the sliding dynamics.

The fact that b needs to be known in the control coefficient transformation (5.126) is a very restrictive requirement as b is, in most cases, uncertain in reality while the signs of the elements of b are generally known. This uncertainty will add a control dependent perturbation term to the total perturbation (5.127) when the control coefficient transformation is used. However, the contribution to the perturbation is larger if only the sign of b is used in the transformation in (5.126), than if an uncertain estimate of b is used instead. Therefore, the control coefficient transformation is, in this report, implemented for all the subsequent control designs with a b matrix that has a 20 % uncertainty. This is done to make the implementation of the control designs more realistic. A brief discussion of the sensitivity of the multivariable control designs to the 20% discrepancy between the b matrix used in the UAV model and the one used in the control design is presented in section 8.8.

Multivariable Saturation Controller

The MSAT is given by

$$u = -K\text{sat}(\sigma) = \begin{cases} -K\frac{\sigma}{\|\sigma\|}, & \text{if } \|\sigma\| > \varepsilon \\ -\frac{K}{\varepsilon}\sigma, & \text{if } \|\sigma\| \leq \varepsilon, \end{cases} \quad \text{sat}(0) = 0, \tag{5.128}$$

where $\varepsilon > 0$ is the size of the boundary layer, and K is the scalar control gain.

The stability of the MSAT (5.128) can only be guaranteed if several assumptions, which are made in chapter 3, are valid. The first assumption is that the sliding variable σ is differentiable in $\mathcal{D}$. From the discussion in subsection 5.5.2, we already know that σ is differentiable. Additionally, the functions a, b, and γ have to be bounded, which they are following the discussion in subsection 5.5.2. In the Lyapunov-analysis in subsection 3.3.3 the function b is assumed to be known and have full rank so that $\det(b) \neq 0$. Since the function b is affected by unknown external disturbances and parametric uncertainties, it is not fully known in reality, so this assumption is not valid. However, we do know the signs and approximate size of the elements in b, which means it is reasonable to assume that b has full rank, i.e. $\det(b) \neq 0$ in $\mathcal{D}$.

A summary of the assumptions for the MSAT can be found in Table 5.4.

Assumption	**MSAT**
The sliding variable σ is differentiable	Yes
The disturbance γ is bounded	Yes
The function a is bounded	Yes
The function b is bounded	Yes
The function b is known	No
The function b is never zero, i.e. $\det(b) \neq 0$	Yes

Table 5.4: A summary of the assumptions made about the MSAT controller. "Yes" implies that the assumption is valid, while "No" implies the opposite.

Multivariable Super-Twisting Algorithm

The MSTA presented in Nagesh and Edwards (2014) is

$$u(\sigma) = -k_1 \frac{\sigma}{\|\sigma\|^{1/2}} + z - k_2\sigma, \quad u(0) \coloneqq 0 \tag{5.129}$$

$$\dot{z}(\sigma) = -k_3 \frac{\sigma}{\|\sigma\|} - k_4\sigma, \quad \dot{z}(0) \coloneqq 0, \tag{5.130}$$

where $k_1, k_3 > 0$ and $k_2, k_4 \geq 0$ are positive control gains.

For the algorithm above to guarantee convergence of the system to the sliding surface, it is assumed that both σ and z are continuous and differentiable everywhere except in the

zero-measure set $\mathcal{S}$ and that the system is of relative degree 1. Firstly, since we already know from the previous discussion that σ is continuous and differentiable everywhere in $\mathcal{D}$ except on $\mathcal{S}$, we also know that z is continuous and differentiable everywhere in $\mathcal{D}$ except on $\mathcal{S}$ from (5.130). This conclusion is only valid if we assume that $\varphi \equiv 0$ following the design methodology in Nagesh and Edwards (2014). Secondly, we know that the control $\bar{u}$ appears in the equation for the sliding dynamics, which means that the relative degree is, in fact, equal to 1.

Furthermore, to perform the control coefficient transformation in (5.126), the function b in (5.124) has to be both known and nonsingular. Since the function b depends on aerodynamic parameters and coefficients that are difficult to determine experimentally, it will never be completely known without any uncertainty. However, it is possible to still use the nominal function b, and view the possible uncertainties compared to the real values of the uncertain parameters as another perturbation in the system. The difference between this kind of perturbation and the other perturbation ϑ is that uncertainty in b will add a control-dependent perturbation to the sliding dynamics so that

$$\vartheta_1(t, x, u) = \Delta b(t, x)\bar{u} + a(t, x) + \gamma(t, x),$$

where Δb is a perturbation that arises from uncertainty in the control coefficient. This kind of control-dependent perturbation is not explicitly mentioned in the MSTA design in Nagesh and Edwards (2014), where the perturbation term is $\gamma = \gamma(t, \sigma)$. However, since we have that $\sigma = \sigma(t, x, u)$ it is reasonable to believe that even if the sliding dynamics include a perturbation such as ϑ_1, convergence to the sliding surface is guaranteed.

Even though the function b is not exactly known, it is assumed to be nonsingular, and the estimate of b used in the simulation model is therefore also nonsingular. Even though the aerodynamic coefficients and parameters are uncertain, their signs are known, which simplifies the process of determining if b is nonsingular. In this report, the Aerosonde model (Beard and McLain, 2012) is used to determine the values of the system parameters in the UAV model. Based on this model and the equation in (5.124) it is possible to see that

$$\det(b) > 0, \ \forall t$$

based on the signs of the aerodynamic coefficients, which means that b is nonsingular.

In addition to the assumptions above, it is assumed that the perturbation ϑ and φ are bounded by

$$\vartheta \leq \delta_1 \|\sigma\|$$
$$\varphi \leq \delta_2.$$

Firstly, we have that φ is bounded since $\varphi \equiv 0$. Secondly, it is already determined that ϑ is bounded in $\mathcal{D}$ since we know that both a and γ are bounded in the subspace $\mathcal{D}$ by some constant upper limit from the discussion in subsection 5.5.2. However, ϑ is not necessarily bounded by a limit that depends on the sliding variable. When the system has reached the sliding surface, we have that $\sigma = 0$ while we cannot be certain that both $a(t, x) = \gamma(t, x) = 0$. Additionally, since γ depends on the disturbance $d = d(t)$ which is not state-dependent, there is no guarantee that $\sigma = 0 \implies d(t) = 0$. Therefore, the first boundedness-assumption above cannot be guaranteed.

A summary of the assumptions discussed above can be found in Table 5.5.

Adaptive Multivariable Super-Twisting Algorithm

The AMSTA presented in Dong et al. (2016) and Hu et al. (2019) is

$$u(\sigma) = \alpha_1 \frac{\sigma}{\|\sigma\|^{1/2}} + z, \quad u(0) \coloneqq 0 \tag{5.131}$$

$$\dot{z}(\sigma) = -\frac{\alpha_2}{2}\frac{\sigma}{\|\sigma\|}, \quad \dot{z}(0) \coloneqq 0, \tag{5.132}$$

with adaptive gain update laws given by

$$\dot{\alpha_1} = \begin{cases} \omega_1 \sqrt{\frac{\gamma_1}{2}}, & \text{if } \|\sigma\| > \sigma_T \\ 0, & \text{if } \|\sigma\| \leq \sigma_T \end{cases} \tag{5.133}$$

$$\alpha_2 = 2\epsilon_1 \alpha_1, \tag{5.134}$$

where $\sigma_T > 0$ is some small threshold value, and ω_1, γ_1, and ϵ_1 are positive constants. Furthermore, according to Hu et al. (2019) and Dong et al. (2016), the constant ϵ_1 should be chosen as.

$$\epsilon_1 = \frac{\omega_3}{2\omega_1}\sqrt{\frac{\gamma_3}{\gamma_1}} \tag{5.135}$$

for positive constants ω_3 and γ_3.

Since the AMSTA is an extension of the MSTA, several of the same assumptions about the system that are made for the MSTA, are also made for the AMSTA. The only additional assumption that is required for the system to reach the sliding surface when the control is generated by the AMSTA above is that the derivative of the perturbation is bounded by

$$\left\|\dot{\vartheta}\right\| \leq \delta_3, \tag{5.136}$$

which means that both $\dot{a}$ and $\dot{\gamma}$ need to be bounded in the subspace $\mathcal{D}$ for the assumption above to be true. Firstly, since γ depends solely on $d(t)$, we know that $\dot{\gamma}$ is bounded based on (2.54). Secondly, a is bounded in $\mathcal{D}$ if $\dot{f}_\sigma, \omega_b, \dot{\omega}_b$, and $\dot{m}_{b_x}$ are bounded in $\mathcal{D}$. From the discussion in subsection 5.5.1 about the boundedness of the system dynamics, we know that x is bounded since it is restricted to the subspace $\mathcal{D}$, and also that $\dot{x}$ is bounded in $\mathcal{D}$. This means that both ω_b and $\dot{\omega}_b$ are bounded in $\mathcal{D}$. The functions $\dot{f}_\sigma$ and $\dot{m}_{b_x}$ are dependent on many variables:

$$\dot{m}_{b_x} = \dot{m}_{b_x}(t, V_a, \dot{V}_a, \dot{\beta}, \dot{\alpha}, \dot{\omega}_b, \delta_t, \dot{\delta}_t) \tag{5.137}$$

$$\dot{f}_\sigma = \dot{f}_\sigma(t, \Gamma, \omega_d, \dot{\omega}_d, \ddot{\omega}_d, \Gamma_d, \phi, \dot{\phi}, \ddot{\phi}, V_a, \dot{V}_a, \ddot{V}_a). \tag{5.138}$$

which need to be bounded in $\mathcal{D}$ for $\dot{f}_\sigma$ and $\dot{m}_{b_x}$ to be bounded in $\mathcal{D}$.

The function $\dot{m}_{b_x}$ is bounded if $V_a, \dot{V}_a, \dot{\beta}, \dot{\alpha}, \dot{\omega}_b, \delta_t$, and $\dot{\delta}_t$. Firstly, we know from previous discussions that V_a and ω_b are bounded in $\mathcal{D}$. Furthermore, we know that the system dynamics $\dot{x}$ are bounded in $\mathcal{D}$. The function $\dot{V}_a$ is already concluded to be bounded following the discussion about the boundedness of the sliding dynamics in subsection 5.5.2. By the same argumentation, both $\dot{\alpha}$ and $\dot{\beta}$ are bounded since they depend on the same variables as $\dot{V}_a$, i.e. $\mathbf{v}_r$ and $\dot{\mathbf{v}}_r$, which are both bounded in $\mathcal{D}$ from the discussion

in subsection 5.5.2. Finally, the throttle and throttle dynamics are bounded, which can be seen in (5.1), since δ_t only depends on V_a and $\dot{\delta}_t$ depends on V_a and $\dot{V}_a$. Both V_a and $\dot{V}_a$ are bounded in $\mathcal{D}$ as previously discussed, so δ_t and $\dot{\delta}_t$ are also bounded in $\mathcal{D}$. Thus, the function $\dot{m}_{b_x}$ is bounded in the subspace $\mathcal{D}$.

Furthermore, the function $\dot{f}_\sigma$ is bounded in $\mathcal{D}$ if $\Gamma, \omega_d, \dot{\omega}_d, \ddot{\omega}_d, \Gamma_d, \phi, \dot{\phi}, \ddot{\phi}, V_a, \dot{V}_a$ and $\ddot{V}_a$ are bounded in $\mathcal{D}$. The functions $\Gamma, \Gamma_d, \omega_d, \phi, \dot{\phi}, V_a$, and V_a are already found to be bounded in $\mathcal{D}$ in previous discussions. It is reasonable to assume that the functions $\dot{\omega}_d$ and $\ddot{\omega}_d$ are both bounded since ω_d is a design variable that can be designed so that $\dot{\omega}_d$ and $\ddot{\omega}_d$ are bounded in $\mathcal{D}$. Furthermore, since $\dot{x}$ is bounded, we know that $\ddot{\phi}$ is bounded from (2.65) since $\ddot{\Theta}$ is a function of $\Theta, \dot{\Theta}, \omega_b$, and $\dot{\omega}_b$, which are all bounded since x and $\dot{x}$ are bounded in $\mathcal{D}$. Finally, $\ddot{V}_a$ is assumed here to simply be a time-varying state-independent signal, which is reasonable to believe is bounded in $\mathcal{D}$ as the UAV cannot have infinitely high acceleration. Therefore, the assumption that $\dot{f}_\sigma$ is bounded is valid in $\mathcal{D}$.

Another difference from the assumptions about the MSTA is that the perturbation ϑ is assumed to be bounded by

$$\|\vartheta\| \leq \delta_1 \|\sigma\|^{\frac{1}{2}},$$

which is not a valid assumption following the discussion about the boundedness of ϑ from the previous paragraphs about the MSTA.

A summary of the assumptions discussed in this paragraph, in addition to the assumptions that the AMSTA share with the MSTA, can be found in 5.5.

Generalized Multivariable Super-Twisting Algorithm

The GMSTA presented in López-Caamal and Moreno (2019) is

$$u = -k_1 \phi_1(\sigma) + k_3 z \tag{5.139}$$
$$\dot{z} = -k_2 \phi_2(\sigma) + \varphi(t, \sigma), \tag{5.140}$$

where

$$\phi_1(\sigma) = (\alpha_g \|\sigma\|^{-p_g} + \beta_g + \gamma_g \|\sigma\|_g^q)\sigma, \quad \phi_1(0) \coloneqq 0 \tag{5.141}$$
$$\phi_2(\sigma) = (\alpha_g (1 - p_g) \|\sigma\|^{-p_g} + \beta_g + \gamma_g (1 + q_g))\phi_1(\sigma), \quad \phi_2(0), \coloneqq 0 \tag{5.142}$$

with

$$0 < p_g \leq \frac{1}{2}, \quad q_g > 0, \quad \alpha_g > 0, \quad \beta_g, \gamma_g \geq 0.$$

As for the MSTA, and the AMSTA, for convergence of the system to the sliding mode to be guaranteed, the system has to be of relative degree 1, both σ and z have to be continuous and differentiable except in $\mathcal{S}$, and the function b has to be known and nonsingular. All these assumptions are already discussed in the previous sections, and whether they are valid or not can be seen in Table 5.5.

Some additional assumptions are made about the GMSTA in (5.139)-(5.142). Firstly, the function ϕ_1 has to satisfy

$$\phi_1 = 0, \text{ if and only if } \sigma = 0 \tag{5.143}$$
$$\|\sigma\| \to \infty \implies \|\phi\|_1 \to \infty. \tag{5.144}$$

Assumption	**MSTA**	**AMSTA**	**GMSTA**
System is of relative degree 1	Yes	Yes	Yes
The sliding variable σ is continuous except in $\mathcal{S}$	Yes	Yes	Yes
The sliding variable σ is differentiable except in $\mathcal{S}$	Yes	Yes	Yes
The function z is continuous except in $\mathcal{S}$	Yes	Yes	Yes
The function z is differentiable except in $\mathcal{S}$	Yes	Yes	Yes
The function ϕ_1 is continuous except in $\mathcal{S}$	-	-	Yes
The function ϕ_1 is differentiable except in $\mathcal{S}$	-	-	Yes
The function b is known	No	No	No
The function b is nonsingular	Yes	Yes	Yes
The total perturbation ϑ is bounded by $\|\vartheta\| \leq \delta_1 \|\sigma\|$	No	-	-
The total perturbation ϑ is bounded by $\|\vartheta\| \leq \delta_1 \|\sigma\|^{\frac{1}{2}}$	-	No	-
The derivative of the perturbation ϑ is bounded by $\left\|\dot{\vartheta}\right\| \leq \delta_3$	-	Yes	-
The perturbation φ is bounded by $\|\varphi\| \leq \delta_2$	Yes	Yes	-
The function $\phi_1 = 0$ if and only if $\sigma = 0$	-	-	Yes
The norm $\|\phi_1\| \to \infty$ as $\|\sigma\| \to \infty$	-	-	Yes
The function ϕ_2 is continuous except, possibly, in $\mathcal{S}$	-	-	Yes
The function $J(\sigma)$ fulfills $J(\sigma) > 0,\ \forall \sigma \in \mathbb{R}^3 \setminus \mathcal{S}$	-	-	Yes
The perturbation ϑ is bounded as in (5.145)	-	-	No
The perturbation φ is bounded as in (5.146)	-	-	Yes

Table 5.5: A summary of the assumptions made about the MSTA, the AMSTA, and the GMSTA controllers. "Yes" implies that the assumption is valid, while "No" implies the opposite. "-" implies that the controller does not rely upon the assumption.

By design, the first assumption (5.143) is satisfied. The second assumption (5.144) is also satisfied as every term of ϕ_1 will grow unbounded if $\|\sigma\| \to \infty$. Secondly, the function ϕ_2 is assumed to be continuous everywhere except, possibly, in $\mathcal{S}$. Since ϕ_2 is a continuous function in σ except in $\mathcal{S}$, and σ is continuous everywhere except in $\mathcal{S}$, the second assumption is also satisfied. Furthermore, the function ϕ_1 is assumed to be both continuous and differentiable everywhere except in $\mathcal{S}$. The function ϕ_1 is also a continuous function in σ and we know that σ is both continuous and differentiable except in $\mathcal{S}$, which means that this assumption is also valid. Another assumption is that the function $J(\sigma)$, which is given by

$$\phi_2(\sigma) = J(\sigma)\phi_1(\sigma),$$

fulfills $J(\sigma) > 0$, $\forall \sigma \in \mathbb{R}^3 \setminus \mathcal{S}$. From the expression for ϕ_2 in (5.142), it is clear that this assumption is valid as the norm is always positive, and the choice of control parameters does not allow negative terms in (5.142).

As for the MSTA and the AMSTA, some assumptions about the boundedness of the perturbations are made for the GMSTA. The boundedness assumptions are given by

$$\vartheta(t, x) = G_1(t)\phi_1(\sigma) + G_3(t)z \tag{5.145}$$

$$\varphi(t, x) = G_2(t)\phi_2(\sigma). \tag{5.146}$$

Since $\varphi \equiv 0$ as previously discussed, the second assumption is valid. The first assumption, however, is not, as it is not satisfied when $\sigma = 0$ since it cannot be guaranteed that $\sigma = 0 \implies a(t, x) = \gamma(t, \sigma) = 0$.

A summary of the assumptions discussed in this paragraph can be found in Table 5.5.

5.6 Stability Analysis of the Longitudinal Internal Dynamics

A prerequisite assumption for the discussion of the control algorithms in the previous sections to be valid is that the internal dynamics of the system are stable in the sliding mode. This is assumed for both the decoupled longitudinal model and the 6DOF model. In this section, the stability of the internal longitudinal dynamics is investigated. Since the system is of dimension $n = 4$, and the relative degree of the system is $r = 1$, there may exist non-trivial internal dynamics that are not bounded in the sliding mode. If this is the case, then none of the control algorithms in 5.3.3 are applicable.

The analysis of the internal dynamics of the longitudinal model includes making some simplifying assumptions about the system, which is done in subsection 5.6.1. Then the equivalent control is defined in subsection 5.6.2. The equilibrium point of the system in the sliding mode is found in subsection 5.6.3 before the zero dynamics of the system in the sliding mode is investigated in subsection 5.6.4.

A similar analysis of the stability of the decoupled lateral internal dynamics is presented in Griffiths (2020).

5.6.1 Assumptions

When performing an analysis of the internal dynamics, the conditions are assumed to be ideal, which means that all disturbances and uncertainties in the system are disregarded, and the model is assumed to be an accurate model of the system without any modeling errors. Additionally, the reference signal θ_d is assumed to be constant, so that $q_d = \dot{q}_d = 0$. Thus, the sliding dynamics simplifies to

$$\sigma_\theta = a_{\theta_1} e + \dot{e} = a_{\theta_1}(\theta - \theta_d) + q \tag{5.147}$$
$$\dot{\sigma}_\theta = a_{\theta_1} q + \dot{q}. \tag{5.148}$$

As previously stated in section 6.1.2, it is assumed that $\theta_d \in \langle -\frac{\pi}{2}, \frac{\pi}{2} \rangle$.

5.6.2 Longitudinal Equivalent Control

The first step in analysing the internal dynamics in the sliding mode is to find the equivalent control. The equivalent control $\delta_{e_{eq}}$ is obtained from solving $\dot{\sigma}_\theta = 0$:

$$\dot{\sigma}_\theta = a_{\theta_1} q + \frac{1}{I_y} m = 0. \tag{5.149}$$

Solving (5.149) for δ_e yields the equivalent control

$$\delta_{e_{eq}} = -\frac{1}{C_{m_{\delta_e}}} \left(\left(\frac{2I_y}{\rho V_a^2 Sc} a_{\theta_1} + C_{m_q} \frac{c}{2V_a} \right) q + C_{m_0} + C_{m_\alpha} \alpha \right). \tag{5.150}$$

The next step is to reformulate the system dynamics in the sliding mode in terms of the error e_θ instead of θ, which are given by

$$\dot{e}_\theta = -a_{\theta_1} e_\theta \tag{5.151}$$
$$\dot{q} = -a_{\theta_1} q \tag{5.152}$$
$$\mathrm{m}\dot{V}_a = T\cos\alpha - D - \mathrm{m}g\sin(e_\theta + \theta_d - \alpha) \tag{5.153}$$
$$\mathrm{m}V_a\dot{\alpha} = \mathrm{m}V_a q + \mathrm{m}g\cos(e_\theta + \theta_d - \alpha) - L - T\sin\alpha, \tag{5.154}$$

and then to insert the equivalent control $\delta_{e_{eq}}$ in the expressions for L and D. The lift and drag forces are then

$$\begin{aligned} L_{eq} &= \frac{1}{2}\rho V_a^2 S C_L(\alpha, q, \delta_{e_{eq}}) \\ &= \left(\frac{1}{4}\rho V_a Sc (C_{L_q} - \frac{C_{L_{\delta_e}}}{C_{m_{\delta_e}}} C_{m_q}) - a_{\theta_1} \frac{C_{L_{\delta_e}}}{C_{m_{\delta_e}}} \frac{I_y}{c} \right) q \\ &\quad + \frac{1}{2}\rho V_a^2 S (C_{L_\alpha} - \frac{C_{L_{\delta_e}}}{C_{m_{\delta_e}}} C_{m_\alpha})\alpha + \frac{1}{2}\rho V_a^2 S (C_{L_0} - \frac{C_{L_{\delta_e}}}{C_{m_{\delta_e}}} C_{m_0}) \\ &= (V_a L_{q1} - L_{q2}) q + V_a^2 L_\alpha \alpha + V_a^2 L_0 \end{aligned} \tag{5.155}$$

$$\begin{aligned} D_{eq} &= \frac{1}{2}\rho V_a^2 S C_D(\alpha, q, \delta_{e_{eq}}) \\ &= \left(\frac{1}{4}\rho V_a S c(C_{D_q} - \frac{C_{D_{\delta_e}}}{C_{m_{\delta_e}}}C_{m_q}) - \frac{C_{D_{\delta_e}}}{C_{m_{\delta_e}}}\frac{I_y}{c}a_{\theta_1}\right) q \\ &\quad + \frac{1}{2}\rho V_a^2 S(C_{D_\alpha} - \frac{C_{D_{\delta_e}}}{C_{m_{\delta_e}}}C_{m_\alpha})\alpha + \frac{1}{2}\rho V_a^2 S(C_{D_0} - \frac{C_{D_{\delta_e}}}{C_{m_{\delta_e}}}C_{m_0}) \\ &= (V_a D_{q1} - D_{q2})q + V_a^2 D_\alpha \alpha + V_a^2 D_0 \end{aligned} \tag{5.156}$$

so that the system dynamics in the sliding mode when using the equivalent control $\delta_{e_{eq}}$ is

$$\dot{e} = -a_{\theta_1} e \tag{5.157}$$

$$\dot{q} = -a_{\theta_1} q \tag{5.158}$$

$$\begin{aligned} \mathrm{m}\dot{V}_a &= T\cos\alpha - ((V_a D_{q1} - D_{q2})q + V_a^2 D_\alpha \alpha + D_0) \\ &\quad - \mathrm{m}g\sin(e + \theta_d - \alpha) \end{aligned} \tag{5.159}$$

$$\begin{aligned} \mathrm{m}V_a\dot{\alpha} &= \mathrm{m}V_a q + \mathrm{m}g\cos(e + \theta_d - \alpha) \\ &\quad - ((V_a L_{q1} - L_{q2})q + V_a^2 L_\alpha \alpha + L_0) - T\sin\alpha \end{aligned}. \tag{5.160}$$

5.6.3 Finding the Equilibrium Point

When the system is in the sliding mode, we know that the values of e and q are $e^* = q^* = 0$ from (5.157)-(5.158) since the system is in an equilibrium so that $\dot{e} = \dot{q} = 0$. However, the values of V_a and α in the sliding mode, denoted V_a^* and α^*, are still unknown. To determine the zero dynamics of the system in the sliding mode, it is necessary to know these values.

The equilibrium

$$x_\theta^* = \begin{bmatrix} e^* \\ q^* \\ V_a^* \\ \alpha^* \end{bmatrix} = \begin{bmatrix} 0 \\ 0 \\ V_a^* \\ \alpha^* \end{bmatrix} \tag{5.161}$$

for a given pitch angle reference θ_d can be found by solving the equations

$$f_{V_a} = \dot{V}_a = 0 \tag{5.162}$$

$$f_\alpha = \dot{\alpha} = 0, \tag{5.163}$$

where the functions f_{V_a} and f_α are given as

$$\begin{aligned} f_{V_a} &= \frac{T}{\mathrm{m}}\cos\alpha - \frac{1}{\mathrm{m}}((V_a D_{q1} - D_{q2})q + V_a^2 D_\alpha \alpha + V_a^2 D_0) \\ &\quad - g\sin(e + \theta_d - \alpha) \end{aligned} \tag{5.164}$$

$$\begin{aligned} f_\alpha &= q + \frac{g}{V_a}\cos(e + \theta_d - \alpha) \\ &\quad - \frac{1}{\mathrm{m}V_a}((V_a L_{q1} - L_{q2})q + V_a^2 L_\alpha \alpha + V_a^2 L_0) - \frac{T}{\mathrm{m}V_a}\sin\alpha \end{aligned} \tag{5.165}$$

based on in (5.160)-(5.159). Due to the fact that $e^* = q^* = 0$, the problem can be reduced to solving

$$f_{V_a} = \frac{T}{\mathrm{m}} \cos\alpha - \frac{V_a^2}{\mathrm{m}}(D_\alpha \alpha + D_0) - g\sin(\theta_d - \alpha) = 0 \tag{5.166}$$

$$f_\alpha = \frac{g}{V_a}\cos(\theta_d - \alpha) - \frac{V_a}{\mathrm{m}}(L_\alpha \alpha + L_0) - \frac{T}{\mathrm{m}V_a}\sin\alpha = 0 \tag{5.167}$$

to find the equilibrium values V_a^* and α^* as a function of the pitch reference θ_d.

Since (5.166)-(5.167) are nonlinear equations, the MATLAB-function `fsolve` is used to find V_a^* and α^* in the MATLAB-script in Listing A.1. The solution of (5.166)-(5.167) for the pitch angle reference $\theta_d \in \langle -\frac{\pi}{2}, \frac{\pi}{2} \rangle$ can be seen in Figure 5.3, where the system parameter values are chosen based on the Aerosonde model (Beard and McLain, 2012).

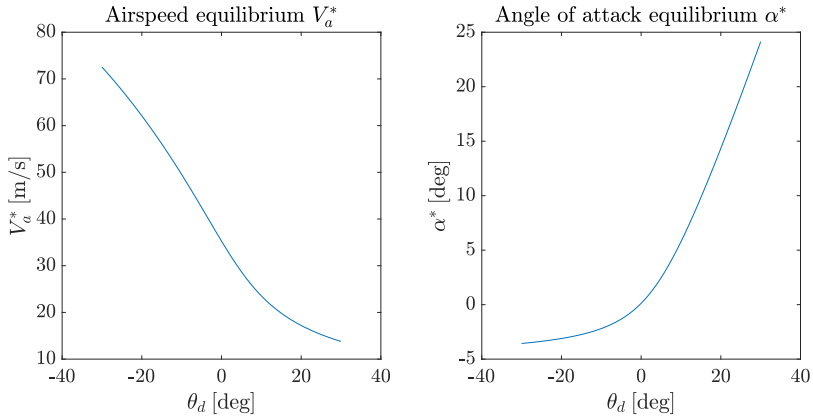

Figure 5.3: Equilibrium values V_a^* and α^* for $\theta_d \in \langle -30, 30 \rangle$ deg found by solving (5.166)-(5.167) with the initial guess $V_{a_0}^* = 45$ m/s and $\alpha_0^* = 2$ deg.

However, the MATLAB-function `fsolve` does not detect multiple solutions, so the solutions displayed in Figure 5.3 may not be unique. Whether (5.166)-(5.167) can have multiple solutions is investigated by using `fsolve` with different initial vectors $x_0 = [V_{a_0}^*,\ \alpha_0^*]^\top$, where $V_{a_0}^*$ is the initial airspeed equilibrium guess, and α_0^* is the initial equilibrium AoA guess. The results of using combinations of the initial airspeed equilibrium values $V_{a_0}^* \in [5,\ 40,\ 100]$ m/s, and AoA values $\alpha_0^* \in [-15,\ 5,\ 20]$ deg, are shown in Figure 5.4. The reason for choosing these initial estimate values is that they represent both the lower and upper limits of the normal range of airspeed and AoA values, in addition to a more typical set of values given by $V_{a_0}^* = 40$ m/s and $\alpha_0^* = 5$ deg.

In Figure 5.4, there are several discontinuities in the solutions when $V_{a_0}^*$ is both small and large independent of initial AoA α_0^*. In these discontinuities, the function `fsolve` is not able to find any solutions. The only solutions that are well-defined are the ones that correspond to the initial airspeed guess $V_{a_0}^* = 40$ m/s. This may be because the trim T is constant and always equal to the thrust at trim conditions, which might contribute to strange behavior in the equilibrium values when there is a large deviance from the airspeed trim condition $V_{a_0} = 35$ m/s (Beard and McLain, 2012). Therefore, the constant trust may

be the reason for the discontinuities in V_a^* and α^* in Figure 5.4 when both a small and large initial guess of V_a^* is used.

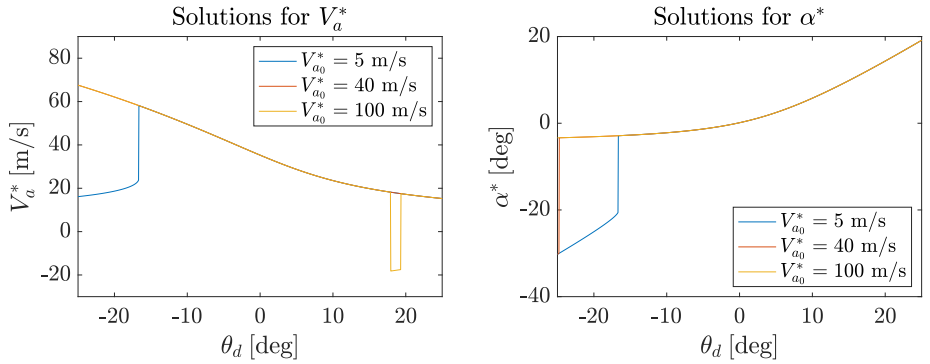

(a) The possible solutions of (5.166)-(5.167) for initial values $V_{a_0}^* \in [5,\ 40,\ 100]$ m/s when the initial angle of attack is $\alpha_0^* = -15$ deg.

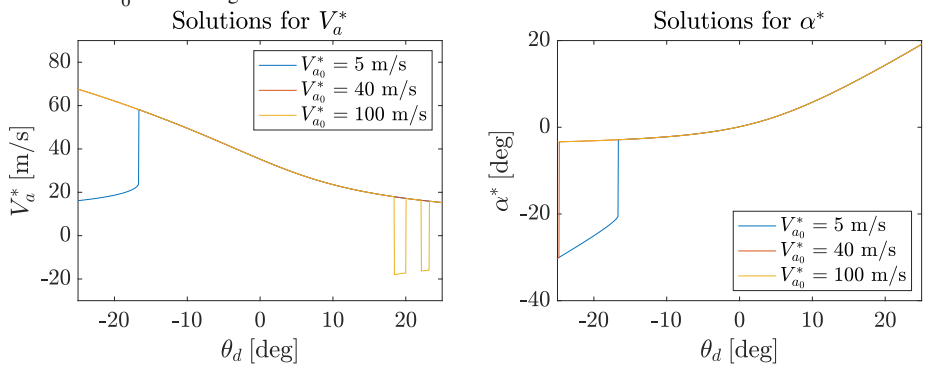

(b) The possible solutions of (5.166)-(5.167) for initial values $V_{a_0}^* \in [5,\ 40,\ 100]$ m/s when the initial angle of attack is $\alpha_0^* = 5$ deg.

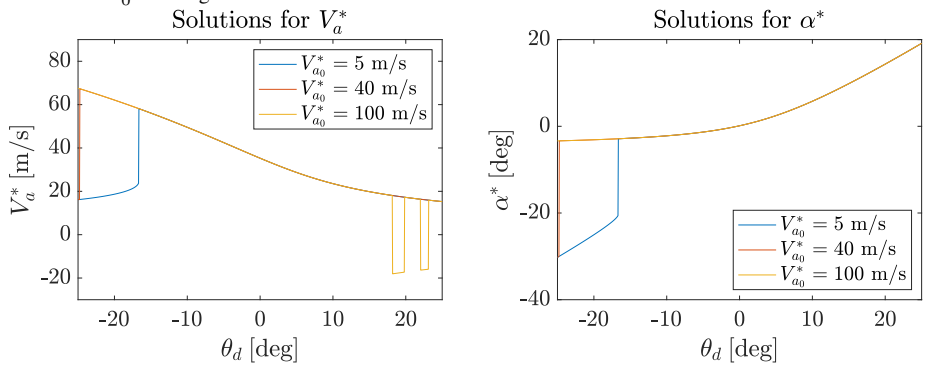

(c) The possible solutions of (5.166)-(5.167) for initial airspeed values $V_{a_0}^* \in [5,\ 40,\ 100]$ m/s when the initial angle of attack is $\alpha_0^* = 20$ deg.

Figure 5.4: The possible solutions for the equilibrium airspeed V_a^* and angle of attack α^* for different initial estimates $V_{a_0}^*$ and α_0^*.

Furthermore, the linearized coefficients do not incorporate stall dynamics, which might also be the reason for the discontinuities and negative solutions in the airspeed equilibrium V_a^* in Figure 5.4. Even though stall angles are typically 15-25 degrees, the discontinuities appear when α^* is between 5 and 10 degrees. This is also something that might be due to the constant thrust. For a higher thrust value than the trim thrust, these discontinuities disappear, as the loss in lift when stall happens is compensated for by the high velocity of the UAV. This can be seen in Figure 5.5, where (5.166)-(5.167) is solved using initial equilibrium values $V_{a_0}^* = 100$ m/s and $\alpha_0^* = 20$ deg. The solution in Figure 5.5 does not contain any discontinuities, while the solution for the same initial values in Figure 5.4c does have discontinuities and even negative solutions for the airspeed equilibrium value V_a^*. The difference between the solutions in Figure 5.4c and Figure 5.5 is that the first one is solved with trim thrust, and the second one is solved with a thrust value that is three times the thrust at trim conditions so that α^* does not grow too large.

Since the scope of this report is to perform pitch angle tracking under typical low-angle-of-attack conditions, the solution for V_a^* and α^* presented in Figure 5.3 is considered the equilibrium values which are used to analyze the zero dynamics in the next subsection.

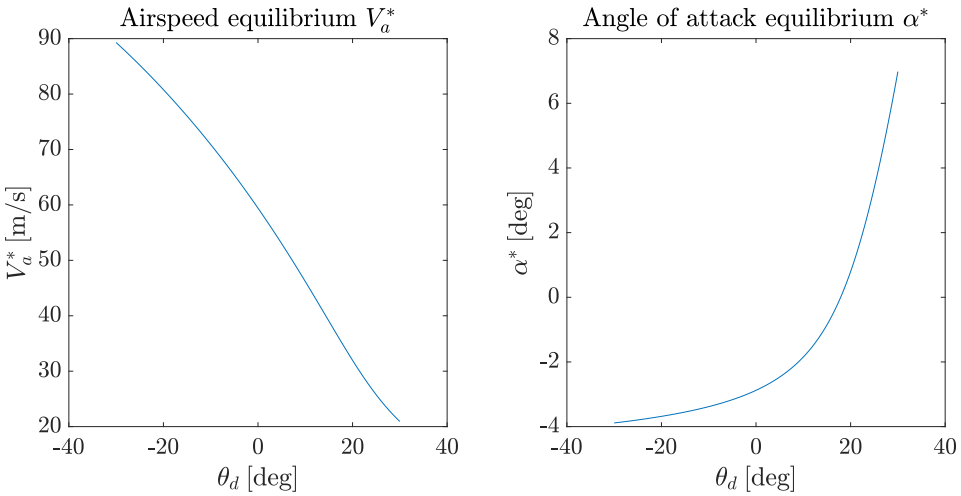

Figure 5.5: The equilibrium values V_a^* and α^* as a function of θ_d for a thrust value that is three times as large as the thrust value at trim conditions.

5.6.4 Zero Dynamics

Now that the equilibrium x_θ^* is determined, it is possible to investigate the zero dynamics of the system in the sliding mode, which may be unstable, in which case the internal states may grow unbounded. To determine the zero dynamics, it is necessary to write the system on a linearized form as

$$\Delta \dot{x}_\theta = \bar{A} \Delta x_\theta, \tag{5.168}$$

where the elements of $\bar{A}$ are found from (5.157)-(5.158) and by linearizing (5.164)-(5.165). The linearized expressions for $\dot{V}_a$ and $\dot{\alpha}$ are given by

$$\begin{aligned}\Delta\dot{V}_a = &\left.\frac{\partial f_{V_a}}{\partial e}\right|_{x_\theta=x_\theta^*}\Delta e + \left.\frac{\partial f_{V_a}}{\partial q}\right|_{x_\theta=x_\theta^*}\Delta q \\ &+ \left.\frac{\partial f_{V_a}}{\partial V_a}\right|_{x_\theta=x_\theta^*}\Delta V_a + \left.\frac{\partial f_{V_a}}{\partial \alpha}\right|_{x_\theta=x_\theta^*}\Delta\alpha\end{aligned} \tag{5.169}$$

$$\begin{aligned}\Delta\dot{\alpha} = &\left.\frac{\partial f_{\alpha}}{\partial e}\right|_{x_\theta=x_\theta^*}\Delta e + \left.\frac{\partial f_{\alpha}}{\partial q}\right|_{x_\theta=x_\theta^*}\Delta q \\ &+ \left.\frac{\partial f_{\alpha}}{\partial V_a}\right|_{x_\theta=x_\theta^*}\Delta V_a + \left.\frac{\partial f_{\alpha}}{\partial \alpha}\right|_{x_\theta=x_\theta^*}\Delta\alpha,\end{aligned} \tag{5.170}$$

so that the partial derivatives in the equilibrium in the expressions above are the elements $\bar{a}_{ij}$ of the linearized system matrix $\bar{A}$ in (5.168).

The partial derivatives in (5.169) are

$$\left.\frac{\partial f_{V_a}}{\partial e}\right|_{x_\theta=x_\theta^*} = -g\cos(\theta_d-\alpha^*) = \bar{a}_{31}(t,x) \tag{5.171}$$

$$\left.\frac{\partial f_{V_a}}{\partial q}\right|_{x_\theta=x_\theta^*} = -\frac{1}{\mathrm{m}}(V_a^*D_{q1}-D_{q2}) = \bar{a}_{32}(t,x) \tag{5.172}$$

$$\left.\frac{\partial f_{V_a}}{\partial V_a}\right|_{x_\theta=x_\theta^*} = -\frac{2V_a^*}{\mathrm{m}}(D_\alpha\alpha^*+D_0) = \bar{a}_{33}(t,x) \tag{5.173}$$

$$\left.\frac{\partial f_{V_a}}{\partial \alpha}\right|_{x_\theta=x_\theta^*} = \frac{T}{\mathrm{m}}\sin\alpha^* - \frac{V_a^{*2}}{\mathrm{m}}D_\alpha + g\cos(\theta_d-\alpha^*) = \bar{a}_{34}(t,x), \tag{5.174}$$

and the partial derivatives in (5.170) are

$$\left.\frac{\partial f_{\alpha}}{\partial e}\right|_{x_\theta=x_\theta^*} = -\frac{g}{V_a}\sin(\theta_d-\alpha^*) = \bar{a}_{41}(t,x) \tag{5.175}$$

$$\left.\frac{\partial f_{\alpha}}{\partial q}\right|_{x_\theta=x_\theta^*} = 1-\frac{1}{\mathrm{m}}(L_{q1}-\frac{1}{V_a^*}L_{q2}) = \bar{a}_{42}(t,x) \tag{5.176}$$

$$\begin{aligned}\left.\frac{\partial f_{\alpha}}{\partial V_a}\right|_{x_\theta=x_\theta^*} = &-\frac{g}{V_a^{*2}}\cos(\theta_d-\alpha^*) - \frac{L_\alpha}{\mathrm{m}}\alpha^* \\ &-\frac{L_0}{\mathrm{m}} + \frac{T}{\mathrm{m}V_a^{*2}}\sin\alpha^* = \bar{a}_{43}(t,x)\end{aligned} \tag{5.177}$$

$$\left.\frac{\partial f_{\alpha}}{\partial \alpha}\right|_{x_\theta=x_\theta^*} = \frac{g}{V_a^*}\sin(\theta_d-\alpha^*) - \frac{V_a^*}{\mathrm{m}}L_\alpha - \frac{T}{\mathrm{m}V_a^*}\cos\alpha^* = \bar{a}_{44}(t,x) \tag{5.178}$$

The linearized system can thus be written as

$$\Delta\dot{x}_\theta = \bar{A}\Delta x_\theta \begin{bmatrix} -a_{\theta_1} & 0 & 0 & 0 \\ 0 & -a_{\theta_1} & 0 & 0 \\ \bar{a}_{31} & \bar{a}_{32} & \bar{a}_{33} & \bar{a}_{34} \\ \bar{a}_{41} & \bar{a}_{42} & \bar{a}_{43} & \bar{a}_{44} \end{bmatrix} \Delta x, \tag{5.179}$$

where the elements in the top two rows of $\bar{A}$ arise from (5.157) and (5.158).

The real part of the eigenvalues of (5.179) for $\theta_d \in \langle -\frac{\pi}{2}, \frac{\pi}{2} \rangle$ can be seen in Figure 5.6 for when the equilibrium values V_a^* and α^* are found as in Figure 5.3. Since all the eigenvalues of the system in Figure 5.6 have negative real parts, it is possible to conclude that the linearized system (5.179) is stable in the sliding mode. Therefore it is possible to conclude that the original longitudinal decoupled system (2.82)-(2.85) is also stable in the sliding mode.

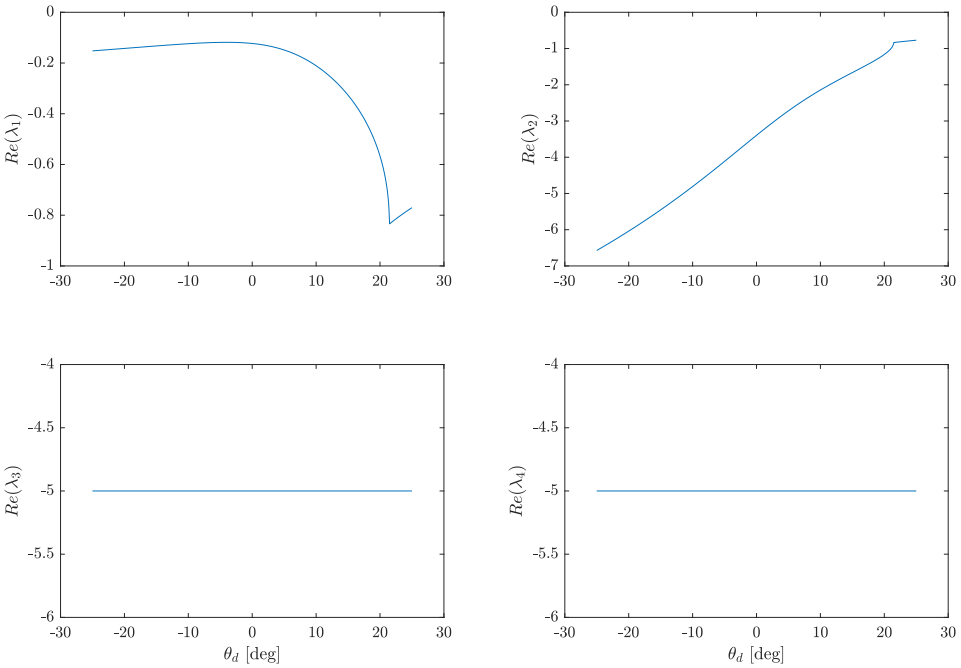

Figure 5.6: The real part of the eigenvalues of the linearized system for $\theta_d \in \langle -30, 30 \rangle$ deg when (5.166)-(5.167) is solved with the initial equilibrium guess $V_{a_0}^* = 40$ m/s and $\alpha_0^* = 2$ deg.

5.7 Evaluation of Control Algorithms

5.7.1 Error Measures

Evaluating the accuracy of the different control algorithms is important in order to make a comparison between them, so the integral square error (ISE) and integral absolute error

(IAE) are used to measure the performances of the controllers, and are also the basis for the tuning of the controllers. The ISE and IAE are given by

$$\text{ISE} = \int_0^t e^2(\tau)\, d\tau \tag{5.180}$$

$$\text{IAE} = \int_0^t |e(\tau)|\, d\tau \tag{5.181}$$

where the error signal e is given in degrees.

The reason for using both the ISE and the IAE is that they emphasize different types of errors. It is desirable to design a controller that provides a fast response with little overshoot, which also achieves close tracking of the reference. The ISE puts more weight on large error values as error values close to zero will become smaller in the calculation of (5.74), and thus have a smaller impact on the ISE. Therefore it is effective to use the ISE as a measure of the response time.

The IAE on the other hand puts equal weight on all error values independent of size. It can therefore be a more useful measure than the ISE when it comes to quantifying the tracking accuracy close to the reference signal, which means it is a better measure of the controller's ability to retain the sliding mode once the sliding surface has been reached.

Additionally, for the decoupled longitudinal model, the maximum absolute value of e for the continuous part of the reference signal θ_d defined in (6.10) is used as a measure of how stable the tracking results of the controllers are. In this report, this measure is called the maximum absolute error after stabilization. The ISE- and IAE-values for the continuous part of θ_d are called ISE after stabilization or IAE after stabilization.

5.7.2 Input Use Measures

In addition to the error measures described in the previous subsection, it is also useful to quantify the amount of input the controllers require to track the reference trajectory, as less input is often better. The measures of input use employed in this report are the integral square input (ISI) and integral absolute input (IAI) given by

$$\text{ISI} = \int_0^t u^2(\tau)\, d\tau \tag{5.182}$$

$$\text{IAI} = \int_0^t |u(\tau)|\, d\tau \tag{5.183}$$

similarly to the equations for the ISE (5.180) and IAE (5.181).

The reason for using both ISI and IAI is similar to the reason for using both ISE and IAE explained in subsection 5.7; they emphasize different types of input use. The ISI is more affected than the IAI by large control commands, while the IAI is more affected than the ISI by chattering in the control signal.

Chapter 6

UAV Simulation Model

This chapter presents the two fixed-wing UAV models that are implemented in Matlab/Simulink, as well as the case studies for both models. Detailed descriptions of the simulation setups for the two models are also included. The implementation of the single-input longitudinal model is described in section 6.1, and the 6DOF simulation model is described in section 6.2.

A similar description of the decoupled lateral simulation model that was used to investigate the behavior of the SISO lateral control algorithms developed in subsection 5.2.3 is presented in Griffiths (2020).

6.1 Longitudinal Simulation Model

The longitudinal simulation model, which is implemented in Simulink, is based on the decoupled longitudinal model in (2.82)-(2.85), and the parameters for the Aerosonde-model (Beard and McLain, 2012), which can be found in Table 6.1.

To investigate the robustness of the different control algorithms described in subsection 5.3.3, several uncertainties are added to the model. These are described in subsection 6.1.1. The simulation setup is described in 6.1.2, while the case study that is used to investigate the behavior of the control algorithms is described in subsection 6.2.3. Finally, the Simulink-implementation of the decoupled longitudinal UAV model is described in subsection 6.1.4.

6.1.1 Disturbances and Unmodeled Dynamics

Wind Gusts

UAVs operate in uncertain environments in the presence of external disturbances which largely take the form of wind gusts. To mimic this during simulation, a time-varying signal $d_g(t)$ is added to the state equation for $\dot{V}_a$ so that $d_g(t)$ is given in $[\mathrm{m/s^2}]$. The

Parameter	Value	Longitudinal Coef.	Value	Lateral Coef.	Value
m	13.5 kg	C_{L_0}	0.28	C_{Y_0}	0
I_x	0.8244 kg-m^2	C_{D_0}	0.03	C_{l_0}	0
I_y	1.135 kg-m^2	C_{m_0}	-0.02338	C_{n_0}	0
I_z	1.759 kg-m^2	C_{L_α}	3.45	C_{Y_β}	-0.98
I_{xz}	0.1204 kg-m^2	C_{D_α}	0.30	C_{l_β}	-0.12
S	0.55 m^2	C_{m_α}	-0.38	C_{n_β}	0.25
b	2.8956 m	C_{L_q}	0	C_{Y_p}	0
c	0.18994 m	C_{D_q}	0	C_{l_p}	-0.26
S_{prop}	0.2027 m^2	C_{m_q}	-3.6	C_{n_p}	0.022
ρ	1.2682 kg/m^2	$C_{L_{\delta_e}}$	-0.36	$C_{Y_{\delta_r}}$	0
k_{motor}	80	$C_{D_{\delta_e}}$	0	$C_{l_{\delta_r}}$	0.14
k_{T_p}	0	$C_{m_{\delta_e}}$	-0.5	$C_{n_{\delta_r}}$	-0.35
k_Ω	0	C_{prop}	1.0	$C_{Y_{\delta_a}}$	0
V_{a_0}	35 m/s	M	50	$C_{l_{\delta_a}}$	0.08
		$C_{n_{\delta_r}}$	-0.032	$C_{n_{\delta_a}}$	0.06
				$C_{Y_{\delta_r}}$	-0.17
				$C_{l_{\delta_r}}$	0.105

Table 6.1: Aerodynamic coefficients and other aerodynamic and system parameters for the Aerosonde UAV as defined in appendix E.2 in Beard and McLain (2012).

wind gusts are modeled by

$$\dot{d}_g = -\frac{1}{T_w} d_g(t) + \frac{1}{T_w} \mathrm{w}_g, \tag{6.1}$$

where $T_w = 2$ s and w_g is band-limited white noise with noise power 5 [m/s$^2 \cdot 1/\sqrt{\mathrm{Hz}}$], which creates a disturbance signal that is approximately 10% of the magnitude of the cruise airspeed V_{a_0}. The signal $d_g(t)$ can be seen in Figure 6.1. The Simulink-Implementation that generates the signal in Figure 6.1 is shown in Figure B.13.

Note that even though the wind gust signal in (6.1) is a stochastic signal because of the white noise w_g, the signal is the same in every simulation. The reason for this is to make it easier to compare the performance of the control algorithms developed in chapter 5, while a more rigorous approach to testing the robustness of the system could be to run Monte Carlo-simulations.

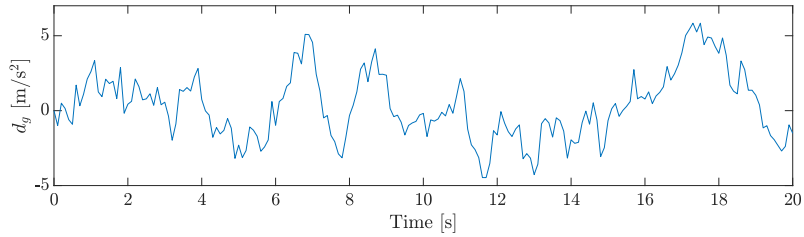

Figure 6.1: The time-varying signal $d_g(t)$ representing the wind gusts in the longitudinal simulation model.

Process Noise

The time-varying signal $d(t)$ that is discussed in subsection 2.4.2 is modeled for the longitudinal model as

$$\dot{d}_{\theta_i} = -\frac{1}{T_{d_\theta}} d_{\theta_i} + \frac{1}{T_{d_\theta}} \mathrm{w}_{d_{\theta_i}} \tag{6.2}$$

for $i = 1, ..., 3$. Here $T_{d_\theta} = 0.7$ s and $\mathrm{w}_{d_{\theta_i}}$ is band-limited white noise with noise power 3 Nm$\cdot 1/\sqrt{\text{Hz}}$ for $i = 1, 2$ or 3 N$\cdot 1/\sqrt{\text{Hz}}$ for $i = 3$. These parameters are chosen so that the magnitude of the vector d_θ contributes with a disturbance that is approximately 20% of the size of the forces L and D, and moment m on average. The signal generated by (6.2) can be seen in Figure 6.2.

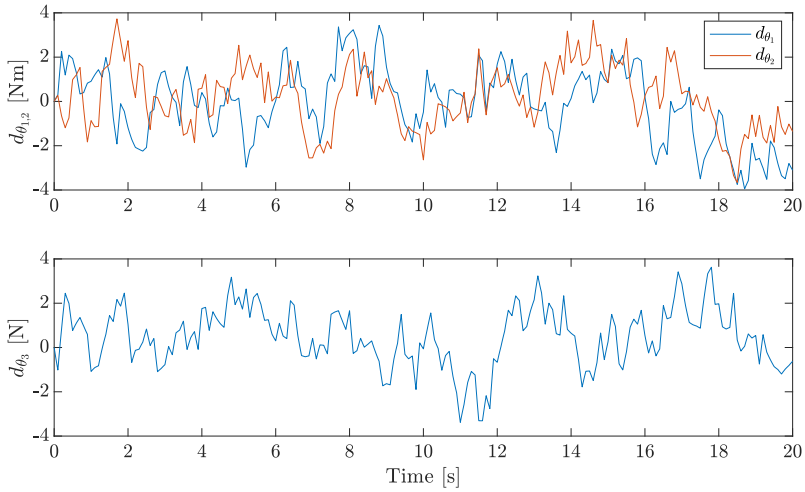

Figure 6.2: The elements of the longitudinal process noise vector d_θ.

In chapter 2, the disturbance d is a six-dimensional signal added to the aerodynamic forces f_a and moments m_a so that they are given by (2.51) and (2.52), respectively. Since the longitudinal model only models the lift and drag forces, and the pitching moment, the

disturbance signal d_θ is added to the forces and moment in (2.43)-(2.45) the same way d is added to the forces and moment in (2.51)-(2.52).

Similar to the wind gust signal discussed in the previous paragraph, the disturbance signal d_θ is the same in every simulation even though it is a stochastic signal in theory. The reason for this is to be able to compare the performance of the control algorithms developed in chapter 5 without running a lot of quite expensive simulations.

Discrete Measurements

The effects of wind gusts and process noise are taken into account in the control design and stability analysis of the control algorithms presented in chapter 5. However, there are more sources of uncertainties present in the system, for example, discrete measurements. In the ideal case considered in the theory presented in chapter 3, the state is continuous and the dynamics of the sensors are disregarded. However, in reality, there is a delay due to the discretization of θ and q when they are measured. In this report, the signals are sampled with a sampling rate given by $f_s = 200$ Hz when simulations are performed with unmodeled dynamics, which is discussed further in subsection 6.1.3.

Actuator Dynamics

Another effect that is not taken into account in the control design is the actuator dynamics. In ideal conditions, a change in the control signals $\bar{\delta}_e$ and δ_t will take place immediately, but in reality actuator response is dynamic. Additionally, the control system runs on a fixed sampling rate $f_s = 200$ Hz, which creates the discrete control signals $\bar{\delta}_e^z$ and δ_t^z. These discrete signals are then used to model the control signals $\bar{\delta}_e^d$ and δ_t^d that are applied to the UAV-model.

The throttle dynamics are modeled using a first-order low-pass filter given by

$$\delta_t^d = \frac{1}{T_{\delta_t} s + 1} \delta_t^z, \tag{6.3}$$

where $T_{\delta_t} = 0.2$ s based on the parameters and methodology in Bøhn et al. (2019). The elevator dynamics are modeled using a first-order low-pass filter which is an approximation of the second-order dynamics used in Bøhn et al. (2019), which is given by

$$H(s) = \frac{\omega_0^2}{s^2 + 2\zeta\omega_0 + \omega_0^2}, \tag{6.4}$$

where $\omega_0 = 100$ and $\zeta = \frac{1}{\sqrt{2}}$. The first-order approximation of (6.4) is calculated by the script in Listing A.3, and is found to be

$$\bar{\delta}_e^d = \frac{1}{T_{\delta_e} s + 1} \bar{\delta}_e^z, \tag{6.5}$$

with $T_{\delta_e} = 0.0154$ s.

The step and frequency responses, as well as the poles and zeros, of the second-order transfer function (TF) in (6.4) and its first-order approximation in (6.5) can be found in Figure 6.3. The characteristics of the step responses can be found in Table 6.2.

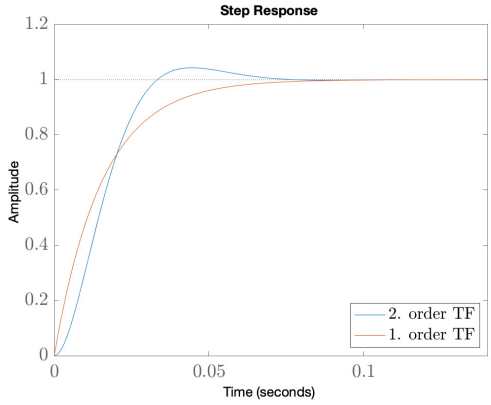

(a) The step responses of transfer functions.

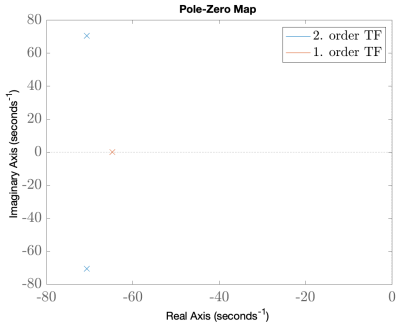

(b) The poles of the transfer functions.

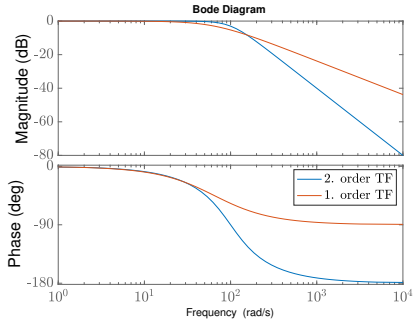

(c) The frequency responses of the transfer functions.

Figure 6.3: The step and frequency responses, and the pole placements, for the second-order TF of the actuator dynamics (6.4), and the first-order TF approximation (6.5).

From Figure 6.3, it is evident that the first-order TF is a good approximation of the second-order TF for small frequencies, while there is a significant difference in both phase and magnitude for large frequencies. Furthermore, since the second-order TF has conjugated complex poles, it is difficult to approximate the response with a first-order TF since neither pole dominates. The response of the first-order TF is slightly slower than the second-order TF, which is also reflected by the rise, settling, and peak times in Table 6.2. The response of the first-order TF is naturally less oscillatory than the second-order response, which can be seen in Figure 6.3a and from the overshoot and peak in Table 6.2. Using the first-order approximation of the actuator dynamics may not be as realistic as the second-order dynamics, but it is also less challenging to tune the controllers developed in chapter 3 to deal with first-order actuator dynamics. The effect of using either the second-order actuator dynamics or the first-order approximation with different time constants is investigated for the 6DOF simulation model in chapter 8.

Property	2. order TF	1. order TF
Rise time	0.0215 s	0.0339 s
Settling time	0.0596 s	0.0604 s
Overshoot	4.3210 %	0
Peak	1.0432	1.000
Peak time	0.0443 s	0.1629 s

Table 6.2: The step response characteristics of the second-order TF (6.4) and the first-order TF approximation (6.5) calculated with the MATLAB-function `stepinfo(sys)`.

6.1.2 Simulation Setup

Reference trajectory

The reference trajectory θ_r is given by a combination of step inputs and a sine wave. Since step inputs are discontinuous functions, the reference is low-pass filtered to generate the desired reference θ_d that is the input to the control system, i.e.

$$\theta_d = \frac{1}{\tau s + 1}\theta_r, \quad \theta_r \in \langle -\frac{\pi}{2}, \frac{\pi}{2} \rangle \tag{6.6}$$

where $\tau = 0.01$ s.

The unfiltered reference signal is given by

$$\theta_r = \theta_{r_1} + \theta_{r_2} + \theta_{r_3} \tag{6.7}$$

where

$$\theta_{r_1} = \begin{cases} 0, & t < 1 \\ 20, & t \geq 1 \end{cases} \tag{6.8}$$

$$\theta_{r_2} = \begin{cases} 0, & t < 1 \\ -20, & t \geq 5 \end{cases} \tag{6.9}$$

$$\theta_{r_3} = \begin{cases} 0, & t < 0 \\ 20.05 \sin(63.03t), & t \geq 10. \end{cases} \tag{6.10}$$

Note that the functions in (6.8)-(6.10) are given in degrees, while the actual input to the control system is converted to radians. Both θ_r and the filtered reference signal θ_d can be seen in Figure 6.4. Finally, the angle rate reference q_d is obtained from (6.6) as

$$q_d = \dot{\theta}_d = \frac{1}{\tau}(\theta_r - \theta_d). \tag{6.11}$$

This way of generating q_d means that q_d can take the form of a step-function. If it is desirable that q_d has a higher degree of smoothness, it would be possible to replace the first-order low-pass filter in (6.11) with a higher-order filter instead.

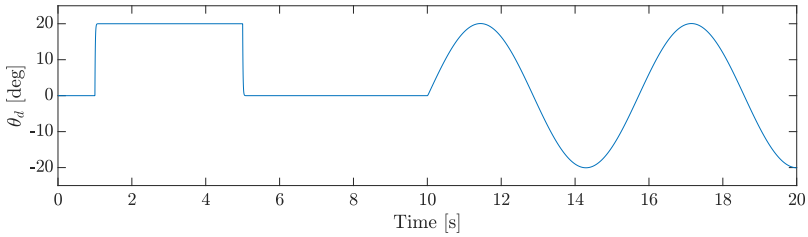

Figure 6.4: The low-pass filtered longitudinal reference signal θ_d.

Initial Conditions

The UAV model is assumed to be in an equilibrium state at the beginning of the simulation. This is achieved by defining the initial conditions of the model to be the trim conditions for a fixed-wing UAV with parameters based on the Aerosonde-model in Table 6.1. The trim conditions are found by specifying the airspeed as $V_a = V_{a_0} = 35\ \mathrm{m/s}$, which is defined in Beard and McLain (2012) as the cruise-speed for the Aerosonde model, and assuming $q = \delta_a = 0$, as well as wings-level, constant altitude flight. Then it is possible to solve an optimization problem by following a similar procedure to the one found in section F.2 in Beard and McLain (2012) to find the values of α, δ_t and δ_e that result in the sums of forces and moments acting on the UAV body being equal to zero. The initial conditions are found to be

$$\begin{aligned} \alpha_0 &= 0.0035 \text{ rad} \\ \delta_{t_0} &= 0.4638 \\ \delta_{e_0} &= -0.0494 \text{ rad} \\ \theta_0 &= \alpha_0 = 0.0035 \text{ rad}. \end{aligned}$$

6.1.3 Case Study

Two simulation cases are considered to investigate the robustness of the control algorithms applied to the longitudinal model. In the first case, the effects of wind gusts and process noise are taken into account, while the rest of the conditions are assumed to be ideal, i.e. continuous feedback signals, instant change in control input, etc. Wind gusts and process noise are also present in the second case, in addition to the measurement and actuator dynamics described in section 6.1.2. For the longitudinal model, these dynamics include the discretization of θ, q, and $\bar{\delta}_e$, and the actuator dynamics. In both cases, the control designs are implemented with the control coefficient transformation given in (5.98) where the nominal system function $b_{\theta_{nom}}$, which has a 20% uncertainty in the model parameters, is used.

The reason for investigating both these cases is that it is known that SMC algorithms are robust to external disturbances and parametric uncertainties as these effects are a part of the control design. However, for a control algorithm to be feasible in practice, it needs to be robust to unmodeled dynamics, such as discrete measurements and delays in the system. Thus, the purpose of the first case is to verify the theoretical results, and the purpose

of the second case is to investigate the control algorithms' suitability under realistic conditions. Additionally, the advantages of using the control coefficient transformation in (5.96) instead of applying the control signal directly to the UAV model are investigated for both case 1 and case 2.

A different configuration of control gains is implemented for each controller for case 1 and case 2. This is because it is possible to choose a configuration for case 1 that produces small error and input measures with little to no chattering in the control signal, while the same configuration will produce chattering in case 2.

In both cases and for all control algorithms, a fixed-step ode4 solver is used in Simulink with a time step size of $h = 0.001$ s.

6.1.4 Model Implementation

An overview of the longitudinal simulation model for the longitudinal system can be seen in Figure 6.5. The Reference-block in Figure 6.5 outputs the reference signal

$$x_{\theta_d} = \begin{bmatrix} \theta_d \\ q_d \end{bmatrix} \tag{6.12}$$

for the SMC system where θ_d and q_d are given in (6.6)-(6.10), and (6.11) respectively. The Reference-block also outputs the airspeed reference, V_{a_0}, which can be found in Table 6.1. These two reference signals are the inputs to the Control system-block, along with the measured state x_{m_θ} from the Sensor-block. In the Sensor-block, the states θ and q are sampled as previously discussed so that the measured state is given as

$$x_{\theta_m} = \begin{bmatrix} \theta^z \\ q^z \\ V_a \\ \alpha \end{bmatrix} \tag{6.13}$$

The Control system-block contains a sliding mode controller and an airspeed hold controller. These two controllers generate a control signal

$$\bar{u}_\theta = \begin{bmatrix} \bar{\delta}_e \\ \delta_t \end{bmatrix} \tag{6.14}$$

based on the discretized state x_{θ_m} and the references from the Reference-block. The control signal is sampled and low-pass filtered as previously discussed, and the resulting signal $\bar{u}^d$ is used as an input to the UAV model-block.

The UAV model-block contains the equations of motions given in (2.82)-(2.85). The other inputs to the UAV model-block are the wind gusts d_g from (6.1) and the process noise d_θ from (6.2) which are generated in the Wind gusts and disturbances-block. The output from the UAV model-block is the continuous state x_θ given by

$$x_\theta = \begin{bmatrix} \theta \\ q \\ V_a \\ \alpha \end{bmatrix} \tag{6.15}$$

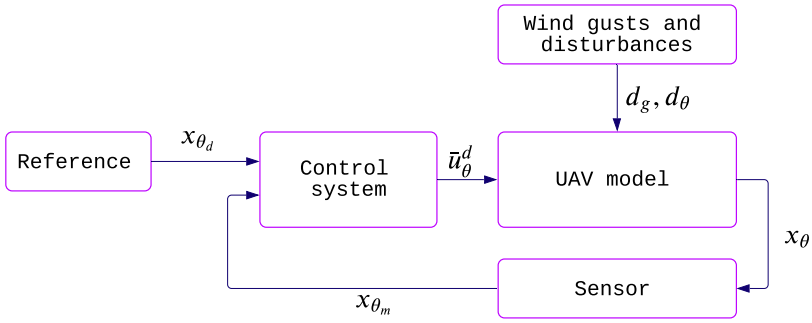

Figure 6.5: An overview of the longitudinal simulation model.

which is then discretized in the Sensor-block.

The Simulink-implementation of the longitudinal simulation model is presented in section B.1.

6.2 6DOF Simulation Model

The 6DOF simulation model is based on the model equations using quaternions (2.88)-(2.91), with parameters based on the Aerosonde-model, which can be found in Table 6.1.

As for the decoupled longitudinal model, several disturbances are added to the 6DOF UAV model (2.88)-(2.91), which are described in subsection 6.2.1. The simulation setup for the 6DOF model is described in subsection 6.2.2. In subsection 6.2.3 the case study for the 6DOF model is presented, while subsection 6.2.4 presents the Simulink-implementation of the system.

6.2.1 Disturbances and Unmodeled Dynamics

Wind

As mentioned in subsection 2.4.4, the Dryden-model in Matlab (MathWorks, 2020b) generates two 3-dimensional signals, $\mathbf{v}_{w_g}^b$ and ω_w^b. The signal $\mathbf{v}_{w_g}^b$ mimics the wind gusts that act on the UAV body, and ω_w^b models the effect of the wind on the angular moment. The aerodynamic coefficients (2.74)-(2.77) are calculated based on the relative airspeed $\mathbf{v}_r^b$ and relative moment ω_r^b instead of using the components of $\mathbf{v}_b$ and ω_b directly.

Process Noise

As discussed in subsection 2.4.2, a time-varying disturbance $d(t)$ is added to the forces f_a and the moments m_a as in (2.51)-(2.52). The signal $d(t)$ is given by (2.54), where the time constant T_d is chosen as $T_d = 0.7$ s, and $\mathrm{w}_d \in \mathbb{R}^{6\times 1}$ is band-limited white noise with noise power 3 N$\cdot 1/\sqrt{\text{Hz}}$ for $i = 1, 2, 3$ or 3 Nm$\cdot 1/\sqrt{\text{Hz}}$ for $i = 4, 5, 6,$. The signal that is generated by (2.54) can be seen in Figure 6.6.

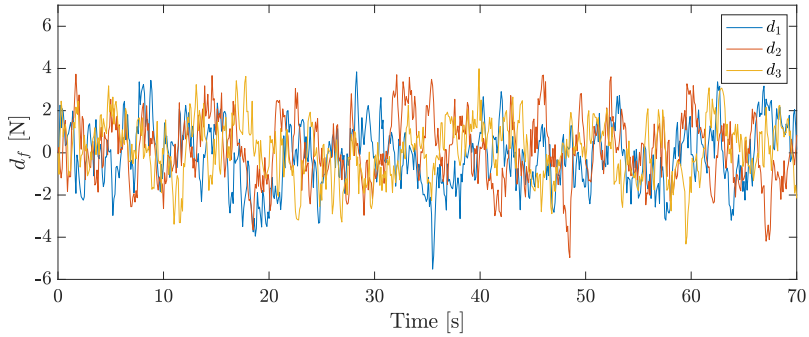

(a) The disturbances in the aerodynamic forces, d_f.

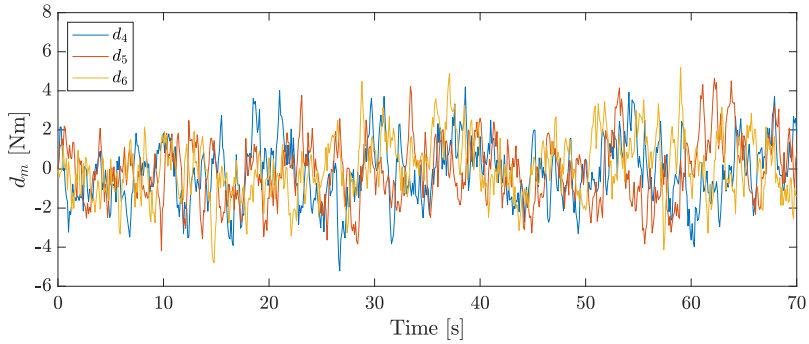

(b) The disturbances in the aerodynamic moments, d_m.

Figure 6.6: The process noise in the 6DOF simulation model.

Discrete Measurements

As discussed in the previous section, there is a discrepancy between the ideal system used to develop the control algorithms in chapter 3, and the physical system that the algorithms are actually used to control. One of these discrepancies is the fact that the state is assumed to be continuous in the control design, while the measurement of the continuous state used in the control design is actually discrete.

The states that have to be discretized in the 6DOF model are the angular position states given by Θ, the angular rates in ω_b, and the airspeed V_a. When the 6DOF model is simulated with a measured state instead of a continuous one, the signals Θ, ω_b, and V_a are sampled with a sampling frequency of $f_s = 200$ Hz. The effect of the choice of sampling frequency is investigated in chapter 8.

Actuator Dynamics

In addition to the state measurements used for feedback control discussed in the previous paragraph, the control signal $\bar{u}$ is also, in reality, a discrete signal. Additionally, there are unmodeled actuator dynamics present in the system, which also need to be accounted

for. As for the longitudinal simulation model described in subsection 6.1.1, actuator dynamics are also present in the 6DOF simulation model. When simulating the 6DOF model with unmodeled dynamics, the control signal generated by the SMC algorithms, $\bar{u}_{smc} = [\bar{\delta}_a, \bar{\delta}_e, \bar{\delta}_r]^\top$, is filtered by

$$\dot{\bar{u}}^d_{smc} = -\frac{1}{T_u}\bar{u}^d_{smc} + \frac{1}{T_u}\bar{u}^z_{smc} \tag{6.16}$$

where $\bar{u}^d_{smc}$ is the control signal that is the input to the 6DOF model, and $\bar{u}^z_{smc}$ is the control signal that is sampled from the continuous control $\bar{u}_{smc}$ with a sampling frequency of $f_s = 200$ Hz. Here, $T_u = 0.0154$ s based on the approximation in subsection 6.1.1. The throttle dynamics are generated by (6.3).

The effect of the choice of actuator dynamics is investigated in chapter 8, where the dynamics above are considered, in addition to the actuator dynamics 6.16 with a higher time-constant and the second-order dynamics described in Bøhn et al. (2019).

6.2.2 Simulation Setup

Reference Trajectory

The reference trajectory for the 6DOF model is produced by a waypoint following navigation and guidance system. The waypoints the UAV should follow are given by a set of waypoints $\mathbf{w}_i$ denoted $\mathcal{W}$, which is in this report defined as a set of five waypoints given by

$$\mathcal{W} = \begin{bmatrix} 0 & 0 & 100 \\ 500 & 0 & 85 \\ 500 & 500 & 75 \\ 0 & 500 & 90 \\ 0 & 0 & 100 \end{bmatrix}, \tag{6.17}$$

where each row is the position of a waypoint in $[\mathrm{m}]$ so that the columns of $\mathcal{W}$ are the x-, y-, and z-coordinates of the waypoints in the NED-frame. The waypoint follower system is implemented with the MATLAB UAV Waypoint Follower-block (MathWorks, 2020d), which outputs the desired height h_d and the desired course angle χ_d based on the pose (the position and heading) of the UAV and on the next waypoint $\mathbf{w}_i$. These commands are used to calculate the desired pitch and roll references.

The desired altitude h_d is used by an altitude hold controller, which is a PI-controller described in Beard and McLain (2012), to generate a desired pitch angle θ_d, and is given by

$$\begin{aligned} \theta_d &= k_{p_h}\mathrm{sat}(h_d - h) + k_{i_h}\int_0^t \mathrm{sat}(h_d - h)\, d\tau, \\ \mathrm{sat}(h_d - h) &= \begin{cases} h_d - h, & |h_d - h| \leq h_{lim} \\ h_{lim}\mathrm{sign}(h_d - h), & |h_d - h| > h_{lim}, \end{cases} \end{aligned} \tag{6.18}$$

where h is the current altitude. Note that there is a limit on the error in height so that the pitch reference does not become too large. In this report, this limit is set to $h_{lim} = 5\,\mathrm{m}$.

The desired course command from the waypoint follower system is used to calculate the desired roll angle ϕ_d, based on the current course and flight path angles, and the ground velocity of the UAV. First, the current course and flight path angles are calculated as

$$\gamma_f = \sin^{-1}(-\frac{v_z}{V_g}) \tag{6.19}$$

$$\chi = \texttt{atan2}(\frac{v_y}{v_x}), \tag{6.20}$$

where v_x, v_y and v_z are the components of in the inertial x-, y-, and z-directions, respectively. The calculation of γ_f in (6.19) is based on (2.19), where we have used that $h = -p_d$, where p_d is the z-position in the NED-frame (not to be confused with the desired roll rate described below). Note that the Matlab-function `atan2` (MathWorks, 2020c) is used in (6.20) to calculate the course angle instead of the normal inverse tangen in (2.20). Based on γ_f and χ, the desired roll angle can be calculated as

$$\phi_d = \texttt{atan2}\left(\frac{V_g \texttt{angdiff}(\chi, \chi_d)}{g\cos(\chi - \psi)}\right), \tag{6.21}$$

where the Matlab-function $\texttt{angdiff}(\nu_1, \nu_2)$ (MathWorks, 2020a), which calculates the difference between two angles ν_1 and ν_2 wrapped in the interval $[-\pi, \pi]$, is used to calculate the difference between χ and χ_d.

The desired roll and pitch rates in the inertial frame, $\dot{\phi}_d$ and $\dot{\theta}_d$, respectively, are approximated by high pass filtering ϕ_d and θ_d:

$$\begin{bmatrix}\dot{\phi}_d \\ \dot{\theta}_d\end{bmatrix} = \frac{s}{T_\Theta s + 1}\begin{bmatrix}\phi_d \\ \theta_d\end{bmatrix}, \tag{6.22}$$

where $T_\Theta = 0.01$ s. The desired yaw rate in the inertial frame, $\dot{\psi}_d$, is found from the equation for the coordinated-turn (Beard and McLain, 2012), which is given by

$$\dot{\psi}_d = \frac{g}{V_a}\tan\phi_d. \tag{6.23}$$

The derivatives, $\dot{\Theta}_d = [\dot{\phi}_d, \dot{\theta}_d, \dot{\psi}_d]^\top$, of the desired Euler angles are then used to calculate the desired angular rates ω_d by inverting (2.23) so that

$$\omega_d = \begin{bmatrix}p_d \\ q_d \\ r_d\end{bmatrix} = \begin{bmatrix}1 & 0 & -\sin\theta_d \\ 0 & \cos\phi_d & \sin\phi_d\cos\theta_d \\ 0 & -\sin\phi_d & \cos\phi_d\cos\theta_d\end{bmatrix}\dot{\Theta}_d. \tag{6.24}$$

Using the angle rate reference ω_d in the MIMO control design and $\dot{\Theta}_d$ in the SISO control design discussed in chapter 5 as described above is one way of performing reference tracking. Another method is to treat the angle references as a series of constant reference values, which means that the angle rate references can be set to zero, i.e. $\omega_d = \dot{\Theta}_d = 0$. The differences between using the angle rate references defined in (6.22)-(6.24) and using a zero angle rate reference for the 6DOF model is investigated in chapter 8.

The final reference signal to the control system is the desired airspeed V_{a_0} which is set to the cruise-speed for the Aerosonde-model, i.e. $V_{a_0} = 35\ \mathrm{m/s}$ (Beard and McLain, 2012). Finally, the full reference vector x_d is defined as

$$x_d = \begin{bmatrix} \Gamma_d \\ \omega_d \\ V_{a_0} \end{bmatrix} \in \mathbb{S}^2 \times \mathbb{R}^3 \times \mathbb{R}, \tag{6.25}$$

where Γ_d is given by

$$\Gamma_d = \begin{bmatrix} -\sin\theta_d \\ \cos\theta_d \sin\phi_d \\ \cos\theta_d \cos\phi_d \end{bmatrix}. \tag{6.26}$$

Initial Conditions

As in the simulations of the longitudinal model, it is assumed that the UAV is in an equilibrium state at the beginning of the simulation of the 6DOF model. The initial position of the UAV is set to

$$p_0 = \begin{bmatrix} h_0 \\ 0 \\ 0 \end{bmatrix} = \begin{bmatrix} -100 \\ 0 \\ 0 \end{bmatrix},$$

where h_0 is the initial altitude in [m]. The initial airspeed is set to the cruise speed of the Aerosonde-model, i.e. $V_{a_0} = 35$ m/s. The initial AoA, throttle and elevator deflection are found by calculating the trim conditions of the UAV assuming $\omega_b = \delta_a = \delta_r = 0$. This means that the initial control is

$$\bar{u}_0 = \begin{bmatrix} \bar{\delta}_{t_0} \\ \bar{\delta}_{a_0} \\ \bar{\delta}_{e_0} \\ \bar{\delta}_{r_0} \end{bmatrix} = \begin{bmatrix} 0.4638 \\ 0 \\ -0.0494 \\ 0 \end{bmatrix},$$

while the initial angular velocity ω_{b_0} is

$$\omega_{b_0} = \begin{bmatrix} 0 \\ 0 \\ 0 \end{bmatrix},$$

and the initial velocity $\mathbf{v}_{b_0}$ of the UAV is

$$\mathbf{v}_{b_0} = \begin{bmatrix} V_{a_0} \cos\alpha_0 \\ 0 \\ V_{a_0} \sin\alpha_0 \end{bmatrix} = \begin{bmatrix} 34.9998 \\ 0 \\ 0.1212 \end{bmatrix}$$

which is calculated based on the initial AoA, $\alpha_0 = 0.0035$ rad. Furthermore, the initial Euler angles are

$$\Theta_0 = \begin{bmatrix} 0 \\ \alpha_0 \\ 0 \end{bmatrix} = \begin{bmatrix} 0 \\ 0.0035 \\ 0 \end{bmatrix}.$$

6.2.3 Case Study

The case study for the 6DOF model is more comprehensive than the longitudinal case study presented in subsection 6.1.3. To test the robustness of the control algorithms to disturbances in the system, a coefficient k_d is multiplied with the disturbance $d(t)$, and a coefficient k_w is multiplied with both the wind gusts $\mathbf{v}_{w_g}$ and the vector ω_w that accounts for the effects of the wind gusts on the angular rate of the UAV. By increasing the coefficients k_d and k_w, the amount of disturbance in the system also increases. These coefficients are used to define the different simulation cases, together with the amount of constant wind $\mathbf{v}_{w_s}$, as seen in Table 6.3.

Similarly to the case study for the longitudinal model presented in subsection 6.1.3, simulation cases both with and without unmodeled dynamics, such as discrete measurements and actuator dynamics, are considered for the 6DOF model. Thus case 1 is the simulation of the 6DOF model affected by the wind disturbances $\mathbf{v}_w$ and ω_w, and the disturbance signal $d(t)$, but without any unmodeled dynamics present in the system. Case 2 is simulating the system with the same disturbances as in case 1, but with the unmodeled dynamics described in subsection 6.2.1 present in the system. The last two cases are also simulated with unmodeled dynamics, but with more severe disturbances present in the system.

	Case 1	**Case 2**	**Case 3**	**Case 4**
Unmodeled dynamics	No	Yes	Yes	Yes
Disturbance coefficient k_d	0.5	0.5	1	1.5
Wind gust coefficient k_d	0.5	0.5	1	1.5
Constant wind vector $\mathbf{v}_{w_s}$	$[-1,\ 2,\ 0]^\top$	$[-1,\ 2,\ 0]^\top$	$[3,\ 5,\ 3]^\top$	$[7,\ -9,\ 6]^\top$

Table 6.3: The values of the disturbance coefficient k_d, the wind gust coefficient k_w, and the constant wind vector $\mathbf{v}_{w_s}$ for each of the simulation cases for the 6DOF model, in addition to which simulation cases take the unmodeled dynamics into account.

To further test the robustness of the controllers, the sampling rate of the control signal $\bar{u}$, the state x, the Euler angles Θ, and the airspeed V_a is investigated. Simulation case 2 is considered with sampling rates set to $f_s = 100$ Hz and $f_s = 20$ Hz. As discussed in subsection 6.2.1, the sampling rate is set to $f_s = 200$ Hz, which is true for simulation case 2-4 in Table 6.3. However, this is quite a high sampling rate, and it is interesting to see whether the SMC algorithms are still robust to the disturbances while managing to produce control signals without too much chattering with lower sampling rates than 200 Hz.

Furthermore, the control coefficient transformations in (5.103)-(5.104) for the single-input control algorithms, and (5.126) for the multivariable control algorithms, are implemented with a 20% uncertainty in the model parameters in all the simulation cases. The functions b_ϕ and b_θ in (5.103)-(5.104), and b in (5.126), are therefore uncertain during simulation, which further tests the robustness of the control algorithms to parameter uncertainties and modeling errors.

In all simulation cases and for all control algorithms, a fixed-step ode4 solver is used in Simulink with a time step size of $h = 0.001$ s.

6.2.4 Model Implementation

The overall structure of the 6DOF simulation model is the same as for the longitudinal model, the only difference is what the signals that are passed between the system blocks contain. An overview of the 6DOF simulation model can be seen in Figure 6.7.

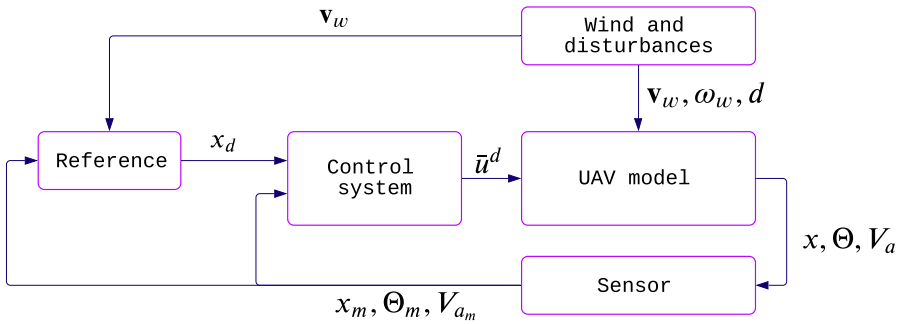

Figure 6.7: An overview of the 6DOF simulation model.

The Reference-block in the 6DOF system generates the reference vector x_d defined in (6.25). The signal from the Reference-block is, together with the measured state, Euler angles and airspeed from the Sensor-block, used as inputs to the Control system-block. The contents of the control block depend on the type of sliding mode controller that is being used, which is described in chapter 5. The complete control signal $\bar{u}$ is

$$\bar{u} = \begin{bmatrix} \delta_t \\ \bar{\delta}_a \\ \bar{\delta}_e \\ \delta_r \end{bmatrix} \text{ or } \bar{u} = \begin{bmatrix} \delta_t \\ \bar{\delta}_a \\ \bar{\delta}_e \\ \bar{\delta}_r \end{bmatrix} \tag{6.27}$$

depending on whether a SISO or a MIMO control design is being used. The control $\bar{u}$ is then measured, and low-pass filtered to create the signal $\bar{u}^d$, which is then passed to the UAV model-block.

In the Wind and disturbances-block, the process noise in the aerodynamic forces and moments, $d = [d_f, d_m]^\top$, defined in (2.54) is generated, along with the wind $\mathbf{v}_w$ and wind moment ω_w generated by the Dryden-model (MathWorks, 2020b).

In the UAV model-block, the equations for the 6DOF model defined in (2.88)-(2.91) are implemented. The resulting continuous state x given as

$$x = \begin{bmatrix} \mathbf{r} \\ \mathbf{v}_b \\ \mathbf{q} \\ \omega_b \end{bmatrix},$$

the vector Θ, and a vector containing the airdata, i.e. V_a, α, and β, are the outputs from the UAV model-block which are passed to the Sensor-block.

In the Sensor-block, the Euler angles and rates, and airspeed are measured so that the resulting signals, x_m, Θ_m and V_{a_m}, becomes

$$x_m = \begin{bmatrix} \mathbf{r} \\ \mathbf{v}_b \\ \mathbf{q} \\ \omega_b^z \end{bmatrix}, \quad \omega_b^z = \begin{bmatrix} p^z \\ q^z \\ r^z \end{bmatrix} \tag{6.28}$$

$$\Theta_m = \begin{bmatrix} \phi^z \\ \theta^z \\ \psi^z \end{bmatrix} \tag{6.29}$$

From the Sensor-block, x_m, Θ_m and V_{a_m} are passed to the Control system-block.

The Simulink-implementation of the longitudinal simulation model is presented in section B.2.

Chapter 7

Results for the Decoupled Longitudinal Model

In this chapter, the results of the decoupled longitudinal simulations for all the controllers and both simulation cases, and the choice of control gains and other control parameters, are presented and discussed. All the control gains presented in this chapter are chosen by trial and error. Furthermore, the sliding variable gain a_{θ_1} is chosen as $a_{\theta_1} = 5$ for all controllers and both simulation cases.

The results for the saturation controller is presented and discussed in subsection 7.1, for the STA in 7.2, for the ASTA in 7.3, and for the GSTA in 7.4. Subsection 7.5 contains the performance measures for the simulation results presented in subsection 7.1-7.4. The results of using different implementations of the control coefficient transformation (5.96) for the longitudinal system are shown and discussed in subsection 7.7. Finally, section 7.8 contains a discussion of the tuning process for the single-input controllers applied to the decoupled longitudinal model.

7.1 Saturation Controller

The control gain for the saturation controller for case 1 is chosen as $k_e = 17.5$, and as $k_e = 4.6$ for case 2. In both cases the size of the boundary layer is chosen as $\varepsilon = 0.1$.

The pitch and pitch rate tracking results for case 1 are presented in Figure 7.1, and the sliding variable and control signal are presented in Figure 7.2, while the tracking results, and the sliding variable and control signal for case 2 are presented in Figure 7.3 and 7.4, respectively.

The performance measures for the saturation controller for both simulation cases are shown in Table 7.1.

Case 1

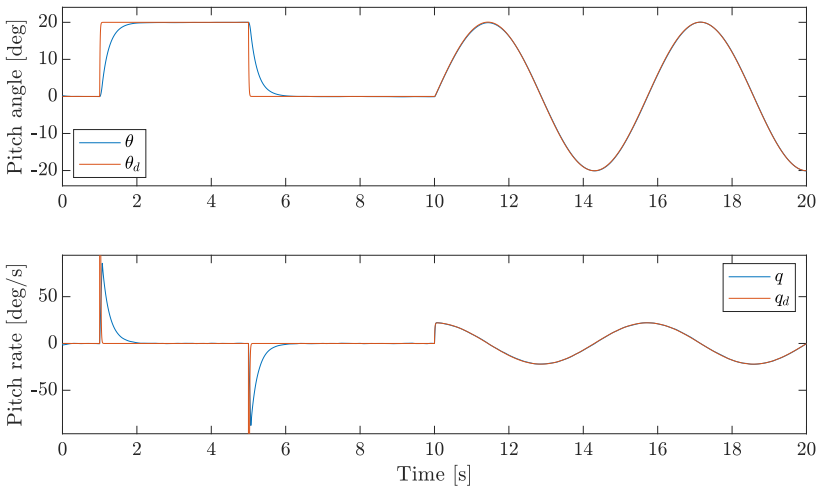

Figure 7.1: Pitch and pitch rate tracking results for the saturation controller applied to the decoupled longitudinal model for simulation case 1.

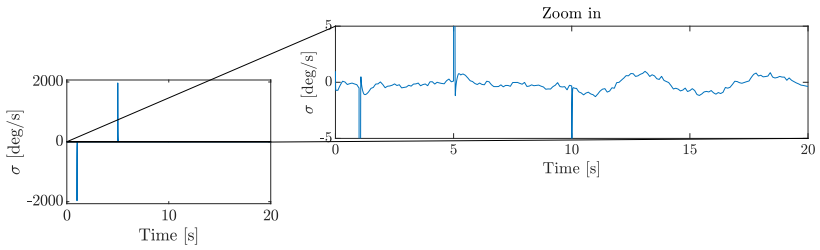

(a) The sliding variable σ_θ.

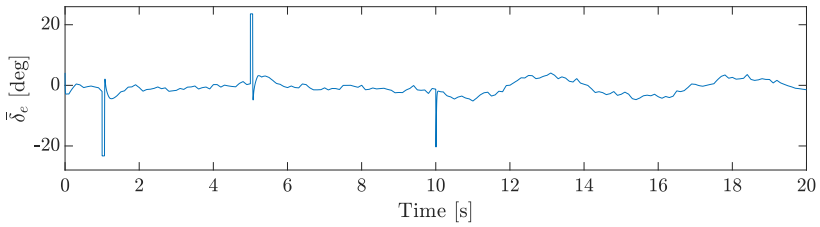

(b) The control signal δ_e.

Figure 7.2: Sliding variable and control signal for the saturation controller applied to the decoupled longitudinal model for simulation case 1.

Case 2

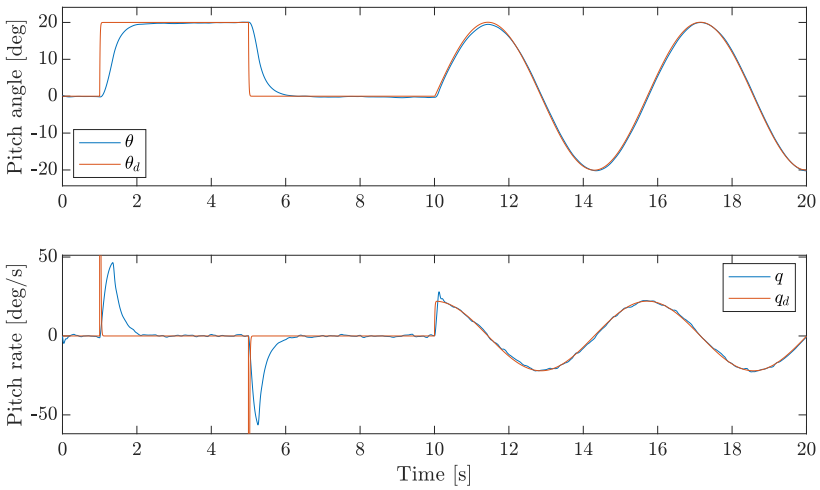

Figure 7.3: Pitch and pitch rate tracking results for the saturation controller applied to the decoupled longitudinal model for simulation case 2.

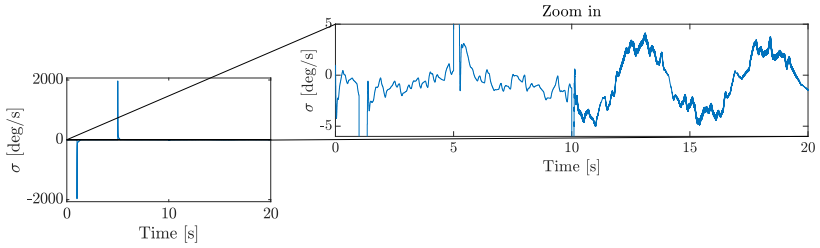

(a) The sliding variable σ_θ.

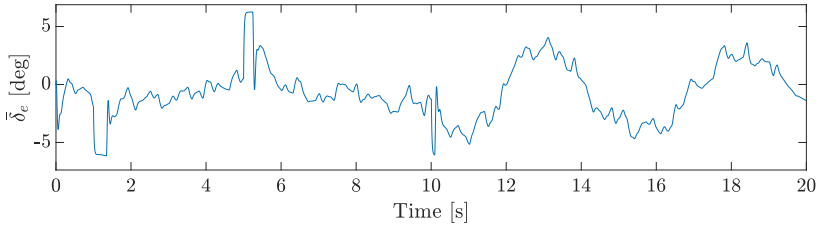

(b) The control signal δ_e.

Figure 7.4: Sliding variable and control signal for the saturation controller applied to the decoupled longitudinal model for simulation case 2.

Discussion

The saturation controller is the only conventional single-input SMC design considered in this report. Even though it is a simple algorithm, it performs well in both case 1 and case 2, as seen in Figure 7.1 and Figure 7.3. In case 1 there are some spikes in the control signal shown in Figure 7.2, which would of course not be realizable in practice due to the physical limits of the elevator. However, these spikes are gone in Figure 7.4 for case 2 when actuator dynamics are taken into consideration, and the saturation controller still manages to perform pitch angle tracking. The sliding variable in both Figure 7.2 and Figure 7.4 approaches zero rapidly but stays closer to zero for case 1 than for case 2, which is expected. Additionally, there is substantial chattering in the sliding variable for case 2 in Figure 7.4, but this chattering affects neither the control signal nor the state. This is probably due to the sampling of the control command, and the actuator dynamics which will attenuate the chattering as it is impossible for the elevator to move as rapidly as the sliding variable. This is also true for the sliding variables for case 2 for the results presented in section 7.2-7.4 below.

In chapter 5, a discussion of the necessary assumptions for the stability of the control design with the saturation controller is presented. All the assumptions are valid for the UAV model, so there is no reason the saturation controller would not be able to perform pitch angle tracking, which is corroborated by the results presented above. The control gain k_e is chosen by trial and error, rather than based on the condition in (5.76). This decision is based on the results presented for the lateral model in Griffiths (2020), where this same condition yielded results that were dominated by chattering and completely unrealizable in a physical system.

7.2 STA

The control gains for the STA for case 1 are chosen as $k_{e_1} = 20, k_{e_2} = 1$, and as $k_{e_1} = 5.3, k_{e_2} = 2.9$ for case 2.

The pitch and pitch rate tracking results for case 1 are presented in Figure 7.5 and the sliding variable and control signal are presented in Figure 7.6, while the tracking results, and the sliding variable and control signal for case 2 are presented in Figure 7.7 and 7.8, respectively.

The performance measures for the STA for both simulation cases are shown in Table 7.1.

Case 1

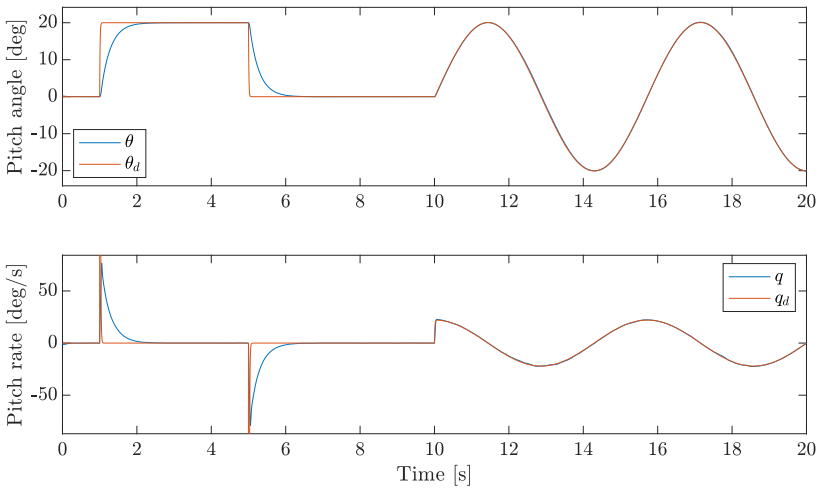

Figure 7.5: Pitch and pitch rate tracking results for the STA applied to the decoupled longitudinal model for simulation case 1.

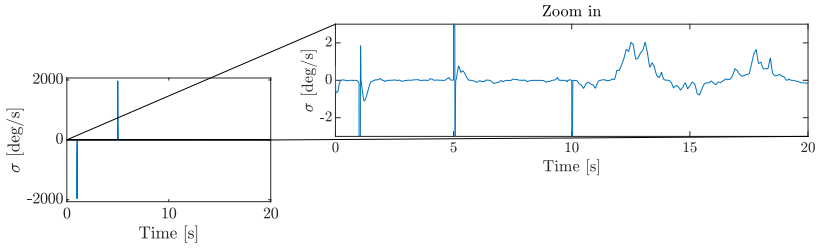

(a) The sliding variable σ_θ.

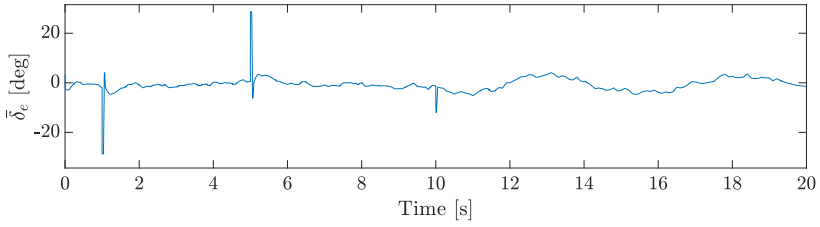

(b) The control signal δ_e.

Figure 7.6: Sliding variable and control signal for the STA applied to the decoupled longitudinal model for simulation case 1.

Case 2

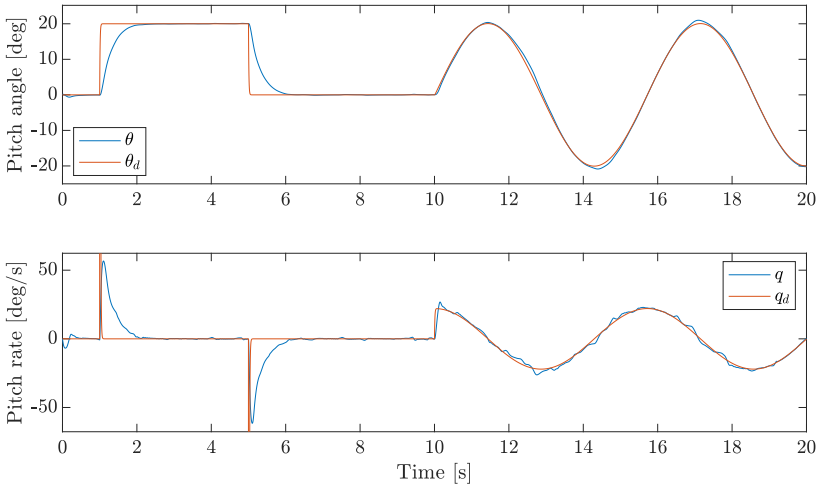

Figure 7.7: Pitch and pitch rate tracking results for the STA applied to the decoupled longitudinal model for simulation case 2.

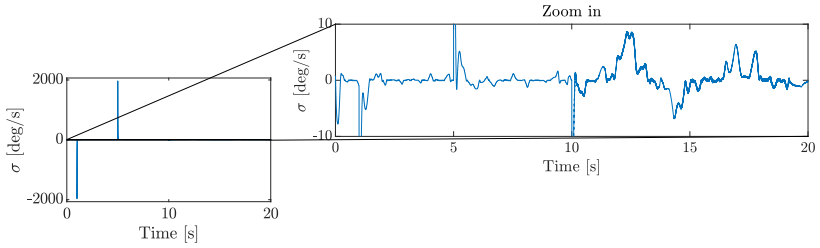

(a) The sliding variable σ_θ.

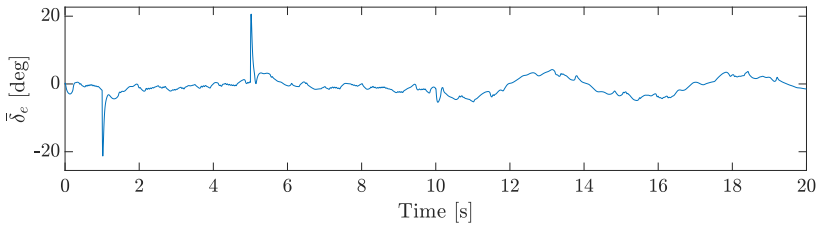

(b) The control signal δ_e.

Figure 7.8: Sliding variable and control signal for the STA applied to the decoupled longitudinal model for simulation case 2.

Discussion

The STA performs pitch angle tracking well for both case 1 and case 2 as seen by Figure 7.5 and Figure 7.7, respectively. In case 2, the STA manages to track the step inputs in the reference signal especially well, while there is some error in the continuous part of the pitch angle reference. This can be seen in Figure 7.6 and Figure 7.8, where the sliding variable is much closer to zero when the reference has been reached after the step inputs, than for the continuous part of the reference signal. The control input in both cases is free of chattering, but there are some unrealistic spikes in the control signal for both simulation cases. The necessary assumptions for the stability of the STA discussed in chapter 5 are all valid. This conclusion is reflected in the satisfactory tracking results presented in this subsection.

Several conditions for the choice of control gains for the STA are presented in subsection 3.5.1. However, the control gains for the STA presented in the results are chosen by trial and error. The reason for this is the results for the STA applied to the simplified lateral dynamics of a UAV presented in Griffiths (2020). These results show that for the control gain configurations presented in subsection 3.5.1, the resulting control signal is dominated by chattering. Therefore, the control gain configurations in subsection 3.5.1 are disregarded in this report.

7.3 ASTA

The control parameters for the ASTA for case 1 are chosen as $\omega_{e_1} = 11, \gamma_{e_1} = 2, \epsilon_e = 2, \lambda_e = 5, \alpha_{e_m} = 0.2$, and as $\omega_{e_1} = 10, \gamma_{e_1} = 0.4, \epsilon_e = 0.08, \lambda_e = 2, \alpha_{e_m} = 0.2$ for case 2. The initial value of α_e is set to $\alpha_{e_0} = 5$ for case 1 and $\alpha_{e_0} = 3$ for case 2.

The pitch and pitch rate tracking results for case 1 are presented in Figure 7.9 and the sliding variable and control signal are presented in Figure 7.10, while the tracking results and the sliding variable and control signal for case 2 are presented in Figure 7.11 and 7.12, respectively.

The performance measures for the ASTA for both simulation cases are shown in Table 7.1.

Case 1

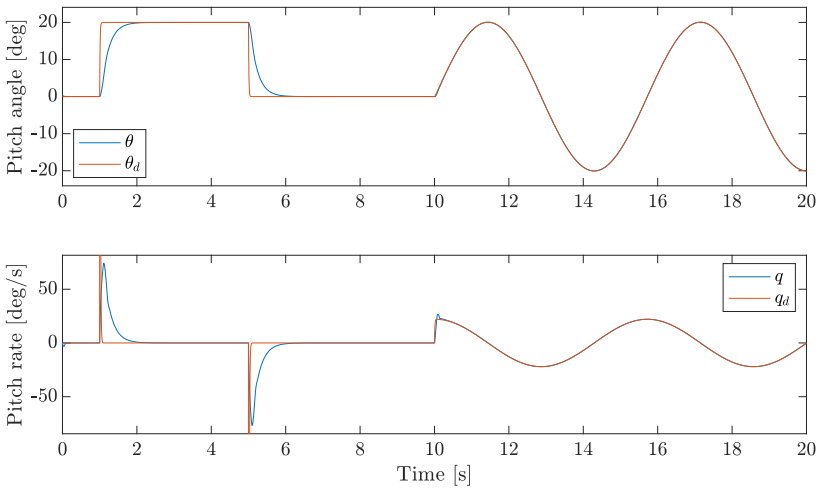

Figure 7.9: Pitch and pitch rate tracking results for the ASTA applied to the decoupled longitudinal model for simulation case 1.

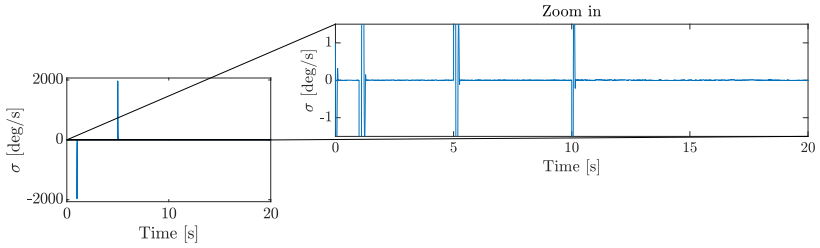

(a) The sliding variable σ_θ.

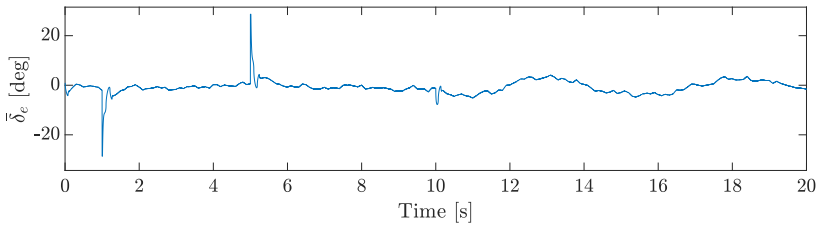

(b) The control signal δ_e.

Figure 7.10: Sliding variable and control signal for the ASTA applied to the decoupled longitudinal model for simulation case 1.

Case 2

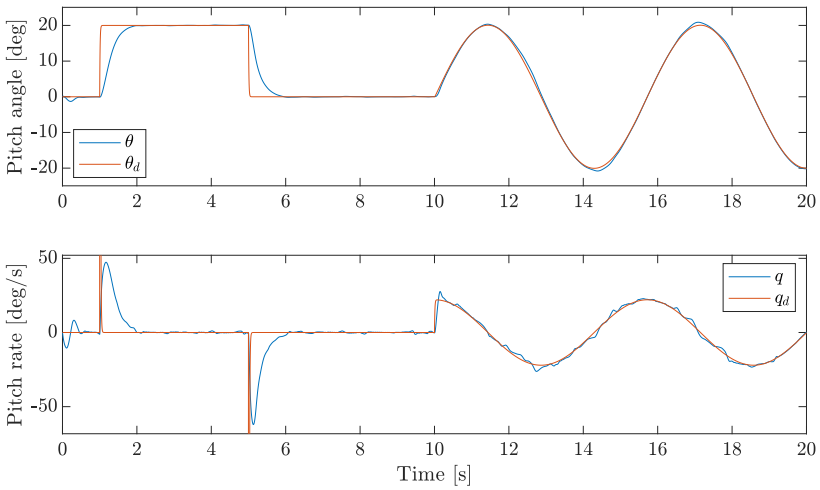

Figure 7.11: Pitch and pitch rate tracking results for the ASTA applied to the decoupled longitudinal model for simulation case 2.

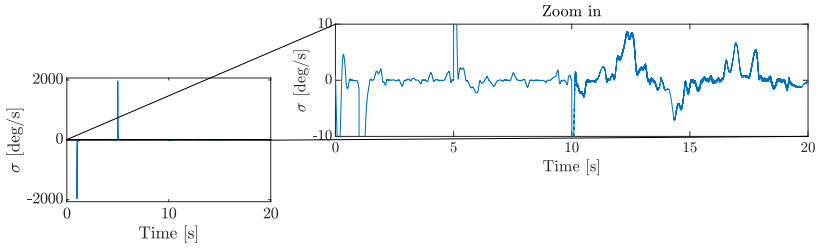

(a) The sliding variable σ_θ.

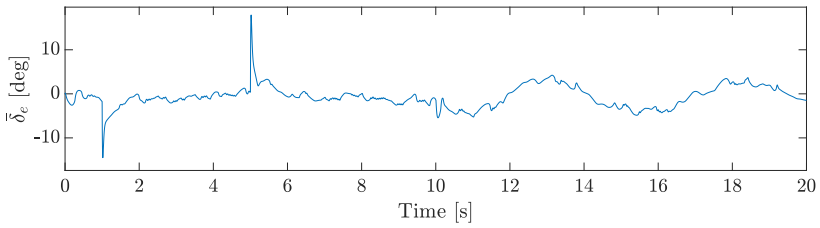

(b) The control signal δ_e.

Figure 7.12: Sliding variable and control signal for the ASTA applied to the decoupled longitudinal model for simulation case 2.

Discussion

The ASTA manages to achieve satisfactory tracking of the pitch angle reference in both simulation cases, which can be seen in Figure 7.9 and Figure 7.11. The tracking results for the continuous part of the reference signal is especially good in case 1, which is reflected in the error measures in Table 7.1. For both case 1 and case 2, the resulting control signal is free of chattering, but there are some unrealizable spikes in the control signal for case 1 and case 2 as seen in Figure 7.10 and Figure 7.12, respectively.

The sliding variable keeps almost exactly to the sliding surface in case 1 in Figure 7.10, but there are some oscillations when there is a discontinuous point in the reference signal at $t = 1$ s, $t = 5$ s, and $t = 10$ s. Even so, these large oscillations do not affect the control signal. In the results for case 2 in Figure 7.12, the sliding variable does not manage to keep the constraint as well as in case 1, which is to be expected, but the increase in the deviations from the sliding surface is quite large from case 1 to case 2.

From the discussion in subsection 5.3.3, we know that all the necessary assumptions about the system to guarantee the stability of the ASTA are valid, except for the fact that the function b_θ has to be known. In the results presented in this subsection, an uncertain $b_{\theta_{nom}}$ was used, which may account for the large increase in error measures from case 1 to case 2 for the continuous part of the pitch angle reference.

There are some small oscillations in the results for the ASTA at the beginning of the simulation in case 2. These oscillations can be removed by choosing a higher initial value α_{e_0} for the adaptive gain α_e. However, a higher value for α_{e_0} results in more chattering in the control signal throughout the simulation. A much smaller value for α_{e_0} made it possible to remove the oscillations for case 1, while there are still oscillations for case 2 with a much higher α_{e_0}. However, choosing an even higher value for α_{e_0} for case 2 removes the oscillations, but renders the control signal unfeasible due to chattering.

7.4 GSTA

The control gains for the GSTA for case 1 are chosen as $\beta_{e_g} = 0.03, k_{e_1} = 24, k_{e_2} = 15$, and as $\beta_{e_g} = 0.01, k_{e_1} = 7, k_{e_2} = 3$ for case 2.

The pitch and pitch rate tracking results for case 1 are presented in Figure 7.13 and the sliding variable and control signal are presented in Figure 7.14, while the tracking results, and the sliding variable and control signal for case 2 are presented in Figure 7.15 and 7.16, respectively.

The performance measures for the GSTA for both simulation cases are shown in Table 7.1.

Case 1

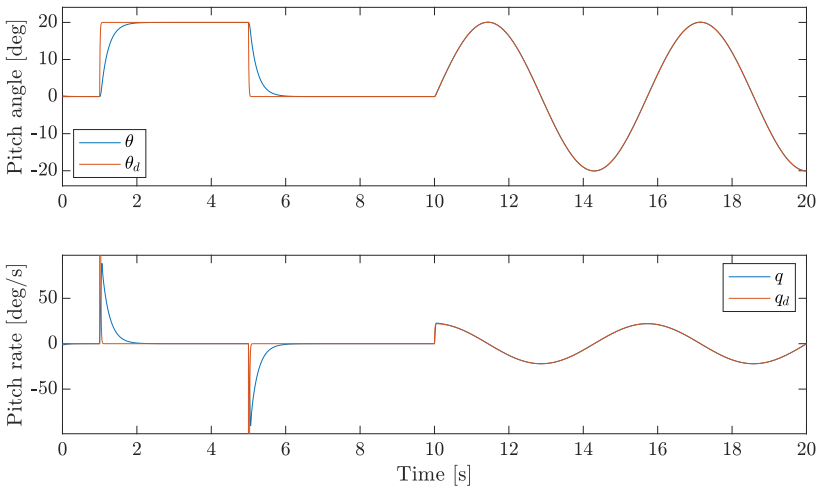

Figure 7.13: Pitch and pitch rate tracking results for the GSTA applied to the decoupled longitudinal model for simulation case 1.

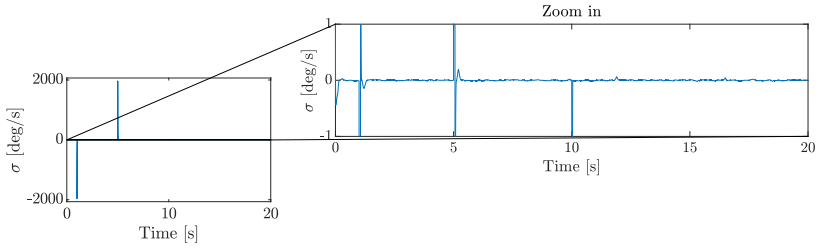

(a) The sliding variable σ_θ.

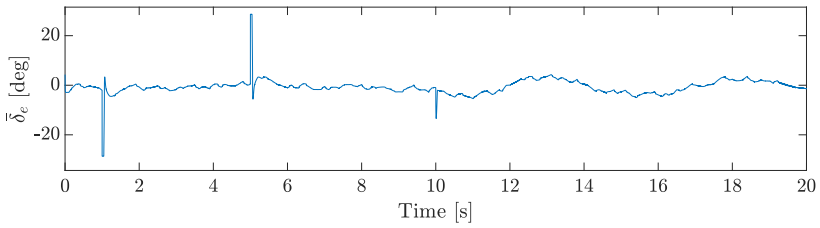

(b) The control signal δ_e.

Figure 7.14: Sliding variable and control signal for the GSTA applied to the decoupled longitudinal model for simulation case 1.

Case 2

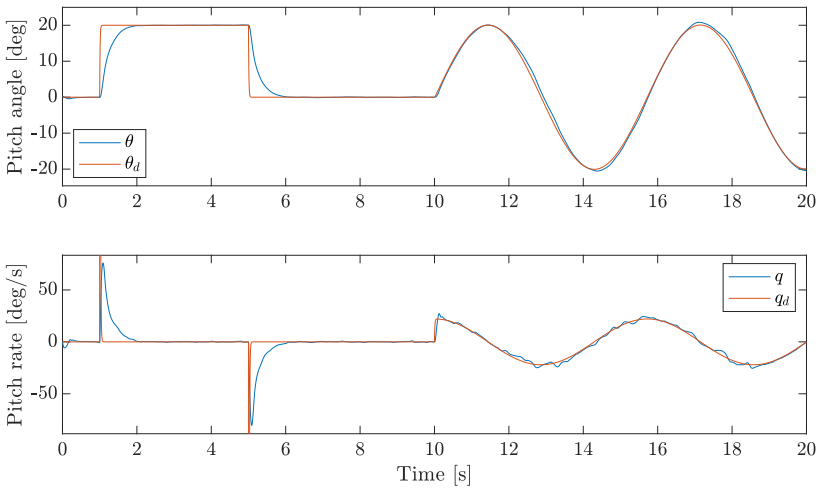

Figure 7.15: Pitch and pitch rate tracking results for the GSTA applied to the decoupled longitudinal model for simulation case 2.

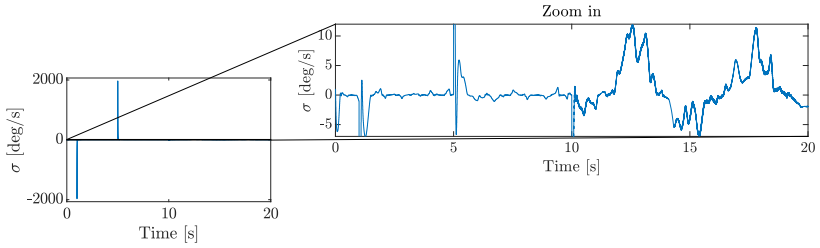

(a) The sliding variable σ_θ.

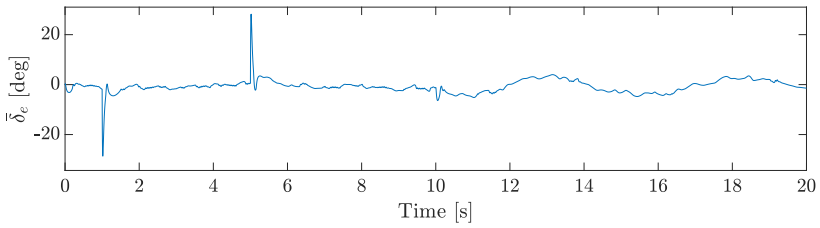

(b) The control signal δ_e.

Figure 7.16: Sliding variable and control signal for the GSTA applied to the decoupled longitudinal model for simulation case 2.

Discussion

The results for the GSTA show that it achieves fast and accurate tracking in case 1 and case 2 without chattering in the control signal which can be seen in Figure 7.13-7.16. In case 2, the tracking of the step inputs in the reference signal is somewhat better than the tracking of the continuous sine wave reference based on the increase in the error measures from case 1 to case 2, and on the difference in the sliding variable for case 1 in Figure 7.14 and for case 2 in Figure 7.16.

The good results of the GSTA reflect the fact that all the assumptions discussed in subsection 5.3.3 are valid, so it was expected that the GSTA would be able to perform pitch angle tracking, which is confirmed by the results in the figures above.

7.5 Performance Measures

The error and input measures for the simulation results presented in subsection 7.1-7.4 are presented in Table 7.1.

Values for case 1				
Error measure	**Saturation controller**	**STA**	**ASTA**	**GSTA**
Total ISE	94.517	105.048	95.826	**88.396**
Total IAE	10.490	11.675	9.088	**8.704**
ISE after stabilization	0.1018	0.230	$\mathbf{4.705 \cdot 10^{-9}}$	$4.983 \cdot 10^{-6}$
IAE after stabilization	0.7900	1.018	$\mathbf{1.597 \cdot 10^{-4}}$	$4.535 \cdot 10^{-3}$
Maximum absolute error after stabilization	0.1983	0.407	$\mathbf{6.340 \cdot 10^{-5}}$	$3.459 \cdot 10^{-3}$
Input measure	**Saturation controller**	**STA**	**ASTA**	**GSTA**
Total ISI	164.23	166.54	**145.331**	178.49
Total IAI	37.514	37.746	**37.370**	37.800
Values for case 2				
Error measure	**Saturation controller**	**STA**	**ASTA**	**GSTA**
Total ISE	193.77	132.77	137.15	**108.10**
Total IAE	20.475	16.602	**15.477**	16.122
ISE after stabilization	**1.670**	3.087	2.154	6.088
IAE after stabilization	**3.203**	3.620	3.018	5.603
Maximum absolute error after stabilization	**0.8355**	1.817	1.512	2.029
Input measure	**Saturation controller**	**STA**	**ASTA**	**GSTA**
Total ISI	**108.93**	129.49	122.32	152.87
Total IAI	**36.947**	37.677	37.863	37.727

Table 7.1: Performance measures for the single-input control algorithms applied to the decoupled longitudinal model for case 1 and case 2.

7.6 Comparison of the Controller Performance

All the controllers that are implemented for the decoupled longitudinal model produce similar results, but there are some relatively minor differences in their performances. The saturation controller has a slightly slower response to the step inputs in case 2 than the other controllers. The reason for this is that the saturation controller in case 2 requires a small

value for the control gain to avoid chattering in the control signal. However, the tracking of the continuous reference is excellent. The saturation controller manages to perform better tracking of the continuous reference than the second-order algorithms even with a lower input use, which can be seen in Table 7.1. However, the overall error measures for the whole simulation are much bigger for the saturation controller than for the second-order algorithms in case 2, which means that the saturation controller is not suitable for tracking discontinuous reference signals in the presence of external disturbances and unmodeled dynamics.

Based on Table 7.1 it is possible to see that the STA, the ASTA, and the GSTA perform better than the saturation controller in case 1. All three second-order algorithms achieve near-perfect tracking of the continuous pitch angle reference, with the ASTA being the best out of the three. The GSTA has the lowest error measures overall, while the ASTA uses the least amount of input. The fact that the error measures for the continuous part of the reference signal are close to zero, while the total error measures are higher or almost equal to the error measures for the STA, implies that the ASTA is more suited to track continuous reference signals instead of discontinuous signals such as step inputs, at least in case 1.

From Table 7.1, it is also possible to see that the GSTA has the lowest ISE in case 2, but the error measures for the continuous part of the reference are much higher than for the rest of the controller, and the IAE is slightly higher than for the STA and the ASTA. This implies that the GSTA is more suitable than the other controllers for tracking discontinuous or rapidly changing reference signals, since a low ISE means fewer large errors, while a higher IAE means that there are more small errors. This can also be seen by comparing the tracking results for case 1 in Figure 7.13 and for case 2 in 7.15, where the tracking of the continuous sine wave reference in case 2 seems to be slower than the tracking of the discontinuous reference, which is almost as good in case 2 as in case 1.

Additionally, the control signals produced by the controllers are similar in both case 1 and case 2. In case 1, they all produce control signals in which the elevator deflection instantly changes to very high or low values, which is only possible in theory. These spikes in the control signals are slightly smaller for all the controllers in case 2, due to the actuator dynamics.

Furthermore, the STA and the GSTA have almost equal ISE and IAE values for case 1. For case 2, however, the GSTA outperforms the STA in terms of ISE values. This might be due to the choice of control gains for the controllers since the STA and the GSTA have similar input use in case 1, while in case 2, the GSTA uses slightly more input than the STA. It is reasonable to think that this will make the STA slower, which is reflected in the ISE value for case 2 compared to the ISE value for the GSTA in case 2. However, this might be different if the STA was tuned differently.

A common phenomenon for all the controllers is the extremely large spikes in the sliding variable, which reach a magnitude of almost 2000 rad/s. This causes the control signals to go from zero to the maximal deflection value almost instantly, which, if implemented, will put unnecessary strain on the actuator. These spikes are caused by the discontinuous steps in the reference signal, which will cause the pitch rate to become very large and then almost instantly go back to zero again. This can be improved by using a higher-order low-pass filter on θ_r so that the q_d will be smoother. Implementing a limit on q_d may also be

beneficial, as this would enable the controller to track q_d for smaller changes in θ_r while avoiding the large sudden changes in δ_e. Another alternative that would reduce the spikes in the sliding variable is to use a zero-signal as the angle rate reference, but this will cause poorer tracking of the angle reference. The effect of using a zero-reference for the angle rate is

7.7 Control Coefficient Transformation

In this subsection, the effect of the control coefficient transformation in (5.96) on the simulation results is presented and discussed. The results of three ways of implementing the transformation in (5.96) are shown for each controller for case 2 for the discontinuous part of the reference trajectory. The reason for only showing the first step input of the reference signal is that the differences between using the different transformations for the continuous part of the reference signal are so small that they are irrelevant. The first way of implementing the transform is with only the sign of b being known. The second implementation is with a function b_θ that has a 20% uncertainty in the model parameters. The third way of implementing the transformation is with an exactly known b_θ, which is only theoretically possible. The three different transformations are given by the equations below:

(T1) The first implementation of the control coefficient transformation is

$$\bar{\delta}_e = -\delta_e,$$

(T2) the second implementation of the transformation is

$$\bar{\delta}_e = b_{\theta_{nom}}^{-1}(t,x)\delta_e,$$

where $b_{\theta_{nom}}(t,x)$ is the nominal, but uncertain, model function,

(T3) and the third implementation of the transformation is

$$\bar{\delta}_e = b_\theta(t,x)^{-1}\delta_e.$$

The results of using the control coefficients transformations in (T1)-(T3) is also investigated for case 1. Most of the tracking results and control signals for case 1 can be found in C, as they are almost identical for each transformation and are therefore not as important as the results in case 2. The one exception is the ASTA, as the results for both simulation cases are included in this section. However, all the performance measures are included in this section for both simulation cases to easily illustrate the difference between implementing the transformations for case 1 and case 2.

7.7.1 Saturation controller

The results of using the control coefficient transformations described in (T1)-(T3) in the design of the saturation controller for case 2 are shown in Figure 7.17. The performance measures can be found in Table 7.2. The control gains are chosen for the three different transformations as

(T1) $k_{e_1} = 0.13, \varepsilon = 0.1$

(T2) $k_{e_1} = 4.6, \varepsilon = 0.1$

(T3) $k_{e_1} = 4.6, \varepsilon = 0.1$

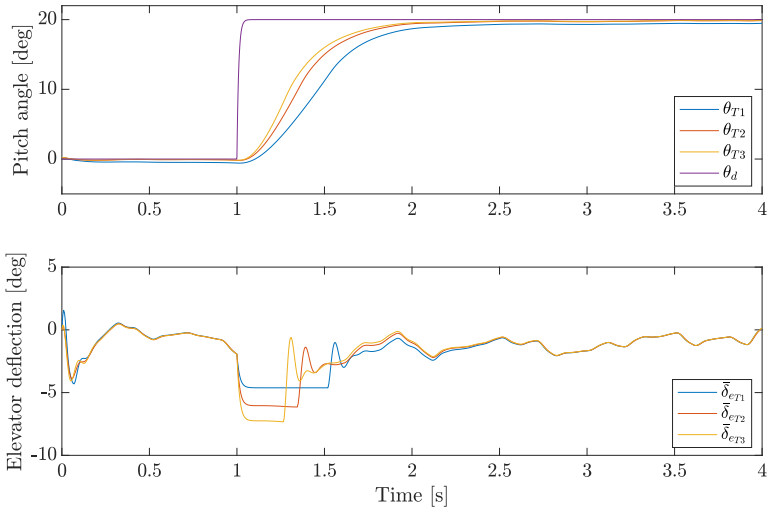

Figure 7.17: The pitch angle tracking results and control signals for the single-input saturation controller applied to the decoupled longitudinal model for case 2. The pitch angle θ_{T1} and elevator deflection $\bar{\delta}^d_{e_{T1}}$ are the results for transformation (T1), θ_{T2} and $\bar{\delta}^d_{e_{T2}}$ are the results for transformation (T2), and θ_{T3} and $\bar{\delta}^d_{e_{T3}}$ are the results for transformation (T3).

Case 1			
Performance measure	**Transformation (T1)**	**Transformation (T2)**	**Transformation (T3)**
Total ISE	47.385	47.887	**45.349**
Total IAE	4.996	4.704	**4.544**
Total ISI	$1.658 \cdot 10^5$	$\mathbf{1.500 \cdot 10^5}$	$1.793 \cdot 10^5$
Total IAI	$3.714 \cdot 10^2$	$\mathbf{3.675 \cdot 10^2}$	$3.744 \cdot 10^2$
Case 2			
Performance measure	**Transformation (T1)**	**Transformation (T2)**	**Transformation (T3)**
Total ISE	141.21	104.584	**90.670**
Total IAE	11.523	8.327	**7.415**
Total ISI	$\mathbf{5.666 \cdot 10^3}$	$6.451 \cdot 10^3$	$7.068 \cdot 10^3$
Total IAI	$3.653 \cdot 10^2$	$3.640 \cdot 10^2$	$\mathbf{3.635 \cdot 10^2}$

Table 7.2: Performance measures for the control coefficient transformations (T1)-(T3) applied in the saturation control design for simulation case 1 and 2.

Implementing either transformation (T2) or (T3) for the saturation controller is clearly beneficial based on the results presented above. In case 2, transformation (T2) and (T3) lead to less standard deviation, and faster convergence to the reference without any additional chattering in the control signal, which can be seen in Figure 7.17. The improvement in the tracking performance in case 2 is also reflected in the error measures in Table 7.2, which are smallest for transformation (T3).

In case 1, Figure C.1 shows that the results are almost identical, which confirms the theoretic robustness property of the saturation controller to disturbances and parametric uncertainties.

7.7.2 STA

The results of using the different control coefficient transformations described in (T1)-(T3) in the design of the STA for case 2 are shown in Figure 7.18. The performance measures can be found in Table 7.3. The control gains are chosen for the three different transformations as

(T1) $k_{e_1} = 0.15, k_{e_2} = 0.08$

(T2) $k_{e_1} = 5.3, k_{e_2} = 2.9$

(T3) $k_{e_1} = 5.3, k_{e_2} = 2.9$

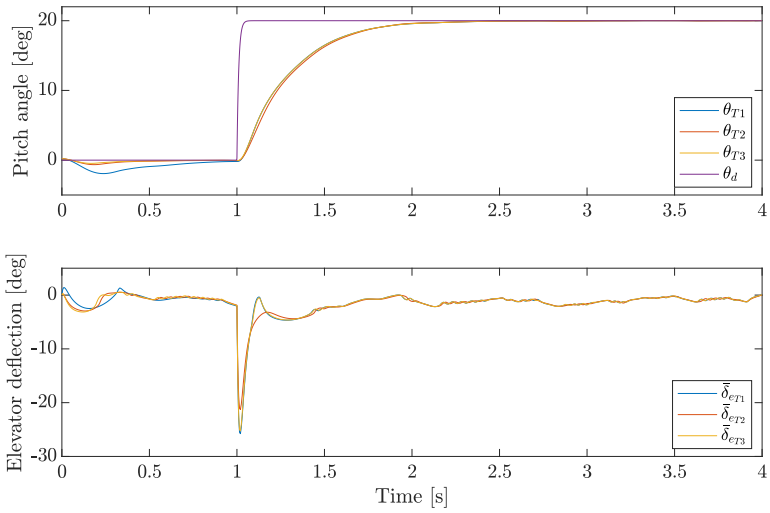

Figure 7.18: The pitch angle tracking results and control signals for the single-input STA applied to the decoupled longitudinal model for case 2. The pitch angle θ_{T1} and elevator deflection $\bar{\delta}^d_{e_{T1}}$ are the results for transformation (T1), θ_{T2} and $\bar{\delta}^d_{e_{T2}}$ are the results for transformation (T2), and θ_{T3} and $\bar{\delta}^d_{e_{T3}}$ are the results for transformation (T3).

Case 1			
Performance measure	**Transformation (T1)**	**Transformation (T2)**	**Transformation (T3)**
Total ISE	53.961	52.881	**52.530**
Total IAE	5.593	5.310	**5.282**
Total ISI	$1.626 \cdot 10^5$	$\mathbf{1.549 \cdot 10^5}$	$1.602 \cdot 10^5$
Total IAI	$3.760 \cdot 10^2$	$\mathbf{3.740 \cdot 10^2}$	$3.757 \cdot 10^2$
Case 2			
Performance measure	**Transformation (T1)**	**Transformation (T2)**	**Transformation (T3)**
Total ISE	61.710	65.271	**60.564**
Total IAE	6.612	6.208	**5.919**
Total ISI	$1.158 \cdot 10^5$	$\mathbf{9.516 \cdot 10^4}$	$1.129 \cdot 10^5$
Total IAI	$3.714 \cdot 10^2$	$3.665 \cdot 10^2$	$\mathbf{3.644 \cdot 10^2}$

Table 7.3: Performance measures for the control coefficient transformations (T1)-(T3) applied in the STA control design for simulation case 1 and 2.

For the STA, the differences between using the three transformations are minor. In case

1, the performance of all the transformations are almost the same, which can be seen in Figure C.2 and Table 7.3. In case 2, the error measures when using transformation (T3) are slightly smaller than for transformations (T1) and (T2). Furthermore, the error measures for case 2 when using transformation (T2) are actually larger than the error measures when using transformation (T1). However, Figure 7.18 shows that the controller follows the reference more closely at the beginning of the simulation when using the transformation (T2).

7.7.3 ASTA

The results of using the different control coefficient transformations described in (T1)-(T3) in the design of the ASTA for case 1 are shown in Figure 7.19. The performance measures for case 1 can be found in Table 7.4. The control gains are chosen for the three different transformations as

$$\text{(T1)} \quad \omega_{e_1} = 1, \gamma_{e_1} = 0.05, \epsilon_e = 0.05, \lambda_e = 0.1, \alpha_{e_m} = 0.2, \alpha_{e_0} = 1$$

$$\text{(T2)} \quad \omega_{e_1} = 11, \gamma_{e_1} = 2, \epsilon_e = 2, \lambda_e = 5, \alpha_{e_m} = 0.2, \alpha_{e_0} = 5$$

$$\text{(T3)} \quad \omega_{e_1} = 11, \gamma_{e_1} = 2, \epsilon_e = 2, \lambda_e = 5, \alpha_{e_m} = 0.2, \alpha_{e_0} = 5$$

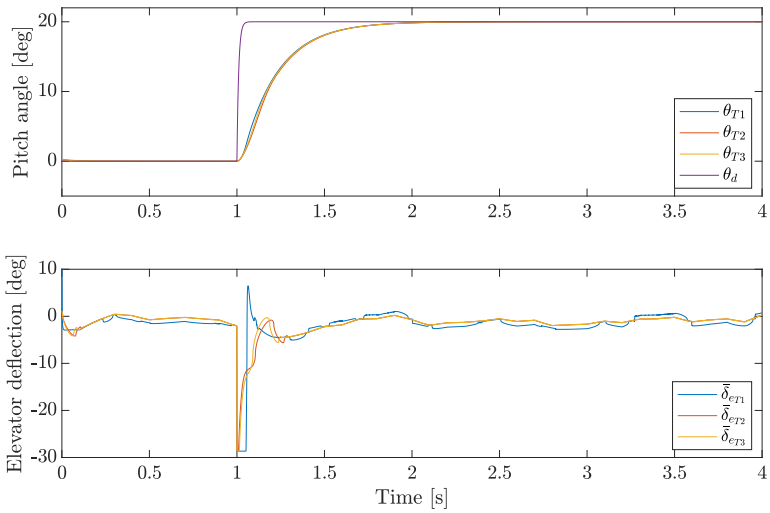

Figure 7.19: The pitch angle tracking results and control signals for the single-input ASTA applied to the decoupled longitudinal model for case 1. The pitch angle θ_{T1} and elevator deflection $\bar{\delta}_{e_{T1}}$ are the results for transformation (T1), θ_{T2} and $\bar{\delta}_{e_{T2}}$ are the results for transformation (T2), and θ_{T3} and $\bar{\delta}_{e_{T3}}$ are the results for transformation (T3).

The results of using the different control coefficient transformations described in (T1)-(T3) in the design of the ASTA for case 2 are shown in Figure 7.20. The performance measures can be found in Table 7.4. The control gains are chosen for the three different transformations as

(T1) $\omega_{e_1} = 0.6, \gamma_{e_1} = 0.01, \epsilon_e = 0.0005, \lambda_e = 0.13, \alpha_{e_m} = 0.2, \alpha_{e_0} = 0.07$

(T2) $\omega_{e_1} = 10, \gamma_{e_1} = 0.4, \epsilon_e = 0.08, \lambda_e = 2, \alpha_{e_m} = 0.2, \alpha_{e_0} = 3$

(T3) $\omega_{e_1} = 10, \gamma_{e_1} = 0.4, \epsilon_e = 0.08, \lambda_e = 2, \alpha_{e_m} = 0.2, \alpha_{e_0} = 3$

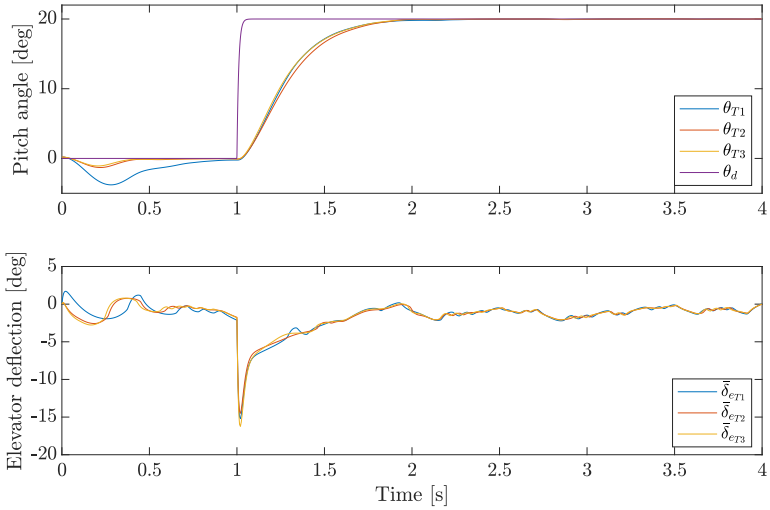

Figure 7.20: The pitch angle tracking results and control signals for the single-input ASTA applied to the decoupled longitudinal model for case 2.The pitch angle θ_{T1} and elevator deflection $\bar{\delta}^d_{e_{T1}}$ are the results for transformation (T1), θ_{T2} and $\bar{\delta}^d_{e_{T2}}$ are the results for transformation (T2), and θ_{T3} and $\bar{\delta}^d_{e_{T3}}$ are the results for transformation (T3).

Case 1			
Performance measure	**Transformation (T1)**	**Transformation (T2)**	**Transformation (T3)**
Total ISE	$\mathbf{44.434}$	48.906	46.924
Total IAE	$\mathbf{4.354}$	4.555	4.460
Total ISI	$2.000 \cdot 10^5$	$\mathbf{1.218 \cdot 10^5}$	$1.319 \cdot 10^5$
Total IAI	$4.723 \cdot 10^2$	$\mathbf{3.644 \cdot 10^2}$	$\mathbf{3.644 \cdot 10^2}$
Case 2			
Performance measure	**Transformation (T1)**	**Transformation (T2)**	**Transformation (T3)**
Total ISE	73.894	74.269	$\mathbf{67.892}$
Total IAE	7.290	6.411	$\mathbf{5.936}$
Total ISI	$8.256 \cdot 10^4$	$\mathbf{7.731 \cdot 10^4}$	$8.327 \cdot 10^4$
Total IAI	$3.793 \cdot 10^2$	$3.709 \cdot 10^2$	$\mathbf{3.708 \cdot 10^2}$

Table 7.4: Performance measures for the control coefficient transformations (T1)-(T3) applied in the ASTA control design for simulation case 1 and 2.

In case 1, the tracking results in Figure 7.19 show that all three control coefficient transformations achieve almost identical tracking of the reference, but the control signals are different. This difference in control signal between (T1), and (T2) and (T3) may be due to the different configuration of control gains, as (T2) and (T3) have the same control gains, and produce similar control signals. The similarity of the tracking results in case 1 can also be seen by the error measures in Table 7.4.

In case 2, there is some difference in the performance measures presented in Table 7.4 for the transformations. Transformation (T3) has the lowest error measures, while (T2) has the largest. However, (T2) also uses the least amount of input, which may explain the slightly higher error measures. The fact that there is an improvement in using transformation (T3) in case 2 may be because of the assumption that b_θ is in fact known in the control design, which would explain the difference between using the transformations (T1) and (T2), and the transformation (T3). Additionally, the results in Figure 7.20 show that the tracking results for transformations (T2) and (T3) follows the reference signal more closely than the result for transformation (T1).

7.7.4 GSTA

The results of using the different control coefficient transformations described in (T1)-(T3) in the design of the GSTA for case 2 are shown in Figure 7.21. The performance measures can be found in Table 7.5. The control gains are chosen for the three different transformations as

(T1) $\beta_{e_g} = 0.0001, k_{e_1} = 0.25, k_{e_2} = 0.01$

(T2) $\beta_{e_g} = 0.01, k_{e_1} = 7, k_{e_2} = 3$

(T3) $\beta_{e_g} = 0.01, k_{e_1} = 7, k_{e_2} = 3$

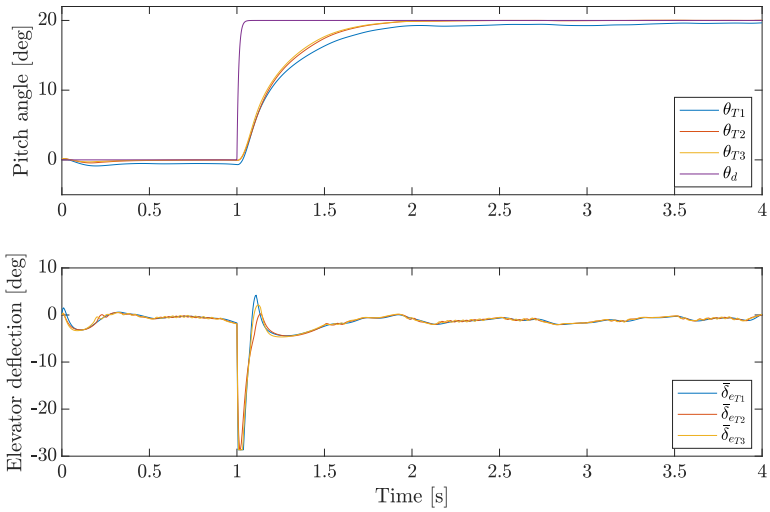

Figure 7.21: The pitch angle tracking results and control signals for the single-input GSTA applied to the decoupled longitudinal model for case 2.The pitch angle θ_{T1} and elevator deflection $\bar{\delta}^d_{e_{T1}}$ are the results for transformation (T1), θ_{T2} and $\bar{\delta}^d_{e_{T2}}$ are the results for transformation (T2), and θ_{T3} and $\bar{\delta}^d_{e_{T3}}$ are the results for transformation (T3).

Case 1			
Performance measure	**Transformation (T1)**	**Transformation (T2)**	**Transformation (T3)**
Total ISE	44.735	44.502	**44.427**
Total IAE	4.391	4.364	**4.361**
Total ISI	$\mathbf{1.701 \cdot 10^5}$	$1.744 \cdot 10^5$	$1.804 \cdot 10^5$
Total IAI	$\mathbf{3.728 \cdot 10^2}$	$3.744 \cdot 10^2$	$3.880 \cdot 10^2$
Case 2			
Performance measure	**Transformation (T1)**	**Transformation (T2)**	**Transformation (T3)**
Total ISE	57.945	51.227	**48.213**
Total IAE	7.322	4.997	**4.738**
Total ISI	$1.625 \cdot 10^5$	$\mathbf{1.338 \cdot 10^5}$	$1.545 \cdot 10^5$
Total IAI	$3.801 \cdot 10^2$	$\mathbf{3.650} \cdot 10^2$	$3.721 \cdot 10^2$

Table 7.5: Performance measures for the control coefficient transformations (T1)-(T3) applied in the GSTA control design for simulation case 1 and 2.

For the GSTA, the results of the transformations are almost identical in case 1, which can be seen from Table 7.5 and Figure C.3. In case 2, there is a more noticeable difference between the transformations, with the error measures for transformation (T3) being lower than for the other transformations, and the error measures for transformation (T1) being the highest. Even so, the responses for case 2 are quite similar which can be seen in Figure 7.21. However, the controller performs better tracking of the reference for transformations (T2) and (T3), which can be seen in Figure 7.21, where the controller using the (T1) transformation does not reach the reference value as fast as the two other signals.

7.8 Tuning of the Single-Input Controllers

The above discussion of and comparison between the controllers presented in section 7.1-7.6 is based on control gain configurations chosen through trial and error. This means that some algorithms may have a more optimal control gain configuration than others, which means that the basis of the discussion above may be unfair. The process of choosing control gains is both difficult and time-consuming, and it is difficult to determine whether the current configuration could be better. This means that algorithms that are difficult to tune will probably end up with a less optimal control gain configuration than an algorithm that is easy to tune. Additionally, some algorithms may give similar results for completely different sets of control gains, which further complicates the tuning process.

Both the saturation controller and the STA have only one or a few control gains and are easy to tune. However, in case 2, the saturation controller proved to be prone to chattering

in the control signal, and it is difficult to determine when the control signal is smooth enough, which may account for the poor error measures for the saturation controller in case 2. The STA, on the other hand, proved to be easy to tune, and performs well for a larger range of control gain values than the saturation controller.

Tuning the ASTA is an especially time-consuming process, even though the control gains are adaptive. Several parameters have to be chosen in the update laws for the adaptive gains, which complicates the design. Additionally, the threshold value α_{e_m} in the update rule for the adaptive gain α_e, and the initial value α_{e_0} have to be chosen. With a larger threshold value, the control signal is smoother, but naturally, this means that there is a pretty substantial loss in accuracy. The initial value α_{e_0} is also an important parameter that has to be chosen carefully. A small initial value would make the oscillations at the beginning of the simulation in case 2, which can be seen in Figure 7.11, even larger. However, choosing a value for α_{e_0} that is too large will increase the chattering in the control signal substantially for the entirety of the simulation.

The GSTA is an example of a control algorithm that can perform satisfactory reference tracking for multiple different configurations of the control gains. This both simplifies and complicates the tuning process as it is easy to produce good results, but it is also difficult to determine the most optimal gain configuration.

Furthermore, in the control coefficient transformations in section 7.7, there is a difference in the tuning process for the control algorithms. Ideally, it would be possible to choose one control gain configuration for each algorithm for the transformation (T1) in which only the sign of the control coefficient is known, and then scale the configuration by the airspeed V_a when using the other transformation in (T2). This is convenient since it would then be possible to produce the same results for a range of different airspeeds. However, this kind of scaling of the control gains is only possible for some of the algorithms considered in this report. The saturation controller and the STA both give similar results for (T1) and (T2) when their control gain configuration is scaled by the airspeed reference V_{a_0}, while the ASTA and the GSTA do not.

Chapter 8

Results for the 6DOF Model

In this chapter, the simulation results for the SISO and MIMO control designs are presented and discussed. The reason for combining the results and the discussion is that the simulation results are extensive, as they include many control designs and also investigate several aspects of the designs. Therefore, this chapter is used to illustrate the overall performance of the different SISO and MIMO control designs, as well as their similarities and differences, rather than showing the simulation results of each control design separately. Additionally, several factors in the modeling of the system are investigated, such as the sensitivity of the control designs to actuator dynamics and modeling errors.

In section 8.1, the effect of using two different types of angular rate reference signals is investigated. The results for the SISO and MIMO control designs are presented and discussed in section 8.2 and section 8.3, respectively, for simulation case 1 and 2. A comparison between the SISO and MIMO results for case 1 and case 2 is then made in section 8.4. Then, the simulation results for case 3 and case 4 for only some of the SISO and MIMO control designs are presented and discussed in section 8.5. The same SISO and MIMO designs are then used to investigate the sensitivity of the designs to the modeling of the actuator dynamics and to the choice of sampling frequency in section 8.6 and 8.7, respectively. Section 8.8 briefly investigates the effect of removing the modeling errors from the simulation model. Finally, the importance of the discontinuous terms in the MSTA and the GMSTA designs is investigated in section 8.9.

8.1 The Effect of the Angular Rate Reference

In this section, the effect of using either the angular rate reference ω_d generated by (6.24) or a zero angular rate reference for the MIMO GMSTA control design is investigated. The tracking results and the generated control signals for simulation case 2 when using a zero angular rate reference are presented in Figure 8.1, and the results when using an angular rate reference $\omega_d \neq 0$ are presented in Figure 8.2.

The GMSTA design performs satisfactory tracking of the roll and pitch references in both Figure 8.1a and Figure 8.2a. When using a non-zero angular rate reference, the

GMSTA also manages to follow the angular rate references, which can also be seen in Figure 8.2a. There are some differences between the two tracking results, as the tracking performance for a non-zero ω_d is slightly better than the performance when $\omega_d = 0$. This comes at a cost, however, as the control commands when $\omega_d = 0$ are smoother than for $\omega_d \neq 0$, which can be seen by comparing Figure 8.1b and Figure 8.2b. Even though there are some spikes in the control signals when $\omega_d = 0$, they are much smaller in size than the spikes in the control signals when $\omega_d \neq 0$, which almost reach the maximal and minimal deflection values several times during the simulation. This might be due to the way the angular rate reference is generated, as a discontinuity in the angle reference will result in a very large angular rate reference. This means that even though the tracking results are better for $\omega_d \neq 0$ than for $\omega_d = 0$ in theory, this might not be the case in reality as the control signals in Figure 8.2b are unrealizable in a physical system.

Even though only the results for the GMSTA design for case 2 are presented here, they are representative of the results for the other MIMO control designs and simulation cases, as well as the SISO control designs. Therefore, the rest of the results are generated when using a zero angular rate reference $\omega_d = \dot{\Theta}_d = 0$.

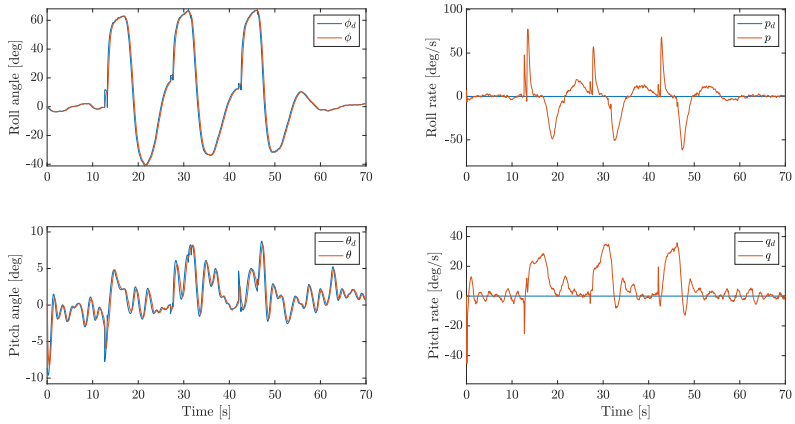

(a) Tracking of the roll and pitch references, and the roll and pitch rate references.

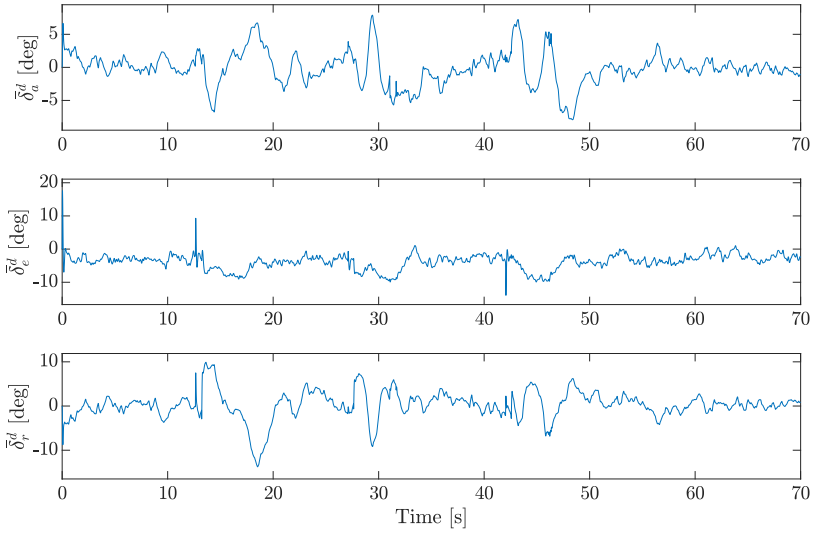

(b) The control input.

Figure 8.1: The simulation results for the MIMO GMSTA for case 2 when $\omega_d = 0$.

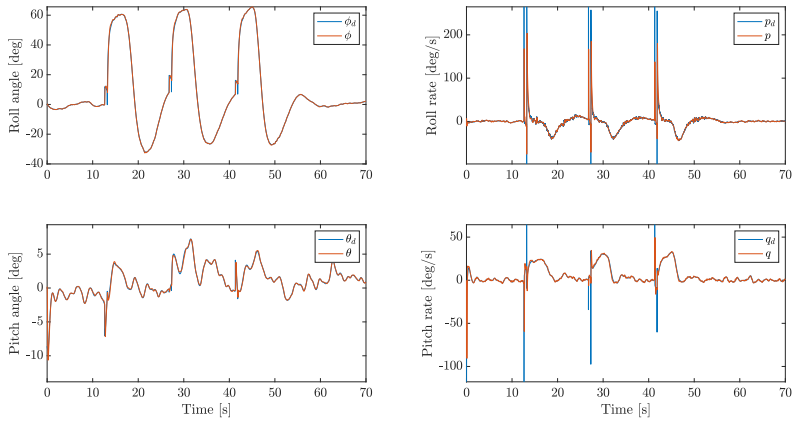

(a) Tracking of the roll and pitch references, and the roll and pitch rate references.

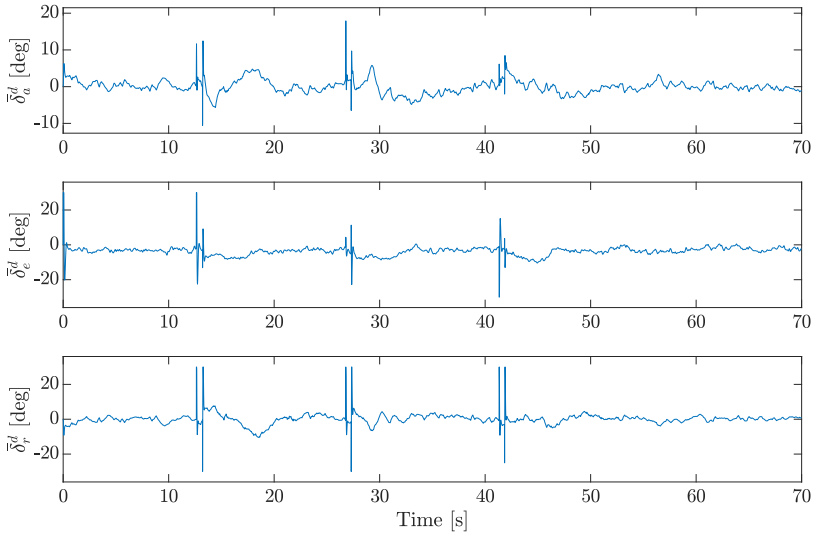

(b) The control input.

Figure 8.2: The simulation results for the MIMO GMSTA design for case 2 when $\omega_d \neq 0$.

8.2 The SISO Control Designs for Case 1 and Case 2

8.2.1 The Tracking Performance

All the SISO control designs can perform satisfactory tracking of the reference signal and reach all the waypoints in the waypoint set $\mathcal{W}$ (6.17), which can be seen in Figure 8.3 for

case 2. The resulting flight paths for case 1 are very similar, with slightly fewer oscillations in the pitch angle, and can be seen in subsection D.1.1.

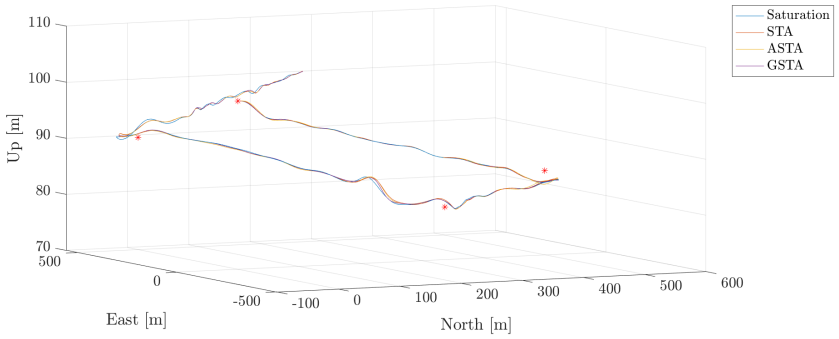

(a) North-East-Up view of the flight paths.

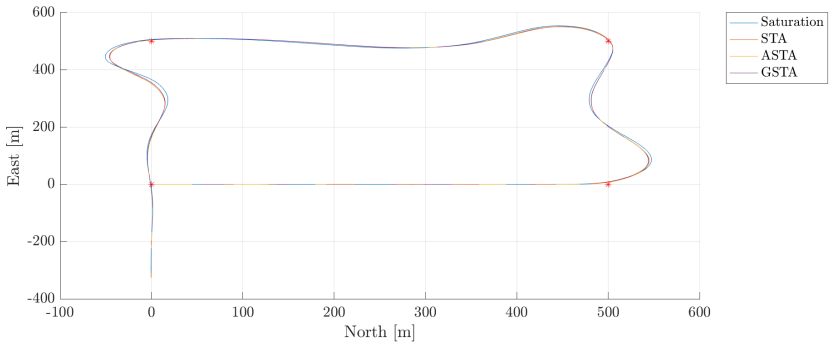

(b) North-East view of the flight paths.

Figure 8.3: The flight paths of all the SISO algorithms for case 2.

The control gains and other parameters for all control designs and for both simulation case 1 and 2 are chosen by trial and error with the goal of achieving approximately the same input use for all the algorithms. The choice of control gains and system parameters can be found in section D.2.

Even though the flight paths in Figure 8.3 are very similar, there are some small differences between the behavior of the control designs. Firstly, the second-order algorithms, i.e. the STA, the ASTA, and the GSTA, all follow approximately the same path in the North-East-plane, while the flight path of the saturation control design is slightly different. That does not necessarily mean that the overall performance of the saturation control design is worse than those of the STA and its extensions, but it is interesting to see that all the second-order methods generate a similar flight path, while the first-order saturation controller produces a slightly different one.

When looking at the flight path in the North-East-Up view in Figure 8.3a, it is possible to see some minor differences between the second-order algorithms, which can also be seen in the performance measures presented in Table 8.1 for simulation case 2. The per-

formance measures are similar, with the GSTA performing slightly better than the other

Simulation case 1				
Performance measure	**Saturation Controller**	**STA**	**ASTA**	**GSTA**
Total ISE	$1.056 \cdot 10^3$	$1.121 \cdot 10^3$	$9.896 \cdot 10^2$	$\mathbf{9.860 \cdot 10^2}$
Total IAE	$1.666 \cdot 10^2$	$1.586 \cdot 10^2$	$1.553 \cdot 10^2$	$\mathbf{1.529 \cdot 10^2}$
Total ISI	$1.429 \cdot 10^3$	$1.392 \cdot 10^3$	$\mathbf{1.377 \cdot 10^3}$	$1.392 \cdot 10^3$
Total IAI	$2.949 \cdot 10^2$	$2.895 \cdot 10^2$	$\mathbf{2.890 \cdot 10^2}$	$2.907 \cdot 10^2$
Simulation case 2				
Performance measure	**Saturation Controller**	**STA**	**ASTA**	**GSTA**
Total ISE	$1.152 \cdot 10^3$	$1.157 \cdot 10^3$	$1.162 \cdot 10^3$	$\mathbf{1.016 \cdot 10^3}$
Total IAE	$1.766 \cdot 10^2$	$1.543 \cdot 10^2$	$1.567 \cdot 10^2$	$\mathbf{1.541 \cdot 10^2}$
Total ISI	$1.439 \cdot 10^3$	$1.396 \cdot 10^3$	$\mathbf{1.392 \cdot 10^3}$	$1.401 \cdot 10^3$
Total IAI	$2.959 \cdot 10^2$	$2.902 \cdot 10^2$	$\mathbf{2.894 \cdot 10^2}$	$2.910 \cdot 10^2$

Table 8.1: The performance measures for the SISO control designs, which includes the saturation controller, the STA, the ASTA, and the GSTA designs, for simulation cases 1 and 2.

algorithms. However, by comparing the tracking results for the ASTA and the GSTA designs in Figure 8.4 it is clear that in practice, the differences in error measures are almost impossible to distinguish without quantifying them with the error measures, as the tracking results for the ASTA and the GSTA designs are almost the same. Overall, however, the difference between the two designs are enough to be able to see some small differences in the flight paths in Figure 8.3.

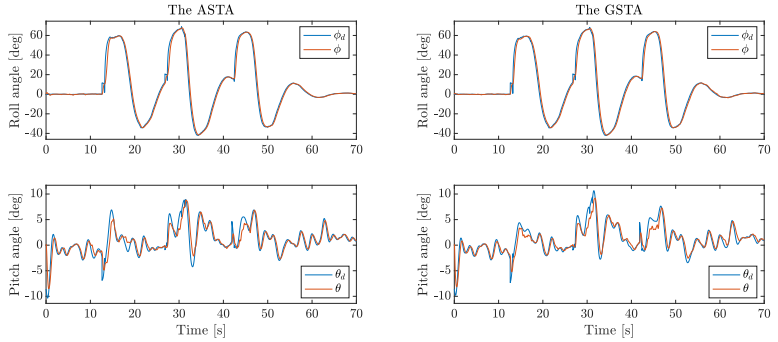

Figure 8.4: The tracking results for the ASTA and GSTA designs for simulation case 2.

The GSTA is the algorithm with the smallest error measures in both case 1 and case 2. The tracking results and control inputs generated by the GSTA design in case 1 and case 2 are shown in Figure 8.5, where it is again possible to see that such a small difference in error measures is almost unnoticeable. This, however, speaks to the robustness of the GSTA design to unmodeled dynamics. There is a small difference in the control signals produced by the GSTA in case 1 and case 2; the large spikes in the control signal for case 1 have been somewhat attenuated by the actuator dynamics. This is a phenomenon that is discussed further in the next subsections.

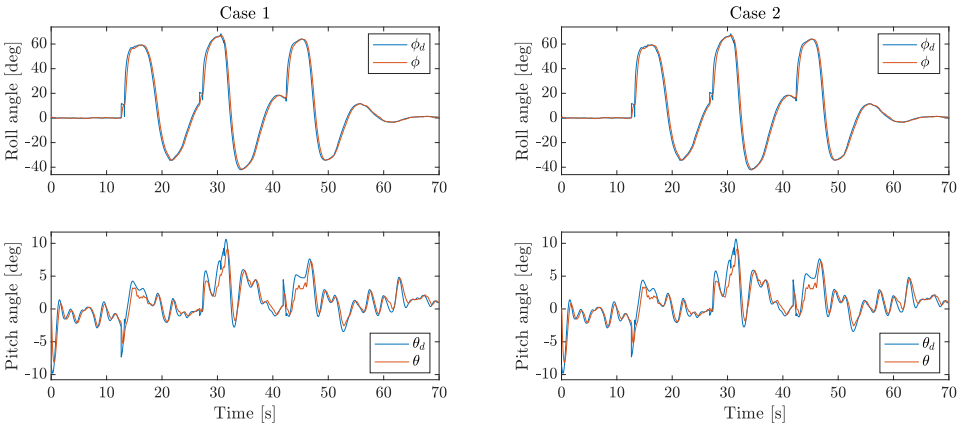

(a) The tracking results for the GSTA design.

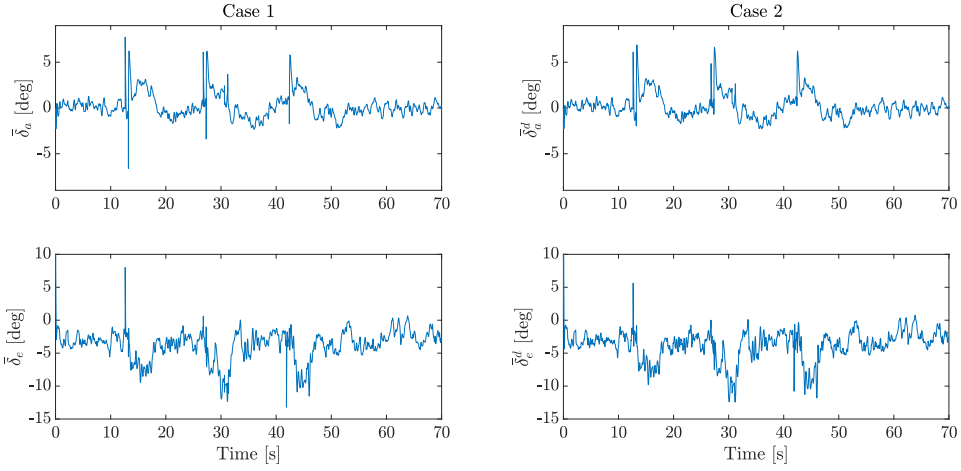

(b) The control input generated by the GSTA design.

Figure 8.5: A comparison of the tracking performance and control input for the GSTA design for case 1 and case 2. The control input $\bar{u}$ is the control input generated by the control system in case 1 which is also the input to the UAV model since actuator dynamics and measurements are disregarded in case 1. The control input $\bar{u}^d$ is the control input to the UAV model in case 2, and is affected by the actuator dynamics (6.16) and measurements.

The comparison between the tracking performance of the ASTA and the GSTA designs for case 2, which is presented in Figure 8.4, can be seen as a testimony to the robustness of the saturation controller, the STA, and the ASTA control designs. The ASTA design has the highest error measures for case 2 and the highest increase in error measures from case 1 to case 2. However, it still performs satisfactorily in case 2. This means that the performances of the other controllers are also acceptable. As the difference in performance between the ASTA and the GSTA designs for case 2, which is presented in Figure 8.4, is minimal despite a difference in error measures, it is a testimony to the robustness of the saturation controller, the STA and the GSTA control designs to unmodeled dynamics. This is because their increases in performance measures from case 1 to case 2 are much smaller than the increase for the ASTA design, which is still able to perform attitude tracking despite having the largest error measures for case 2, as well as the largest increase from case 1 to case 2.

8.2.2 Sliding Variable

The objective of SMC design is to drive the sliding variable to zero, which in the case of the SISO control designs means to drive the system to the sliding surfaces $\sigma_a = \sigma_e = 0$. All the control designs drive the sliding variables toward zero, but there are some differences in how well the control designs manage to keep the system in the sliding mode.

The error measures for the ASTA and the GSTA designs are almost identical for case 1, which can be seen in Table 8.1, so it is reasonable to believe that the two control designs should have similar sliding variables or at least sliding variables that overall have the same magnitude. This is confirmed by Figure 8.6, where we can see that the ASTA is better than the GSTA at driving the lateral sliding variable to zero and enforcing the sliding mode for the lateral dynamics, while the GSTA is better than the ASTA at enforcing the sliding mode in the longitudinal dynamics. Thus, it makes sense that the overall error measures are very similar for the ASTA and the GSTA designs.

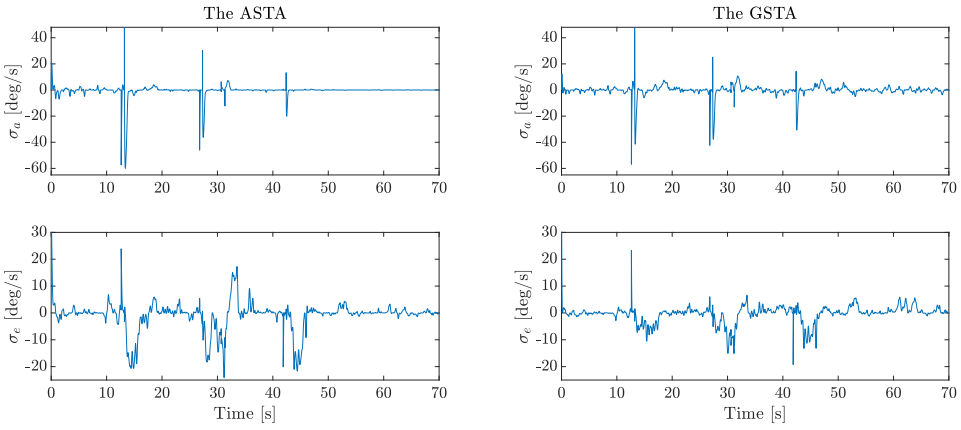

Figure 8.6: The sliding variables for the ASTA and the GSTA designs for case 1.

The sliding variables for case 1 are similar for the saturation and the GSTA control

designs, and for the STA and ASTA designs. The STA and the ASTA designs enforce the sliding mode in the lateral dynamics better than the saturation and the GSTA designs with less oscillations and smaller amplitudes of the deviance of σ_a from zero. However, for the longitudinal dynamics, the saturation and the GSTA control designs are better at keeping the sliding variable from growing too large, while the STA and the ASTA designs are still better at enforcing the sliding mode once the sliding surface has been reached. For all the control designs it seems that the longitudinal dynamics are more sensitive and prone to chattering and oscillations in the control input $\bar{\delta}_e$ than the lateral dynamics and control input $\bar{\delta}_a$.

For case 2, there is more chattering in the control surface, which is caused by the actuator dynamics and the fact that the control designs now use a measured state instead of the actual continuous state. The difference in the sliding variable from case 1 to case 2 is shown for the saturation and the ASTA control designs in Figure 8.7.

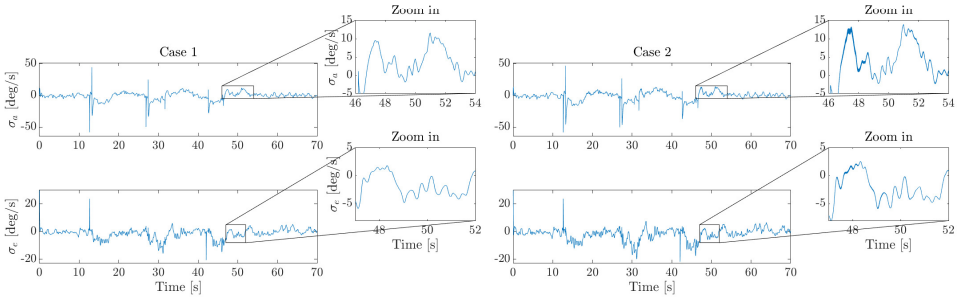

(a) The sliding variables for the saturation control design.

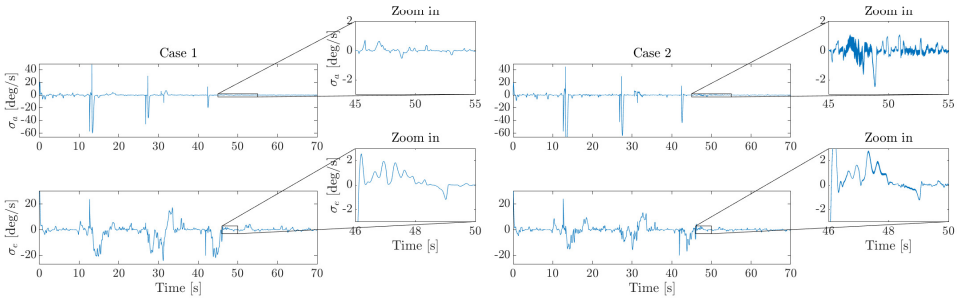

(b) The sliding variables for the ASTA design.

Figure 8.7: A comparison of the sliding variables generated for case 1 and case 2 for the saturation and the ASTA control designs.

In Figure 8.7 we can see that neither the sliding variables for the saturation design nor those for the ASTA design contain chattering. However, for case 2, there is a significant increase in chattering in the sliding variables, especially in the lateral sliding variable σ_a.

Additionally, there are more oscillations in the sliding variables for case 2 than for case 1 for both controllers, which is as expected. As we will see in the next subsection, chattering in the sliding variable does not necessarily mean that there is more chattering in the control input.

8.2.3 Control Input

The control commands are similar for all control designs and for simulation case 1 and case 2. As for the sliding variables, the input generated by the saturation control design is similar to the one generated by the GSTA design, and the control input for the STA design is similar to that of the ASTA design. The fact that the control designs with similar sliding variables produce similar control inputs is as expected.

The control inputs for simulation case 1 tend to have large spikes, such as the ones that appear in the control inputs generated by the longitudinal control design discussed in the previous chapter but have smaller and fewer oscillations. In the control inputs generated in case 2, these large spikes are attenuated by the actuator dynamics, but there are slightly more small high-frequent oscillations in the control signals, which reflect the increase in oscillations in the sliding variables described in the previous subsection. The increase in oscillations from case 1 to case 2 is also visible in the input use measures in Table 8.1, which are slightly higher for case 2 than for case 1. The control inputs generated by the saturation and the STA designs for case 1 and case 2 can be seen in Figure 8.8. The results for the saturation and the STA control designs highlight the attenuation of the spikes, and the oscillations in case 2 compared to case 1. As discussed for the longitudinal model in the previous chapter, these spikes in the control signal are not realizable in practice, and therefore give a better result during simulations than would be the case in reality. Furthermore, it seems that the saturation control design, and the GSTA design which produces a similar control input, are more prone to these spikes than the STA and the ASTA designs.

An important thing to note is that it is necessary to re-tune the control gains and system parameters from case 1 to case 2, as the control gains for case 1 cause too much chattering in case 2 for the control input to be feasible. In most cases, the tuning of the control gains for case 2 is less aggressive than for case 1. An exception of this is the GSTA, which has the same control gain configuration for both case 1 and case 2, something that speaks to the robustness of the GSTA design as it also has the lowest error measures for both case 1 and case 2. Additionally, the control gain configurations for the longitudinal dynamics have to be chosen less aggressively than the lateral control gain configurations, as the longitudinal dynamics are more sensitive to the disturbances that are present in the system, so that $\bar{\delta}_e$ is generally less smooth than $\bar{\delta}_a$ in both case 1 and case 2.

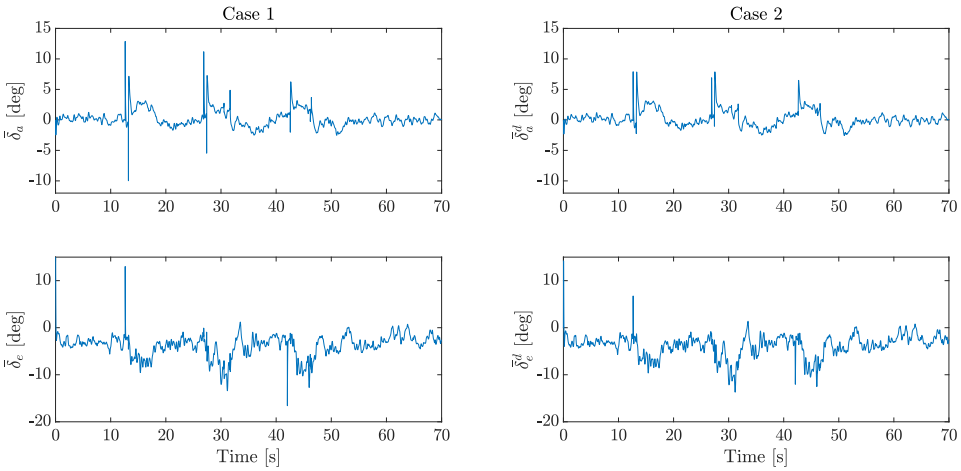

(a) The control input generated by the saturation control design.

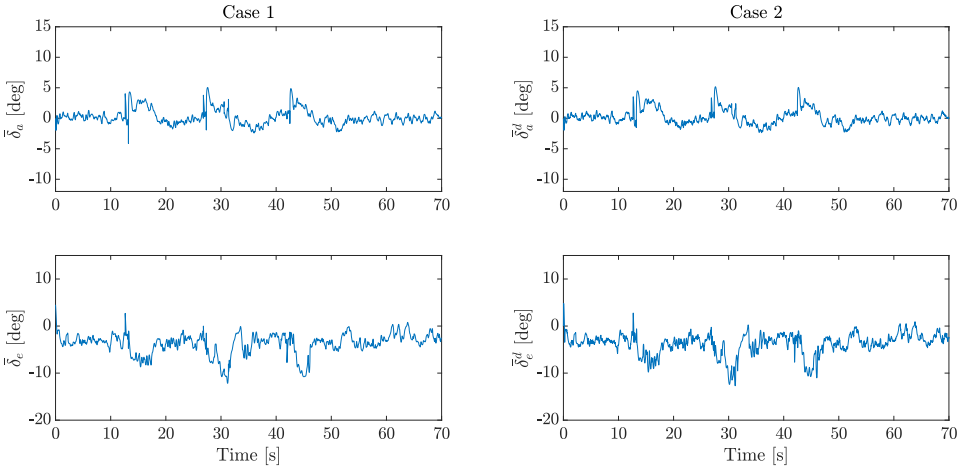

(b) The control input generated by the STA design.

Figure 8.8: A comparison of the control inputs generated for case 1 and case 2 for the saturation and the STA control designs.

For case 2, it is interesting how the increased chattering in the sliding variables discussed in the previous section affects the control signals. In Figure 8.9 the commanded control signals that are generated by the sliding mode controllers, $\bar{u}$, and the actual control input to the model, $\bar{u}^d$ (6.16), after actuator dynamics and measurements are presented for the ASTA and the GSTA.
In Figure 8.9 it is clear that the measurements and the actuator dynamics significantly attenuate the chattering in the commanded control signal caused by the chattering in the sliding surface. However, the ASTA is more sensitive to this chattering than the GSTA, and some chattering remains in the control input to the UAV model which is shown in Figure

8.9. Additionally, it can be seen in Figure 8.9a that $\bar{\delta}_e^d$ is affected more by chattering than $\bar{\delta}_a^d$, even though there is more chattering in $\bar{\delta}_a$ than in $\bar{\delta}_e$ and the longitudinal control gains are much smaller than the lateral control gains, which can be seen in Table D.1.

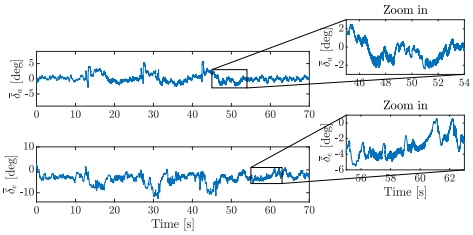

(a) The control command generated by the ASTA design.

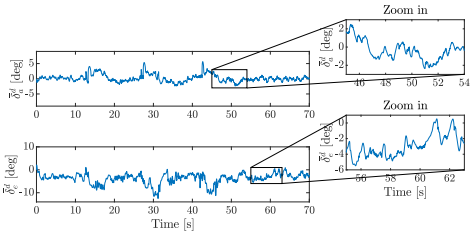

(b) The control input generated by the ASTA control design.

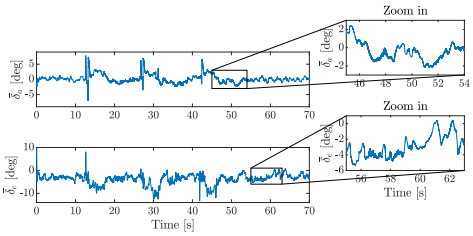

(c) The control command generated by the GSTA control design.

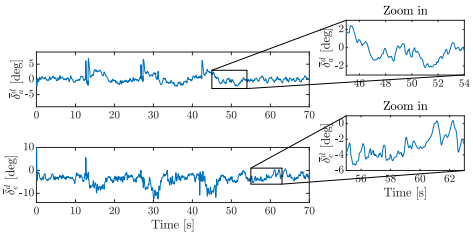

(d) The control input generated by the GSTA control design.

Figure 8.9: A comparison of the commanded control signal $\bar{u}$ generated for the ASTA and the GSTA control designs and the resulting control input to the UAV model $\bar{u}^d$ for case 2.

8.3 The MIMO Control Designs for Case 1 and Case 2

8.3.1 The Tracking Performance

The MIMO control designs, which include the MSAT, the MSTA, the AMSTA, and the GMSTA, are all capable of following the waypoints in the waypoint set for both simulation case 1 and case 2. The flight paths for all the control designs for case 2 are shown in Figure 8.10.

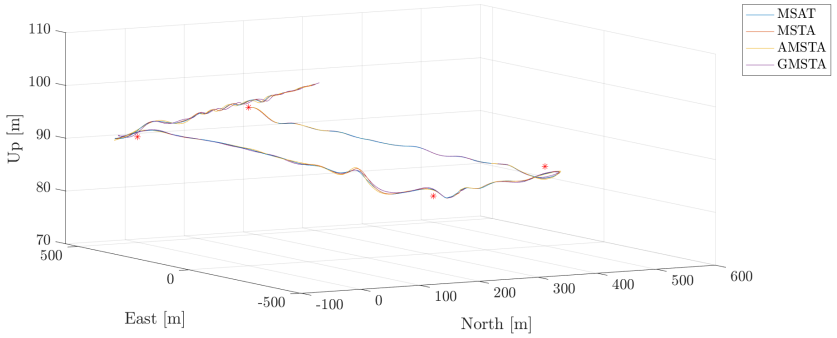

(a) North-East-Up view of the flight paths.

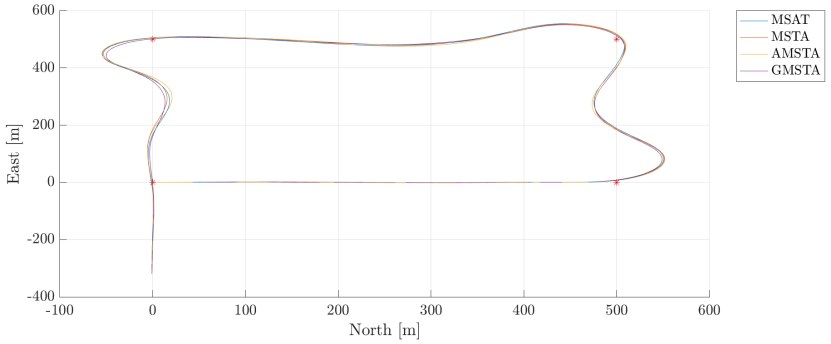

(b) North-East view of the flight paths.

Figure 8.10: The flight paths of all the MIMO algorithms for case 2.

and the flight paths for case 1 are shown in subsection D.1.

The control gains for the MIMO control designs are chosen by trial and error while trying to achieve approximately the same input use for all the control algorithms in each simulation case. The choice of control gains and other parameters can be found in subsection D.2.2 for case 1 and case 2.

The flight paths for case 1 are all very similar to each other, while Figure 8.10 shows that in case 2, the flight paths are still very similar, except for the flight path of the AMSTA, which is slightly different from the rest. This can be seen in the tracking results for case 2 in Figure 8.11, where the MSTA and the AMSTA have similar performances for case 1, with the AMSTA performing only slightly better.

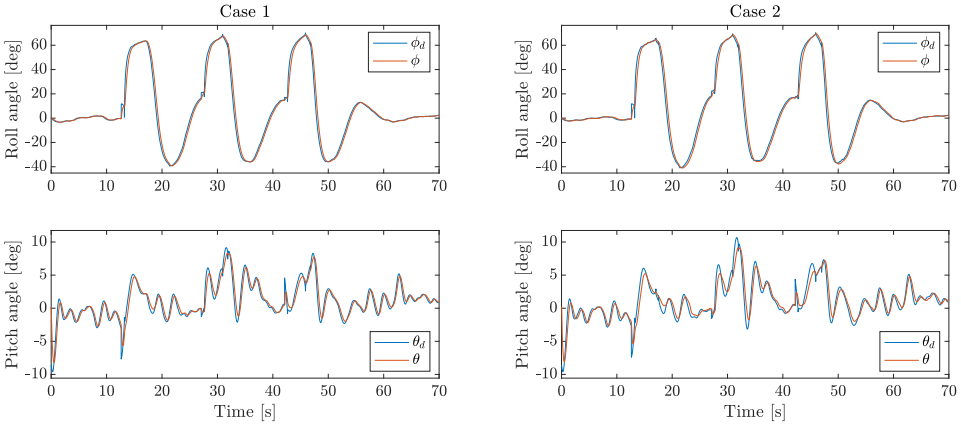

(a) The tracking results for the MSTA.

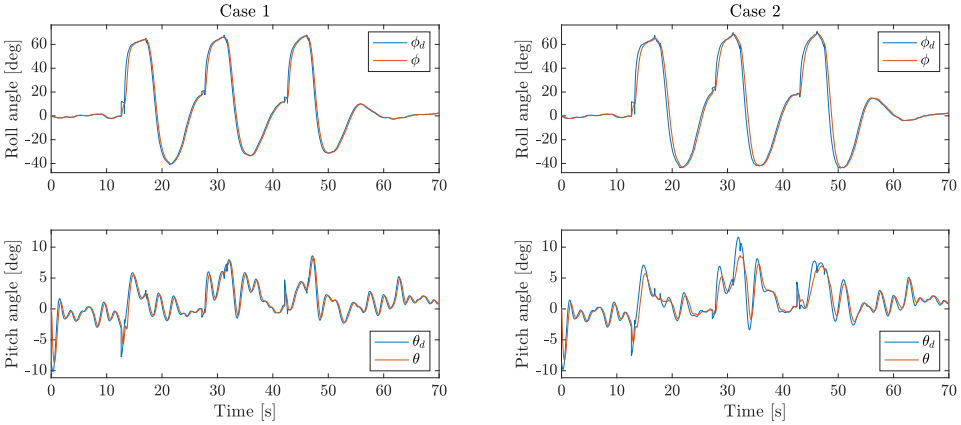

(b) The tracking results for the AMSTA.

Figure 8.11: A comparison of the tracking results for the MSTA and the AMSTA for both case 1 and case 2.

In case 2, however, the MSTA clearly outperforms the AMSTA in the tracking of the pitch reference, while the tracking of the roll reference is approximately the same for both control designs. This is also reflected in the error measures in Table 8.2, where the increase in error measures from case 1 to case 2 is bigger for the AMSTA than for the MSTA. Even so, the AMSTA still performs satisfactorily for case 2. Another interesting thing about the tracking results in Figure 8.11 is that the tracking of the roll reference barely changes from case 1 to case 2, while the change in the tracking of the pitch reference is noticeable for both the MSTA and the AMSTA. Therefore, it seems that the longitudinal dynamics are more sensitive to disturbances than the lateral dynamics, which becomes clear in case 2 when unmodeled dynamics are present.

In subsection 5.5.2, the sliding variable for the MIMO control designs is chosen so that when σ is zero we have that $e_\omega = -k_\Gamma e_\Gamma$ so that the control design tracks the roll

Case 1				
Performance measure	**MSAT**	**MSTA**	**AMSTA**	**GMSTA**
Total ISE	$1.251 \cdot 10^3$	$1.086 \cdot 10^3$	$9.906 \cdot 10^2$	$\mathbf{7.809 \cdot 10^2}$
Total IAE	$1.792 \cdot 10^2$	$1.591 \cdot 10^2$	$1.454 \cdot 10^2$	$\mathbf{1.365 \cdot 10^2}$
Total ISI	$\mathbf{1.497 \cdot 10^3}$	$1.522 \cdot 10^3$	$1.611 \cdot 10^3$	$1.602 \cdot 10^3$
Total IAI	$\mathbf{3.115 \cdot 10^2}$	$3.351 \cdot 10^2$	$3.355 \cdot 10^2$	$3.351 \cdot 10^2$
Case 2				
Performance measure	**MSAT**	**MSTA**	**AMSTA**	**GMSTA**
Total ISE	$1.180 \cdot 10^3$	$1.277 \cdot 10^3$	$2.341 \cdot 10^3$	$\mathbf{8.122 \cdot 10^2}$
Total IAE	$1.731 \cdot 10^2$	$1.760 \cdot 10^2$	$2.207 \cdot 10^2$	$\mathbf{1.376 \cdot 10^2}$
Total ISI	$1.520 \cdot 10^3$	$1.544 \cdot 10^3$	$\mathbf{1.511 \cdot 10^3}$	$1.608 \cdot 10^3$
Total IAI	$\mathbf{3.180 \cdot 10^2}$	$3.226 \cdot 10^2$	$3.213 \cdot 10^2$	$3.334 \cdot 10^2$

Table 8.2: Performance measures for the MIMO control designs, which includes the MSAT, the MSTA, the AMSTA, and the GMSTA, for simulation case 1 and case 2.

and pitch references, and that $\omega_b^{\parallel} = \frac{g \tan \phi}{V_a} \Gamma$ so that it is possible to track the angular rate references. The fact that the control designs are able to track the roll and pitch rate references are confirmed in section 8.1, while the results in Figure 8.12 shows that the yaw rate in the inertial frame $\dot{\psi}$ follows the desired yaw rate generated by the coordinated-turn equation (6.23). Thus, it is confirmed that driving the sliding variable to zero generates the desired results.

In Figure 8.12, the inertial yaw rates for the MSAT and the GMSTA control designs for both case 1 and case 2 are shown. For the MSAT, the yaw rate in case 2 is perhaps slightly closer to the desired yaw rate than in case 1, which makes sense as the error measures for the MSAT in Table 8.2 are actually lower for case 2 than for case 1. However, the change in error measures from case 1 to case 2 is relatively minor, so it makes sense that there is not a very noticeable change in the generated yaw rate. The results for the GMSTA changes from case 1 to case 2 as well, as there is an increase in oscillations in $\dot{\psi}$ in case 2. This increase in oscillations does not appear for the MSAT from case 1 to case 2, so it seems that this is a phenomenon that only appears in the second-order methods, which is confirmed by the results in Figure 8.13. In Figure 8.13, the results show that the yaw rates generated by the MSTA and the AMSTA for case 2 are much less smooth than the yaw rates for case 1. This implies that the second-order algorithms are theoretically more robust than the first-order MSAT, which is a surprisingly efficient and robust control method compared to the MSTA and the AMSTA. This is also reflected in the error measures in Table 8.2, where the error measures for the MSAT are higher than those for the second-order algorithms in case 1, while in case 2, the error measures for the MSAT are lower than those for the MSAT and the AMSTA. However, the GMSTA outperforms the other algorithms in both case 1 and case 2 in terms of error measures.

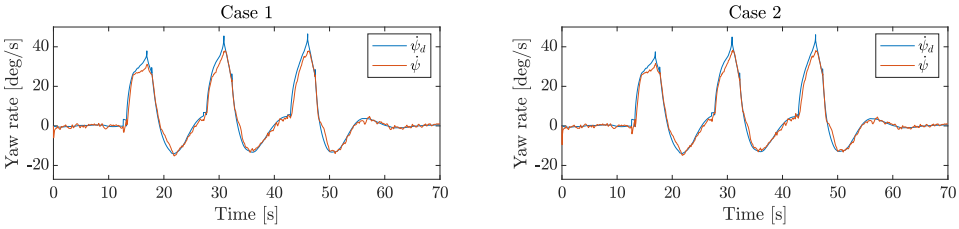

(a) The MSAT results.

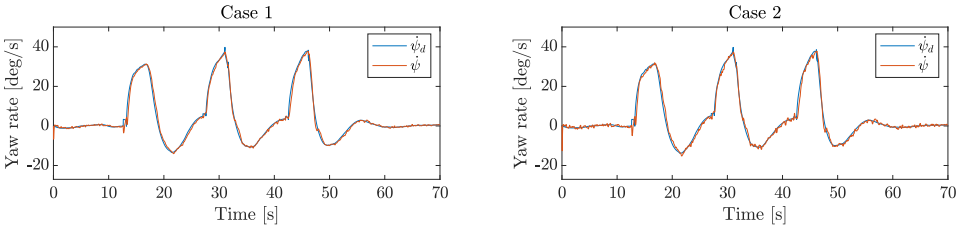

(b) The GMSTA results.

Figure 8.12: The yaw rates in the inertial frame, $\dot{\psi}$, for the MSAT and the GMSTA compared to the inertial yaw rate generated by the coordinated-turn equation (6.23) for both simulation case 1 and case 2.

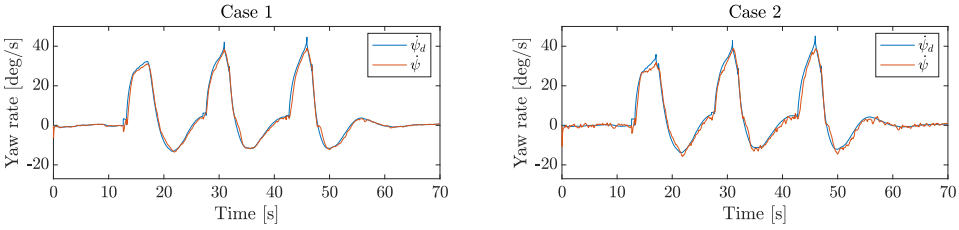

(a) The MSTA results.

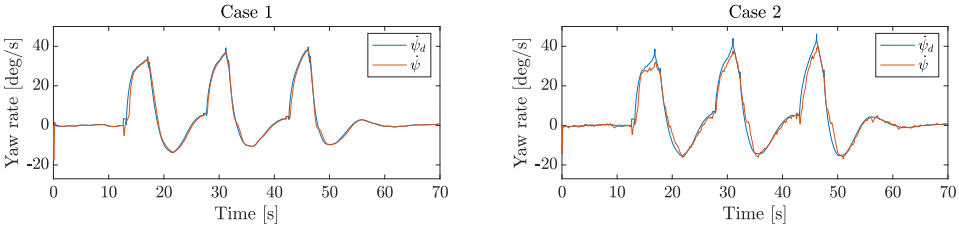

(b) The AMSTA results.

Figure 8.13: The yaw rates in the inertial frame, $\dot{\psi}$, for the MSTA and the AMSTA compared to the inertial yaw rate generated by the coordinated-turn equation (6.23) for both simulation case 1 and case 2.

8.3.2 Sliding Variable

All the MIMO control designs manage to drive the sliding variable to zero for case 1 and case 2, with some algorithms driving σ to zero faster than others, and some algorithms being better at enforcing the sliding mode once the sliding surface has been reached.

The MSAT and the MSTA designs have similar sliding surfaces in both case 1 and case 2, which can be seen in Figure 8.14. However, it seems that the sliding variable approaches zero slightly faster for the MSTA design than for the MSAT design in case 1. This might also be the case for simulation case 2, but the size of the deviations of the sliding variable from the sliding surface is larger for the MSTA than for the MSAT in case 2. Therefore, the sliding variables for both control design approach the sliding surface at approximately the same time in case 2.

Furthermore, the sliding variable is much smoother for the MSTA than for the MSAT in case 1, while the increase in chattering in the sliding surface from case 1 to case 2 is much more noticeable for the MSTA design than for the MSAT design. The components of σ for the MSAT design appears to follow approximately the same trajectories in both case 1 and case 2, but with slightly more chattering in case 2. For the MSTA design, on the other hand, the peaks in the components of the sliding variable are clearly bigger in case 2 than in case 1, with the peaks in σ_1 even being bigger than the peaks in σ_1 for the MSAT design. The increase in the magnitude of the sliding variable from case 1 to case 2 for the MSTA design is especially true for the last component of σ, σ_3. However, σ_3 is only slightly larger for the MSTA design in case 2 than for the MSAT design in both case 1 and case 2.

The increase in oscillations in σ from case 1 to case 2 for the MSTA design is as expected based on the results presented in Figure 8.12-8.13, where the oscillations in $\dot{\psi}$ increased more for the second-order algorithms than for the MSAT design.

Even though there is a larger increase in oscillations for the MSTA design than for the MSAT design, the sliding variables have approximately the same amount of chattering in case 2, which can be seen in Figure 8.14. However, it is not possible to find any chattering in σ_3 for the MSTA design in case 2, while there is a small amount in σ_3 for the MSAT design. Another thing that can be noted in Figure 8.14 is that it seems that σ_1 is more prone to chattering than σ_2 and σ_3.

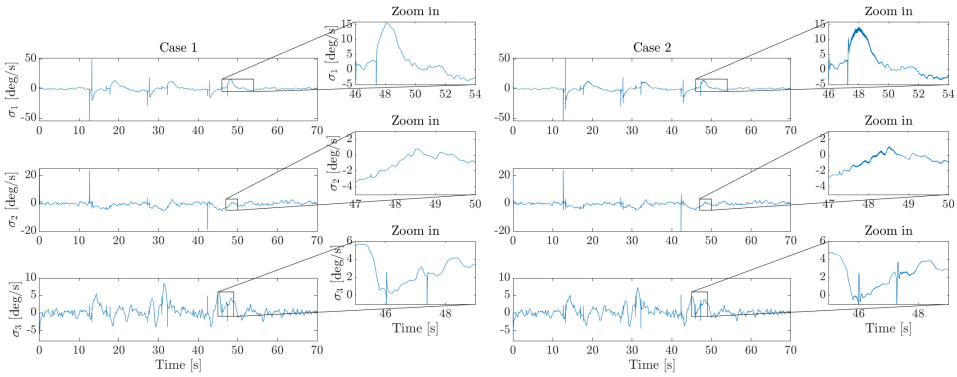

(a) The sliding variable for the MSAT design.

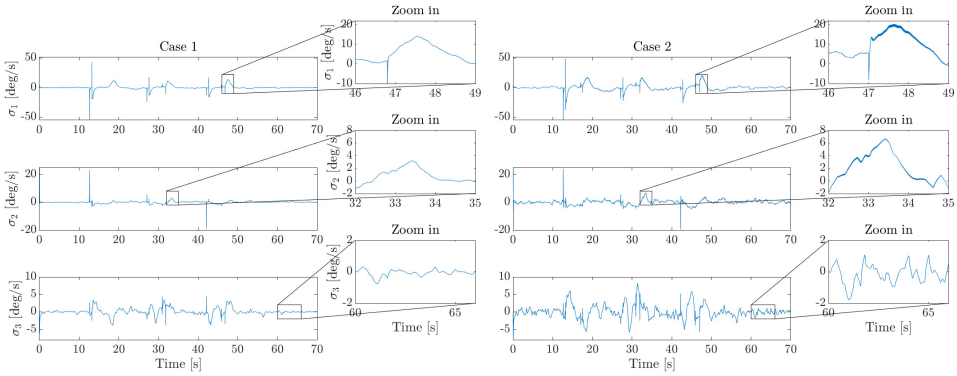

(b) The sliding variable for the MSTA design.

Figure 8.14: The components of the sliding variable σ generated by the MSAT and the MSTA designs in case 1 and case 2.

The sliding variables for the AMSTA and GMSTA designs are both different from the sliding variables for the MSAT and MSTA designs but are similar to each other. This can be seen in Figure 8.15. In case 1, the AMSTA and the GMSTA designs show that they are better at enforcing the sliding mode in the system once the sliding surface has been reached, than the MSAT and the MSTA designs presented in Figure 8.14. Especially the AMSTA shows robust behavior by keeping the system almost exactly on the sliding surface once it has been reached, which separates it from the rest of the control designs. The GMSTA also keeps the first two components of σ, σ_1 and σ_2, approximately at zero with some minor oscillations, while there are more oscillations in σ_3, which separates it from the AMSTA design in case 1.

In case 2, however, the sliding variable for the AMSTA design has several large peaks, which are much smaller for the GMSTA design. This is expected considering the measures in Table 8.2, where the error measures for case 1 are similar, while the error measures for the AMSTA design in case 2 are much higher than for the GMSTA. Additionally, the chattering in the sliding variable is more prominent for the AMSTA design than for the

GMSTA design for case 2. The GMSTA design barely has any chattering, and σ_3 does not contain any at all.

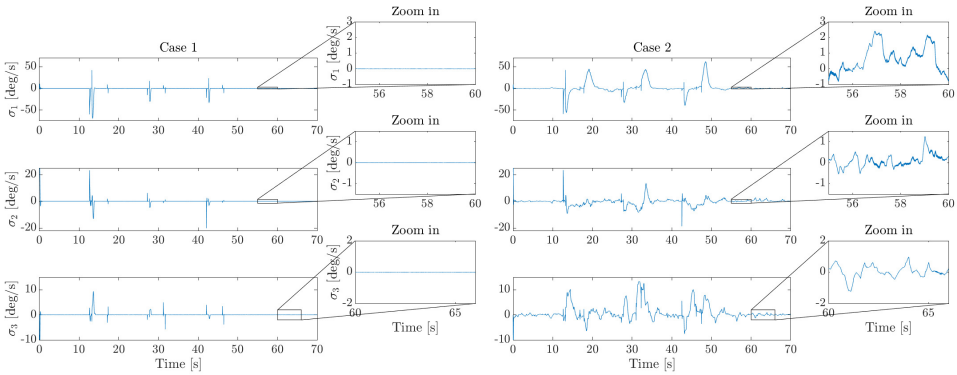

(a) The sliding variable for the AMSTA design.

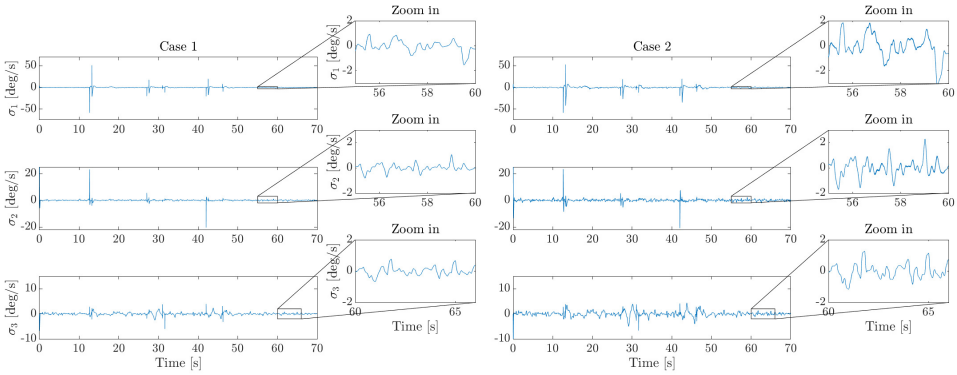

(b) The sliding variable for the GMSTA design.

Figure 8.15: The components of the sliding variable σ generated by the AMSTA and the GMSTA in case 1 and case 2.

Overall, the sliding variables for the MIMO control designs have large spikes in σ_1 and σ_2, while the spikes in σ_3 are much smaller in magnitude. Furthermore, there is more chattering in σ_1 and σ_2 for all the control designs in case 2, while σ_3 contains little to no chattering.

8.3.3 Control Input

The control inputs generated by the MSAT, the MSTA, and the GMSTA designs are all very similar. The control inputs generated by the MSTA and the AMSTA control designs are shown in Figure 8.16 for both case 1 and case 2. In Figure 8.16, we can see that the control signals generated by the MSTA design have several large spikes that are not as present in the control signals generated by the AMSTA design. These spikes are attenuated by the

actuator dynamics in case 2, even though additional spikes in the control input generated by the AMSTA appears in case 2.

In addition to the attenuation of the spikes in the control signals, the aileron control signal is slightly smoother in case 2 both for MSTA and for the AMSTA. However, the elevator and rudder control signals are slightly less smooth for both control designs in case 2. This is as expected based on the input use measures in Table 8.2, where there is a minor increase in the input use measures for the MSTA design from case 1 to case 2. The input measures for the AMSTA, however, actually decrease from case 1 to case 2, while the rest of the control designs have higher input measures for case 2 than case 1. This makes sense by looking at the control inputs in Figure 8.16, where $\bar{\delta}_a^d$ is smaller in amplitude than $\bar{\delta}_a$, while the other control inputs are approximately the same for case 1 and case 2.

As there is some chattering in the sliding variables for case 2 discussed in the previous subsection, it is natural to expect that there is also chattering in the control signals produced by the multivariable controllers. This is confirmed by Figure 8.17, where there is clearly chattering in the commanded control signals for both the AMSTA and the GMSTA designs, which is the control $\bar{u}$ before actuator dynamics and measurements. However, due to the coupling in the sliding variable, it is not straightforward to determine just by looking at the simulation results which component of the sliding variable that causes chattering in the commanded control signals. A common trait of the sliding variables for all the control designs discussed in the previous subsection is that there is more chattering in σ_1 and σ_2, than in σ_3. In Figure 8.17, however, $\bar{\delta}_r$ is the control signal that is the least affected by chattering for the AMSTA design, while it is the control signal with the most chattering for the GMSTA. On the other hand, $\bar{\delta}_a$ is the control signal with the smallest amount of chattering for the GMSTA, while $\bar{\delta}_a$ and $\bar{\delta}_e$ are the control signals that are the most affected by chattering for the AMSTA. Even though the chattering in the commanded control signals are sufficiently attenuated by the actuator dynamics and measurements for the GMSTA, some chattering remains in $\bar{\delta}_a^d$ and $\bar{\delta}_e^d$ for the AMSTA.

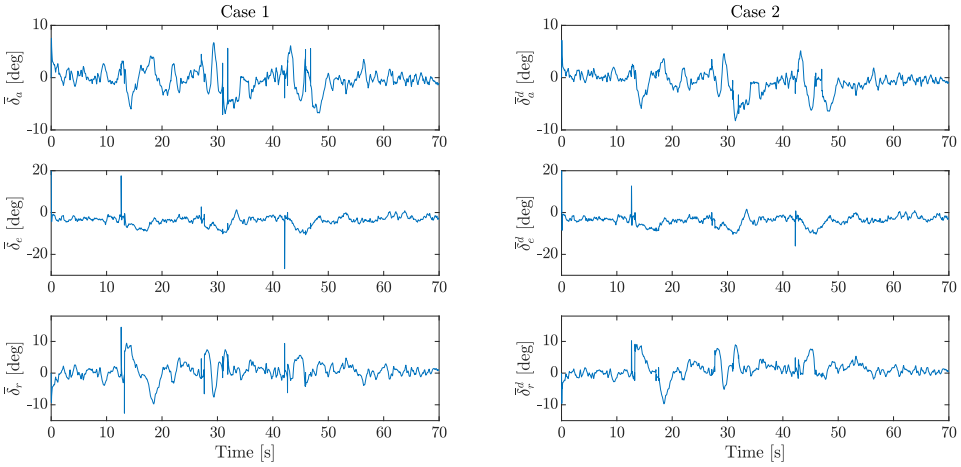

(a) The control input generated by the MSTA design.

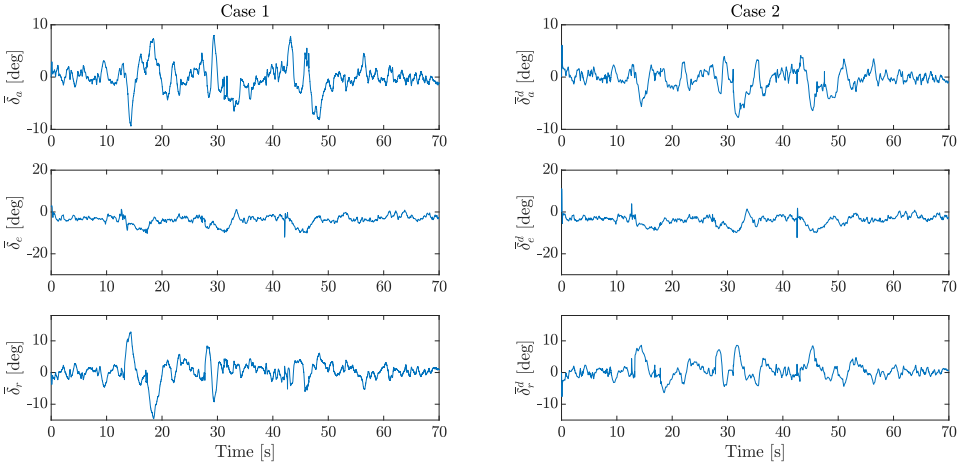

(b) The control input generated by the AMSTA design.

Figure 8.16: The control input generated by the MSTA and the AMSTA in case 1 and case 2.

Note that a significant re-tuning of most of the control designs from case 1 to case 2 was necessary to produce adequate tracking results in case 2. This can be seen by looking at the control gains presented in subsection D.2.2. For the MSAT and the GMSTA the re-tuning involves slightly increasing or decreasing the control gains, while for the MSTA and AMSTA, the control configurations in case 1 and case 2 are completely different.

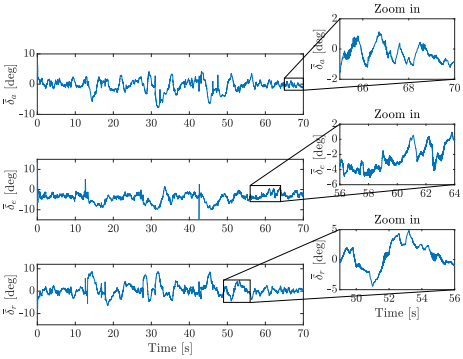

(a) The control command $\bar{u}$ generated by the AMSTA design.

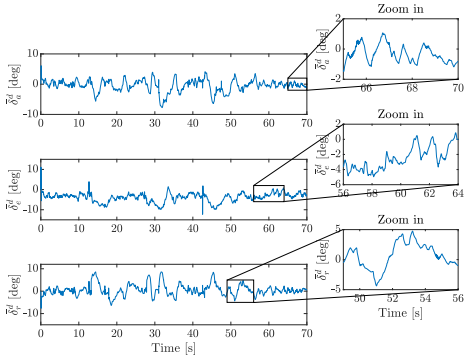

(b) The control input $\bar{u}^d$ generated by the AMSTA design.

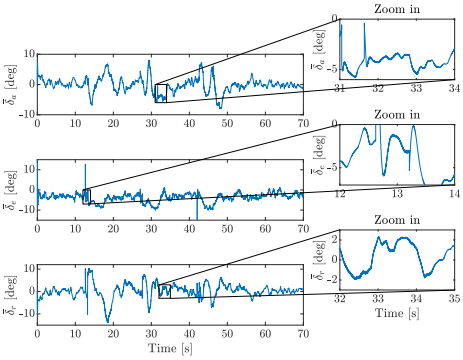

(c) The control command $\bar{u}$ generated by the GMSTA design.

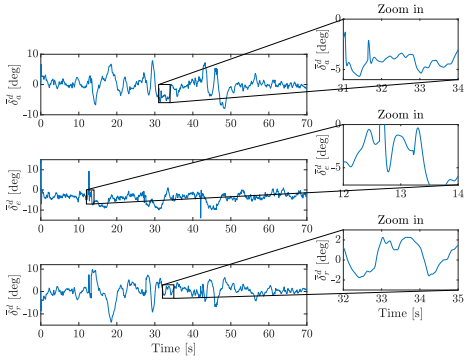

(d) The control input $\bar{u}^d$ generated by the GMSTA design.

Figure 8.17: The commanded signal $\bar{u}$ input generated by the AMSTA and GMSTA controllers compared to the resulting control input to the UAV model $\bar{u}^d$ for case 2.

8.4 Comparison of the SISO and the MIMO Designs

8.4.1 Tracking Performance

As seen in the previous two sections, all the SISO and MIMO control designs are capable of following the waypoints in $\mathcal{W}$. All the algorithms achieve approximately the same error measures for case 1 and case 2, which can be seen in Table 8.1 and Table 8.2. Interestingly, the control designs based on the GSTA and the GMSTA have the lowest error measures for both the SISO and MIMO control designs, respectively, with the GMSTA design having the lowest error measures out of all the control designs in both case 1 and case 2. However, the GMSTA also has the highest input use measures in both simulation cases. In case 1, the MIMO control designs have lower error measures than the SISO designs, except for the MSAT design, which has the highest error measures of all the control designs for case 1. The MSAT, however, is the only control design with lower error measures for case 2 than for case 1, even though it still has higher error measures than the SISO control designs

in case 2. Overall, the SISO control designs have smaller error measures than the MIMO control designs in case 2, except for the GMSTA design, even though the MIMO control designs all have higher input use measures than the SISO algorithms. This implies that the MIMO designs are theoretically more efficient and robust to disturbances than the SISO control designs, while in more realistic conditions, the SISO control designs are actually more robust than the MIMO control designs overall.

The SISO and MIMO control designs are also very similar in the kind of reference signal they produce. As the error measures are approximately the same for all the control designs, which means that the tracking performances are similar, this is expected since the reference trajectory is generated based on the ability of the control design to follow the reference. This means that if a control design does not track the reference closely enough, the reference will grow unbounded. This proved to be a challenge during the tuning process as it is difficult to remove high-frequent oscillations in the control signal, while still producing a feasible reference trajectory. Especially the pitch angle reference proved to be vulnerable if the controller is not tuned aggressively enough. The similarities between the reference signals produced by the SISO and the MIMO control designs are demonstrated in Figure 8.18, where the reference signals for the STA and the MSTA designs for case 2 are presented.

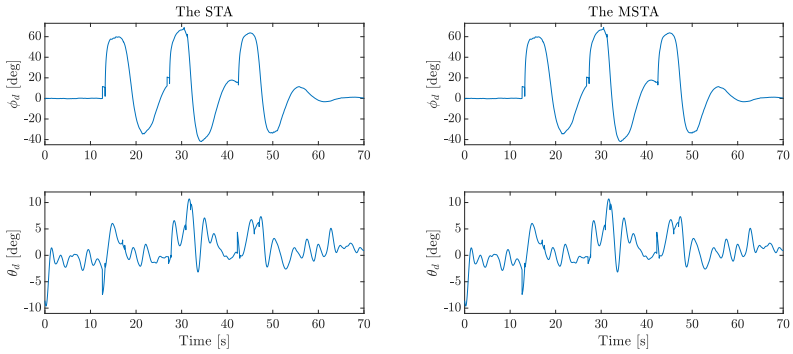

Figure 8.18: The reference signals for the STA and the MSTA designs for case 2.

Another interesting thing that can be noted in Figure 8.18 is that there are several small discontinuities in the reference signals, both in ϕ_d and θ_d for both control designs. This is unfortunate, as a sudden change in the reference signal may contribute to the spikes in the control signals presented in the two previous sections. As the scope of this report is the design of attitude control systems, minimal focus has been placed on the guidance and navigation aspect in the simulation model, which may be improved by generating a more continuous signal that is easier to track for the control system.

Even though the error measures for the SISO control designs are generally lower than for the MIMO designs in case 2, the MIMO designs still manage to track the pitch reference better than the SISO designs. This is demonstrated in Figure 8.19, where the tracking results for the STA and the MSTA designs are presented for case 2. In case 2, the error measures for the STA design are smaller than for the MSTA design. Yet, the MSTA design tracks the pitch reference as well, or even better, than the STA design. The fact that the

error measures are smaller for the STA design is because of the tracking of the pitch angle reference, which is only slightly better for the STA design than for the MSTA design. This is because it is possible to tune the lateral controllers in the SISO designs to track the roll reference extremely well without requiring a much higher input use. However, the longitudinal control input tends to be prone to high-frequent oscillations in the SISO designs, which is why the tracking of the pitch reference is not as good for the SISO designs as for the MIMO designs.

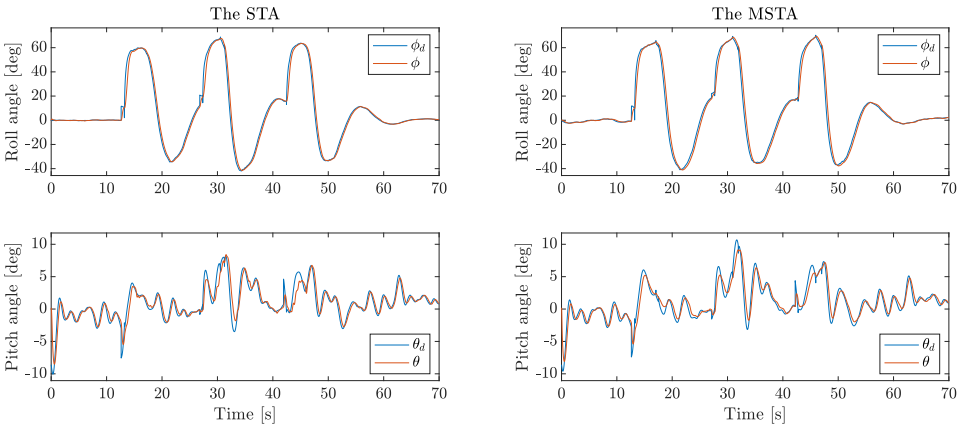

Figure 8.19: The tracking results for the STA and the MSTA designs for case 2.

The fact that the error measures for the SISO control designs are lower than for the MIMO control designs is solely due to the tracking of the roll angle reference, as the tracking of the pitch angle reference is as good or worse than the tracking performance of the MIMO control designs. This is proven in Figure 8.20, where the tracking performance of the MIMO control designs are better at tracking the pitch angle reference in every case, except, perhaps, the AMSTA control design for case 2. This makes sense, however, as the AMSTA for case 2 has the highest error measures of all the control designs.

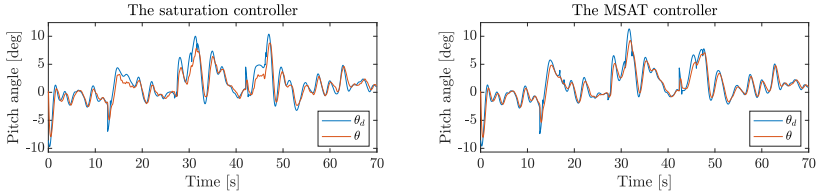

(a) The saturation and the MSAT control designs for case 1.

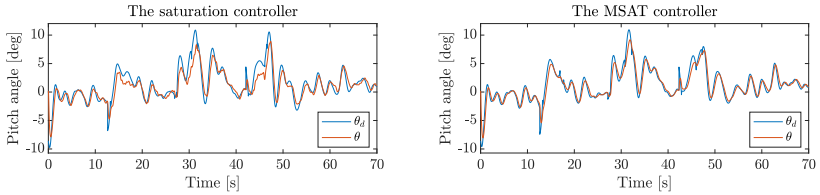

(b) The saturation and the MSAT control designs for case 2.

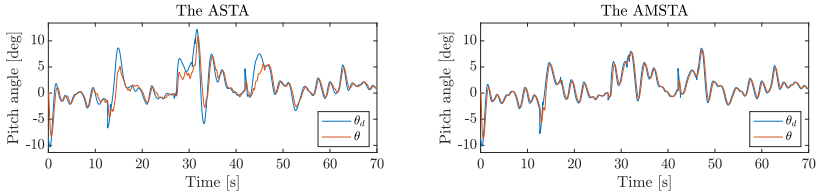

(c) The ASTA and the AMSTA designs for case 1.

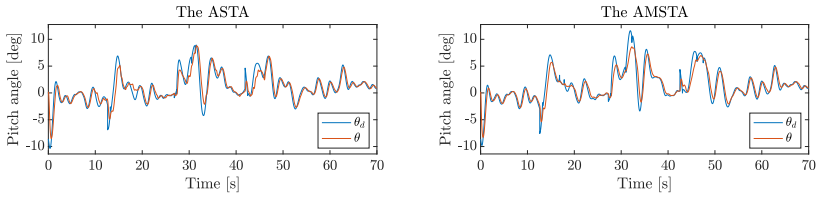

(d) The ASTA and the AMSTA designs for case 2.

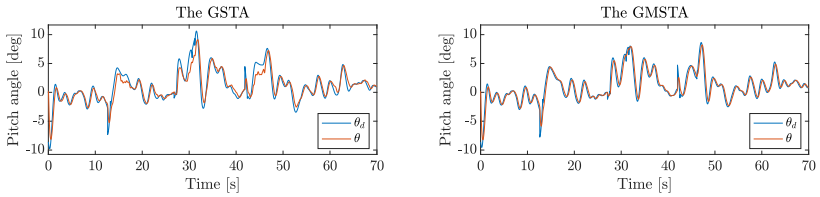

(e) The GSTA and the GMSTA designs for case 1.

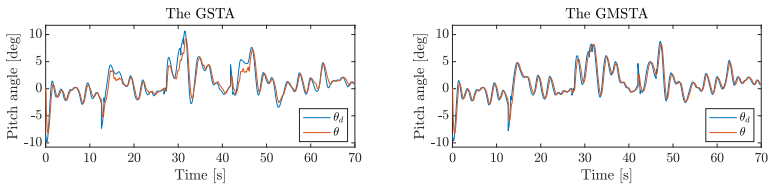

(f) The GSTA and the GMSTA designs for case 2.

Figure 8.20: The pitch angle tracking results for the saturation, the MSAT, the ASTA, the AMSTA, the GSTA, and the GMSTA control designs for case 1 and case 2.

8.4.2 Sliding variable

The sliding variables for the SISO and the MIMO control designs are similar in pairs, but they are different for each type of control design: the sliding variables for the saturation and the GSTA designs, and those for the STA and the ASTA designs are similar for the SISO control designs, while the sliding variables for the MSAT and MSTA designs and those for the AMSTA and GMSTA designs are similar for the MIMO control designs.

The sliding variables for the SISO control designs generally contain more chattering for simulation case 2, and more high-frequent oscillations than the MIMO control designs in both case 1 and case 2. This is demonstrated in Figure 8.21 and Figure 8.22 for the saturation and MSAT control designs, and for the GSTA and the GMSTA designs, respectively.

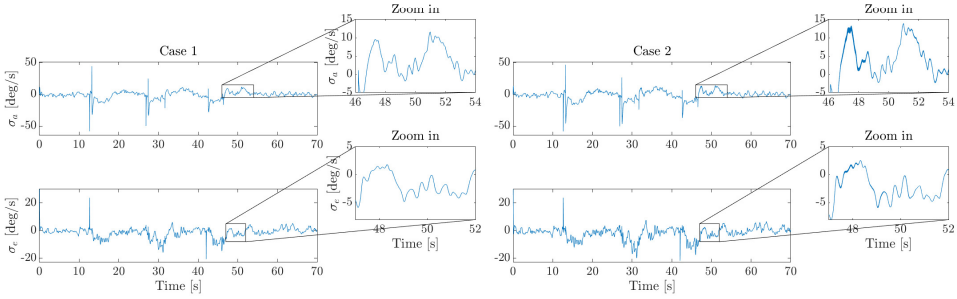

(a) The sliding variable for the saturation control design.

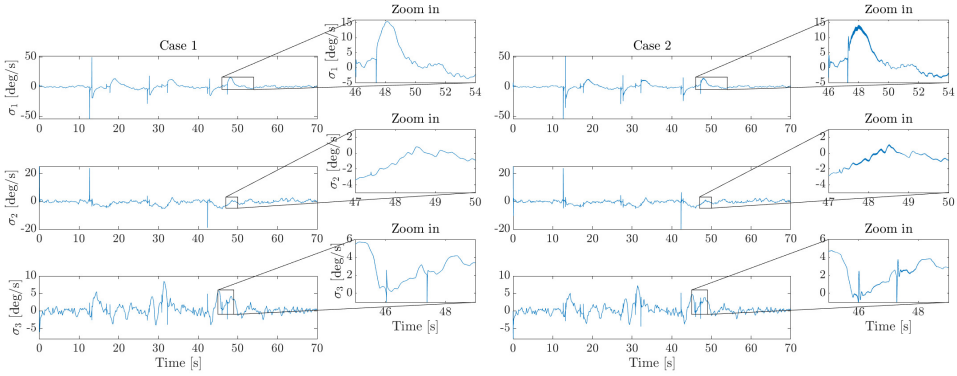

(b) The sliding variable for the MSAT design.

Figure 8.21: The sliding variables for the saturation and the MSAT control designs for case 1 and case 2.

In Figure 8.21, the components of the sliding variable for the MSAT design are smoother than for the saturation control design, while they both contain the same spikes due to the discontinuities in the reference signals discussed in the previous subsection. The sliding

variable components are also smoother for the MSAT than for the saturation design in case 2 and contain less chattering as well. Figure 8.22 confirms that the sliding variable for the GMSTA control design is smoother in case 1 than for the GSTA design and that the sliding variable for the GSTA contains the most chattering in case 2. Figure 8.21 and Figure 8.22 are representative for the sliding variables for the STA and the MSTA designs, and for the ASTA and AMSTA designs as well.

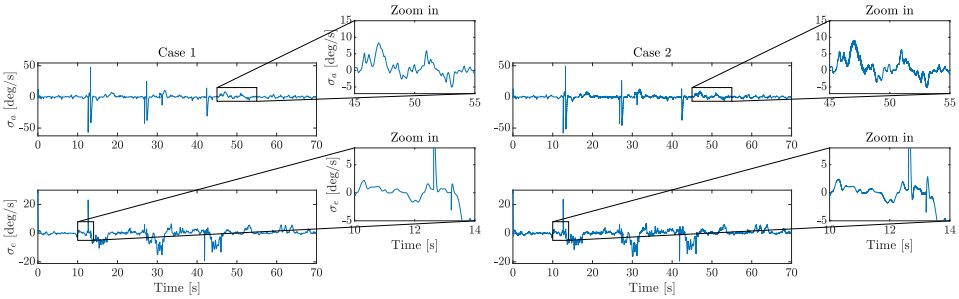

(a) The sliding variable for the GSTA design.

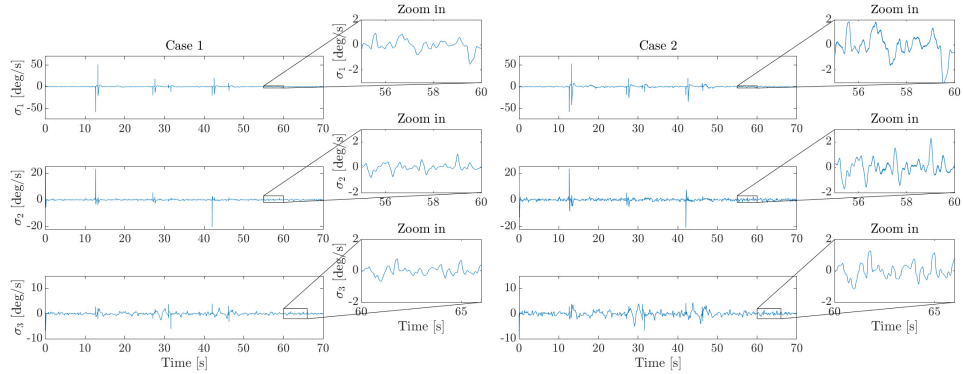

(b) The sliding variable for the GMSTA design.

Figure 8.22: The sliding variables for the GSTA and the GMSTA control designs for case 1 and case 2.

8.4.3 Control Input

A big difference between the SISO and MIMO control designs is that in the MIMO design, the rudder command is included in the SMC design instead of being generated by a PI-controller, which is the case for the SISO control design. This puts a strain on the elevator command in the SISO designs, which is typically less smooth than the elevator command produced by the MIMO control designs. The aileron commands produced by the SISO control designs also contain oscillations, but they are small in magnitude compared to the oscillations in the elevator command. This is exemplified in Figure 8.23.

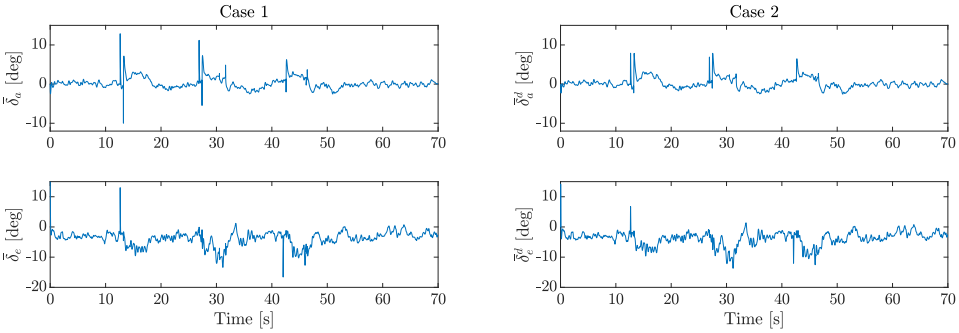

(a) The control input produced by the saturation control design.

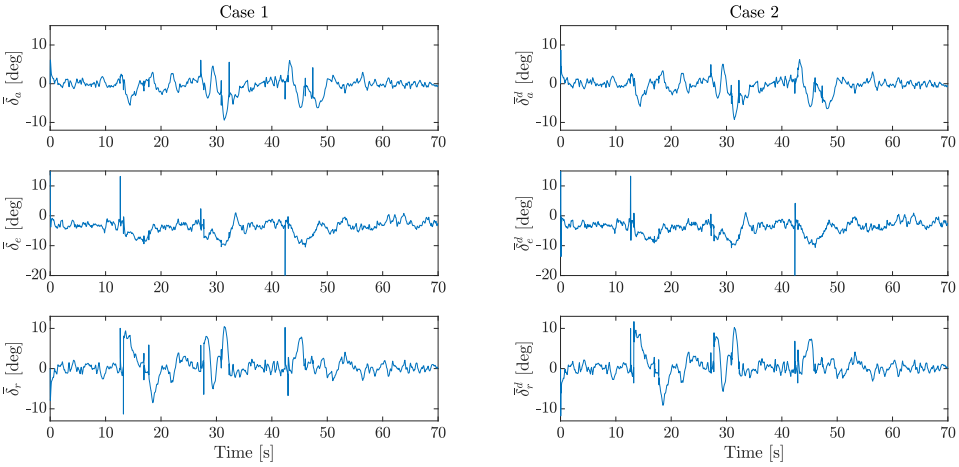

(b) The control input produced by the MSAT control design.

Figure 8.23: The control input produced by the sliding mode controllers in the saturation and the MSAT control designs in case 1 and case 2. The control $\bar{u}$ for case 1 is the control input generated by the controllers, which is also the input to the UAV model, as there are no unmodeled dynamics present in case 1. The control $\bar{u}^d$ for case 2 is the control input to the UAV model after actuator dynamics and measurements.

Another thing that can be seen in Figure 8.23 most of the SISO and the MIMO control designs produce control input that contain the characteristic spikes that have already been mentioned in the previous subsections. However, it seems that the MIMO control designs are overall more prone to these discontinuities in the control input, which might give an unrealistically good impression of the MIMO designs compared to the SISO control designs. A commonality for all the control commands produced by both the SISO and the MIMO control designs is that they contain high-frequent motion around $\bar{u} = 0$, or slightly less than zero for the elevator deflection, and more rigorous testing of the systems is therefore necessary to guarantee that the control signals are smooth enough to be feasible in reality.

Additionally, several of the control inputs produced by the SISO and the MIMO de-

signs, namely the ASTA, the MSTA, and the AMSTA control designs, contain a small amount of chattering due to the chattering contained in the sliding variables for simulation case 2. This can be seen in Figure 8.9 for the ASTA design and in Figure 8.17 for the AMSTA designs. As can be seen in the previously mentioned figures, the chattering is minimal, but it is difficult to remove it completely without sacrificing too much of the tracking ability of the control designs. The AMSTA actually has some of the lowest input use measures of the MIMO control designs for case 2, with the input use being lower for case 2 than for case 1, so this speaks to the difficulty of removing the chattering in the signal compared to many of the other control designs considered in this report. The same can also be said for the ASTA design, which has the lowest input use measures for case 2 of the SISO control designs but still produces a control input that contains chattering.

8.4.4 Tuning

There is a big difference in the tuning process for the SISO and the MIMO designs. The fact that the sliding variable is modeled by two separate decoupled sliding variables, σ_ϕ, and σ_θ, allows us to choose the control gains for the lateral and longitudinal controllers separately. When designing an attitude control system for a fixed-wing UAV, this is an especially good thing, as the longitudinal dynamics seem to be more sensitive to external disturbances and other uncertainties in the system than the lateral dynamics. Therefore, it is beneficial that it is possible to choose a less aggressive control configuration for the longitudinal controller than for the lateral controller so that both $\bar{\delta}_a$ and $\bar{\delta}_e$ are smooth enough. However, this doubles the number of control gains that have to be chosen for each control design, which complicates the tuning process significantly. From only that perspective it is easier to choose control gains for the MIMO control designs. However, the MIMO designs do not have the ability to choose control gains for each control signal, so to produce three control signals that are smooth enough, it may be necessary to allow higher tracking errors.

Furthermore, it is hard choosing the system parameters for both the SISO ASTA and the AMSTA designs, despite the control gains being adaptive. In case 2 for both control designs there are some remnants of chattering in the control signals from the chattering in the sliding variables that could not be removed while still producing adequate tracking results. For the MSTA design, it is easier to choose control gains than for the ASTA and the AMSTA designs, since it is possible to achieve acceptable tracking performances for a wider range of control gains, while it was surprisingly difficult to choose control gains for the STA design for case 2. The control designs that are the easiest to tune are the saturation and the MSAT designs, as these only have two parameters per controller. Adjusting the size of the boundary layer proved to be a very effective tool to minimize chattering and produce smooth control signals. Finally, the GSTA and the GMSTA are also easy to tune, as they produce good results for several different control gain configurations. However, it is difficult to determine the optimal configuration, which is also true for the other SISO and MIMO control designs.

Of the second-order SISO and MIMO control designs, the ASTA and the AMSTA designs definitely have the most difficult tuning processes, with the STA also being slightly more difficult to tune than the other algorithms. There is a difference in the design of the GSTA, the MSTA, and the GSTA, from the design of the STA, the ASTA, and the AMSTA,

which is that the latter do not have added linear correction terms. The linear correction terms were first added to the GSTA (Moreno, 2009) with the intention of making the algorithm more robust. Due to the performance of the GSTA for the lateral dynamics in Griffiths (2020) and for the longitudinal dynamics presented in chapter 7, it is possible to conclude that the GSTA definitely have an advantage over the original STA. As the SISO GSTA, the MSTA and GMSTA designs have also proven to be robust in the results presented in this chapter, it would be reasonable to accredit some of this robustness to the extra linear correction terms. The control gains for these terms were discovered to be very useful and efficient in the tuning process, and are generally chosen quite large compared to the other control gains for the MSTA, the GSTA, and the GMSTA designs.

8.4.5 Angle of Attack

The AoA is an important factor when designing an attitude control system for a UAV, as it is dangerous if the AoA approaches the stall angle since this will cause a sudden drop in the lift. It is necessary to determine whether the AoA reaches the stall angle, which is typically around 15-20 deg (Beard and McLain, 2012), during the simulation, as the system would not be stable in reality should this happen. The AoA for the STA and the MSTA designs are presented in Figure 8.24 for case 1 and case 2. The results presented in this figure are representative of all the control designs, which produce AoAs that satisfy $\alpha \in [-5, 12]$ deg. Thus, the AoA does not reach the stall angle for either the SISO or the MIMO control designs.

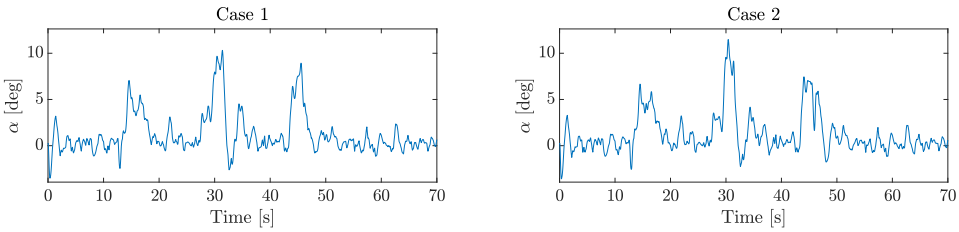

(a) The AoA for the STA design.

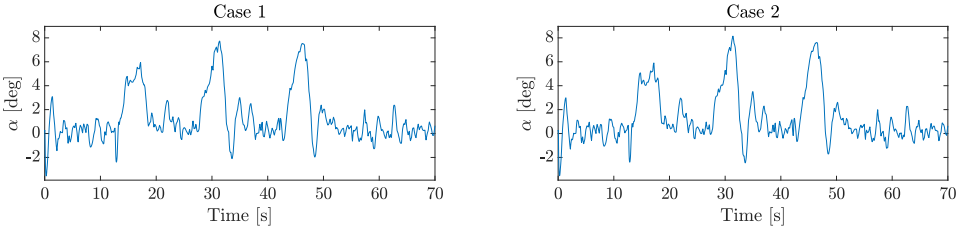

(b) The AoA for the MSTA design.

Figure 8.24: The AoA for the STA and MSTA control designs for case 1 and case 2.

8.5 Results for Case 3 and Case 4

8.5.1 Tracking Results

The algorithms that are considered for case 3 and case 4 are the saturation, the GSTA, the MSAT, and the GMSTA control designs. The reason for choosing these designs is that it is interesting to compare the results of first-order and second-order designs, and the GSTA and GMSTA is the control designs that have proven to be the most robust in case 1 and case 2, together with the saturation control design.

The flight paths of these algorithms for case 3 can be found in Figure 8.25 and for case 4 in Figure 8.26. Compared to the flight paths of the SISO and MIMO algorithms for case 2 shown in Figure 8.3 and Figure 8.10, respectively, there is a much bigger difference between the flight paths of the control designs for both case 3 and case 4 than for case 2. Surprisingly, the algorithms produce flight paths that are more similar for case 4 than for case 3, despite the increase in external disturbances and process noise from case 3 to case 4. The flight paths produced in case 4 also seems to be smoother than the flight paths for case 3. Especially the GMSTA seems to produce a flight path with fewer oscillations than the other flight paths.

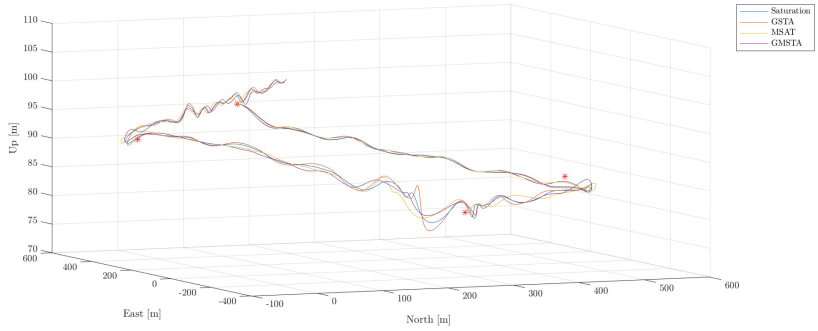

(a) North-East-Up view of the flight paths.

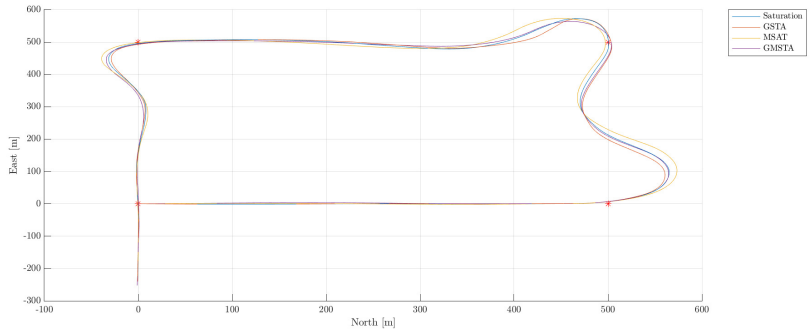

(b) North-East view of the flight paths.

Figure 8.25: The flight paths of all the algorithms considered for case 3.

As for case 1 and case 2, the flight paths of the algorithms are much more similar to each other when only regarding the North-East view than when regarding the full North-East-Up view, both in case 3 and case 4. This means that the control designs track the roll reference approximately to the same degree in both case 3 and case 4. An example of the tracking of the roll reference is given in Figure 8.27, which shows the roll angle tracking performance of the GSTA design for case 3 and case 4. As for the results in case 1 and case 2, the SISO control designs are overall slightly better at tracking the roll angle than the MIMO designs due to the lateral controllers having more aggressive control gains. The choice of control gains and system parameters for case 3 and case 4 can be found in subsection D.2.3.

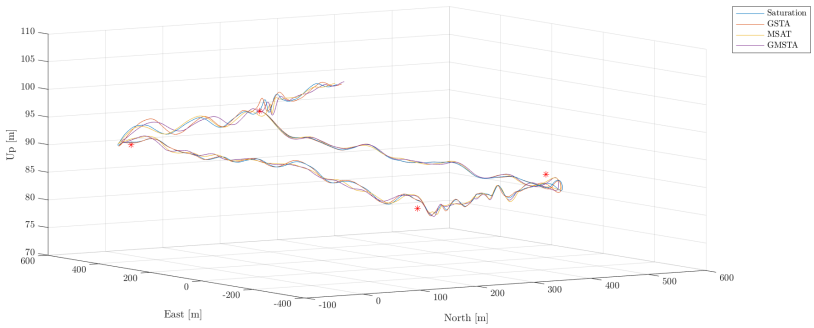

(a) North-East-Up view of the flight paths.

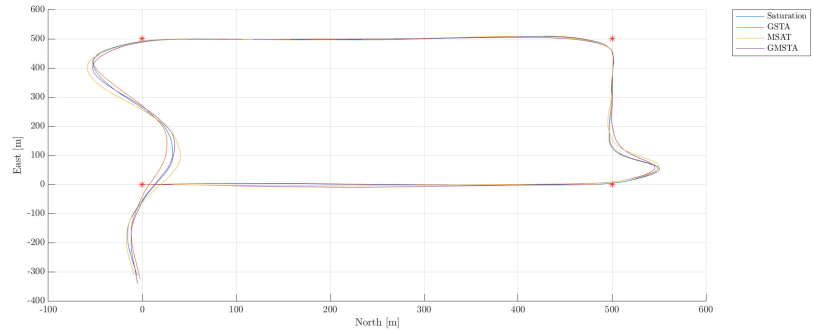

(b) North-East view of the flight paths.

Figure 8.26: The flight paths of all the algorithms considered for case 4.

The roll angle tracking results shown in Figure 8.27 are very similar to the results for case 1 and case 2. However, there is slightly more error in the tracking results for cases 3 and 4, than for cases 1 and 2. In the results for case 4, the reference trajectory is not as smooth as for the other simulation cases. This is natural, as the wind speed in case 4 is about 40% of the airspeed, which is in the upper range of possible wind speeds, which is generally 20%-50% of the airspeed (Beard and McLain, 2012).

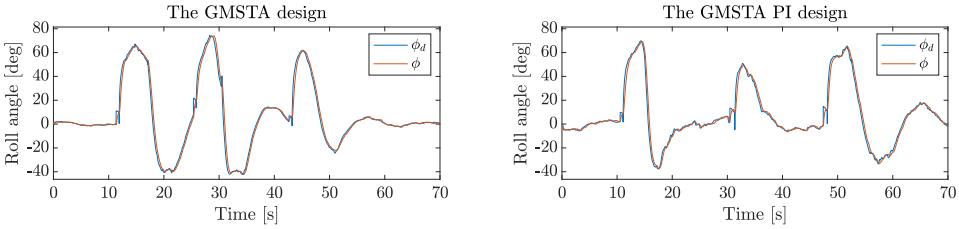

Figure 8.27: The roll angle tracking results for the GSTA design in case 3 and case 4.

Based on the results for case 1 and case 2 presented in the previous sections, it is expected that the pitch angle tracking performance of the control designs will be more affected by the increase in external disturbances and process noise than the roll angle tracking. The pitch angle tracking results for the saturation, the GSTA, the MSAT, and the GMSTA control designs are shown in Figure 8.28 for case 3 and case 4. When looking at just the pitch angle tracking results, it is clear that the MIMO designs considered here outperform the SISO control designs in terms of tracking the reference closely, and in providing smooth tracking. Especially the GMSTA manages to track the pitch reference closely in both case 3 and case 4.

Even though Figure 8.28 shows that the MIMO designs are better at tracking the pitch reference than the SISO designs, the error measures for the SISO designs are lower than the measures for the MSAT in both case 3 and case 4. The error measures for case 3 and case 4 can be found in Table 8.3. This is because the SISO designs generally perform better roll angle tracking than the MIMO control designs, which is also the case for simulation cases 1 and 2. However, the GMSTA has the smallest error measures out of all the control designs considered in this section. This is as expected since the GMSTA also had the smallest error measures for case 1 and case 2 of all the control designs considered in this report.

Furthermore, the MSAT and the GMSTA still manage to produce inertial yaw rates that correspond to the yaw rate given by the coordinated-turn equation (6.23). This is shown for the GMSTA in Figure 8.29. However, there is a clear loss of smoothness in $\dot{\psi}$ produced by the GMSTA for case 3 and case 4 compared to $\dot{\psi}$ for the MIMO algorithms presented in Figure 8.13 for case 1 and case 2, which makes sense due to the increase in process noise and wind speed.

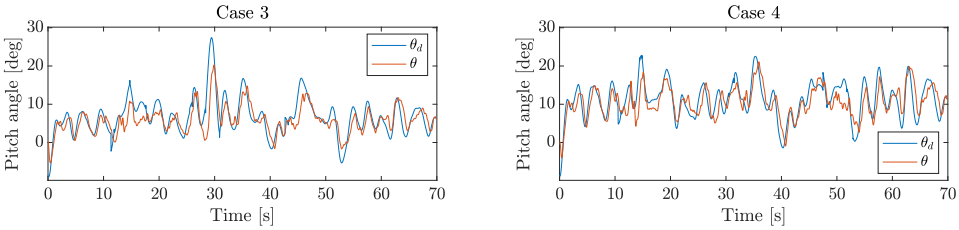

(a) The saturation control design.

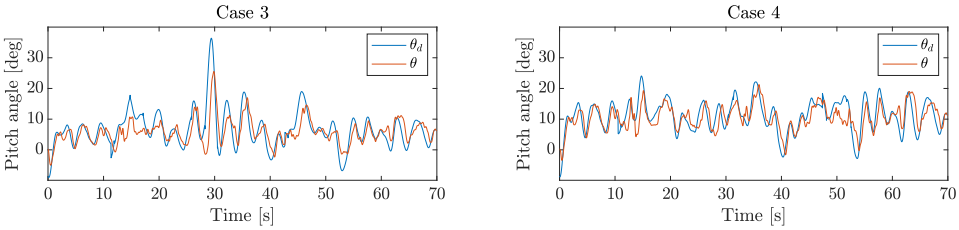

(b) The GSTA design.

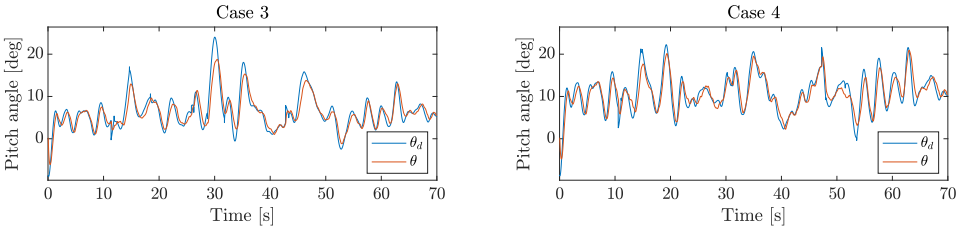

(c) The MSAT control design.

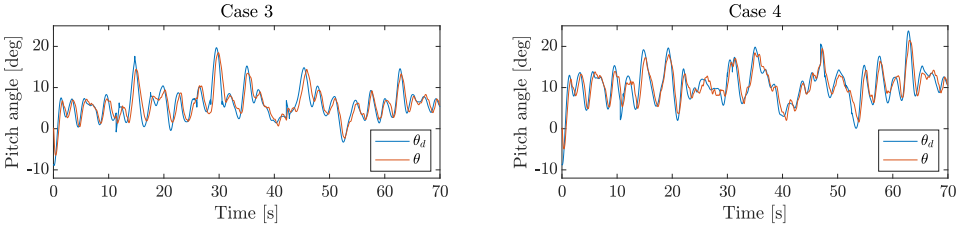

(d) The GMSTA design.

Figure 8.28: The pitch angle tracking results for the saturation, the GSTA, the MSAT, and the GMSTA control designs for case 3 and case 4.

Case 3				
Performance measure	**Saturation design**	**GSTA**	**MSAT**	**GMSTA**
Total ISE	$1.389 \cdot 10^3$	$1.699 \cdot 10^3$	$1.885 \cdot 10^3$	$\mathbf{1.382 \cdot 10^3}$
Total IAE	$2.310 \cdot 10^2$	$2.603 \cdot 10^2$	$2.269 \cdot 10^2$	$\mathbf{1.961 \cdot 10^2}$
Total ISI	$\mathbf{1.847 \cdot 10^3}$	$1.988 \cdot 10^3$	$2.102 \cdot 10^3$	$2.074 \cdot 10^3$
Total IAI	$\mathbf{3.247 \cdot 10^2}$	$3.278 \cdot 10^2$	$3.761 \cdot 10^2$	$3.749 \cdot 10^2$
Case 4				
Performance measure	**Saturation design**	**GSTA**	**MSAT**	**GMSTA**
Total ISE	$1.270 \cdot 10^3$	$1.285 \cdot 10^3$	$1.398 \cdot 10^3$	$\mathbf{1.162 \cdot 10^3}$
Total IAE	$2.508 \cdot 10^2$	$2.420 \cdot 10^2$	$2.279 \cdot 10^2$	$\mathbf{2.203 \cdot 10^2}$
Total ISI	$1.998 \cdot 10^3$	$\mathbf{1.984 \cdot 10^3}$	$2.405 \cdot 10^3$	$2.354 \cdot 10^3$
Total IAI	$3.402 \cdot 10^2$	$\mathbf{3.390 \cdot 10^2}$	$4.075 \cdot 10^2$	$4.078 \cdot 10^2$

Table 8.3: Performance measures for the saturation, the GSTA, the MSAT and the GMSTA control design for simulation cases 3 and 4.

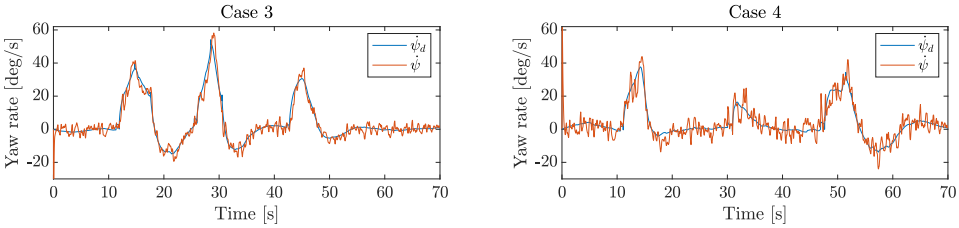

Figure 8.29: The yaw rate in the inertial frame, $\dot{\psi}$, for the GMSTA compared to the inertial yaw rate generated by the coordinated-turn equation (6.23) for simulation case 3 and case 4.

8.5.2 Sliding Variable

The sliding variables produced in case 3 and case 4 by the saturation and the MSAT control designs can be found in Figure 8.30, and the sliding variables produced by the GSTA and the GMSTA control designs can be found in Figure 8.31.

The saturation and the GSTA control designs are much better at enforcing the sliding mode for the lateral sliding variable σ_ϕ than for the longitudinal sliding variable σ_θ. This is as expected based on the tracking results discussed in the previous subsection and the sliding variables produced by the SISO control designs in case 1 and case 2. The GSTA is slightly better at keeping σ_ϕ at zero than the saturation control design in both case 3 and case 4, while the saturation control design is perhaps slightly better at enforcing the

sliding mode for σ_θ than the GSTA design. This makes sense based on the error measures in Table 8.3, which are higher for the GSTA design than for the saturation control design in case 3, and approximately the same in case 4.

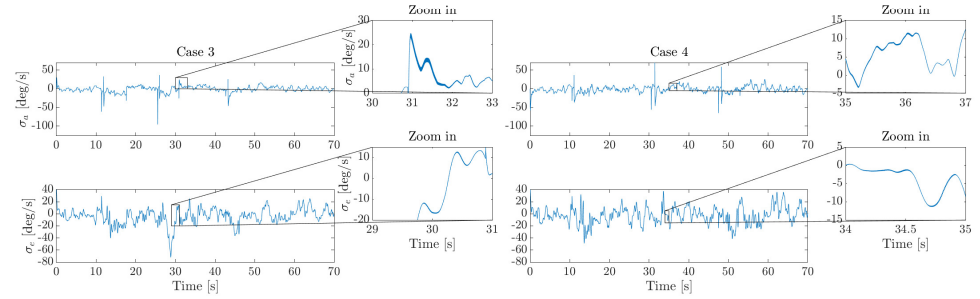

(a) The sliding variable for the saturation control design.

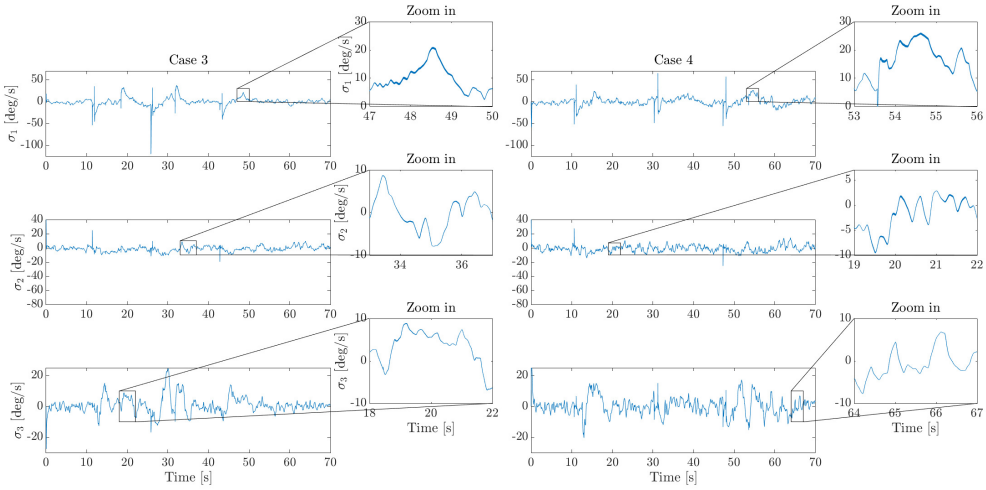

(b) The sliding variable for the MSAT control design.

Figure 8.30: The sliding variables for the saturation and the MSAT control designs for case 3 and case 4.

The sliding variables produced by the MSAT and GMSTA control designs are very similar in both case 3 and case 4. In case 3, the GMSTA is better at keeping σ_1 at zero, while in case 4 σ_1 are approximately the same for both control designs. The error measures for the MSAT control design are much closer to the error measures for the GMSTA design in case 4 than in case 3, so this is as expected.

Furthermore, there seems to be approximately the same amount of chattering in each simulation case for both SISO and both MIMO designs, with more chattering in case 3 than in case 4. Overall there is more chattering in the sliding variables for the SISO

control designs than in the ones produced by the MIMO designs. For the saturation and the GSTA control designs there is more chattering in σ_ϕ than in σ_θ, while for the MSAT and the GMSTA control designs, σ_1 contains more chattering than σ_2 and σ_3. Both these results are as expected based on the sliding variables produced by the SISO and MIMO control designs in case 1 and case 2. Overall, the sliding variables produced by the control designs considered in this section contain approximately the same amount of oscillations, and the motion of the sliding variables is much more high-frequent than the motion of those produced in case 1 and case 2.

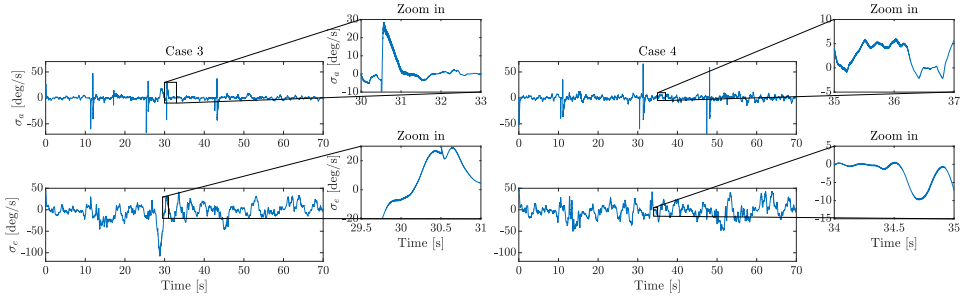

(a) The sliding variable for the GSTA design.

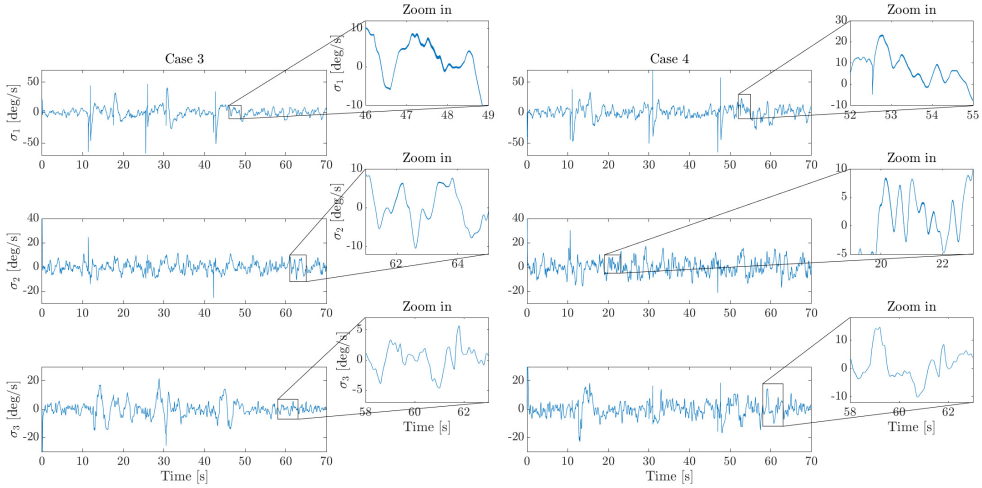

(b) The sliding variable for the GMSTA design.

Figure 8.31: The sliding variables for the GSTA and the GMSTA designs for case 3 and case 4.

8.5.3 Control Input

The increase in oscillations in the control input is significant for both the SISO and MIMO control designs for case 3 and case 4 compared to case 1 and case 2. The control inputs

produced by the saturation, the GSTA, the MSAT, and the GMSTA control designs in case 3 can be found in Figure 8.32, and the control inputs produced in case 4 can be found in Figure 8.33. For case 3, the MSAT produces the least feasible control input, with many large oscillations compared to the control inputs generated by the other control designs. The MSAT has the largest input use measures for case 3 so it makes sense that its control input is the one with the most oscillations. On the other hand, the GMSTA has the most feasible control signal due to the smaller size of the oscillations, even though the GMSTA has the second larges input use measures for case 3. This is due to the large size of the peaks in the control signal, which is not a bad thing as the peak values of the control inputs are still a long way from the saturation value at ± 30 deg.

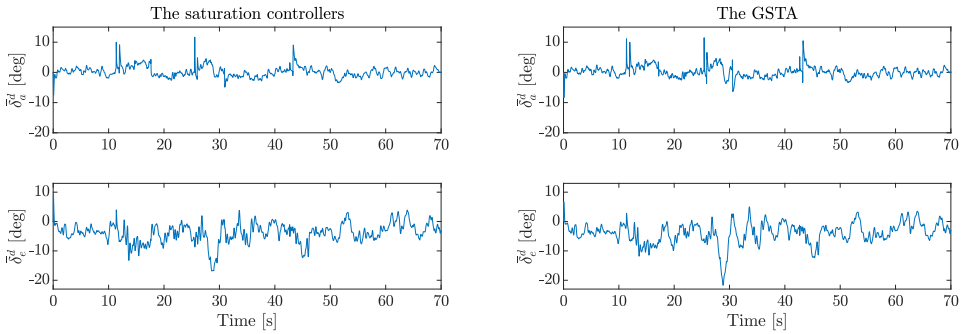

(a) The saturation and the GSTA control designs.

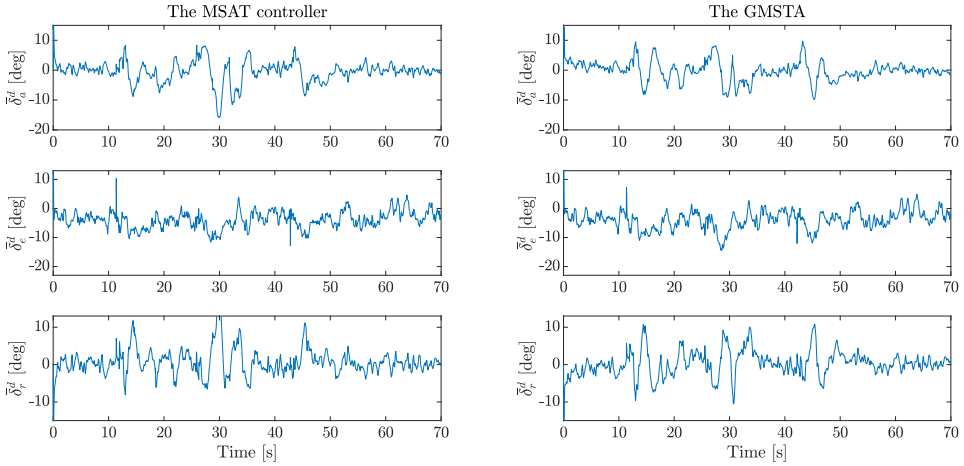

(b) The MSAT and GMSTA control designs.

Figure 8.32: The control input generated by the saturation, the GSTA, the MSAT and the GMSTA control designs for case 3.

In case 4, however, the control input produced by the GMSTA is not more feasible than the control inputs produced by the other control signals. In fact, the amount and size of the oscillations render the control inputs shown in Figure 8.33 close to unrealizable in reality.

At the very least, the control inputs for case 4 would put a very high strain on the actuators, which is not desirable. The control input that is the most feasible in case 4 is either the one produced by the saturation control design or by the GSTA design. This makes sense as the increase in input use measures from case 3 to case 4 is much smaller for the SISO control designs than for the MIMO control designs. However, the fact that the GMSTA design produces such an oscillatory control input makes sense as the error measures for the GMSTA are quite a bit smaller than the error measures for the other control designs. Therefore, the control input produced by the GMSTA in case 4 might be more feasible with a more optimal control gain configuration.

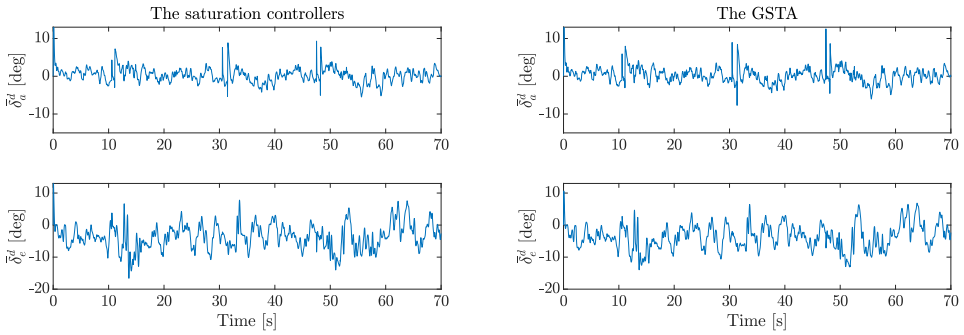

(a) The saturation and the GSTA control designs.

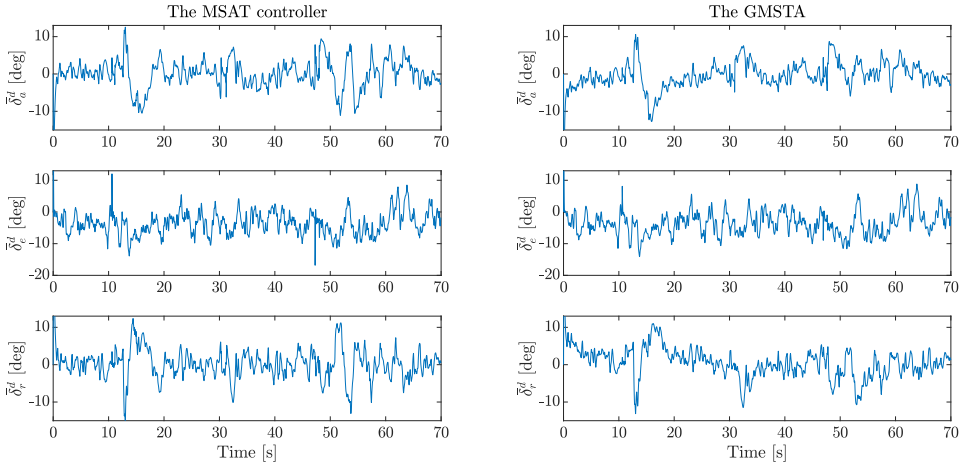

(b) The MSAT and GMSTA control designs.

Figure 8.33: The control input generated by the saturation, the GSTA, the MSAT and the GMSTA control designs for case 4.

8.5.4 Angle of attack

All the control designs considered for case 1 and case 2 produce values for the AoA that are all well below the typical stall angle values of 15-20 deg. However, in case 3 and case

4, the saturation and the GSTA control designs both produce values for α that are higher than 15 deg, with the peak in the AoA being larger for case 3 than for case 4. This can be seen in Figure 8.34, which shows the AoA for the saturation and the MSAT control designs for case 3 and case 4. The AoA produced by the MIMO control designs is below 12 deg, which is reasonable. The fact that both SISO control designs considered for case 3 and case 4 produces and AoA which reaches the potential stall angle range, is a clear drawback to using the decoupled SISO design instead of the MIMO design.

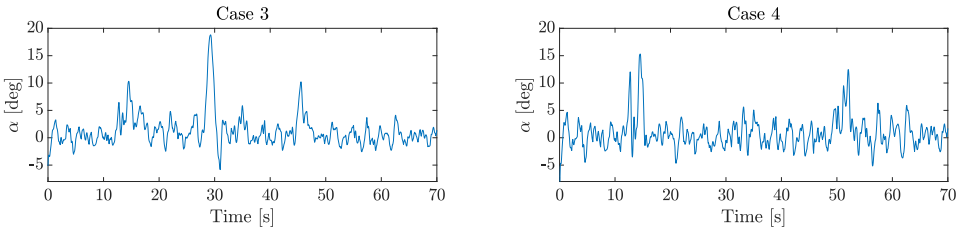

(a) The AoA for the saturation control design.

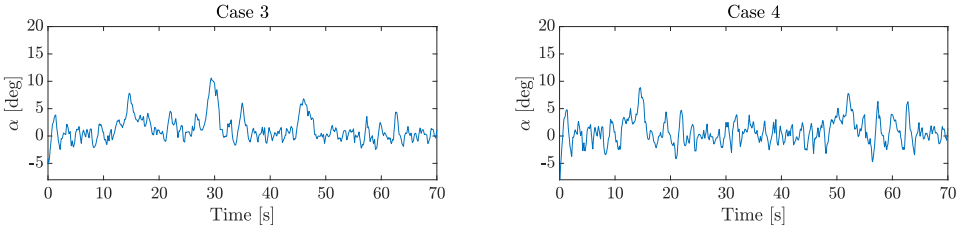

(b) The AoA for the MSAT control design.

Figure 8.34: The AoA for the saturation and the GMSTA control designs for case 3 and case 4.

8.6 Sensitivity to Actuator Dynamics

In this section, the sensitivity of the saturation, the GSTA, the MSAT, and the GMSTA to the modeling of the actuator dynamics is investigated. In the previous simulation results presented in this chapter, the actuator dynamics are modeled using the first-order TF in (6.16) with time constant $T_u = 0.0154$ s. This section presents a comparison of the results when using the same first-order TF with the time constant $T_u = 0.1$ s so that the actuator dynamics are slower, and when using the second-order dynamics (6.4) from Bøhn et al. (2019), which means that the actuator dynamics are more complex. It is necessary to re-tune the control designs to achieve adequate tracking performance without chattering when changing the actuator dynamics. The control gains used in this section can be found in subsection D.2.4.

8.6.1 Tracking Results

The flight paths of the control designs considered in this section can be found in Figure 8.35 for both the first- and second-order dynamics. Figure 8.35 shows that the flight paths

are generally smoother for the second-order dynamics than for the first-order dynamics. The one exception is the saturation control design, which produces approximately the same flight path for both types of actuator dynamics. The flight paths are also more similar for the second-order dynamics than for the first-order dynamics. This means that the control designs are less robust to slower actuator dynamics, which makes sense since the basis of SMC is a discontinuous control action that switches at an infinitely high switching frequency. Slow actuator dynamics limit the oscillations in the control signals which would also limit the tracking ability of the control designs.

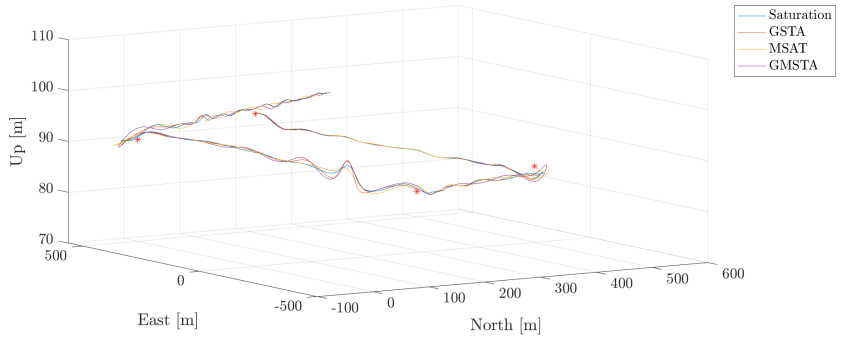

(a) The flight paths for the first-order actuator dynamics with $T_u = 0.1$ s.

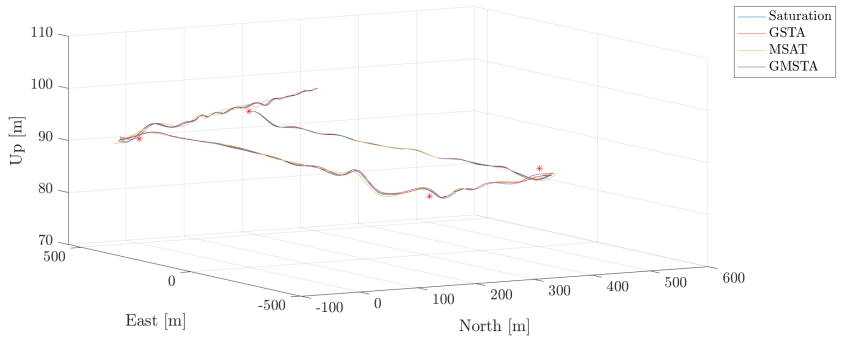

(b) The flight paths for the second-order actuator dynamics.

Figure 8.35: The flight paths of the saturation, the GSTA, the MSAT, and the GMSTA control designs for case 2 when the actuator dynamics are modeled using the first-order TF (6.16) with $T_u = 0.1$ s, and when they are modeled using the second-order TF (6.4).

Overall, the longitudinal dynamics are more affected than the lateral dynamics by the choice of actuator dynamics. This is shown in Figure 8.36, where the roll angle tracking of the GSTA design is almost unchanged for the different actuator dynamics, with the tracking performance being only slightly worse for the second-order dynamics than for the first-order dynamics. The GMSTA design is the one exception, as its tracking performance is clearly degraded when using the slower first-order dynamics than the second-order dynamics. This is also reflected in the error measures presented in Table 8.4 where the

decrease in the error measures for the first-order dynamics to the second-order dynamics is substantial for the GMSTA design.

Interestingly, the saturation and the GSTA designs perform much better than the MSAT and the GMSTA for the first-order dynamics, while the error measures increase for both SISO designs when using the second-order dynamics. The increase of the error measures for the saturation control design is especially big compared to the increase for the GSTA design. The change in error measures from using the first-order dynamics to using the second-order dynamics is also reflected in the pitch tracking results of the control designs, which are shown in Figure 8.37.

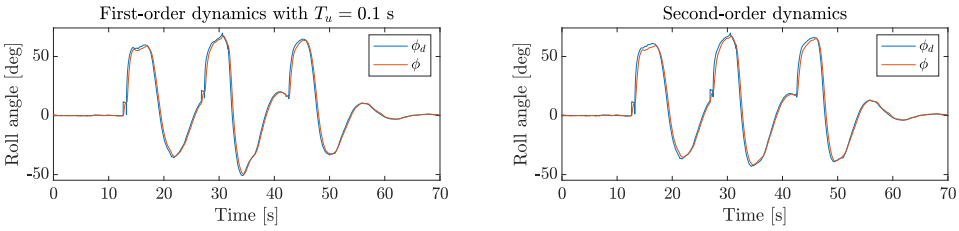

(a) The GSTA design.

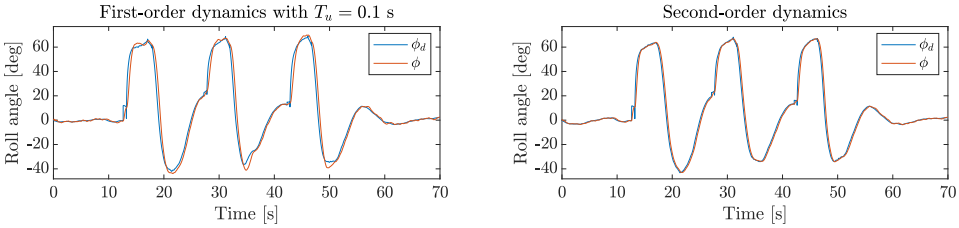

(b) The GMSTA design.

Figure 8.36: The roll angle tracking results for the GSTA and the GMSTA control designs for case 2 when the actuator dynamics are modeled using the first-order TF (6.16) with $T_u = 0.1$ s, and when they are modeled using the second-order TF (6.4).

Case 2 when using first-order actuator dynamics with $T_u = 0.1$ s				
Performance measure	**Saturation design**	**GSTA**	**MSAT**	**GMSTA**
Total ISE	$\mathbf{9.754 \cdot 10^2}$	$1.141 \cdot 10^3$	$2.240 \cdot 10^3$	$2.299 \cdot 10^3$
Total IAE	$\mathbf{1.694 \cdot 10^2}$	$1.863 \cdot 10^2$	$2.504 \cdot 10^2$	$2.402 \cdot 10^2$
Total ISI	$\mathbf{1.438 \cdot 10^3}$	$1.479 \cdot 10^3$	$1.594 \cdot 10^3$	$1.734 \cdot 10^3$
Total IAI	$\mathbf{2.937 \cdot 10^2}$	$2.943 \cdot 10^2$	$3.211 \cdot 10^2$	$3.307 \cdot 10^2$
Case 2 when using second-order actuator dynamics				
Performance measure	**Saturation design**	**GSTA**	**MSAT**	**GMSTA**
Total ISE	$1.292 \cdot 10^3$	$1.153 \cdot 10^3$	$1.882 \cdot 10^3$	$\mathbf{9.002 \cdot 10^2}$
Total IAE	$1.924 \cdot 10^2$	$1.695 \cdot 10^2$	$2.276 \cdot 10^2$	$\mathbf{1.463 \cdot 10^2}$
Total ISI	$1.442 \cdot 10^3$	$\mathbf{1.433 \cdot 10^3}$	$1.536 \cdot 10^3$	$1.639 \cdot 10^3$
Total IAI	$2.969 \cdot 10^2$	$\mathbf{2.951 \cdot 10^2}$	$3.159 \cdot 10^2$	$3.315 \cdot 10^2$

Table 8.4: Performance measures for the saturation, the GSTA, the MSAT and the GMSTA control design for simulation case 2 for different actuator dynamics.

Figure 8.37 shows the reason for the smoothness of the flight paths for the second-order dynamics compared to the first-order dynamics, as the changes in the pitch reference are much larger for the first-order dynamics. This is especially noticeable for the second-order control designs, i.e. the GSTA and the GMSTA designs, compared to the first-order saturation and MSAT control designs. Even though the pitch tracking performances of the saturation and the GSTA designs are slightly better for the second-order dynamics than for first-order dynamics, the error measures are higher for the second-order dynamics. This is probably due to the roll tracking performance, which in Figure 8.36 is shown to be slightly worse for the GSTA design when using the second-order dynamics. On the other hand, the pitch tracking results in Figure 8.37 show that the performance of the MSAT and the GMSTA designs is better for the second-order dynamics, which agrees with the error measures presented in Table 8.4.

Furthermore, the MSAT and the GMSTA still generate yaw rates that correspond to the yaw rate generated by the coordinated-turn equation (6.23), which means that the desired dynamics are achieved by enforcing the sliding mode in the system. The yaw rates generated by the MSAT and the GMSTA designs are shown in Figure 8.38. Figure 8.38 shows that the yaw rate generated by the GMSTA for the first-order dynamics is much further from the coordinated-turn yaw rate than the yaw rate generated when using the second-order dynamics. Additionally, the yaw rates generated by both control designs when using the second-order dynamics are smoother than the ones generated when using the first-order actuator dynamics. This implies that the sliding variables for the second-order dynamics are less smooth than the sliding variables for the first-order dynamics, which is investigated

in the next subsection.

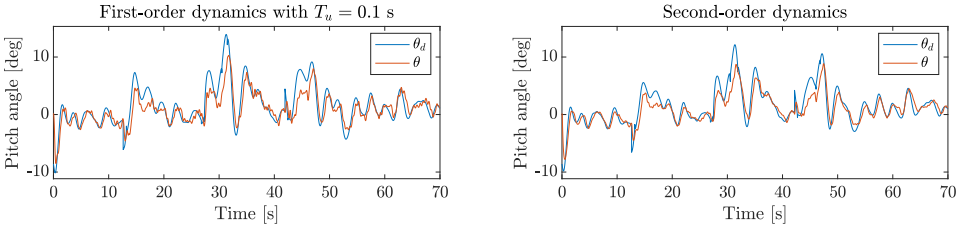

(a) The saturation control design.

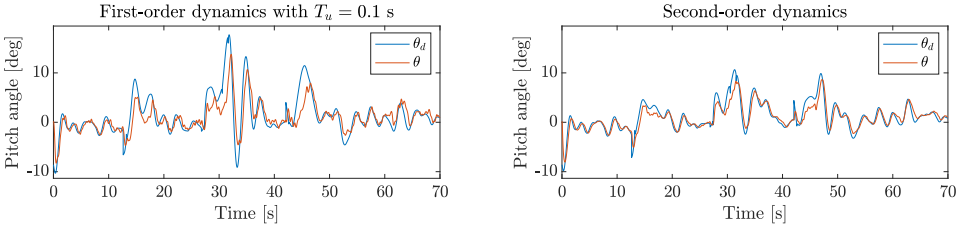

(b) The GSTA design.

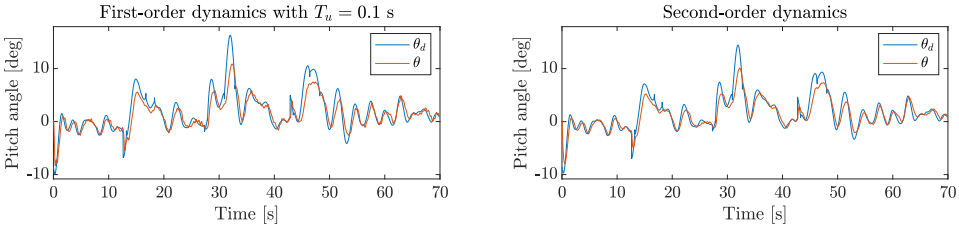

(c) The MSAT control design.

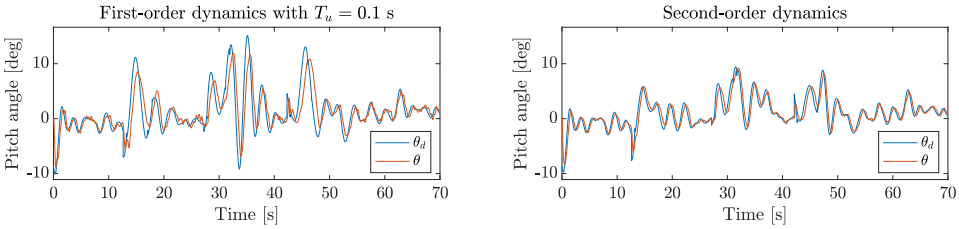

(d) The GMSTA design.

Figure 8.37: The pitch angle tracking results for the saturation, the GSTA, the MSAT, and the GMSTA control designs for case 2 when the actuator dynamics are modeled using the first-order TF (6.16) with $T_u = 0.1$ s, and when they are modeled using the second-order TF (6.4).

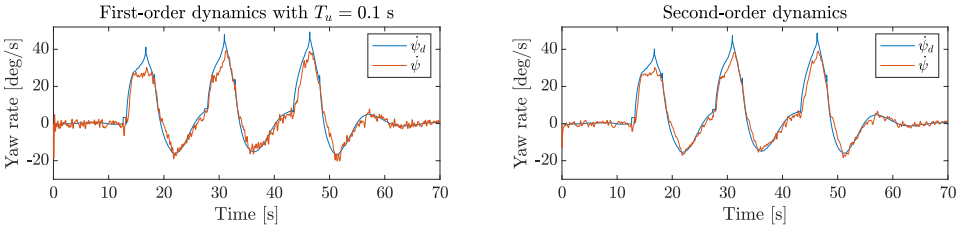

(a) The MSAT control design.

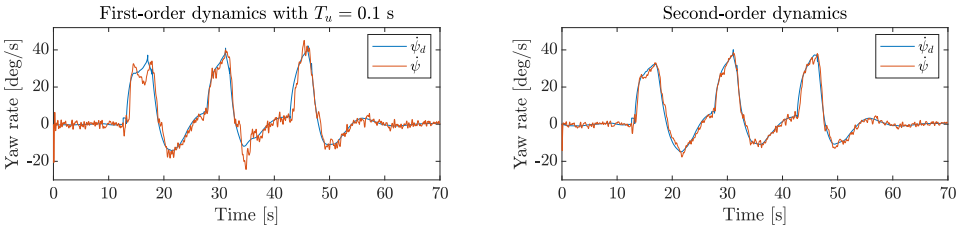

(b) The GMSTA design.

Figure 8.38: The yaw rate in the inertial frame, $\dot{\psi}$, for the MSAT and the GMSTA control designs compared to the inertial yaw rate generated by the coordinated-turn equation (6.23) for simulation case 2 when the actuator dynamics are modeled using the first-order TF (6.16) with $T_u = 0.1$ s, and when they are modeled using the second-order TF (6.4).

8.6.2 Sliding Variable

The sliding variables generated by the saturation and the GSTA control designs for the first- and second-order actuator dynamics are shown in Figure 8.39 and for the MSAT and the GMSTA control designs in Figure 8.40.

For the first-order actuator dynamics, the sliding variable produced by the saturation control design is slightly smoother than the sliding variable produced by the GSTA design, and the lateral and longitudinal sliding modes are enforced only slightly better by the saturation control design than by the GSTA design. This makes sense as the error measures are lower for the saturation control design than for the GSTA design when using first-order dynamics. For the second-order dynamics, on the other hand, the GSTA design is slightly better at enforcing the sliding modes in the system, and produces a smoother sliding variable, than the saturation control design, which also agrees with the error measures in Table 8.4, which are smaller for the GSTA than for the saturation control design when using the second-order dynamics. Both sliding variables have the same amount of chattering in σ_ϕ for both types of actuator dynamics, and both are free of chattering in σ_θ.

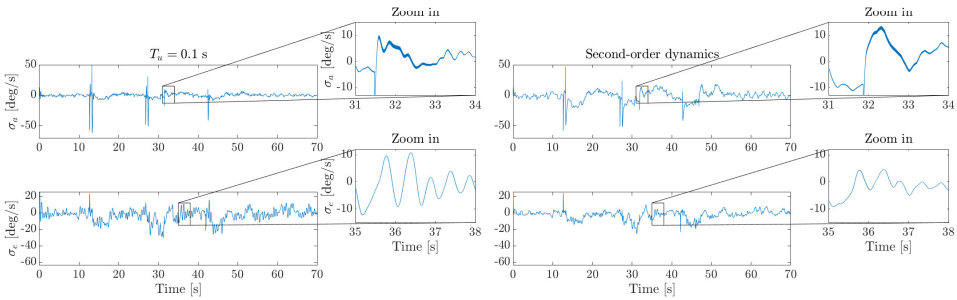

(a) The sliding variable for the saturation control design.

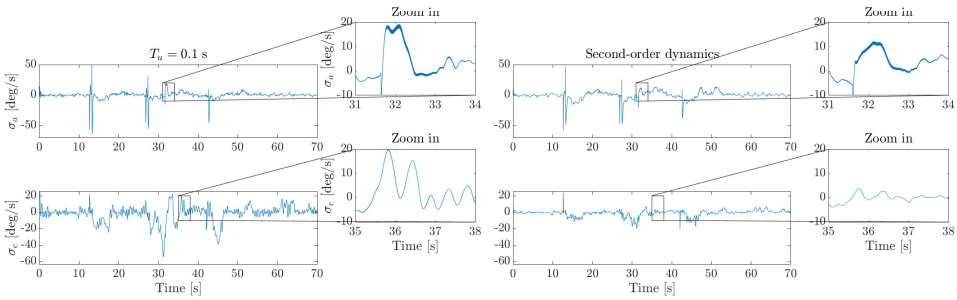

(b) The sliding variable for the GSTA control design.

Figure 8.39: The sliding variables for the saturation and the GSTA control designs for case 2 when the actuator dynamics are modeled using the first-order TF (6.16) with $T_u = 0.1$ s, and when they are modeled using the second-order TF (6.4).

Figure 8.40 shows that the sliding variables produced by the MSAT and the GMSTA designs for the first-order dynamics are similar in smoothness, except for σ_2 which has more oscillations for the GMSTA design than for the MSAT control design. However, the sliding variable produced by the GMSTA design has several large peaks that are larger than the peaks in the sliding variable for the MSAT control design. The reduction in the size and amount of oscillations in the sliding variables produced for the second-order dynamics compared to the first-order dynamics is approximately the same for both control designs. The peaks in the sliding variable for the MSAT control design are slightly smaller for the second-order dynamics, while the peaks in the sliding variable for the GMSTA design are almost gone. Thus, the GMSTA design is much better than the MSAT control design at enforcing the sliding mode in the system when using second-order actuator dynamics. This agrees with the error measures in Table 8.4, which are slightly higher for the GMSTA than for the MSAT control design when using the first-order dynamics, while the situation is reversed for the second-order dynamics, with the GMSTA design having substantially smaller error measures than the MSAT control design.

Both sliding variables in Figure 8.40 contain little to no chattering, with σ_1 being the

only component of the sliding variable where chattering is present. However, σ_1 generated by the MSAT control design contains slightly more chattering than σ_1 produced by the GMSTA design for both kinds of actuator dynamics.

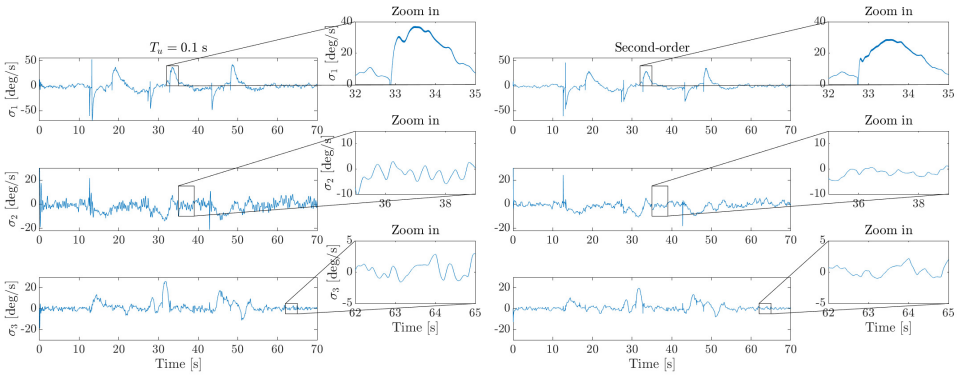

(a) The sliding variable for the MSAT control design.

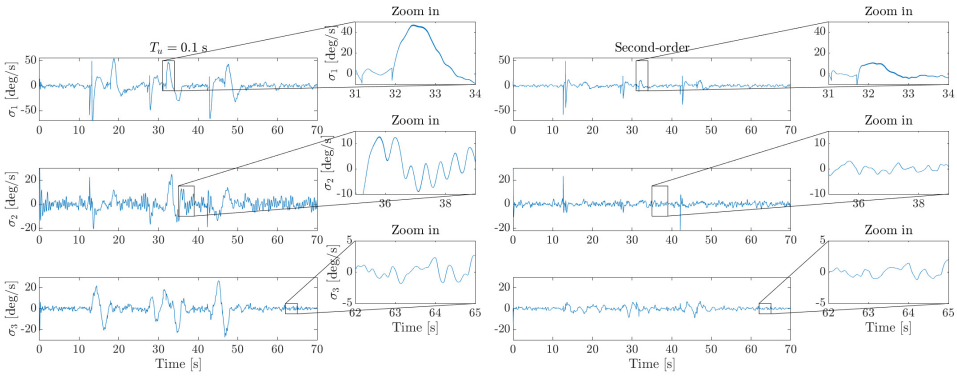

(b) The sliding variable for the GMSTA control design.

Figure 8.40: The sliding variables for the MSAT and the GMSTA control designs for case 2 when the actuator dynamics are modeled using the first-order TF (6.16) with $T_u = 0.1$ s, and when they are modeled using the second-order TF (6.4).

8.6.3 Control Input

The control inputs generated for both types of actuator dynamics by the saturation and the GMSTA control designs are shown in Figure 8.41. The GMSTA is the control design with input use measures that are among the highest in Table 8.4 for both the second- and first-order actuator dynamics, while the saturation control design has input measures that are among the smallest for both kinds of actuator dynamics. Even so, the GMSTA control design produces a control input that is smoother than the one produced by the saturation control design for the second-order dynamics, which means that the large input

use measures for the GMSTA design are due to the large peaks in the control signals, which is not necessarily a bad thing, as they are well within the control deflection limit of ± 30 deg.

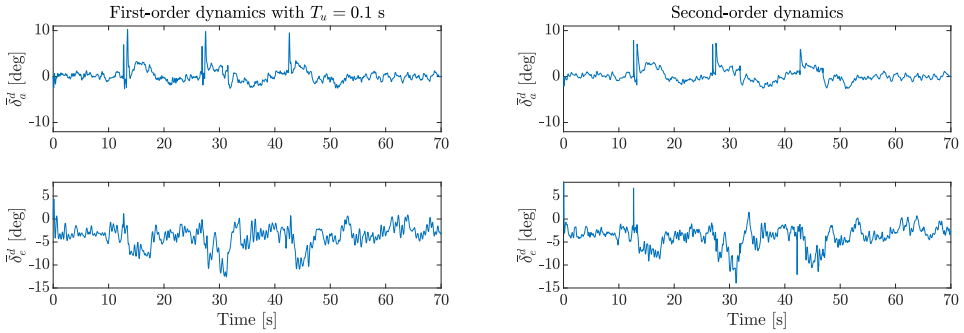

(a) The saturation control design.

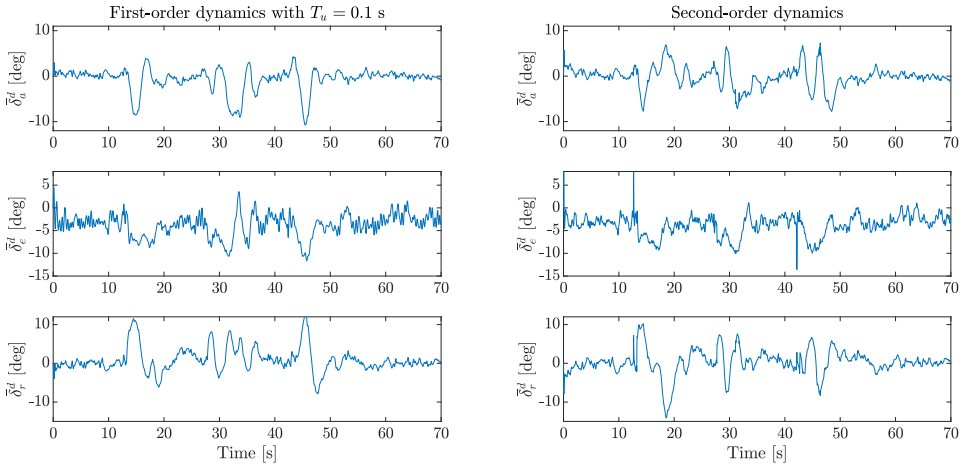

(b) The GMSTA design.

Figure 8.41: The control input generated by the saturation and the GMSTA control designs for case 2 when the actuator dynamics are modeled using the first-order TF (6.16) with $T_u = 0.1$ s, and when they are modeled using the second-order TF (6.4).

The control commands generated by the GSTA and the MSAT control designs for the first-order dynamics are presented in Figure 8.42, where the control command generated by the control system is compared with the control input to the UAV model. Firstly, the control command produced by the GSTA design contains too many oscillations to be feasible, even after the oscillations have been attenuated by the actuator dynamics. The MSAT produces a more feasible control input, but some oscillations still remain.

Furthermore, the commanded control signal generated by the GSTA design contains more chattering than the control command produced by the MSAT control design, which contains only some minor chattering. However, the final control input to the UAV model

is free of chattering for both control designs.

The commanded control and the final control inputs generated by the GSTA and the MSAT control designs are also investigated for the case when the second-order actuator dynamics are used. These results can be found in Figure 8.43. The control commands generated by the control designs are substantially smoother for the second-order dynamics than for the first-order dynamics, so the control inputs generated for the second-order dynamics are much more realizable than the control input for the first-order dynamics. However, the control input produced by the GSTA design contains more oscillations than the control input produced by the MSAT control design.

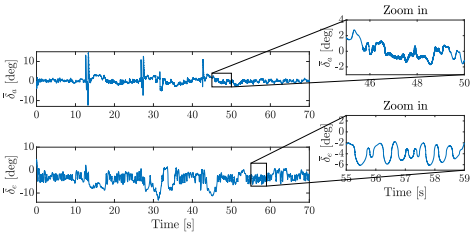

(a) The control command generated by the GSTA design.

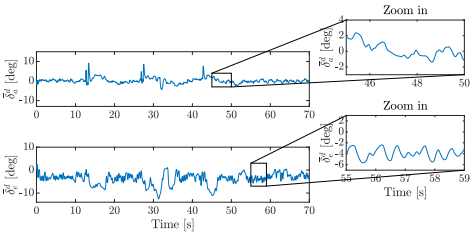

(b) The control input generated by the GSTA design.

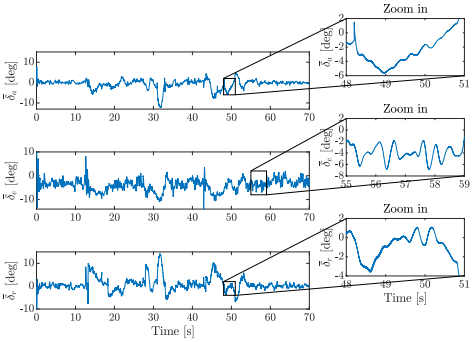

(c) The control command generated by the MSAT control design.

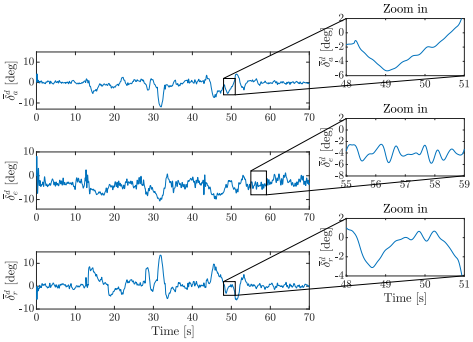

(d) The control input generated by the MSAT control design.

Figure 8.42: The commanded control signal $\bar{u}$ generated by the GSTA and the MSAT control designs compared to the control input to the UAV model $\bar{u}^d$ for case 2 when the actuator dynamics are modeled using the first-order TF (6.16) with $T_u = 0.1$ s.

There is some chattering in the control commands produced by the GSTA and the MSAT control designs for the second-order dynamics, but it is less than the chattering contained in the control commands produced for the first-order actuator dynamics. As for the case when the first-order dynamics is used, the control input to the model does not contain any chattering.

Overall, using the second-order dynamics produce the best results in terms of smoothness of the control input for the control designs considered in this section. Additionally, the SISO designs are much more robust to the slower first-order dynamics than the MIMO control designs, while the MIMO designs are more robust than the SISO designs to the

more complex second-order dynamics.

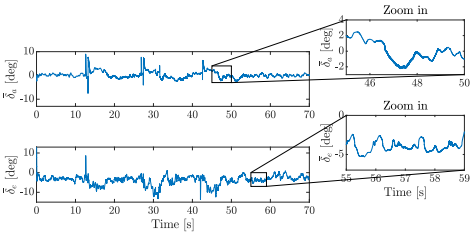

(a) The control command generated by the GSTA design.

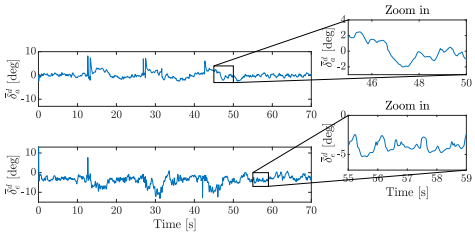

(b) The control input generated by the GSTA design.

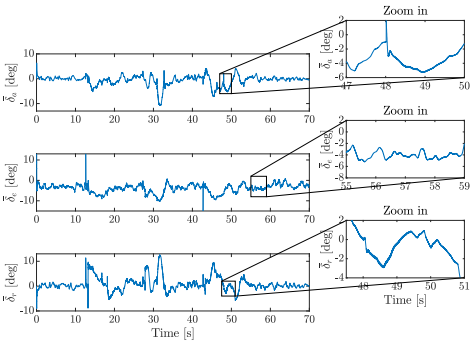

(c) The control command generated by the MSAT control design.

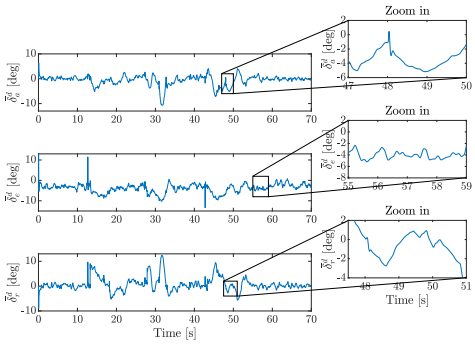

(d) The control input generated by the MSAT control design.

Figure 8.43: The commanded control signal $\bar{u}$ generated by the GSTA and the MSAT control designs compared to the control input to the UAV model $\bar{u}^d$ for case 2 when the actuator dynamics are modeled using the second-order TF (6.4).

8.7 Sensitivity to the Choice Sampling Frequency

In this section, the sensitivity of some of the saturation, the GSTA, the MSAT, and the GMSTA to the sampling frequency of the continuous state and to the fixed sampling frequency of the controller is investigated. In the previous simulation results presented in this chapter, the sampling frequency is chosen as $f_s = 200$ Hz, which is quite high so it is interesting to see whether the control designs still produce adequate results for lower sampling frequencies.

This section presents a comparison of the simulation results for case 2 for when the sampling frequency is $f_s = 100$ Hz, and when it is $f_s = 20$ Hz. The control gains that are used for $f_s = 100$ Hz are the same as for case 2, and can be found in subsection D.2.1 and subsection D.2.2, while the control gains for when $f_s = 20$ Hz can be found in subsection D.2.4.

8.7.1 Tracking Results

The flight paths of the saturation, the GSTA, the MSAT, and the GMSTA designs can be found in Figure 8.44 for the case when the sampling frequency is $f_s = 100$ Hz and $f_s = 20$ Hz. Figure 8.44 shows that the flight paths of the control designs are very similar when $f_s = 100$ Hz, while the difference between the flight paths is more noticeable when $f_s = 20$ Hz. Even so, the flight paths are generally quite smooth for both sampling frequencies, with a slight increase in the size of the oscillations in the pitch reference signal when $f_s = 20$ Hz.

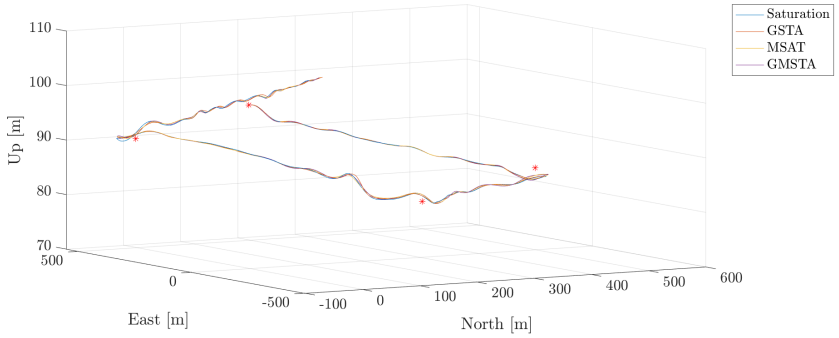

(a) The flight paths when $f_s = 100$ Hz.

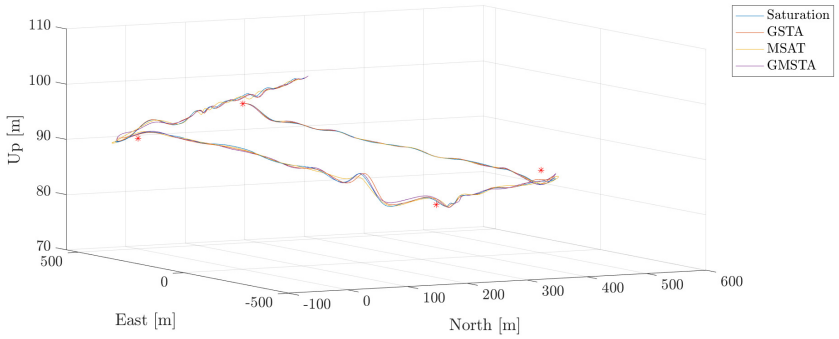

(b) The flight paths when $f_s = 20$ Hz.

Figure 8.44: The flight paths of the saturation, the GSTA, the MSAT, and the GMSTA control designs for case 2 when using a sampling frequency of $f_s = 100$ Hz, and $f_s = 20$ Hz.

Also for a change in sampling frequency, the longitudinal dynamics are more affected by the lateral dynamics, but there is a minor change in the roll tracking results as well. This can be seen in Figure 8.45, where the roll tracking results for the GSTA and the GMSTA designs for $f_s = 100$ Hz and $f_s = 20$ Hz are presented. The roll tracking performance of the GSTA design is clearly more affected than the performance of the GMSTA design by the reduction in sampling frequency. Both control designs track the roll angle well when $f_s = 100$ Hz, while the GSTA does not track the reference as well as the GMSTA

design when $f_s = 20$ Hz. Even so, the tracking results of both designs for both sampling frequencies are adequate.

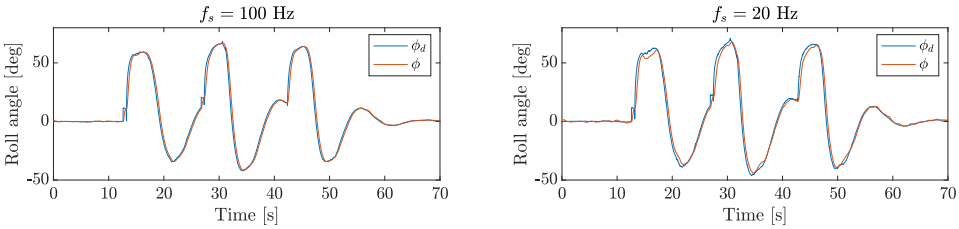

(a) The GSTA design.

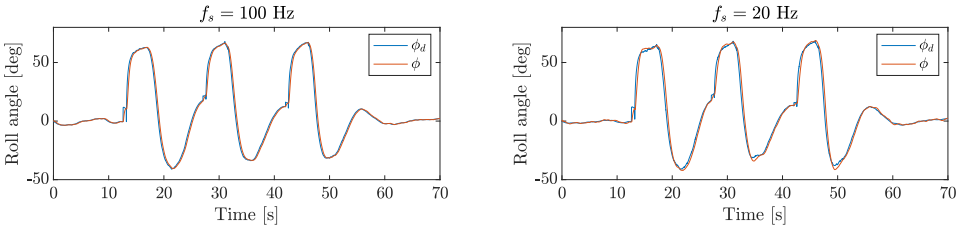

(b) The GMSTA design.

Figure 8.45: The roll angle tracking results for the GSTA and the GMSTA control designs for case 2 when using a sampling frequency of $f_s = 100$ Hz, and $f_s = 20$ Hz.

The change in tracking performance for the different sampling frequencies is reflected in the error measures presented in Table 8.5, which show that the error measures for $f_s = 100$ Hz are only slightly higher than for the case 2 performance measures presented in Table 8.1 and Table 8.2. However, there is an increase in the error measures for all the control designs considered in this section when $f_s = 20$ Hz.

The increase in error measures is not only due to a worsened roll tracking performance but also to a change in the pitch tracking performance, which can be seen in Figure 8.46. When $f_s = 100$ Hz, all control designs track the pitch reference well, with the tracking performance of the GMSTA being the best. However, the performances of all the control designs experience a loss in accuracy when the sampling frequency is $f_s = 20$ Hz. The tracking of the pitch reference is still acceptable for all the control designs, but there is a clearer latency in the tracking results for $f_s = 20$ Hz than for $f_s = 100$ Hz. This is expected as a decrease in sampling frequency will delay the response of the control design to changes in the continuous state of the UAV model, and the change in control deflections based on the commands generated in the control system.

Case 2 when $f_s = 100$ Hz				
Performance measure	**Saturation design**	**GSTA**	**MSAT**	**GMSTA**
Total ISE	$1.102 \cdot 10^3$	$1.028 \cdot 10^3$	$1.183 \cdot 10^3$	$\mathbf{7.943 \cdot 10^2}$
Total IAE	$1.546 \cdot 10^2$	$1.546 \cdot 10^2$	$1.732 \cdot 10^2$	$\mathbf{1.358 \cdot 10^2}$
Total ISI	$1.442 \cdot 10^3$	$\mathbf{1.402 \cdot 10^3}$	$1.592 \cdot 10^3$	$1.608 \cdot 10^3$
Total IAI	$2.961 \cdot 10^2$	$\mathbf{2.910 \cdot 10^2}$	$3.134 \cdot 10^2$	$3.331 \cdot 10^2$

Case 2 when $f_s = 20$ Hz				
Performance measure	**Saturation design**	**GSTA**	**MSAT**	**GMSTA**
Total ISE	$1.878 \cdot 10^3$	$1.785 \cdot 10^3$	$2.047 \cdot 10^3$	$\mathbf{1.301 \cdot 10^3}$
Total IAE	$2.518 \cdot 10^2$	$2.236 \cdot 10^2$	$2.236 \cdot 10^2$	$\mathbf{1.787 \cdot 10^2}$
Total ISI	$\mathbf{1.462 \cdot 10^3}$	$1.465 \cdot 10^3$	$1.580 \cdot 10^3$	$1.614 \cdot 10^3$
Total IAI	$2.993 \cdot 10^2$	$\mathbf{2.973 \cdot 10^2}$	$3.191 \cdot 10^2$	$3.207 \cdot 10^2$

Table 8.5: Performance measures for the saturation, the GSTA, the MSAT and the GMSTA control design for simulation case 2 for different sampling frequencies.

Furthermore, the pitch tracking results in Figure 8.46 shows the increase in oscillations for $f_s = 20$ Hz in the pitch reference that causes the change in flight paths from when $f_s = 100$ Hz to $f_s = 20$ Hz in Figure 8.44. The increase in the number and size of oscillations in the pitch reference is probably due to the latency in the response that occurs when $f_s = 20$ Hz, which causes the altitude hold controller (6.18) in the waypoint follower system to compensate for the altitude error by generating a larger desired pitch angle.

The MSAT and the GMSTA still generate yaw rates that correspond to the yaw rate generated by the coordinated-turn equation (6.23), which means that the desired dynamics are achieved by enforcing the sliding mode in the system. The yaw rates generated by the MSAT and the GMSTA designs are shown in Figure 8.47. In Figure 8.47 it is shown that the generated yaw rates correspond to the yaw rate from the coordinated-turn equation to a higher degree when $f_s = 100$ Hz than when $f_s = 20$ Hz. Additionally, there yaw rates generated when $f_s = 20$ Hz are smoother when $f_s = 100$ Hz than when $f_s = 20$ Hz.

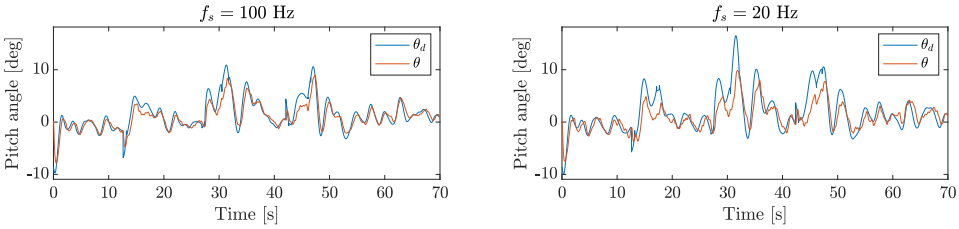

(a) The saturation control design.

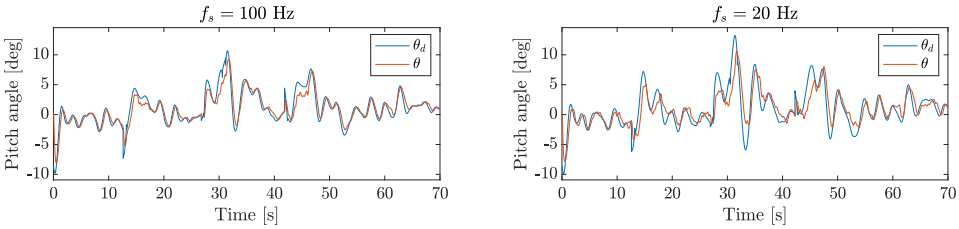

(b) The GSTA design.

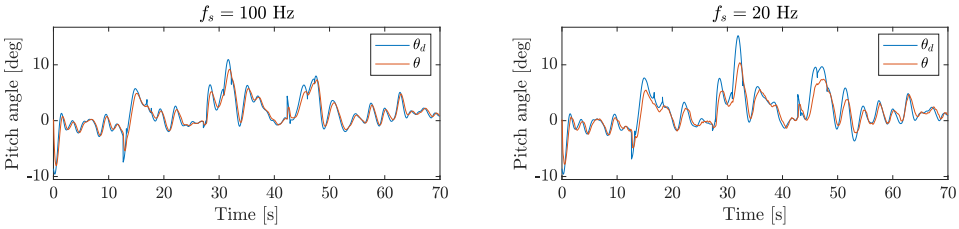

(c) The MSAT control design.

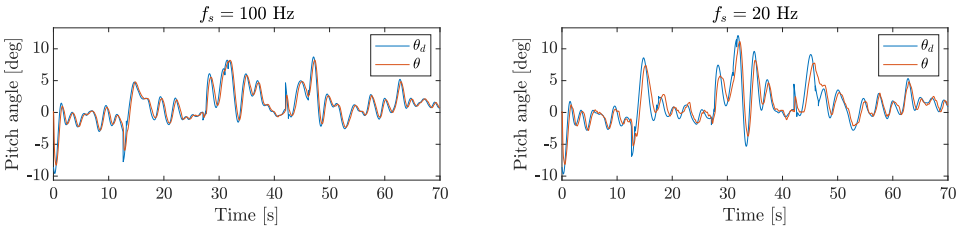

(d) The GMSTA design.

Figure 8.46: The pitch angle tracking results for the saturation, the GSTA, the MSAT, and the GMSTA control designs for case 2 when using a sampling frequency of $f_s = 100$ Hz, and $f_s = 20$ Hz.

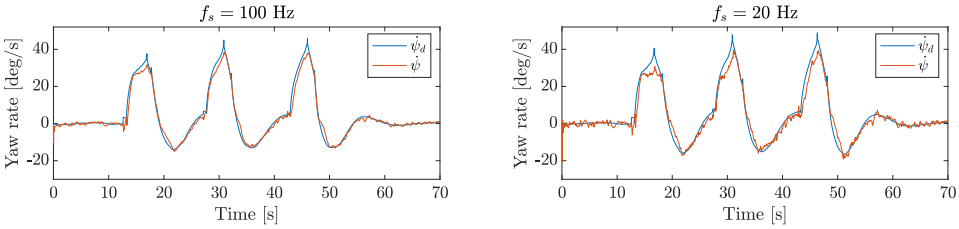

(a) The MSAT control design.

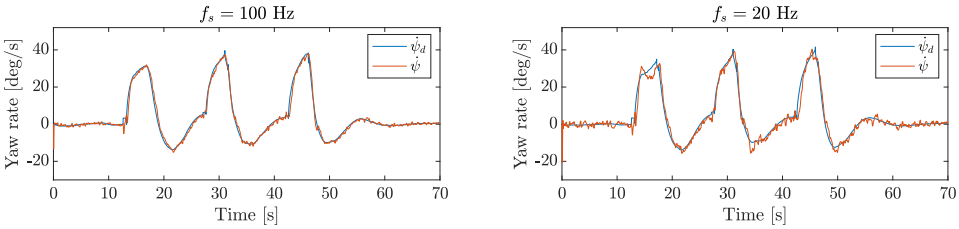

(b) The GMSTA design.

Figure 8.47: The yaw rate in the inertial frame, $\dot{\psi}$, for the MSAT and the GMSTA control designs compared to the inertial yaw rate generated by the coordinated-turn equation (6.23) for simulation case 2 when using a sampling frequency of $f_s = 100$ Hz, and $f_s = 20$ Hz.

8.7.2 Sliding Variable

The sliding variables generated by the saturation and the GSTA control designs for the first- and second-order actuator dynamics are shown in Figure 8.48 and for the MSAT and the GMSTA control designs in Figure 8.49.

Figure 8.48 shows that when $f_s = 100$ Hz, the sliding variables for the saturation and the GSTA control designs are very similar to the sliding variables for case 2 presented in subsection 8.2.1. The sliding variables contain some chattering when $f_s = 100$ Hz, with σ_ϕ containing more chattering than σ_θ. This is probably due to the control gains for the lateral controller being more aggressive than the control gains for the longitudinal control gains. When $f_s = 100$ Hz, the GSTA design is better than the saturation control design at enforcing the sliding mode in the system. This agrees with the error measures in Table 8.5, which are lower for the GSTA design than for the saturation control design when $f_s = 100$ Hz. The same is also the case for $f_s = 20$ Hz, where the GSTA design is still slightly better at enforcing the sliding mode in the system, which corresponds to the GSTA design having smaller error measures than the saturation control design when $f_s = 20$ Hz.

When $f_s = 20$ Hz, there is an increase in the amount of chattering in the sliding variables, as well as in the size of the chattering. However, the frequency of the chattering is now lower than when $f_s = 100$ Hz. Both the saturation and the GSTA control designs have more oscillations and struggle more at enforcing the sliding mode in the system when $f_s = 20$ Hz than when $f_s = 100$ Hz.

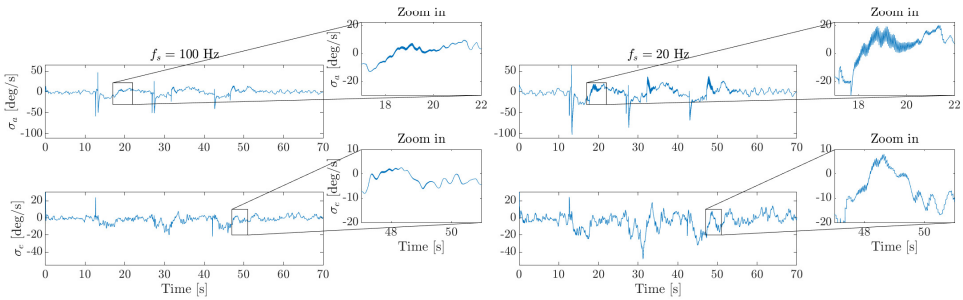

(a) The sliding variable for the saturation control design.

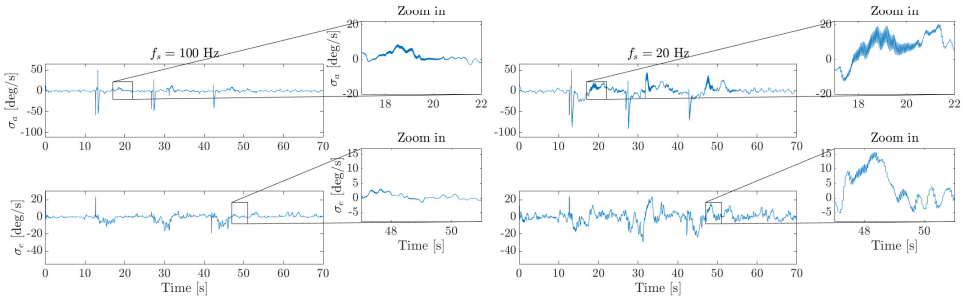

(b) The sliding variable for the GSTA control design.

Figure 8.48: The sliding variables for the saturation and the GSTA control designs for case 2 when using a sampling frequency of $f_s = 100$ Hz, and $f_s = 20$ Hz.

The sliding variables for the MSAT and the GMSTA control designs are shown in Figure 8.49, where we can see that the sliding variables for the MIMO control designs are smoother and that the designs are better at enforcing the sliding mode in the system than the SISO control designs by comparing Figure 8.48 and Figure 8.49. This is the case for both $f_s = 100$ Hz and $f_s = 20$ Hz. The sliding variables for both the SISO and MIMO designs contain approximately the same amount of chattering when $f_s = 100$ Hz. However, there is a difference between the sliding variables when $f_s = 20$ Hz, which is that the chattering in σ_ϕ and σ_θ has a higher frequency than the chattering in the components of σ.

The sliding variables for the MSAT and GMSTA control designs are very similar when $f_s = 100$ Hz, and when $f_s = 20$ Hz, which can be seen in Figure 8.49. However, there are some differences between them. Firstly, the sizes of the peaks in the sliding variable for the MSAT control design are slightly larger than for the GMSTA design when $f_s = 100$ Hz, and in σ_1 when $f_s = 20$ Hz. Secondly, the GMSTA is slightly better at enforcing the sliding mode in the system when $f_s = 100$ Hz. This makes sense, as the error measures for the GMSTA design are smaller than those for the MSAT control design both when $f_s = 100$ Hz and when $f_s = 20$ Hz.

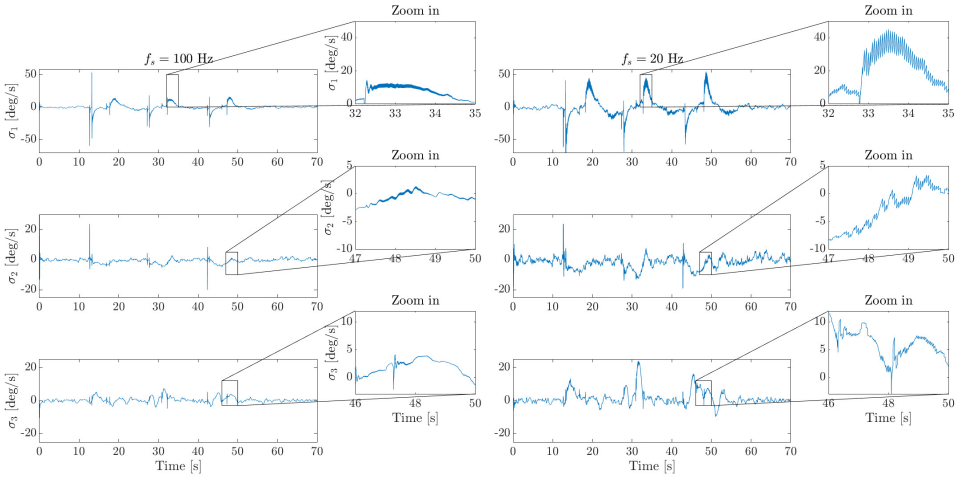

(a) The sliding variable for the MSAT control design.

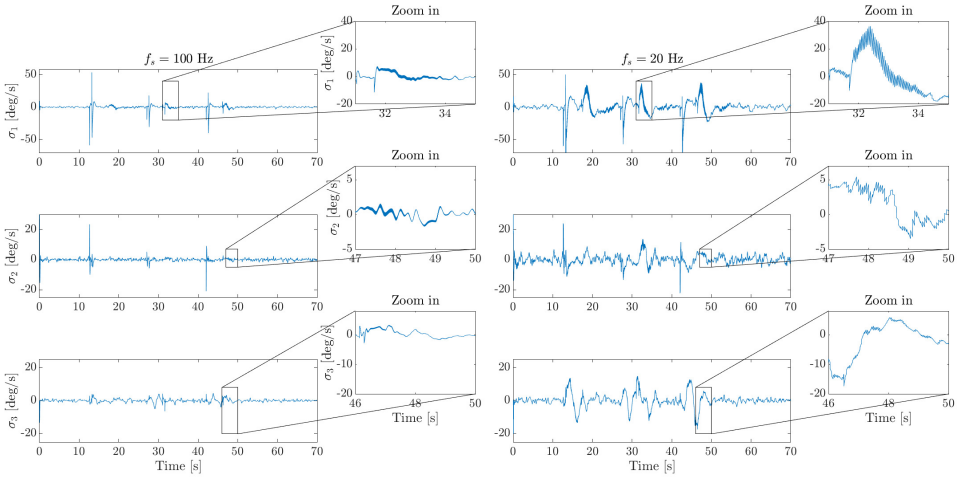

(b) The sliding variable for the GMSTA control design.

Figure 8.49: The sliding variables for the MSAT and the GMSTA control designs for case 2 when using a sampling frequency of $f_s = 100$ Hz, and $f_s = 20$ Hz.

8.7.3 Control Input

The control inputs generated for both sampling frequencies by the saturation and the MSAT control designs are shown in Figure 8.50. The saturation control design has smaller input use measures than the MSAT design both for $f_s = 100$ Hz and $f_s = 20$ Hz, which can be seen in Table 8.5. Even so, the MSAT control design produces an elevator control

input that is smoother than the elevator control input produced by the saturation control signal when $f_s = 100$ Hz. Thus, the high input use measures of the MSAT is probably due to the peaks in the control input, which is characteristic for the control input generated by the MIMO control designs, which can be seen in subsection 8.3.3. When $f_s = 20$ Hz, however, the control input produced by the saturation control design appears to be smoother than the input produced by the MSAT control design.

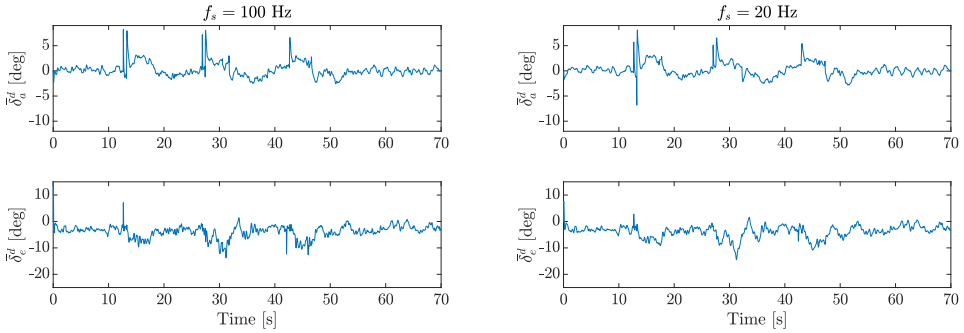

(a) The saturation control design.

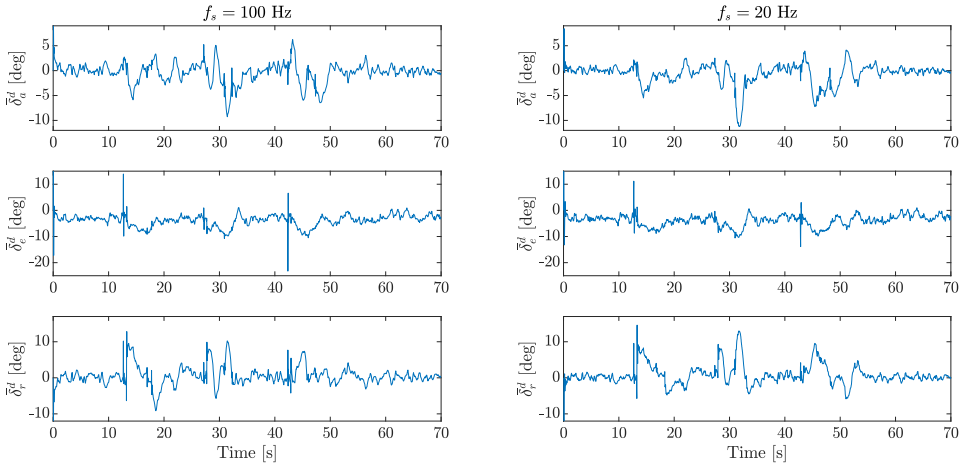

(b) The MSAT control design.

Figure 8.50: The control input generated by the saturation and the GMSTA control designs for case 2 when using a sampling frequency of $f_s = 100$ Hz, and $f_s = 20$ Hz.

The control command generated by the GSTA and the GMSTA control designs, $\bar{u}$, when $f_s = 100$ Hz are presented in Figure 8.51, where the control command generated by the control system is compared with the delayed and sampled control input to the UAV model after the actuator dynamics and measurements, $\bar{u}^d$. The control input generated by the GMSTA design is slightly smoother than the control input generated by the GSTA design, both before and after the actuator dynamics and measurements. Furthermore, the commanded control signal generated by the GSTA design contains more chattering than

the control command produced by the GMSTA design. However, the final control input to the UAV model is free of chattering for both control designs.

The commanded control and the final control input generated by the GSTA and the GMSTA designs are also investigated for the case when $f_s = 20$ Hz. These results can be found in Figure 8.52. The final control inputs to the UAV model have approximately the same degree of smoothness when $f_s = 20$ Hz as when $f_s = 100$ Hz for both the GSTA and the GMSTA designs, with the control input produced by the GMSTA design being smoother than the input produced by the GSTA design also for $f_s = 20$ Hz. Additionally, there is an increase in the amount of chattering in the commanded control signal generated by the control systems from when $f_s = 100$ Hz to when $f_s = 20$ Hz for both control designs. Also for $f_s = 20$ Hz, the GSTA design produces a control signal that contains more chattering than the control produced by the GMSTA design. However, as for $f_s = 100$ Hz, the control input generated by both the GSTA and the GMSTA designs are free of chattering, which is attenuated by the actuator dynamics and measurements.

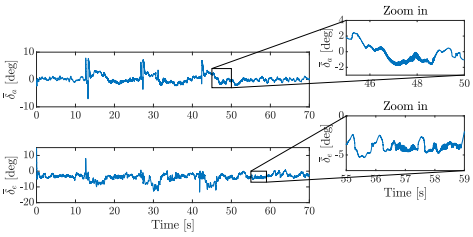

(a) The control command produced by the GSTA design.

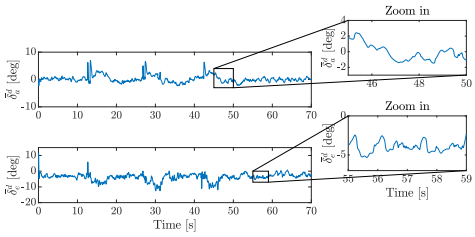

(b) The control input produced by the GSTA design.

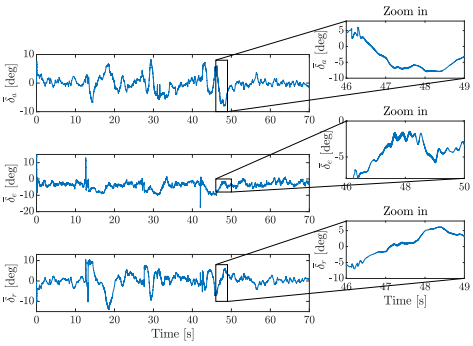

(c) The control command produced by the GMSTA design.

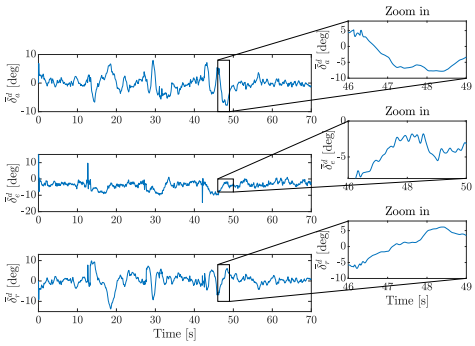

(d) The control input produced by GMSTA design.

Figure 8.51: The commanded control signal $\bar{u}$ generated by the GSTA and the GMSTA control designs compared to the control input to the UAV model $\bar{u}^d$ for case 2 when using a sampling frequency of $f_s = 100$ Hz, and $f_s = 20$ Hz.

Overall, the control designs considered in this section are capable of tracking the roll and pitch references while still producing acceptable control signals for both $f_s = 100$ Hz and $f_s = 20$ Hz without any chattering in the control input to the UAV model,$\bar{u}^d$.

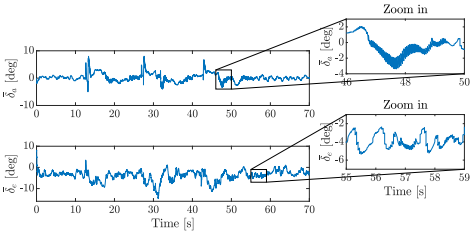

(a) The control command produced by the GSTA design.

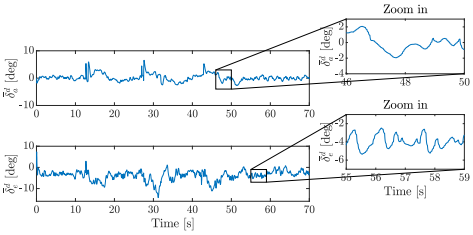

(b) The control input produced by the GSTA design.

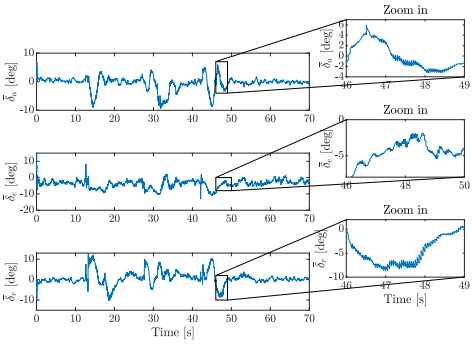

(c) The control command produced by the GMSTA design.

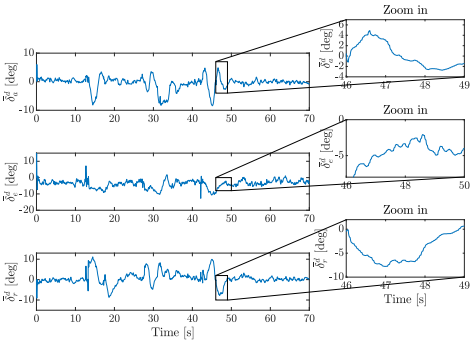

(d) The control input produced by GMSTA design.

Figure 8.52: The commanded control signal $\bar{u}$ generated by the GSTA and the MSAT control designs compared to the control input to the UAV model $\bar{u}^d$ for case 2 when using a sampling frequency of $f_s = 100$ Hz, and $f_s = 20$ Hz.

8.8 Sensitivity to Modeling Uncertainties

In this chapter, every simulation is done with a 20% uncertainty in the sliding dynamics matrix $b(t, x)$, which is used in the transformation

$$\bar{u} = b^{-1}(t, x)u,$$

where $\bar{u}$ is the control command produced by the control system before actuator dynamics and measurements. For the longitudinal dynamics discussed in the previous chapter, an analysis of the performance of the controllers is performed for when b is known, b is uncertain, and for when only the sign of b is known. As the results of using an uncertain b are more beneficial than using only the sign of b in the transformation above for the longitudinal dynamics, the control designs for the 6DOF model is implemented with an uncertain b. However, it is interesting to investigate the performance of the control designs when using an exactly known b compared to an uncertain b. For the SISO control designs, this means that $b_\phi(t, x)$ and $b_\theta(t, x)$ are known. In this section, the performance measures for simulations case 2 are presented for all the SISO and MIMO control design for both the case when there are modeling uncertainties present in the system and for when there

is not. The performance measures for the case of an uncertain b, or b_ϕ and b_θ, are thus the same as the ones presented in Table 8.2 and Table 8.1, respectively. The control gains used for the simulations when b is known are the same as the ones used in the case 2 simulations presented earlier in this chapter and can be found in section D.2.

The performance measures for the SISO control designs are presented in 8.6. Even though the control designs are tuned using the uncertain matrices b_ϕ and b_θ, all the control designs perform better when the matrices are known while using almost exactly the same amount of input. This is as expected following the discussion of the longitudinal control coefficient transformation results in section 7.7, where the controllers generally performed better when b_θ is known. However, the decrease in error measures is minor for the SISO control designs, which shows that they are quite robust to modeling uncertainties.

Uncertain $b_\phi(t,x)$ and $b_\theta(t,x)$				
Performance measure	**Saturation Controller**	**STA**	**ASTA**	**GSTA**
Total ISE	$1.152 \cdot 10^3$	$1.157 \cdot 10^3$	$1.162 \cdot 10^3$	$\mathbf{1.016 \cdot 10^2}$
Total IAE	$1.766 \cdot 10^2$	$1.543 \cdot 10^2$	$1.567 \cdot 10^2$	$\mathbf{1.541 \cdot 10^2}$
Total ISI	$1.439 \cdot 10^3$	$1.396 \cdot 10^3$	$\mathbf{1.392 \cdot 10^3}$	$1.401 \cdot 10^3$
Total IAI	$2.959 \cdot 10^2$	$2.902 \cdot 10^2$	$\mathbf{2.894 \cdot 10^2}$	$2.910 \cdot 10^2$
Known $b_\phi(t,x)$ and $b_\theta(t,x)$				
Performance measure	**Saturation Controller**	**STA**	**ASTA**	**GSTA**
Total ISE	$1.070 \cdot 10^3$	$1.029 \cdot 10^3$	$1.120 \cdot 10^3$	$\mathbf{9.357 \cdot 10^2}$
Total IAE	$1.670 \cdot 10^2$	$\mathbf{1.462 \cdot 10^2}$	$1.522 \cdot 10^2$	$1.468 \cdot 10^2$
Total ISI	$1.443 \cdot 10^3$	$1.398 \cdot 10^3$	$\mathbf{1.392 \cdot 10^3}$	$1.405 \cdot 10^3$
Total IAI	$2.954 \cdot 10^2$	$2.904 \cdot 10^2$	$\mathbf{2.897 \cdot 10^2}$	$2.909 \cdot 10^2$

Table 8.6: The performance measures for the SISO control designs, which includes the saturation controller, the STA, the ASTA, and the GSTA, for simulation case 2 when $b_\phi(t,x)$ and $b_\theta(t,x)$ are uncertain, and for when $b_\phi(t,x)$ and $b_\theta(t,x)$ are exactly known.

The performance measures for case 2 when using a known b in the MIMO control designs are presented in Table 8.7. Interestingly, the results for the MIMO control designs are the complete opposite of the results for the SISO control designs. The error measures for all the MIMO designs increase when using a known b, while the input use measures decrease. The control design with the smallest increase in error measures is the GMSTA, for which the increase is minimal. As the control gains are chosen for the case when b is uncertain, this might imply that the MIMO designs are more sensitive to the choice of control gain configurations than the SISO designs, which would be a drawback of the MIMO control designs compared to the SISO designs.

Case 1				
Performance measure	**MSAT**	**MSTA**	**AMSTA**	**GMSTA**
Total ISE	$1.180 \cdot 10^3$	$1.277 \cdot 10^3$	$2.341 \cdot 10^3$	$\mathbf{8.122 \cdot 10^2}$
Total IAE	$1.731 \cdot 10^2$	$1.760 \cdot 10^2$	$2.207 \cdot 10^2$	$\mathbf{1.376 \cdot 10^2}$
Total ISI	$1.520 \cdot 10^3$	$1.544 \cdot 10^3$	$\mathbf{1.511 \cdot 10^3}$	$1.608 \cdot 10^3$
Total IAI	$\mathbf{3.180 \cdot 10^2}$	$3.226 \cdot 10^2$	$3.213 \cdot 10^2$	$3.334 \cdot 10^2$
Case 2				
Performance measure	**MSAT**	**MSTA**	**AMSTA**	**GMSTA**
Total ISE	$1.214 \cdot 10^3$	$1.345 \cdot 10^3$	$2.617 \cdot 10^3$	$\mathbf{8.196 \cdot 10^2}$
Total IAE	$1.767 \cdot 10^2$	$1.819 \cdot 10^2$	$2.343 \cdot 10^2$	$\mathbf{1.380 \cdot 10^2}$
Total ISI	$1.505 \cdot 10^3$	$1.519 \cdot 10^3$	$\mathbf{1.470 \cdot 10^3}$	$1.588 \cdot 10^3$
Total IAI	$\mathbf{3.083 \cdot 10^2}$	$3.167 \cdot 10^2$	$3.121 \cdot 10^2$	$3.301 \cdot 10^2$

Table 8.7: The performance measures for the MIMO control designs, which includes the MSAT, the MSTA, the AMSTA, and the GMSTA, for simulation case 2 when $b(t, x)$ is uncertain, and for when $b(t, x)$ is exactly known.

8.9 The STA Without Discontinuous Terms

As increasing the control gains for the linear correction terms proves to be a very effective tool for lowering error measures, while still avoiding additional chattering in the control input, the possibility of implementing the MSTA and the GMSTA without the discontinuous terms is investigated in this section. Note that even though the GSTA also contain the added linear correction terms, the framework in which it is presented in Moreno (2009) does not allow us to remove the discontinuous terms by choosing certain control gains to be zero. This is easily done, however, for the MSTA and the GMSTA.

The equations for the MSTA (5.129)-(5.130) reduces to a PI-controller that drives σ to zero if the control gains are chosen as $k_1 = k_3 = 0$ and $k_2, k_4 > 0$ so that the control law is given by

$$u = -k_2\sigma - k_4 \int_0^t \sigma(\tau)\, d\tau \tag{8.1}$$

The same can be done for the GMSTA (3.88)-(3.91), for which the parameters and control gains need to be chosen as $\alpha_g = \gamma_g = 0$ and $k_1, k_2, k_3, \beta_g > 0$ so that the control law is given by

$$u = -k_1\beta_g\sigma - k_2k_3\beta_g \int_0^t \sigma(\tau)\, d\tau \tag{8.2}$$

which also is a PI-controller with codependent control gains, as β_g appears in the control gain for both the proportional and the integral term of the controller.

The tracking results for the MSTA PI (8.1) and the GMSTA PI (8.2) designs compared to the original MSTA and GMSTA designs are presented in Figure 8.53 for simulation case 1. The tracking results show that the GMSTA PI produces a very similar reference trajectory and show the same tracking capabilities as the original GMSTA design. The MSTA PI design, on the other hand, does not track the reference as well as the MSTA design. Additionally, the GMSTA and the GMSTA PI designs outperform the MSTA and MSTA PI designs in terms of tracking errors, which is also reflected in the error measures in Table 8.8. The tracking results of the PI designs for case 2 is also very similar to the tracking results of the original control designs, which is also shown by the error measures for case 2 presented in Table 8.8.

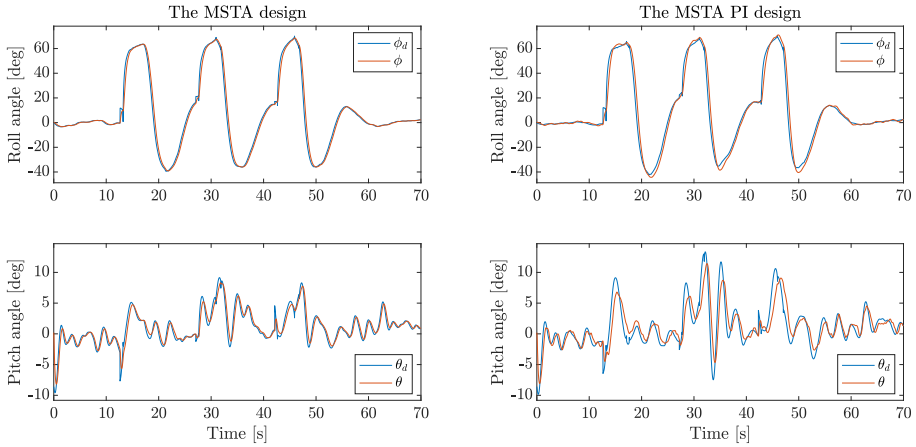

(a) The MSTA and the MSTA PI designs.

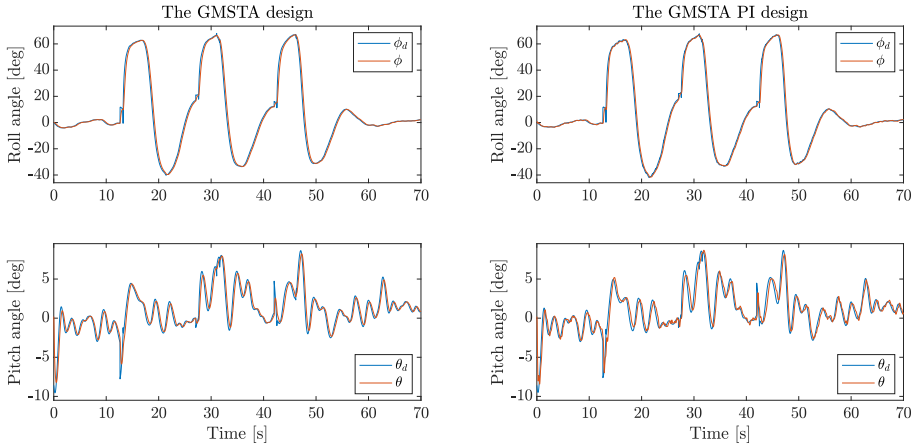

(b) The GMSTA and the GMSTA PI designs.

Figure 8.53: The tracking results for the MSTA and the GMSTA compared to a MSTA PI and a GMSTA PI control design, respectively, for case 1.

Case 1				
Performance measure	**MSTA**	**MSTA PI**	**GMSTA**	**GMSTA PI**
Total ISE	$1.086 \cdot 10^3$	$1.941 \cdot 10^3$	$\mathbf{7.809 \cdot 10^2}$	$8.648 \cdot 10^2$
Total IAE	$1.591 \cdot 10^2$	$2.316 \cdot 10^2$	$\mathbf{1.365 \cdot 10^2}$	$1.438 \cdot 10^2$
Total ISI	$\mathbf{1.522 \cdot 10^3}$	$1.648 \cdot 10^3$	$1.602 \cdot 10^3$	$1.617 \cdot 10^3$
Total IAI	$3.351 \cdot 10^2$	$3.350 \cdot 10^2$	$3.351 \cdot 10^2$	$\mathbf{3.309 \cdot 10^2}$
Case 2				
Performance measure	**MSTA**	**MSTA PI**	**GMSTA**	**GMSTA PI**
Total ISE	$1.277 \cdot 10^3$	$1.352 \cdot 10^3$	$\mathbf{8.122 \cdot 10^2}$	$8.488 \cdot 10^2$
Total IAE	$1.760 \cdot 10^2$	$1.836 \cdot 10^2$	$\mathbf{1.376 \cdot 10^2}$	$1.423 \cdot 10^2$
Total ISI	$\mathbf{1.544 \cdot 10^3}$	$1.557 \cdot 10^3$	$1.608 \cdot 10^3$	$1.632 \cdot 10^3$
Total IAI	$\mathbf{3.226 \cdot 10^2}$	$3.258 \cdot 10^2$	$3.334 \cdot 10^2$	$3.312 \cdot 10^2$

Table 8.8: Performance measures for the original MSTA and GMSTA designs, as well as the measures for the MSTA and GMSTA based PI designs.

The control inputs generated by the MSTA, the MSTA PI, the GMSTA, and the GMSTA PI designs for case 2 are presented in 8.54. The control signals generated by the PI designs are very similar to the ones produced by the original control designs, but they are slightly smoother than the original control inputs. Since the error measures and most of the input use measures for the PI designs are higher than for the original designs, it can be concluded that adding the discontinuous terms in the control law is beneficial for the tracking performance of the attitude control designs.

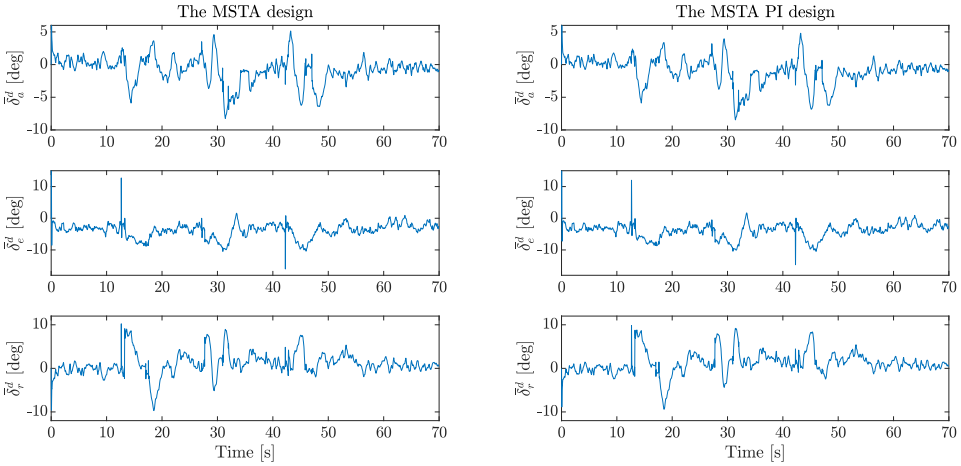

(a) The MSTA and the MSTA PI designs.

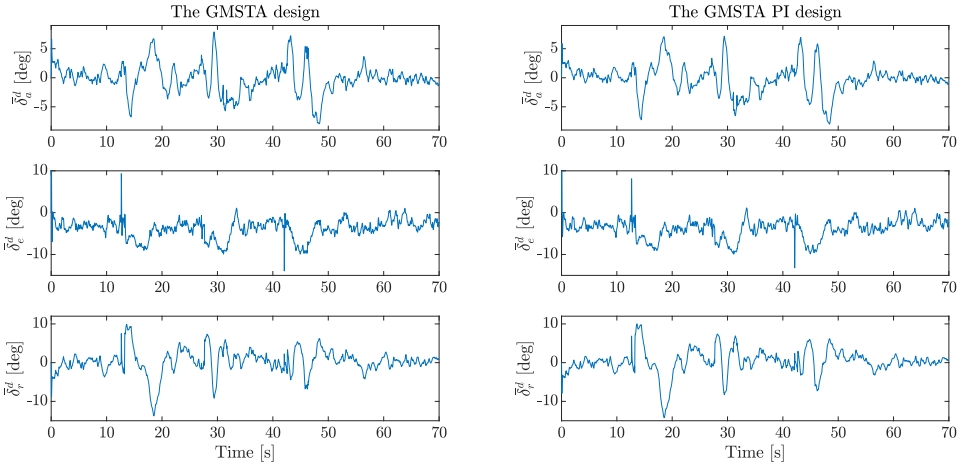

(b) The GMSTA and the GMSTA PI designs.

Figure 8.54: The control inputs for the MSTA and the GMSTA designs compared to the control inputs for the MSTA PI and the GMSTA PI design, respectively, for case 2.

Chapter 9

Conclusions and Future Work

9.1 Conclusions

9.1.1 The Decoupled Longitudinal Model

Several aspects of the single-input control designs are investigated in this report, including the robustness properties, the properties of the different control coefficient transformations, and the stability of the designs and of the longitudinal dynamics in the sliding mode. The conclusion that can be drawn from the results presented in subsection 7.7, is that the choice of transformation does not matter in theory. However, in realistic conditions, the better choice is to use a control coefficient transformation with some uncertainty. This is because the SMC algorithms are robust enough to modeling errors and parametric uncertainties to handle the discrepancy between the actual true system and the model function used in the transformation.

The main conclusion that can be made about the single-input control algorithms, is that the second-order algorithms, i.e. the STA, the ASTA, and the GSTA, perform better than the saturation controller in the simulation cases considered in this report. Still, the saturation controller is surprisingly robust compared to the complexity of the controller. It is difficult to determine which algorithm performs the best, as they are very similar. However, for a discontinuous reference signal, either the STA or the GSTA would be the better choice, while the saturation controller or the ASTA would give the best results for a continuous reference signal.

9.1.2 The 6DOF Model

The main objective of this report is to investigate the robustness of four SISO and four MIMO control designs when applied to an uncertain model of a fixed-wing UAV operating that is affected by external disturbances and process noise. The control designs were evaluated based on their tracking performance of a roll and pitch reference generated by a waypoint follower system.

The robustness of the control designs has been investigated by adding unmodeled dynamics, such as actuator dynamics, and increasing amounts of disturbances due to wind and process noise to the simulation model. All of the control designs were able to reach the waypoints when a minimal amount of disturbances were present in the system, both with and without additional unmodeled dynamics present, which shows the robustness of the designs. For a larger amount of disturbances in the simulation model, the control designs were also able to reach the waypoints, albeit with a substantial loss in smoothness of the control input, which resulted in unfeasible control input for some of the control designs.

It is difficult to determine whether the SISO or the MIMO modeling approach is the best, as they produce very similar results. However, the MIMO control designs have the advantage of using all three control surfaces to achieve tracking of the reference signals, while the SISO designs only uses the aileron and elevators, which puts a strain on the elevator command and causes the control input produced by the SISO designs to be overall less smooth than the control input produced by the MIMO designs. This also means that the pitch tracking performance of the SISO designs to be less smooth than that of the MIMO designs. Additionally, the SISO designs produce an angle of attack that is within the stall angle range when there are more disturbances in the system, which is a drawback to the SISO modeling of the control design.

The robustness of some of the SISO and MIMO control designs were investigated with respect to changes in the modeling of the actuator dynamics and to changes in sampling frequency. Here, the SISO control designs outperformed the MIMO designs for slower actuator dynamics, while the MIMO control designs handled the more complex second-order actuator dynamics better. For changes in sampling frequency, the MIMO designs proved to be more robust for lower sampling frequencies than the SISO designs in terms of tracking accuracy and smoothness of the control input.

Additionally, it is difficult to determine which of the SISO and MIMO control designs is the most robust and effective. There are, however, some control algorithms that are more promising than others. The saturation control design is a simple design that performed well in most of the aspects investigated in the previous chapter, even outperforming several of the STA based SISO and MIMO designs. This does not come as a surprise as the saturation controller performed well for the lateral dynamics in Griffiths (2020), and reasonable well for the longitudinal dynamics presented previously in this report. Another algorithm that performed well is the GSTA, but it tends to produce control input that is less smooth than those of the other control designs with the same tracking performance as the GSTA. Finally, the most promising algorithm is the GMSTA which consistently had the smallest, or among the smallest, error measures in this report, while still producing a relatively smooth and feasible control input. However, the tracking performance of the GMSTA was noticeably more affected by slow actuator dynamics than for example the performance of the saturation control design. Each of the most promising algorithms has its own separate strengths and weaknesses, and more rigorous testing of the algorithms is necessary to fully conclude which one is the most effective and robust algorithm.

9.2 Future Work

The goal of future work should be to further investigate the robustness of the control algorithms considered in this report by developing a simulation model that is closer to a realistic UAV, and by performing more rigorous testing of the control algorithms. This can, for example, be done by using Monte Carlo simulations. Additionally, the control designs should be compared to an attitude control design that is currently being used in UAV applications. Additionally, the use of sliding mode disturbance and/or state observers, such as in Fang et al. (2015); Singh et al. (2020); Hu et al. (2019); Fan and Tian (2016); Wei et al. (2019); López-Caamal and Moreno (2015), should be investigated, as this may increase the robustness of the control design to external disturbances.

Another improvement that may make the control design more robust is to employ the equivalent control for the 6DOF model, such as in Gonzalez et al. (2012); Fang et al. (2015); Tian et al. (2019), since this will lower the bound on the control gains by decreasing the perturbations the control algorithms need to dominate. This can easily be done by including the function $a(t, x)$ in the sliding dynamics in the control coefficient transformation, such as in Nagesh and Edwards (2014), instead of using only the function $b(t, x)$.

Furthermore, the problem of choosing optimal control gains should be investigated. There already exist some rules for choosing the control gains based on Lyapunov analysis, where the conditions on the control gains are based on the bounds on the disturbances and perturbations in the system. The control gain configurations presented in subsection 3.5.1 provides rules for choosing the control gains for the STA, which proved unsuccessful in Griffiths (2020). It may, however, be possible to formulate an optimization problem for choosing the control gains such as in You et al. (2004), where an optimization algorithm is used to choose the control gains for a sliding mode controller and disturbance observer design. Achieving more optimal control gain configurations would be an improvement for the results presented in this report, as it would be easier to achieve more similar performances of the system which are easier to compare.

Several improvements can also be made to the stability analysis of the internal dynamics of the system, and to the discussion of the application of SISO controllers to the 6DOF model. In the analysis of the internal longitudinal dynamics in section 5.6 and of the lateral dynamics in Griffiths (2020), several simplifying assumptions are made, and only the stability of the decoupled dynamics is determined. It may be interesting to perform a more comprehensive analysis with fewer simplifications of the internal dynamics of the 6DOF model in the sliding mode to fully determine the internal stability of the 6DOF model dynamics since the stability of the internal dynamics in the sliding mode is a necessary condition for the stability of the SISO and MIMO control designs. Furthermore, only the validity of the system assumptions for the decoupled dynamics is verified for the SISO controllers, even though they are applied to the 6DOF model. This means that even though the validity of the assumptions is confirmed for the SISO controllers applied to the decoupled models, this might not be the case when they are applied to the 6DOF model.

Even though several versions of the MSTA are implemented in this report, the extension of the MSTA presented in Wei et al. (2019) is not considered in this report, which is the adaptive multivariable generalized STA. Because of the good results of the AMSTA and GMSTA in this report, it would be interesting to compare these algorithms to the

AMGSTA.

Finally, the inclusion of an anti-windup scheme for the STA should be considered as this may improve the tracking results. An example of an implementation of the STA with anti-windup is presented in Golkani et al. (2019), where it is shown to be more effective than the original STA. If implementing the anti-windup scheme in Golkani et al. (2019) improves the results for the STA applied in the SISO control design, the possibility of extending the anti-windup scheme to extensions of the STA, as well as the MSTA and its extensions, should be investigated.

Bibliography

Beard, R. W. and McLain, T. W. (2012). *Small unmanned Aircraft: Theory and Practice*. Princeton University Press.

Borlaug, I. G., Pettersen, K. Y., and Gravdahl, J. T. (2020). The generalized super-twisting algorithm with adaptive gains. In *2020 European Control Conference (ECC)*, pages 1624–1631.

Bøhn, E., Coates, E. M., Moe, S., and Johansen, T. A. (2019). Deep reinforcement learning attitude control of fixed-wing uavs using proximal policy optimization. In *2019 International Conference on Unmanned Aircraft Systems (ICUAS)*, pages 523–533.

Castillo, I., Fridman, L., and Moreno, J. A. (2018). Super-twisting algorithm in presence of time and state dependent perturbations. *International Journal of Control*, 91(11):2535–2548.

Chalk, C., Neal, T. P., Harris, T. M., Pritchard, F. E., and Woodcock, R. J. (1969). *Background Information and User Guide for Mil-F-8785B (ASG), 'Military Specification-Flying Qualities of Piloted Airplanes'*. Cornell Aeronautical Laboratory INC.

Coates, E. M. L., Reinhardt, D. P., and Fossen, T. (2020). Reduced-attitude control of fixed-wing unmanned aerial vehicles using geometric methods on the two-sphere. *IFAC-PapersOnLine*.

Dong, Q., Zong, Q., Tian, B., and Wang, F. (2016). Adaptive-gain multivariable super-twisting sliding mode control for reentry rlv with torque perturbation: Sliding mode control for reentry rlv. *International Journal of Robust and Nonlinear Control*, 27.

Edwards, C. and Spurgeon, S. (1998). *Sliding Mode Control: Theory And Applications*. CRC Press.

Fan, W. and Tian, B. (2016). Adaptive multivariable super-twisting sliding mode controller and disturbance observer design for hypersonic vehicle. *Mathematical Problems in Engineering*, 2016:1–9.

Fang, X., Wu, A., Shang, Y., and Du, C. (2015). Multivariable super twisting based robust trajectory tracking control for small unmanned helicopter. *Mathematical Problems in Engineering*, 2015:1–13.

Fridman, L., Moreno, J. A., and Iriarte, R. (2011). *Sliding Modes after the First Decade of the 21st Century*. Springer-Verlag Berlin Heidelberg.

Golkani, M. A., Koch, S., Seeber, R., Reichhartinger, M., and Horn, M. (2019). An anti-windup scheme for the super-twisting algorithm. In *2019 IEEE 58th Conference on Decision and Control (CDC)*, pages 6947–6952.

Gonzalez, T., Moreno, J. A., and Fridman, L. (2012). Variable gain super-twisting sliding mode control. *IEEE Transactions on Automatic Control*, 57(8):2100–2105.

Griffiths, J. B. (2020). Project thesis: Super-Twisting Sliding Mode Control of Fixed-Wing UAVs.

Hu, C., Qin, Y., Cao, H., Song, X., Jiang, K., Rath, J. J., and Wei, C. (2019). Lane keeping of autonomous vehicles based on differential steering with adaptive multivariable super-twisting control. *Mechanical Systems and Signal Processing*, 125:330 – 346.

Khalil, H. (2002). *Nonlinear Systems*. Prentice Hall, 3rd edition.

Levant, A. (1993). Sliding order and sliding accuracy in sliding mode control. *International Journal of Control*, 58(6):1247–1263.

Levant, A. (1998). Robust exact differentiation via sliding mode technique. *Automatica*, 34(3):379–384.

Levant, A. (2003). Higher-order sliding modes, differentiation and output-feedback control. *International Journal of Control*, 76(9-10):924–941.

Lovren, N. and Pieper, J. K. (1997). A strapdown inertial navigation system for the flat-earth model. *IEEE Transactions on Aerospace and Electronic Systems*, 33(1):214–224.

López-Caamal, F. and Moreno, J. A. (2015). Qualitative differences of two classes of multivariable super-twisting algorithms. In *2015 54th IEEE Conference on Decision and Control (CDC)*, pages 5414–5419.

López-Caamal, F. and Moreno, J. A. (2019). Generalised multivariable supertwisting algorithm. *International Journal of Robust and Nonlinear Control*, 29(3):634–660.

MathWorks (2020a). Calculate the Difference Between Two Angles. `https://se.mathworks.com/help/robotics/ref/angdiff.html`.

MathWorks (2020b). Dryden Wind Turbulence Model (Continuous). `https://se.mathworks.com/help/aeroblks/drydenwindturbulencemodelcontinuous.html`.

MathWorks (2020c). Four-Quadrant Inverse Tangent. `https://se.mathworks.com/help/matlab/ref/atan2.html`.

MathWorks (2020d). Waypoint follower. `https://se.mathworks.com/help/uav/ref/waypointfollower.html`.

Moreno, J. A. (2009). A linear framework for the robust stability analysis of a generalized super-twisting algorithm. In *2009 6th International Conference on Electrical Engineering, Computing Science and Automatic Control (CCE)*, pages 1–6.

Moreno, J. A. and Osorio, M. (2008). A lyapunov approach to second-order sliding mode controllers and observers. In *2008 47th IEEE Conference on Decision and Control*, pages 2856–2861.

Moreno, J. A. and Osorio, M. (2012). Strict Lyapunov functions for the super-twisting algorithm. *IEEE Transactions on Automatic Control*, 57(4):1035–1040.

Nagesh, I. and Edwards, C. (2014). A multivariable super-twisting sliding mode approach. *Automatica*, 50(3):984 – 988.

Reinhardt, D. P., Coates, E. M. L., and Johansen, T. (2020). Hybrid control of fixed-wing uavs for large-angle attitude maneuvers on the two-sphere. *IFAC-PapersOnLine*.

Seeber, R. and Horn, M. (2017). Stability proof for a well-established super-twisting parameter setting. *Automatica*, 84:241–243.

Shtessel, Y., Edwards, C., Fridman, L., and Levant, A. (2014). *Sliding Mode Control and Observation*. Springer.

Shtessel, Y. B., Moreno, J. A., Plestan, F., Fridman, L. M., and Poznyak, A. S. (2010). Super-twisting adaptive sliding mode control: A Lyapunov design. In *49th IEEE Conference on Decision and Control (CDC)*, pages 5109–5113.

Singh, P., Agrawal, P., Nandanwar, A., Behera, L., Verma, N. K., Nahavandi, S., and Jamshidi, M. (2020). Multivariable event-triggered generalized super-twisting controller for safe navigation of nonholonomic mobile robot. *IEEE Systems Journal*, pages 1–12.

Stevens, B. L., Lewis, F. L., and Johnson, E. N. (2015). *Aircraft Control and Simulation: Dynamics, Controls Design, and Autonomous Systems*. Wiley-Blackwell, 3rd edition.

Tian, B., Cui, J., Lu, H., Zuo, Z., and Zong, Q. (2019). Adaptive finite-time attitude tracking of quadrotors with experiments and comparisons. *IEEE Transactions on Industrial Electronics*, 66(12).

Tian, B., Liu, L., Lu, H., Zuo, Z., Zong, Q., and Zhang, Y. (2018). Multivariable finite time attitude control for quadrotor uav: Theory and experimentation. *IEEE Transactions on Industrial Electronics*, 65(3):2567–2577.

Utkin, V., Guldner, J., and Shi, J. (2009). *Sliding Mode Control in Electro-Mechanical Systems*. CRC Press, 2nd edition.

Vidal, P. V. N. M., Nunes, E. V. L., and Hsu, L. (2016). Multivariable super-twisting algorithm for a class of systems with uncertain input matrix. In *2016 American Control Conference (ACC)*, pages 7201–7206.

Vidal, P. V. N. M., Nunes, E. V. L., and Hsu, L. (2017). Output-feedback multivariable global variable gain super-twisting algorithm. *IEEE Transactions on Automatic Control*, 62(6):2999–3005.

Wei, J., Yuan, J., and Wang, Z. (2019). Adaptive multivariable generalized super-twisting algorithm based robust coordinated control for a space robot subjected to coupled uncertainties. *Proceedings of the Institution of Mechanical Engineers, Part G: Journal of Aerospace Engineering*, 233(9):3244–3259.

Xuehui, L., Shenmin, S., and Yong, G. (2015). Multivariable super-twisting sliding mode approach for attitude tracking of spacecraft. In *2015 34th Chinese Control Conference (CCC)*, pages 5789–5794.

You, K. S., Lee, M. C., and Yoo, W. S. (2004). Sliding mode controller with sliding perturbation observer based on gain optimization using genetic algorithm. In *KSME International Journal*, volume 18, pages 630–639.

Young, K. D., Utkin, V. I., and Ozguner, U. (1999). A control engineer's guide to sliding mode control. *IEEE Transactions on Control Systems Technology*, 7(3):328–342.

Appendix A

MATLAB files

A.1 Zero Dynamics

A.1.1 *eigvals.m*

Description

Calculates the eigenvalues of the linearized system in the sliding mode presented in section 5.6. Also plots the equilibrium values V_a^* and α^*.

Code

Listing A.1: *eigvals.m*

```
close all;
clear eigvalues;
aerosonde;

V_a_0 = 35;
[alpha_0,delta_t_0,delta_e_0] = trim(V_a_0,P);
theta_0=alpha_0;

plot_text = '';

a_1 = 5; % dummy sliding variable constant

%% Constants
L_0 = 0.5*P.rho*P.S*(P.C_L_0 - (P.C_L_delta_e/P.C_m_delta_e)*P.C_m_0);
L_q1 = 0.25*P.rho*P.S*P.c*(P.C_L_q - (P.C_L_delta_e/P.C_m_delta_e)*P.C_m_q
    );
L_q2 = (P.C_L_delta_e/P.C_m_delta_e)*(-P.I_b(2,2)/P.c)*a_1;
L_alpha = 0.5*P.rho*P.S*(P.C_L_alpha - (P.C_L_delta_e/P.C_m_delta_e)*P.
    C_m_alpha);

D_0 = 0.5*P.rho*P.S*(P.C_D_0 - (P.C_D_delta_e/P.C_m_delta_e)*P.C_m_0);
```

```
D_q1 = 0.25*P.rho*P.S*P.c*(P.C_D_q - (P.C_D_delta_e/P.C_m_delta_e)*P.C_m_q
    );
D_q2 = (P.C_D_delta_e/P.C_m_delta_e)*(-P.I_b(2,2)/P.c)*a_1;
D_alpha = 0.5*P.rho*P.S*(P.C_D_alpha_1 - (P.C_D_delta_e/P.C_m_delta_e)*P.
    C_m_alpha);


%% Solver
% x = [V_a, alpha]
N = 1000;
V_a_star_0 = 45;
alpha_star_0 = deg2rad(3);
theta_lim = deg2rad(25); % stall angle
theta_d = linspace(-theta_lim,theta_lim,N);
T = 0.5*P.rho * P.S_prop * P.C_prop * ((P.k_m*delta_t_0)^2 - V_a_0^2);

x_vec = zeros(N,2);
Tx = zeros(1,N);

for i=1:N
    % solve equation set
    F = @(x) [(1/P.m)*(T*cos(x(2)) - x(1)^2*(D_alpha*x(2) + D_0) - P.m*P.g
        *sin(theta_d(i) - x(2)));
        (P.g/x(1))*cos(theta_d(i) - x(2)) - (x(1)/P.m)*(L_alpha*x(2) + L_0
            ) - (T/(P.m*x(1)))*sin(x(2))];
    x0 = [V_a_star_0,alpha_star_0];
    options = optimoptions('fsolve');
    [x,fval(:,i),exitflag(i),output(i)] = fsolve(F,x0,options);
    x_vec(i,:) = x;

    Tx(i) = 0.5*P.rho * P.S_prop * P.C_prop * ((P.k_m*delta_t_0)^2 - x(1)
        ^2);

    % calculate linearized matrix
    a_31 = -P.g*cos(theta_d(i) - x(2));
    a_32 = -(1/P.m)*(x(1)*D_q1 - D_q2);
    a_33 = -((2*x(1))/P.m)*(D_alpha*x(2) + D_0);
    a_34 = (1/P.m)*(-T*sin(x(2)) - x(1)^2*D_alpha) + P.g*cos(theta_d(i) -
        x(2));

    a_41 = -(P.g/x(1))*sin(theta_d(i) - x(2));
    a_42 = 1 - (1/P.m)*(L_q1 - (1/x(1))*L_q2);
    a_43 = -(P.g/(x(1)^2))*cos(theta_d(i) - x(2)) - (1/P.m)*(x(2)*L_alpha
        + L_0) + (T/(P.m*x(1)^2))*sin(x(2));
    a_44 = (P.g/x(1))*sin(theta_d(i) - x(2)) - (x(1)/P.m)*L_alpha - (T/(P.
        m*x(1)))*cos(x(2));

    % calculate eigenvalues
    A_lin = [-a_1 0 0 0;
        0 -a_1 0 0;
        a_31 a_32 a_33 a_34;
        a_41 a_42 a_43 a_44];

    eigvalues(:,i) = real(eig(A_lin));

end
```

```
%% Plot equilibrium values for theta_d vector

f1 = figure(1);
set(gcf, 'Units', 'Normalized', 'OuterPosition', [0, 0.1, 0.6, 0.50]);
subplot(1,2,1)
plot(rad2deg(theta_d),x_vec(:,1))
title('Airspeed equilibrium $V_a^*$')
ylabel('$V_a^* \: [$m/s$]$')
xlabel('$\theta_d \: $[deg$]$')


subplot(1,2,2)
plot(rad2deg(theta_d),rad2deg(x_vec(:,2)))
title('Angle of attack equilibrium $\alpha^*$')
ylabel('$\alpha^* \: [$deg$]$')
xlabel('$\theta_d \: $[deg$]$')

path = '/Stability Analysis/';
filename = [path plot_text '_equilibrium.eps'];
print(f1,[pwd filename],'-depsc');

data.eigvalues = eigvalues;
data.alpha_star_0 = alpha_star_0;
data.V_a_star_0 = V_a_star_0;
data.theta_d = theta_d;
data.x_vec = x_vec;

path = 'Stability Analysis/';
filename = [path plot_text '.mat'];
save(filename, 'data');



%% Plot eigenvalues
plot_eigvals(eigvalues, rad2deg(theta_d), plot_text);
```

A.1.2 *plot_eigvals.m*

Description

Plots the eigenvalues of the linearized system in the sliding mode presented in section 5.6.

Code

Listing A.2: *plot_eigvals.m*

```
function plot_eigvals(eigvals,theta_d,plot_text)
%PLOT_EIGVALS Plot eigvals for values of phi_r
%   inputargs:  eigvals is an 4xn matrix
%               phi_r is an 1xn vector

    f2 = figure(2);
    set(gcf, 'Units', 'Normalized', 'OuterPosition', [0, 0.1, 0.5, 0.60]);
    subplot(2,2,1)
    plot(theta_d,eigvals(1,:))
```

```
    title('$Re(\lambda_1)$')
    xlabel('$\theta_d$ [deg]')

    subplot(2,2,2)
    plot(theta_d,eigvals(2,:))
    title('$Re(\lambda_2)$')
    xlabel('$\theta_d$ [deg]')

    subplot(2,2,3)
    plot(theta_d,eigvals(3,:))
    title('$Re(\lambda_3)$')
    xlabel('$\theta_d$ [deg]')

    subplot(2,2,4)
    plot(theta_d,eigvals(4,:))
    title('$Re(\lambda_4)$')
    xlabel('$\theta_d$ [deg]')

    path = '/Stability Analysis/';
    filename = [path plot_text '_eigvals.eps'];
    print(f2,[pwd filename],'-depsc');

end
```

A.2 Approximate Actuator Dynamics

A.2.1 *approximate_dynamics.m*

Description

Approximates the step-response of the second-order actuator dynamics used in Bøhn et al. (2019) to a first-order transfer function.

Code

Listing A.3: *approximate_dynamics.m*

```
close all;

% second-order
omega_0 = 100;
zeta = 1/sqrt(2);

sys = tf(omega_0^2,[1 2*zeta*omega_0 omega_0^2]); % second-order TF

step_time = 0;
sim('Aux Files/second_order_actuator_dynamics.slx',100);

% first-order approximation
np=1; % number of poles
nz=0; % number of zeros
Ts = 0.001; % sampling time step

data = iddata(ans.y.Data,ans.u.Data,Ts);
```

```
sys2 = tfest(data,np,nz); % approximate first-order TF

T_delta_e = 1/sys2.Denominator(2); % low-pass filter time constant
disp(T_delta_e);

% Plotting
step(sys) % second-order response
hold on;
step(sys2) % approximate first-order response
```

Appendix B

Simulink Models

B.1 Longitudinal Model

In this section, the implementation of the longitudinal simulation model is presented. An overview of the model is shown in Figure B.1. Subsection B.1.1 contains the implementation of the decoupled longitudinal dynamics. The contents of the Control-block, which includes the saturation controller, the STA, the ASTA, the GSTA, the airspeed hold controller, the measuring of the continuous control signals, and the implementation of the actuator dynamics are shown in subsection B.1.2. The contents of the Reference-block are shown in subsection B.1.3, while the contents of the Wind and disturbance-block are shown in subsection B.1.4. Finally, the implementation of the Sensor-block is shown in subsection B.1.5.

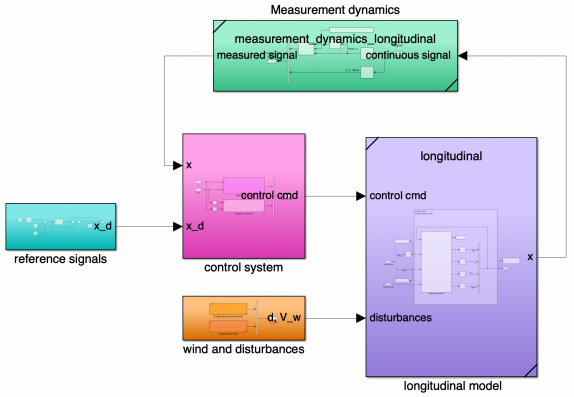

Figure B.1: Overview of the longitudinal simulation model in Simulink.

B.1.1 Model Implementation

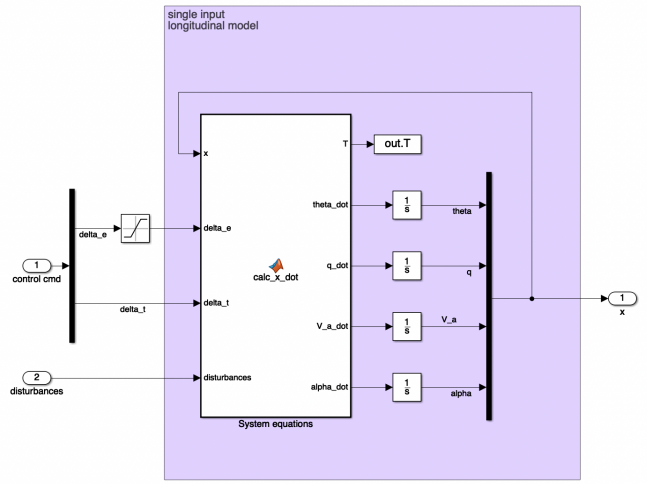

Figure B.2: The Simulink-implementation of the longitudinal model.

B.1.2 Control System

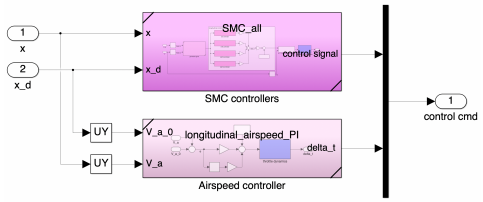

Figure B.3: The Simulink-implementation of the longitudinal control system.

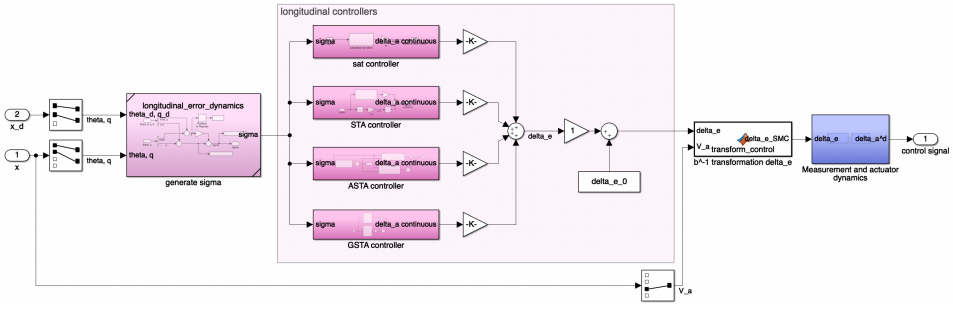

Figure B.4: The Simulink-implementation of the longitudinal SMC control system.

Saturation Controller

Figure B.5: The Simulink-implementation of the single-input saturation controller.

STA

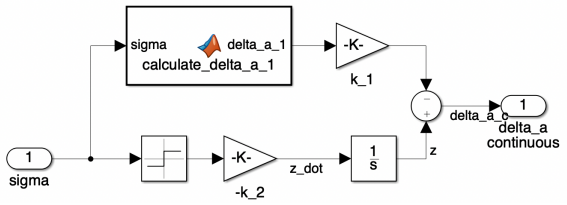

Figure B.6: The Simulink-implementation of the single-input STA controller.

ASTA

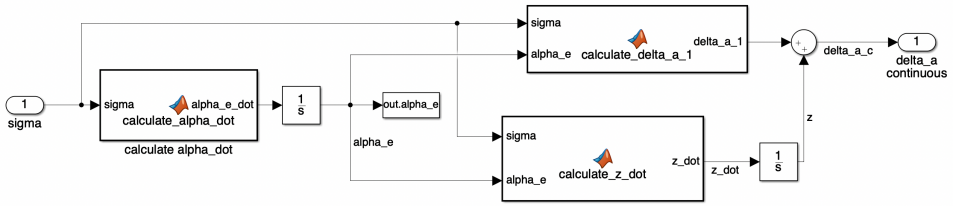

Figure B.7: The Simulink-implementation of the single-input ASTA controller.

GSTA

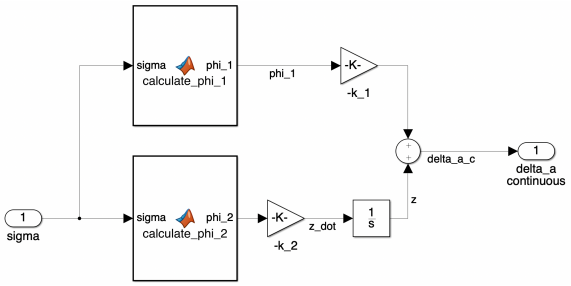

Figure B.8: The Simulink-implementation of the single-input GSTA controller.

Airspeed Hold Using Throttle

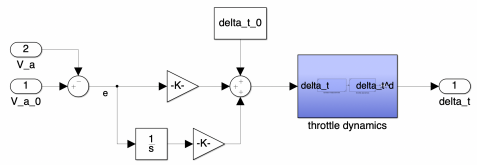

Figure B.9: The Simulink-implementation of the airspeed PI-controller.

Actuator Measurement and Dynamics

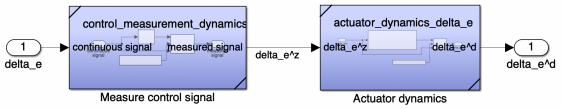

Figure B.10: The Simulink-implementation of the measurement and actuator dynamics in the control system.

B.1.3 Reference Trajectory

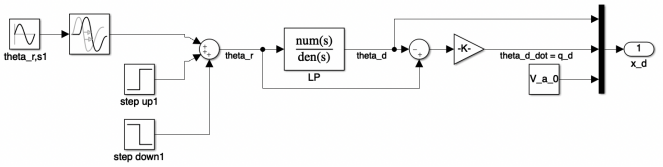

Figure B.11: The Simulink-implementation of the longitudinal reference signal θ_d.

B.1.4 Wind and Disturbances

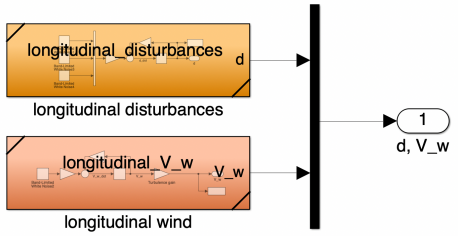

Figure B.12: The Simulink-implementation of the longitudinal disturbances.

Wind Disturbance

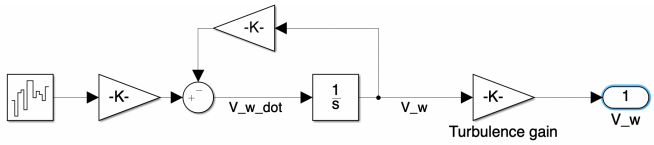

Figure B.13: The Simulink-implementation of the wind gust signal d_g.

Process Noise

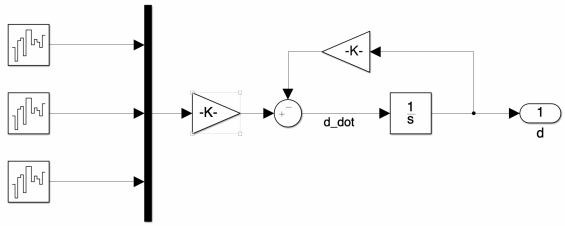

Figure B.14: The Simulink-implementation of the parametric uncertainty signal $d_\theta(t)$.

B.1.5 Sensor Block

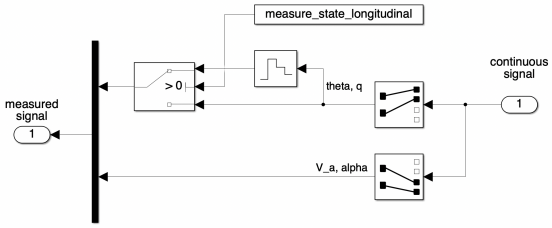

Figure B.15: The Simulink-implementation of the sensor block.

B.2 6DOF Simulation Model

In this section, the implementation of the 6DOF simulation model, and of the SISO and MIMO control designs, are presented. An overview of the 6DOF simulation model is shown in Figure B.16. The implementation of the 6DOF UAV dynamics is shown in subsection B.2.1. Subsection B.2.2 contains the implementation of the waypoint following system. Subsection B.2.3 presents the implementation of the wind and process noise that is present in the simulation model. The implementations of the sensor and actuator dynamics are shown in subsection B.2.4. Finally, the SISO and MIMO control designs are presented in subsection B.2.5 and subsection B.2.6, respectively.

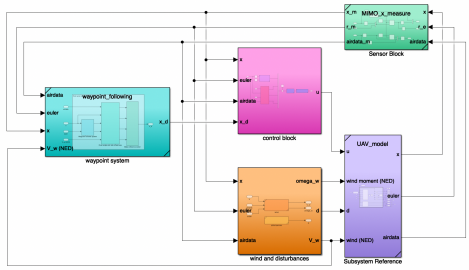

Figure B.16: Overview of the 6DOF simulation model in Simulink.

B.2.1 Model Implementation

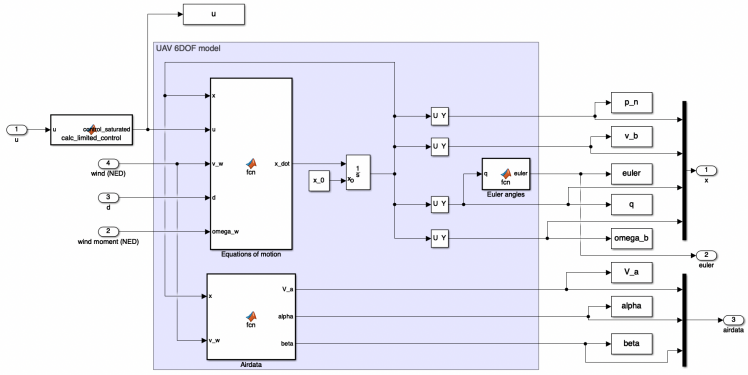

Figure B.17: The implementation of the 6DOF model in Simulink.

B.2.2 Reference Block

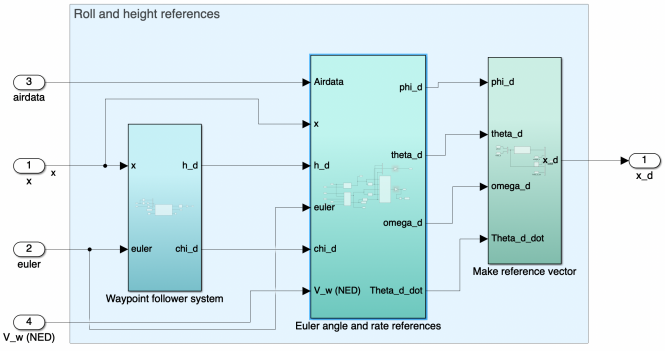

Figure B.18: Overview of the Reference-block in the 6DOF model in Simulink.

Waypoint Follower

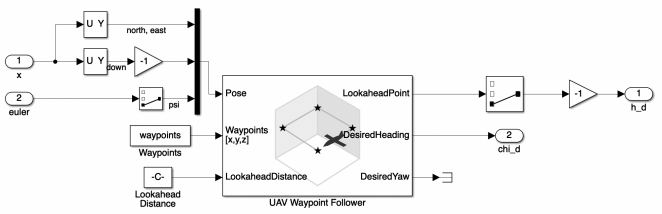

Figure B.19: The waypoint follower system in the 6DOF model in Simulink.

Control Commands

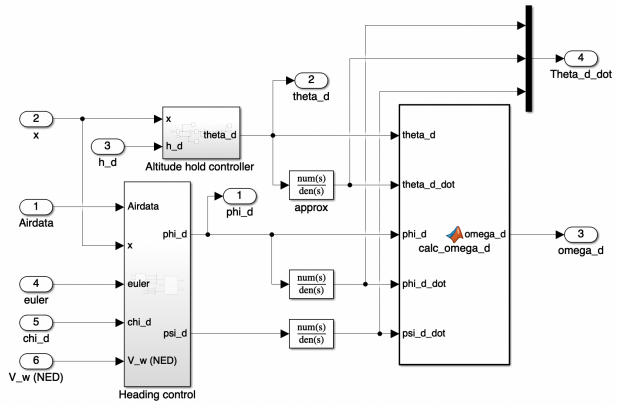

Figure B.20: The system that generates the reference trajectories based on the commands from the waypoint follower subsystem in Simulink.

Heading Control Block

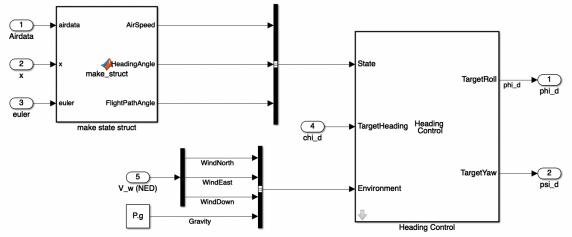

Figure B.21: The system that generates the desired roll angle ϕ_d in Simulink.

Altitude Hold Controller

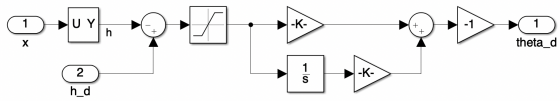

Figure B.22: The altitude hold controller that generates the desired pitch angle θ_d in Simulink.

B.2.3 System Disturbances

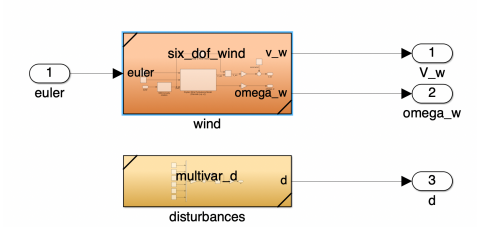

Figure B.23: Overview of the Wind and disturbance-block in Simulink.

Wind

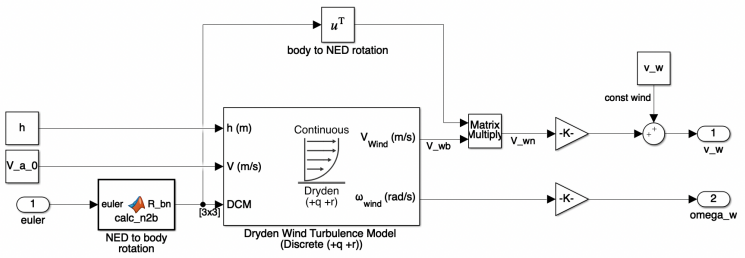

Figure B.24: The system that generates the wind disturbances $\mathbf{v}_w$ and ω_w in Simulink.

Parametric Uncertainties

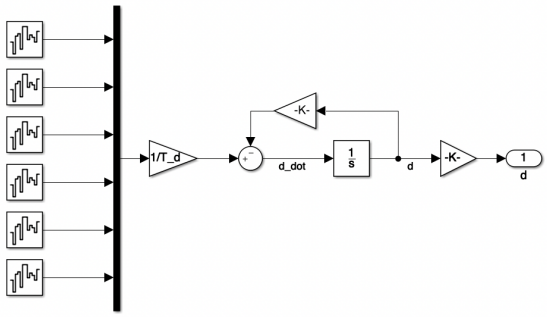

Figure B.25: The system that generates the disturbance vector d in Simulink.

B.2.4 Sensor Blocks and Actuator Dynamics

Sensor Block for the State

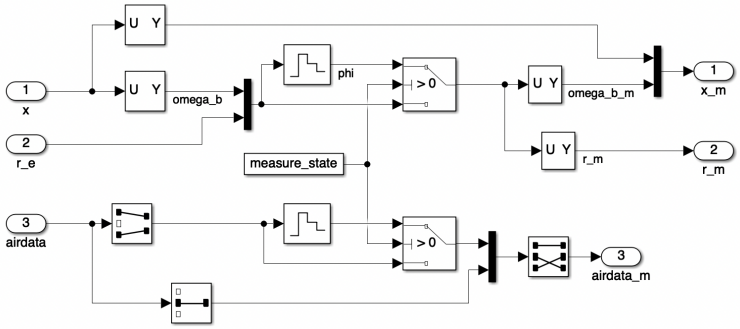

Figure B.26: The sensor block that measures the state x, the Euler angles Ω, and the airdata variables V_a and α in Simulink.

Sensor Block for the Control

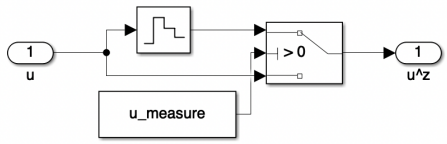

Figure B.27: The sensor block that measures the control $\bar{u}$ in Simulink.

Actuator Dynamics

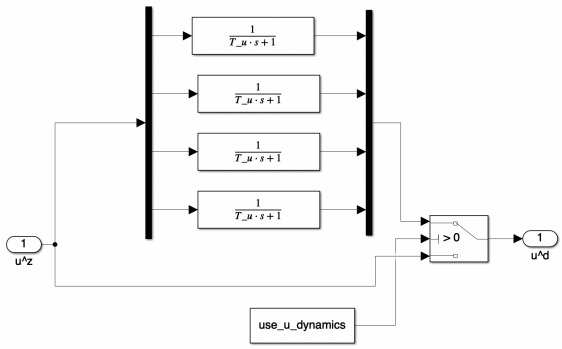

Figure B.28: The system that generates the delayed control signal $\bar{u}^d$ in Simulink.

B.2.5 SISO Control Design

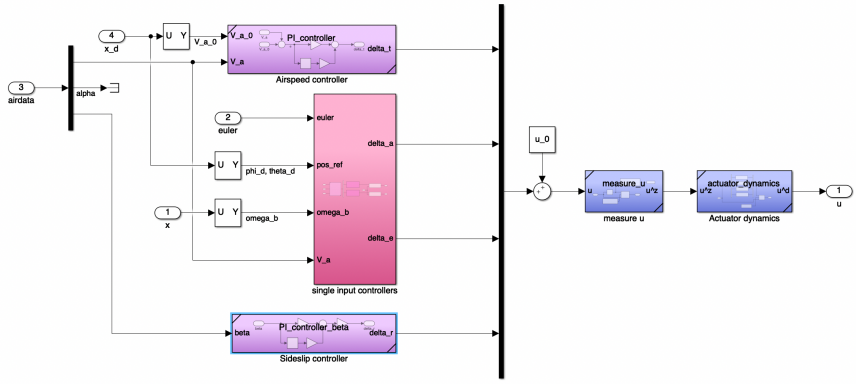

Figure B.29: Overview of the SISO control design in Simulink.

SISO Controllers

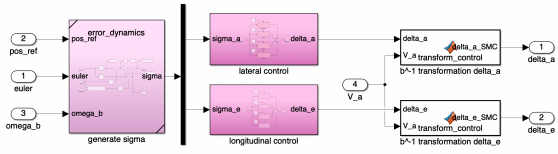

Figure B.30: The SISO controllers in Simulink.

Sliding Variable-Subsystem

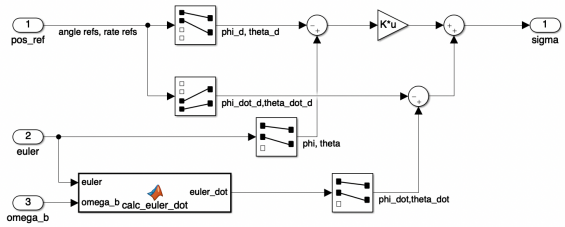

Figure B.31: The implementation of the sliding variable for the SISO control design in Simulink.

Single-Input Controllers

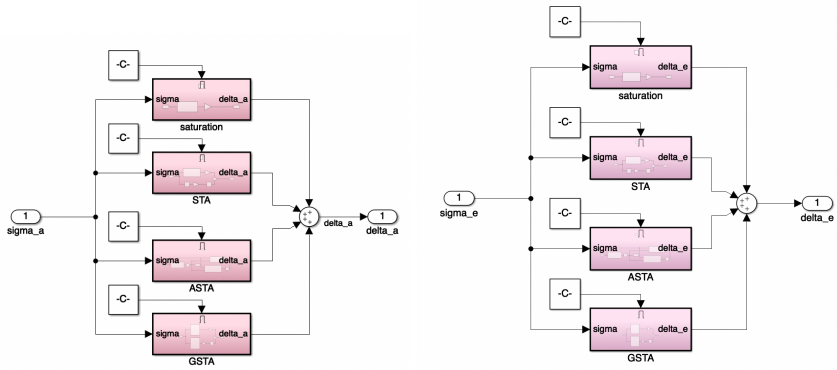

(a) The implementation of the lateral controllers in the SISO control design in Simulink.

(b) The implementation of the longitudinal controllers in the SISO control design in Simulink.

Figure B.32: The single-input lateral and longitudinal controllers in the SISO control design in Simulink.

Sideslip Hold

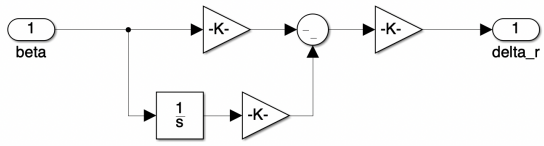

Figure B.33: Implementation of the sideslip hold controller in Simulink.

B.2.6 MIMO Control Design

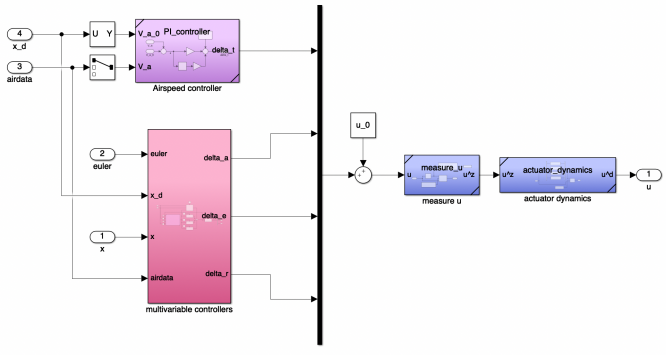

Figure B.34: Overview of the MIMO control design in Simulink.

MIMO Controllers

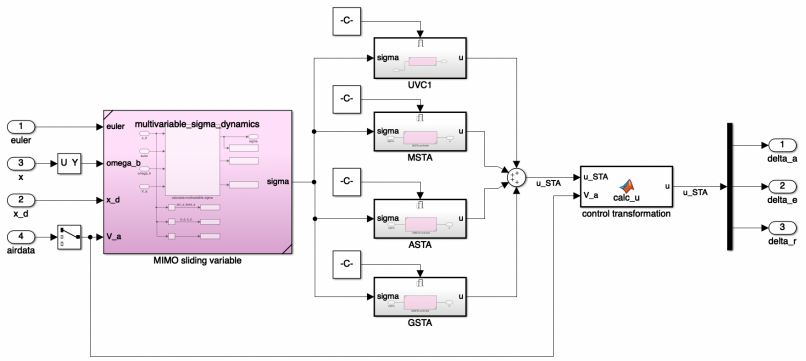

Figure B.35: The MIMO controllers in Simulink.

Sliding Variable-Subsystem

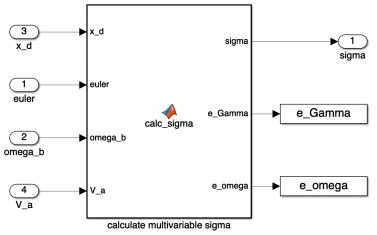

Figure B.36: The implementation of the sliding variable for the MIMO control design in Simulink.

Appendix C

Additional Control Coefficient Transformation Results

In this chapter, the results of using the control coefficient transformations in (T1)-(T3) for simulation case 1 are presented. The results for the saturation controller are presented in section C.1, for the STA in C.2, and for the GSTA in C.3.

C.1 Saturation Controller

The results of using the different control coefficient transformations in the design of the saturation controller for case 1 are shown in Figure C.1. The performance measures for case 1 can be found in Table 7.2. The control gains are chosen for the three different transformations as

(T1) $k_{e_1} = 0.5, \varepsilon = 0.1$

(T2) $k_{e_1} = 17.5, \varepsilon = 0.1$

(T3) $k_{e_1} = 17.5, \varepsilon = 0.1$

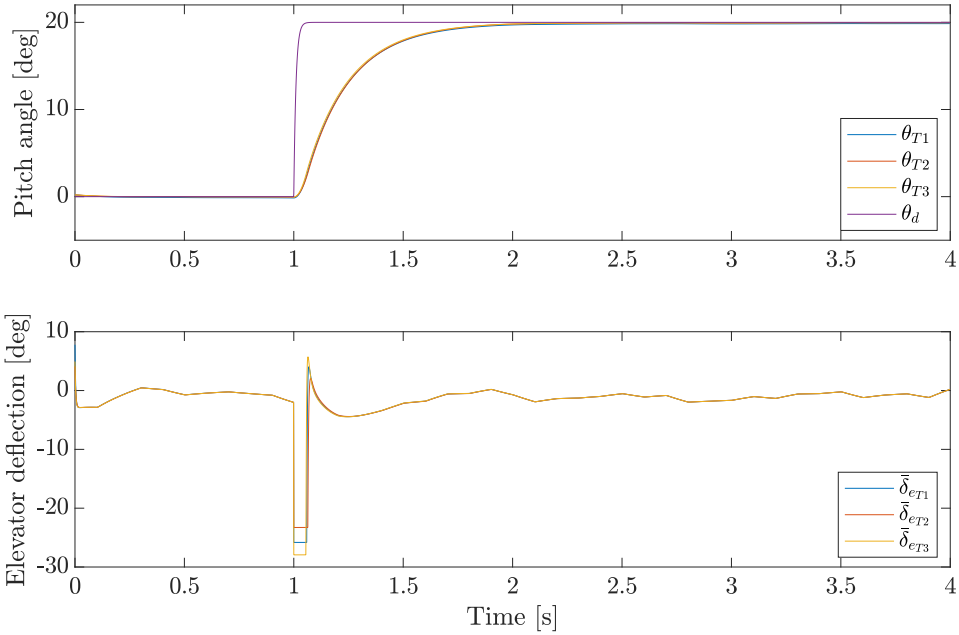

Figure C.1: The pitch angle tracking results and control signals for the single-input saturation controller applied to the decoupled longitudinal model for case 1. The pitch angle θ_{T1} and elevator deflection $\bar{\delta}_{e_{T1}}$ are the results for transformation (T1), θ_{T2} and $\bar{\delta}_{e_{T2}}$ are the results for transformation (T2), and θ_{T3} and $\bar{\delta}_{e_{T3}}$ are the results for transformation (T3).

C.2 The STA

The results of using the different control coefficient transformations described in (T1)-(T3) in the design of the STA for case 1 are shown in Figure C.2. The performance measures for case 1 can be found in Table 7.3. The control gains are chosen for the three different transformations as

(T1) $k_{e_1} = 0.7, k_{e_2} = 0.008$

(T2) $k_{e_1} = 20, k_{e_2} = 1$

(T3) $k_{e_1} = 20, k_{e_2} = 1$

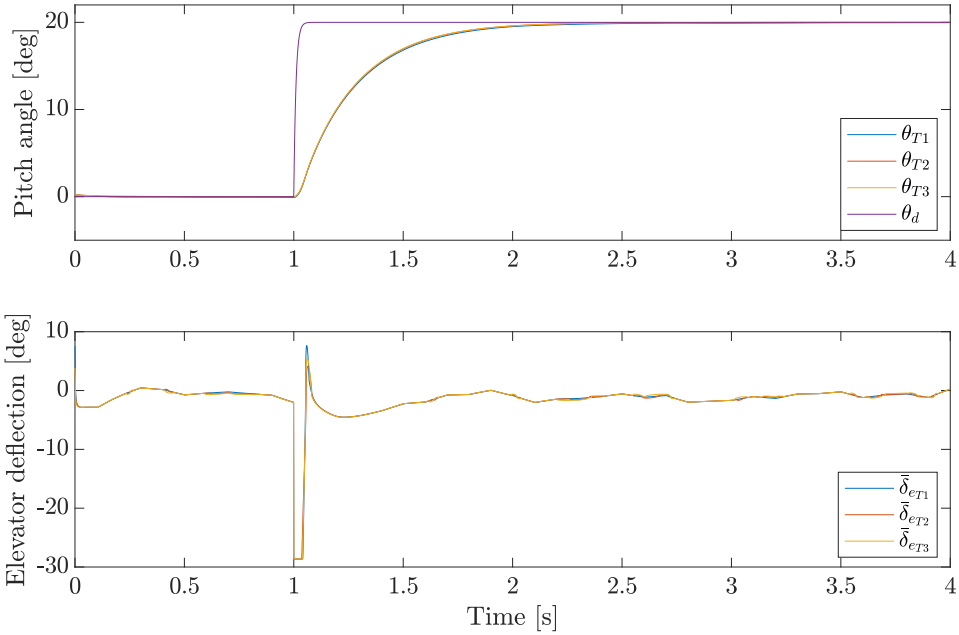

Figure C.2: The pitch angle tracking results and control signals for the single-input STA applied to the decoupled longitudinal model for case 1. The pitch angle θ_{T1} and elevator deflection $\bar{\delta}_{e_{T1}}$ are the results for transformation (T1), θ_{T2} and $\bar{\delta}_{e_{T2}}$ are the results for transformation (T2), and θ_{T3} and $\bar{\delta}_{e_{T3}}$ are the results for transformation (T3).

C.3 The GSTA

The results of using the different control coefficient transformations described in (T1)-(T3) in the design of the GSTA for case 1 are shown in Figure C.3. The performance measures for case 1 can be found in Table 7.5. The control gains are chosen for the three different transformations as

(T1) $\beta_{e_g} = 0.001, k_{e_1} = 0.5, k_{e_2} = 0.2$

(T2) $\beta_{e_g} = 0.03, k_{e_1} = 24, k_{e_2} = 15$

(T3) $\beta_{e_g} = 0.03, k_{e_1} = 24, k_{e_2} = 15$

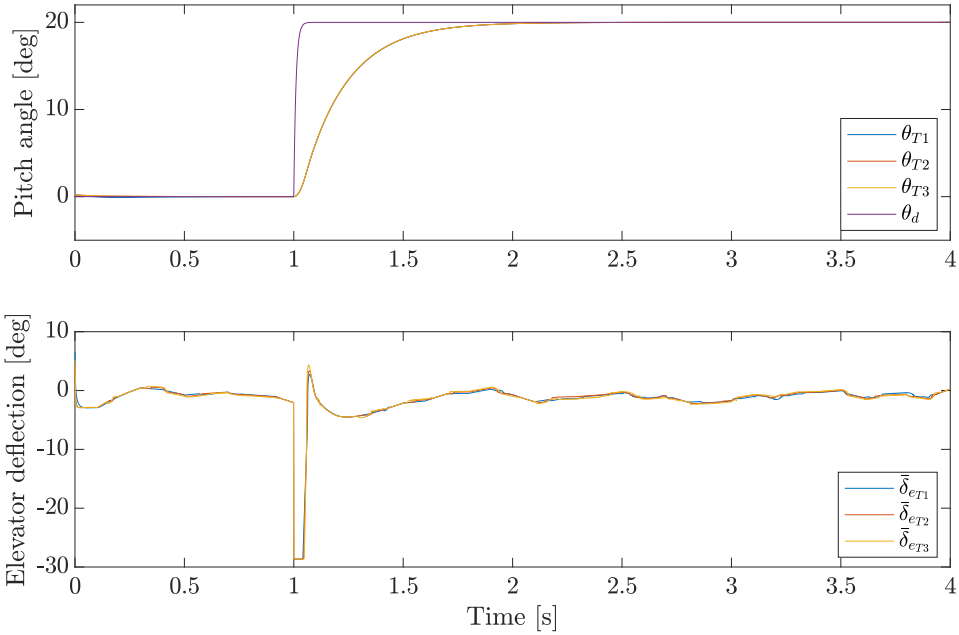

Figure C.3: The pitch angle tracking results and control signals for the single-input GSTA applied to the decoupled longitudinal model for case 1.The pitch angle θ_{T1} and elevator deflection $\bar{\delta}_{e_{T1}}$ are the results for transformation (T1), θ_{T2} and $\bar{\delta}_{e_{T2}}$ are the results for transformation (T2), and θ_{T3} and $\bar{\delta}_{e_{T3}}$ are the results for transformation (T3).

Appendix D

Additional 6DOF Simulation Results

D.1 Flight Paths for Case 1 and Case 2

This chapter contains the waypoint following performance of the SISO control design for case 1 in section D.1.1, and the performances of the MIMO control designs for case 1 in section D.1.2. The flight paths of the SISO and MIMO control designs for case 2 are presented in sections 8.2 and 8.3, respectively.

D.1.1 All SISO Control Designs for Case 1

The flight paths for all the SISO control designs for case 1 are shown in Figure D.1.

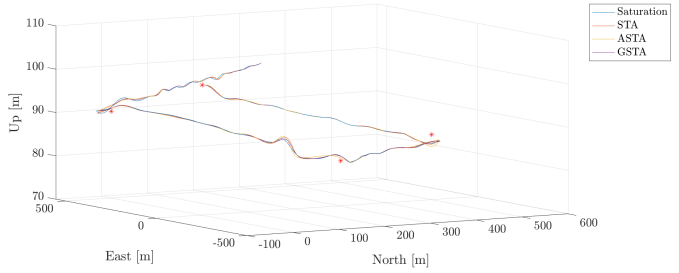

(a) North-East-Up view of the flight paths.

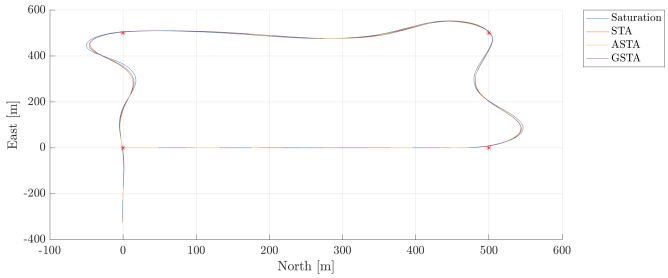

(b) North-East view of the flight paths.

Figure D.1: The flight paths of all the SISO algorithms for case 1.

D.1.2 All MIMO Control Designs for Case 1

The flight paths for all the MIMO control designs for case 1 are shown in Figure D.2.

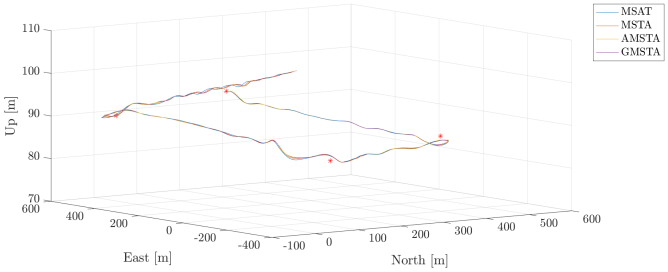

(a) North-East-Up view of the flight paths.

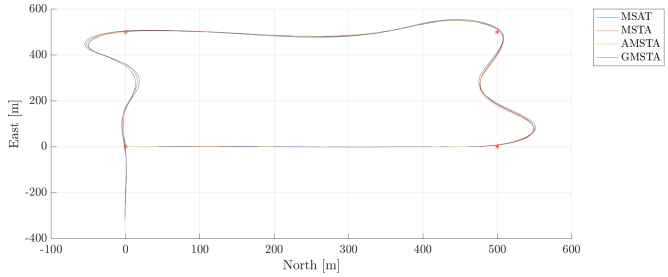

(b) North-East view of the flight paths.

Figure D.2: The flight paths of all the MIMO algorithms for case 1.

D.2 Control Gains and System Parameters

In this section, the control gain configurations and other system parameters for the SISO and MIMO control designs are presented for simulation cases 1 and 2. The parameters

for the SISO designs are presented in subsection D.2.1, and for the MIMO designs in subsection D.2.2. The choice of control gains and system parameters for case 3 and case 4 can be found in subsection D.2.3.

D.2.1 The SISO Control Designs

The sliding surface gain is the same for all controllers and simulation cases, and is chosen as $a_{\phi_1} = a_{\theta_1} = 5$ rad/s. The rest of the control gains and system parameters can be found in Table D.1.

Simulation Case 1							
Saturation		**STA**		**ASTA**		**GSTA**	
k_a	35	k_{a_1}	11	ω_{a_1}	1	k_{a_1}	7
k_e	30	k_{a_2}	5	γ_{a_1}	1	k_{a_2}	2
ε	1	k_{e_1}	7	ϵ_a	0.1	β_{a_g}	2
		k_{e_2}	1	λ_a	0.1	k_{e_2}	6
				α_{a_0}	5	k_{e_2}	0.1
				α_{a_m}	0.001	β_{e_g}	2
				ω_{e_1}	0.6		
				γ_{e_1}	0.6		
				ϵ_e	0.05		
				λ_e	0.05		
				α_{e_0}	5		
				α_{e_m}	0.1		
Simulation Case 2							
Saturation		**STA**		**ASTA**		**GSTA**	
k_a	30	k_{a_1}	11	ω_{a_1}	2	k_{a_1}	7
k_e	25	k_{a_2}	5	γ_{a_1}	1	k_{a_2}	2
ε	1	k_{e_1}	8	ϵ_a	0.4	β_{a_g}	2
		k_{e_2}	2	λ_a	0.1	k_{e_2}	6
				α_{a_0}	5	k_{e_2}	0.1
				α_{a_m}	0.05	β_{e_g}	2
				ω_{e_1}	0.6		
				γ_{e_1}	0.6		
				ϵ_e	0.1		
				λ_e	0.05		
				α_{e_0}	5		
				α_{e_m}	0.1		

Table D.1: The choice of control gains and system parameters for the SISO control designs for simulation cases 1 and 2.

D.2.2 The MIMO Control Designs

The sliding surface gain k_Γ is the same for all controllers and simulation cases, and is chosen as $k_\Gamma = 5$ rad/s. The rest of the control gains and system parameters can be found in Table D.2.

Simulation Case 1							
MSAT		**MSTA**		**AMSTA**		**GMSTA**	
K	30	k_1	23	ω_1	5	k_1	8
ε	0.5	k_2	17	γ_1	5	k_2	11
		k_3	0.1	ϵ_1	3	k_3	1
		k_4	13	α_0	5	α_g	0.4
				σ_T	0.4	β_g	5
						p_g	0.5
						q_g	1
						γ_g	0
Simulation Case 2							
MSAT		**MSTA**		**AMSTA**		**GMSTA**	
K	35	k_1	3	ω_1	80	k_1	6
ε	0.5	k_2	40	γ_1	40	k_2	11
		k_3	0.1	ϵ_1	0.01	k_3	0.8
		k_4	15	α_0	16	α_g	0.4
				σ_T	2	β_g	4
						p_g	0.5
						q_g	1
						γ_g	0

Table D.2: The choice of control gains and system parameters for the MIMO control designs for simulation cases 1 and 2.

D.2.3 Simulation Case 3 and Case 4

In this section, the control gains and system parameters for the control designs considered for case 3 and case 4 are presented. They can be found in Table D.3. The sliding variable gains for the SISO and MIMO control designs are chosen as $a_{\phi_1} = a_{\theta_d} = k_\Gamma = 5$ rad/s.

Simulation Case 3							
Saturation		**GSTA**		**MSAT**		**GMSTA**	
k_a	35	k_{a_1}	8	K	28	k_1	7
k_e	12	k_{a_1}	1.2	ε	0.8	k_2	8
ε	1	β_{a_g}	4			k_3	0.5
		k_{a_1}	1			α_g	0.00002
		k_{a_1}	0.0007			β_g	3
		β_{a_g}	8			p_g	0.5
						q_g	1
						γ_g	0
Simulation Case 4							
MSAT		**MSTA**		**AMSTA**		**GMSTA**	
k_a	35	k_{a_1}	8	K	35	k_1	7
k_e	13	k_{a_1}	1.2	ε	1	k_2	6
ε	1	β_{a_g}	4			k_3	0.5
		k_{a_1}	2			α_g	0.00002
		k_{a_1}	0.0007			β_g	3
		β_{a_g}	4			p_g	0.5
						q_g	1
						γ_g	0

Table D.3: The choice of control gains and system parameters for the saturation, the GSTA, the MSAT, and the GMSTA control designs for simulation case 3 and 4.

D.2.4 Choice of Control Gains for Different Actuator Dynamics

In this section, the control gains and system parameters for the saturation, the GSTA, the MSAT, and the GMSTA control designs for case 2 with different actuator dynamics are presented. They can be found in Table D.4. The sliding variable gains for the SISO and MIMO control designs are chosen as $a_{\phi_1} = a_{\theta_d} = k_\Gamma = 5$ rad/s.

Case 2 when $T_u = 0.1$ s							
Saturation		**GSTA**		**MSAT**		**GMSTA**	
k_a	35	k_{a_1}	9	K	25	k_1	15
k_e	8	k_{a_1}	0.05	ε	1	k_2	20
ε	0.5	β_{a_g}	3			k_3	1
		k_{a_1}	5			α_g	0.3
		k_{a_1}	0.1			β_g	0.5
		β_{a_g}	0.5			p_g	0.5
						q_g	1
						γ_g	0

Case 2 when using second-order dynamics							
MSAT		**MSTA**		**AMSTA**		**GMSTA**	
k_a	35	k_{a_1}	6	K	60	k_1	5
k_e	30	k_{a_1}	0.05	ε	2	k_2	10
ε	1.5	β_{a_g}	3			k_3	0.6
		k_{a_1}	4			α_g	0.1
		k_{a_1}	0.01			β_g	4
		β_{a_g}	4			p_g	0.5
						q_g	1
						γ_g	0

Table D.4: The choice of control gains and system parameters for the saturation, the GSTA, the MSAT, and the GMSTA control designs for simulation case 2 with different actuator dynamics.

D.2.5 Choice of Control Gains for Different Sampling Frequencies

In this section, the control gains and system parameters for the saturation, the GSTA, the MSAT, and the GMSTA control designs for case 2 with different sampling frequencies are presented. They can be found in Table D.5. The sliding variable gains for the SISO and MIMO control designs are chosen as $a_{\phi_1} = a_{\theta_d} = k_\Gamma = 5$ rad/s.

Sampling frequency $f_s = 100$ Hz							
Saturation		**GSTA**		**MSAT**		**GMSTA**	
k_a	30	k_{a_1}	7	K	35	k_1	6
k_e	25	k_{a_1}	2	ε	0.5	k_2	11
ε	1	β_{a_g}	2			k_3	0.8
		k_{a_1}	6			α_g	0.4
		k_{a_1}	0.1			β_g	4
		β_{a_g}	2			p_g	0.5
						q_g	1
						γ_g	0
Sampling frequency $f_s = 20$ Hz							
MSAT		**MSTA**		**AMSTA**		**GMSTA**	
k_a	50	k_{a_1}	5	K	110	k_1	6
k_e	35	k_{a_1}	0.1	ε	4	k_2	8
ε	3	β_{a_g}	2			k_3	0.3
		k_{a_1}	1.85			α_g	0.2
		k_{a_1}	0.1			β_g	3
		β_{a_g}	5			p_g	0.5
						q_g	1
						γ_g	0

Table D.5: The choice of control gains and system parameters for the saturation, the GSTA, the MSAT, and the GMSTA control designs for simulation case 2 with different sampling frequencies.

Jenny Bogen Griffiths

Multivariable Super-Twisting Control of Fixed-Wing UAVs

NTNU
Kunnskap for en bedre verden